

Studying Transition Metal Chemistry inside a Metal-Organic Framework

A thesis presented to
The School of Physical Sciences
at
The University of Adelaide
in fulfilment of the requirements for
The Degree of
Doctor of Philosophy in Chemical Science
by
Michael Huxley



THE UNIVERSITY
of ADELAIDE

Adelaide, Australia

March 2019

Declaration

I certify that this work contains no material which has been accepted for the award of any other degree or diploma in my name, in any university or other tertiary institution and, to the best of my knowledge and belief, contains no material previously published or written by another person, except where due reference has been made in the text. In addition, I certify that no part of this work will, in the future, be used in a submission in my name, for any other degree or diploma in any university or other tertiary institution without the prior approval of the University of Adelaide and where applicable, any partner institution responsible for the joint-award of this degree.

I acknowledge that copyright of published works contained within this thesis resides with the copyright holder(s) of those works.

I also give permission for the digital version of my thesis to be made available on the web, via the University's digital research repository, the Library Search and also through web search engines, unless permission has been granted by the University to restrict access for a period of time.

I acknowledge the support I have received for my research through the provision of an Australian Government Research Training Program Scholarship.



Michael Huxley

Publications

Huxley, M., Coghlan, C.J., Burgun, A., Tarzia, A., Sumida, K., Sumbly, C.J., Doonan, C.J., *et al.* 2016, Site-specific metal and ligand substitutions in a microporous Mn²⁺-based metal-organic framework. *Dalton Trans* 45 (10), 4431.

Huxley, M. T., Coghlan, C.J., Bloch, W.M., Burgun, A., Doonan, C.J., Sumbly, C.J., *et al.* 2017, X-ray crystallographic insights into post-synthetic metalation products in a metal-organic framework. *Phil. Trans. R. Soc. A* 375 (2084), 20160028.

Huxley, M. T., Burgun, A., Ghodrati, H., Coghlan, C.J., Lemieux, A., Champness, N.R., Huang, D.M., Doonan, C.J., Sumbly, C.J., *et al.* 2018, Protecting-Group-Free Site-Selective Reactions in a Metal-Organic Framework Reaction Vessel. *J Am Chem Soc* 140 (20), 6416.

Acknowledgements

It has been a privilege to work under the supervision of Prof. Christian J. Doonan and Prof. Christopher J. Sumbly, whom I sincerely thank for their constant support throughout my PhD. The guidance from every member of the Sumbly-Doonan group has been outstanding, and I particularly acknowledge the guidance I have received from Dr. Alexandre Burgun, Dr. Kenji Sumida, Kate Flint, Ricardo Peralta, Oliver Linder-Patton, Dr. Campbell Coghlan, Hanieh Ghodrati, Rosemary Young, Em. Prof. Richard Keene and Dr. Witold Bloch.

Aspects of this work were performed in conjunction with Prof. Neil Champness and Prof. Mike George from the University of Nottingham, UK. Travelling to Nottingham to work for two months in 2016 was an inspiring experience and I thank Prof. Champness and Prof. George for their support and the provision their laboratories during this time.

Much of the X-ray crystallography work conducted in this project was performed at the Australian Synchrotron using the MX1 and MX2 beamlines. The outcomes of the project revolve heavily around the ability to observe chemical process taking place within MOFs using X-ray crystallography, thus access to such an outstanding facility has been pivotal to the success of the project. I extend a sincere thankyou to the MX team, particularly Dr Jason Price and Dr Alan Riboldi-Tunncliffe for their willingness to accommodate our photocystallography experiments which required significant alterations to the standard MX1 and MX2 beamline operating procedures.

Analysis of the chemical composition of MOF crystals is critical to determining the outcome of chemical reactions taking place within the materials. The Energy Dispersive X-ray Spectroscopy (EDX) and Inductively Coupled Plasma Mass Spectrometry (ICP-MS) facilities provided by Adelaide Microscopy was integral to the analysis of MOF samples throughout the project. I thank the staff at Adelaide Microscopy for their support and training in the use of their instruments.

Throughout the last four years the support of my family and friends has been steadfast. Thankyou to my parents, Karen and Lynton, for their constant support and encouragement without which this undertaking would have been immeasurably more difficult.

Finally, thank you to my little feathered friend Fred, you filled the last nineteen years with so much laughter and happiness, and I will miss you always.

Table of Contents

Thesis Abstract	vi
1.0 Chapter 1: Introduction	
1.1 Chemical reactivity inside heterogenous matrices	1
1.2 The advantages of the crystal lattice	2
1.3 Metal-organic Frameworks: Robust, crystalline reaction matrices	9
1.4 The case for MOFs in heterogeneous chemistry	11
1.5 Metal-organic Frameworks: Crystallographic insights into catalysis	18
1.6 Contextual Statement	22
1.7 References	26
2.0 Chapter 2: X-ray Crystallographic Insights into Post-synthetic Metalation Products in a MOF	
Statement of Authorship	34
2.1 Abstract	36
2.2 Introduction	36
2.3 Experimental	38
2.4 Results and Discussion	40
2.5 Conclusion	48
2.6 Additional Information	49
2.7 References	50
3.0 Chapter 3: Site-Specific Metal and Ligand Substitutions in a Microporous Mn²⁺-Based MOF	
Statement of Authorship	54
3.1 Abstract	57
3.2 Introduction	57
3.3 Experimental Section	58
3.4 Results and Discussion	61
3.5 Summary and Outlook	70
3.6 Acknowledgements	71
3.7 Notes and References	71

4.0	Chapter 4: Protecting-Group-Free Site-Selective Reactions in a MOF Reaction Vessel	
	Statement of Authorship	74
4.1	Abstract	78
4.2	Introduction	78
4.3	Results and Discussion	80
4.4	Conclusion	89
4.5	Experimental	90
4.6	Associated Content	95
4.7	Acknowledgements	95
4.8	References	95
5.0	Chapter 5: Photochemistry of $1 \cdot [\text{Mn}(\text{CO})_3\text{Br}]$	
5.1	Introduction	99
5.2	Results and Discussion	126
5.3	Conclusions and Future Directions	152
5.4	References	155
6.0	Chapter 6: Conclusion and Future Outlook	
6.0	Conclusion and Future Outlook	164
7.0	Chapter 7: Appendices	
7.1	Supplementary Information for Chapter 2	168
7.2	Supplementary Information for Chapter 3	177
7.3	Supplementary Information for Chapter 4	188
7.4	Computational Procedures for Chapter 4	231
7.5	Supplementary Information for Chapter 5	240
7.6	Computational Procedures for Chapter 5	271

Thesis Abstract

Metal-organic Frameworks (MOFs) are porous, crystalline materials built from metal 'nodes' and interconnecting organic ligands. The combination of crystallinity, porosity and building block design allows MOFs to be tailored at the nanoscale and functionalised to suit specific applications. Reactive metal complexes can be installed inside MOFs, producing well-defined reactive sites with long range order, thereby allowing metal-centred chemical processes to be studied in-situ via X-ray crystallography. Furthermore, the physical isolation of active metal complexes prevents unwanted side-reactions such as cluster formation from occurring, allowing reactive species to be trapped within the crystalline matrix while the surrounding microenvironment can be tuned, via judicious ligand design, to augment their reactivity.

The Mn-based MOF $[\text{Mn}_3(\text{L})_2(\text{L}')]$ (where L = bis-(4-carboxyphenyl-3,5-dimethylpyrazolyl)methane; **1**) is well suited to this application because its pores are decorated with well-defined N,N-chelation sites that bind metal complexes, which allows **1** to be post-synthetically metalated and the resulting metal complexes can be studied using X-ray crystallography. In chapter 2, a series of transition metal nitrate complexes were incorporated within **1** and their structures determined. The structural features of the complexes were compared to those of solution and solid-state analogues to elucidate the effect of the MOF pore-environment on their coordination chemistry.

The distribution of metal sites within a MOF framework is important to consider for heterogenous catalysis applications; quantitative metalation can result in the MOF pores becoming 'burdened' with metal sites that impede mass transport through the crystal. Work in chapter 3 demonstrates that by using a mixed ligand synthesis approach, the ligand bearing the free N,N-chelating site in **1** could be partially replaced with a modified ligand that is incapable of metalation. The resulting structure possesses the same topology as **1** but is doped, specifically in the non-coordinated donor sites, with a ligand that will not readily bind to metal complexes, allowing the overall degree of metalation to be tuned.

Work in chapter 4 utilised the observation that within **1** the metal complexes are site-isolated and separated by 13 Å. By incorporating a Mn(I) azide complex within **1**, the site-isolation was harnessed to perform site-selective 'click' chemistry on small dialkynes that are shorter than the azide separation. Within **1**, this 'click' chemistry cycle, using both simple mono- and di-alkynes, was monitored using X-ray

crystallography. This work demonstrates that the nanoscale spatial control of reactive sites within MOFs, supported with X-ray crystallographic insights, can affect highly selective chemical transformations.

Finally in chapter 5, advancing the concept of site-isolation within MOFs, **1** was functionalised with a Mn(I) carbonyl complex. When exposed to visible light the complex releases a portion of its carbonyl ligands which escape the porous crystalline lattice. It was envisaged that photolysis could generate site-isolated, reactive metal complexes that can activate small molecules. Preliminary experiments demonstrated that CO is successfully liberated under photolysis, while in-situ X-ray crystallography suggests that the CO ligands are replaced by weakly coordinating solvent molecules. In this way, **1** acts as a matrix for isolating and studying the reactive metal complexes formed using photolysis.

Chapter 1. Introduction

1.1 Chemical reactivity inside heterogenous matrices

The use of transition metal catalysts is integral to the preparation of commodity and fine-chemicals.¹⁻³ Transition metal catalysts are defined by two broad classes: homogenous and heterogeneous. These are classified by whether the catalyst exists in the same phase as the reagents (homogenous) or as a 'solid' with which the reagents interact (heterogeneous).⁴ Homogenous catalysts are derived from discrete transition metal complexes and benefit from the well-developed field of organometallic and coordination chemistry which allows the chemical properties of the transition metal centre to be precisely modified via the appended ligands.⁵⁻⁶ Accordingly, the reactivity and selectivity of molecular catalysts can be controlled and through a variety of spectroscopic techniques a mechanistic understanding developed. This process has led to the design and synthesis of more efficient catalysts. However, a drawback of homogenous catalysts is that they can be difficult to separate from their reaction mixtures,⁷⁻⁸ furthermore, they can be expensive due to the prevalence of rare metals. The development of catalysts formed from cheaper earth abundant metals such as Fe, Co and Ni is a burgeoning field, but the active sites of these catalysts are often protected by sterically demanding ligands⁹⁻¹¹ to prevent decomposition. The result is an increase in their complexity and subsequent cost, as well as reduced catalytic activity.¹²⁻¹³ Compared to homogeneous systems, heterogeneous catalysts offer key advantages, for example they are typically robust, can be separated from the reaction mixture and the active sites are not encumbered by sterically demanding ligands.¹²

Owing to the positive attributes of both homogenous and heterogenous catalysts, a significant body of research has focused on 'heterogenising' homogenous catalysts to obtain new materials which combine the best attributes of both regimes. Perhaps the simplest embodiment of this concept are the 'solid-state catalysts' in which single-crystals of transition metal complexes can be used to perform gas-phase catalysis. At a practical level crystallinity ensures a uniform chemical- and micro-environment for the catalyst throughout the material, while allowing the compound to be structurally characterised via X-ray crystallography. As will be revealed in later chapters, X-ray crystal structures obtained from solid-state catalysts (and reactive complexes immobilised in crystals) have provided valuable insight into the reactive intermediates postulated to play key roles in transition metal chemistry. More recently, the

burgeoning field of Metal-organic Frameworks (MOFs) has demonstrated immense potential in heterogeneous catalysis. MOFs are composed of metal ions interconnected by organic ligands to form a 3D-extended structure with a high degree of crystallinity and porosity. The robust structure of MOFs is a key advantage over molecular crystal catalysts in industrial applications. As will be elaborated in later chapters, MOFs can be functionalised with active transition metal catalysts which are accessible to reagents via the porous network within their extended structure. With structural insights from X-ray crystallography, the supporting crystal lattice can be systematically varied to produce iso-reticular materials in which the environment surrounding the immobilised catalyst is fine-tuned to form idealised nano-scale reaction vessels reminiscent of enzyme reactive sites. Together, MOFs and solid-state materials are leading a new paradigm in the application and study of transition metal chemistry, guided by the structural insight provided by X-ray crystallography.

1.2 The advantages of the crystal lattice

Important transition metal-mediated processes such as C-H bond activation are often postulated to occur via highly reactive intermediates, such as coordinatively unsaturated complexes formed from loss of coordinating ligands, for example under photolysis.^{2, 14-16} Although the existence of such species can be inferred from spectroscopic techniques, their direct structural characterisation is hampered by their inherent instability. The single crystal provides a unique environment in which the constituent molecules are highly ordered and protected from coordinating solvent. In recent years, this combination of order and protective environment has provided remarkable insight into the structure of highly reactive transition metal complexes that are near impossible to structurally characterise outside the crystal lattice. By housing reactive metal complexes in a crystal lattice at low temperature, unstable intermediates or products can be stabilised and characterised, without the need to grow crystals of species that would undoubtedly decompose outside the protective environment of the crystal lattice. A notable example is the direct observation of nitride complexes, which are formed when a metal azide undergoes photolysis to give a nitride and N₂ gas.¹⁷ Nitrides are notoriously reactive,¹⁸ readily undergoing decomposition via amination of adjacent C-H bonds, insertion into metal-ligand bonds or dimerization to give the corresponding N₂ complex.¹⁹⁻²⁴ The reactivity of nitrides towards almost any substrate precludes their structural characterisation using conventional X-ray crystallography techniques. To overcome this limitation, Das *et al.* prepared a single crystal of the azide complex [Ru₂(N,N'-bis(3,5-dichlorophenyl)formamidinate)₄(N₃)] which was photolysed at 95 K.¹⁷ The resulting

nitride complex $[\text{Ru}_2(\text{N},\text{N}'\text{-bis}(3,5\text{-dichlorophenyl})\text{formamidinate})_4(\text{N})]$ was isolated within the crystal lattice, with X-ray crystallography revealing the nitride complex and lattice-confined N_2 by-product which resides in a cavity formed by the aromatic components of the formamidinate ligands (Figure 1.2.1). The crystal was warmed in an attempt to induce amination of an aromatic C-H bond, however the crystals became severely cracked upon warming, which the authors attribute to the movement of N_2 gas within the crystal. This latter point highlights the sensitivity of single crystals (of discrete complexes) towards cracking when strained by dramatic structural changes or volatile 'solvates'; this issue is mitigated to some extent by the porosity and 3D structural interconnectivity within MOFs.

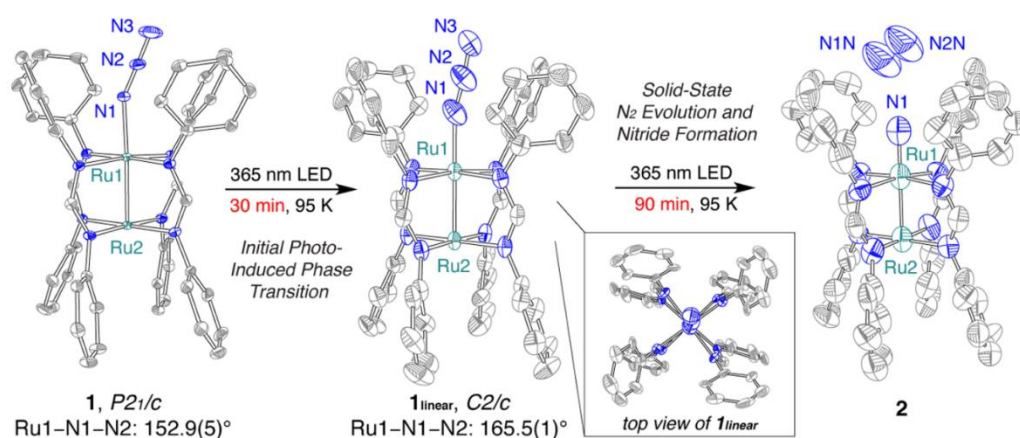


Figure 1.2.1: Under UV photolysis at 95 K the Ru₂ azide precursor forms the Ru₂ nitride and N₂ by-product which are protected by the cavity created by the aromatic components of the formamidinate ligands, allowing the photoproduct to be characterised via X-ray crystallography. Figure from ref. ¹⁷.

Single crystals can be susceptible to crystal cracking if the changes in coordination environment during the reaction of interest are significant. One way to attenuate these effects is to encapsulate the precursor complex of interest within a spectator lattice that provides structural integrity but is not (or minimally) disrupted by structural changes in the target complex. The ultimate extension of this concept is the use of MOFs which provide a rigid, three-dimensionally interconnected framework. However, simpler solid-state systems can allow a similar effect via use of large spectator molecules such as bulky tetraphenylborate anions or metal-organic cages. A notable example of the cage strategy was published by Fujita *et al.* who encapsulated a $[\text{Cp}'\text{Mn}(\text{CO})_3]$ (Cp' = 1-methyl cyclopentadienyl) complex within a coordination cage composed of Pd(II) nodes and triazine-derived ligands.²⁵ The cage molecules serve as a crystalline host for the guest Mn(I) complex which is well ordered within the cage cavity. Metal

carbonyl complexes are susceptible to undergoing CO loss under photolysis, forming reactive coordinatively unsaturated complexes which are implicated in several catalytic cycles. Although coordinatively unsaturated photoproducts have been characterised spectroscopically,²⁶⁻³¹ their reactivity precludes their direct observation using conventional crystallographic techniques. When a single crystal is subjected to UV photolysis at 100 K, the cage-encapsulated Mn(I) carbonyl precursor loses a CO ligand to form the 16e⁻ dicarbonyl complex [Cp'Mn(CO)₂]. The dicarbonyl complex was directly observed in the X-ray crystal structure, with the photo-dissociated CO accommodated within the cage adjacent to the Mn complex. The crystal structure revealed the dicarbonyl complex to be pyramidal rather than planar, which is supported by earlier computational results³²⁻³³ but was impossible to prove via conventional spectroscopy techniques using matrix isolation. Since the guest is encapsulated, changes in its structure such as CO loss, do not impact the crystal packing, thereby allowing dynamic processes to be mapped in single crystals without cracking the crystal. The low density packing of the manganese carbonyl moieties within the cage cavities (which required the use of a methyl substituted Cp' ligand) provides room for the photodissociated CO and thereby prevents the rapid re-combination of the dissociated fragments. When a single crystal of the metal carbonyl complex was photolyzed under equivalent conditions, no reaction was observed because the tight crystal-packing promotes the rapid re-combination of photodissociated fragments. Thus the low-density immobilisation of the precursor complex is critical for the preservation of the reactive dicarbonyl complex, which provides structural insights that cannot be obtained via conventional techniques.

The photocrystallography technique, in which a precursor complex is housed in a single crystal and converted into the reactive target in-situ, demonstrates the power of the single crystal as a matrix for the isolation of reactive transition metal complexes. In an extension of this concept, single crystals that possess a degree of porosity can facilitate chemical reactions between the immobilised transition metal complexes and small guest molecules, particularly gases.³⁴⁻³⁶ Early examples of solid-state reactivity in single-crystals extend back to the 1960s but have become more prevalent and insightful in recent years.³⁷⁻⁴¹ Generally, these systems consist of single-crystals of molecular complexes to which reagents gain access via the inefficient packing of large anions or bulky ligands. As will be discussed, the single crystal can offer exquisite control over the reactivity of immobilised catalysts due to the highly ordered, uniform microenvironment replicated throughout the crystal lattice. These subtle effects are reminiscent of the finely tuned arrangement of components in enzyme active sites, the elucidation of such relationships via crystallography has the potential to revolutionise catalysis by providing insight into the relationship between reactivity and structure.

The reaction between the solid-state complex $[\text{Pt}(\text{acac})_2]$ (acac= acetylacetonate) and I_2 to form the oxidative addition product *trans*- $[\text{Pt}(\text{I})_2(\text{acac})_2]$ was reported in 1973 by Cook *et al.* and serves as an early example of solid-state-gas reactions.⁴² More recently, several examples of hydrogenation of unsaturated hydrocarbon complexes within single crystals have been reported. In 1989 Siedle *et al.* reported the preparation of solid-state material, $[(\text{Ph}_3\text{P})_2\text{Ir}(\text{C}_8\text{H}_{12})]_3\text{PW}_{12}\text{O}_{40}$, comprising of an Ir(I) complex which resides in the interstitial sites of the polyoxometalate ($\text{PW}_{12}\text{O}_{40}^{3-}$) lattice. When exposed to D_2 gas, the coordinated cyclooctene was hydrogenated to form partially deuterated cyclooctane.⁴³ Similarly, Bianchini *et al.* successfully hydrogenated ethylene coordinated to an Ir(I) phosphine di-hydride, $[\text{Ir}(\text{triphos})(\text{H})_2(\text{C}_2\text{H}_2)]\text{BPh}_4$, by reacting the solid-state material with H_2 gas which permeates through the crystal lattice.³⁴ The reaction was performed at 70°C with H_2 gas and forms ethane gas and a 1:1 mixture of the hydride bridged dimer $[\text{Ir}(\text{triphos})(\text{H})_2]_2$ and coordinatively unsaturated dihydride $[\text{Ir}(\text{triphos})(\text{H})_2]$ in the solid-state. When exposed to ethylene gas, the dimer fails to reform the starting material and is therefore not active as a catalyst for ethylene hydrogenation. The close proximity of the Ir(I) moieties in the solid-state allows the coordinatively unsaturated dihydride to undergo dimerization. However, the unsaturated complex can be stabilised in the solid-state by replacing the tetra-arylborate anions for the larger polyoxometalate ($\text{PW}_{12}\text{O}_{40}^{3-}$) which induces greater separation of the Ir(I) centres and prevents dimerization. This work highlights the activity of organometallic catalysts in the solid state as well as the site-isolating properties of the crystal lattice, a concept of tremendous interest in MOF chemistry.¹²

Seminal work by Brookhart *et al.* reported the immobilisation of the Ir(I) pincer complex $[\text{Ir}(\text{C}_6\text{H}_2(\text{OP}(\text{C}_6\text{H}_2(\text{CF}_3)_3-2,4,6)_2-1,3)(\text{N}_2))]$ in a single crystal.⁴¹ The Ir centre is accessible to small ligands via solvent filled pores that run through the material, allowing the N_2 ligand to undergo facile exchange with CO , NH_3 , C_2H_2 and H_2 to yield the corresponding Ir(I) complexes (in the case of H_2 , the product is a dihydride dihydrogen complex). The ligand exchange reactions occur via a single-crystal to single-crystal transition and the products were characterised via X-ray crystallography, in each case only the transition took place without disrupting the unit cell of the crystal. Coordinated ethylene can undergo hydrogenation in the presence of H_2 , generating ethane. However, the small channels within the single crystal do not admit the larger substrate propylene. When the surface Ir(I) sites are 'poisoned' using CO gas, the material demonstrates 25:1 selectivity in the hydrogenation of ethylene over propylene due to the size excluding properties of the molecular crystal.

A significant advancement of this field has emanated from Andrew Weller's research group at the University of Oxford. In 2012, Weller *et al.* reported the preparation of a Rh diphosphine complex, $[\text{Rh}(\text{iBu}_2\text{PCH}_2\text{CH}_2\text{P}^i\text{Bu}_2)(\eta^2, \eta^2\text{-NBA})][\text{BAR}^{\text{CF}_3}_4]$ (iBu = isobutyl group; NBA = norbornadiene, $\text{Ar}^{\text{CF}_3} = 3,5\text{-(CF}_3)_2\text{C}_6\text{H}_3$), which was characterised crystallographically.⁴⁴ The inefficient packing of the bulky $\text{BAR}^{\text{CF}_3}_4$ anions around the Rh(I) complex in the solid state allows small gaseous molecules to travel through the crystal and access the Rh(I) complexes without compromising the crystallinity of the material. The reaction between $[\text{Rh}(\text{iBu}_2\text{PCH}_2\text{CH}_2\text{P}^i\text{Bu}_2)(\eta^2, \eta^2\text{-NBA})][\text{BAR}^{\text{CF}_3}_4]$ and H_2 gas results in the hydrogenation of the norbornadiene C=C bond to form norbornane (NBA). Remarkably, the norbornane remains coordinated to the Rh centre as a σ -alkane complex due to the rigid crystalline lattice, allowing structural characterisation using X-ray crystallography (Figure 1.2.2). When dissolved, the σ -alkane complex immediately decomposes to form the zwitterionic complex featuring an aryl-bound $[\text{BAR}^{\text{CF}_3}_4]$. Structurally characterised σ -alkane complexes are extremely rare due to the poor ligating ability of alkanes.⁴⁵⁻⁴⁸ However, σ -alkane complexes are implicated as key reaction intermediates in C-H bond activation at metal centres, a process of tremendous importance in organic synthesis.¹⁵ Thus, the in-situ hydrogenation of an alkene complex within a single crystal offers a rare opportunity to obtain structural evidence of σ -alkane complexes (Figure 1.2.2). Since this seminal work, Weller *et al.* have published several papers in which the alkene, substituents of the phosphine ligand and tetra-arylborate anion have been varied.^{38-40, 49-51}

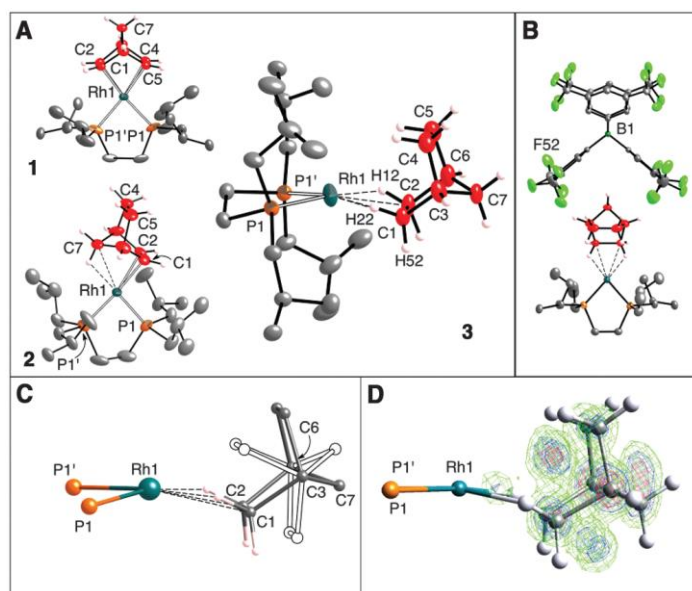


Figure 1.2.2 The reaction between the norbornadiene complex $[\text{Rh}(\text{iBu}_2\text{PCH}_2\text{CH}_2\text{P}^i\text{Bu}_2)(\eta^2, \eta^2\text{-NBA})][\text{BAR}^{\text{CF}_3}_4]$ and H_2 gas results in the hydrogenation of the norbornadiene C=C bond to form the norbornane complex. Figure adapted from ref. 44.

Highly unstable, transient species such as the σ -alkane complexes, nitrides and bare metal-cation photo-products discussed above are believed to be the critical reactive species in many organometallic transformations.^{2, 14-16} For example, σ -alkane complexes are implicated in key catalytic cycles either as a precursor for C-H activation of the alkane or as a 'virtual vacant site' in which the σ -alkane is readily displaced by an incoming substrate which reacts with the vacant metal site. The norbornane σ -alkane complex reported by Weller *et al.* also serves as a reactive precursor; the weakly coordinated alkane can be readily displaced by incoming substrates in a single-crystal to single-crystal transformation.³⁹⁻⁴⁰ When crystals of $[\text{Rh}(\text{Cy}_2\text{PCH}_2\text{CH}_2\text{PCy}_2)\text{NBA}][\text{BAr}^{\text{CF}_3}_4]$ are placed under an ethylene atmosphere, the corresponding bis-ethylene complex forms which slowly transforms into the butadiene complex via dehydrogenative coupling of the coordinated ethylene.³⁹ The bis-ethylene complex is not accessible via solution phase ligand exchange reactions due to the rapid decomposition of the product in solution to form the corresponding zwitterionic complex. Similarly, NBA can be exchanged for propene and butene to give $[\text{Rh}(\text{Cy}_2\text{PCH}_2\text{CH}_2\text{PCy}_2)(\text{propene})][\text{BAr}^{\text{CF}_3}_4]$ and $[\text{Rh}(\text{Cy}_2\text{PCH}_2\text{CH}_2\text{PCy}_2)(\text{butene})][\text{BAr}^{\text{CF}_3}_4]$ respectively. Neither of these complexes are inert: propene undergoes rapid H/D exchange via a facile oxidative addition mechanism, while the 1-butene introduced to $[\text{Rh}(\text{Cy}_2\text{PCH}_2\text{CH}_2\text{PCy}_2)\text{NBA}][\text{BAr}^{\text{CF}_3}_4]$ is largely converted to 2-butene upon coordination and then slowly converts to butadiene via transfer dehydrogenation and concomitant formation of butane. These results confirm the activity of immobilised molecular catalysts towards gaseous hydrocarbons and that these processes can be followed using X-ray crystallography, although degradation of the single-crystallinity prevented detailed analysis of bond lengths. It is notable that systems bearing long-range interconnectivity and permanent porosity, such as MOFs; could provide a more robust platform for such crystallography studies.

The microenvironment, enforced to nano-scale precision throughout the crystalline lattice, is a unique feature of the single crystal which can be harnessed to control the selectivity of chemical processes. Within the $[\text{Rh}(\text{Cy}_2\text{PCH}_2\text{CH}_2\text{PCy}_2)\text{NBA}][\text{BAr}^{\text{CF}_3}_4]$ crystal lattice (analogous to those described above), the bulky anions form an octahedral cage around the Rh cations. The resulting cavity allows the structural changes required at the Rh centre to occur during hydrogenation while providing enough spatial restriction to promote the desired chemistry.³⁹⁻⁴⁰ Weller *et al.* investigated this effect in a series of Rh diphosphine complexes, $[\text{Rh}(\text{Cy}_2\text{PCH}_2\text{CH}_2\text{PCy}_2)\text{NBD}][\text{BAr}^{\text{X}}_4]$ (where $\text{Ar}^{\text{X}} = 3,5\text{-X}_2\text{C}_6\text{H}_3$ and $\text{X} = \text{CF}_3, \text{Cl}, \text{F}, \text{H}$).⁴⁰ By influencing the microenvironment, anion substitution alters the rate at which the norbornadiene complex undergoes hydrogenation and the stability and preferred binding motif of the resulting σ -alkane complex. For instance, when the anion is functionalised with CF_3 substituents, the resulting *endo* σ -alkane complex is indefinitely stable; however the equivalent chloro-functionalised analogue produces a

different microenvironment and favours the *exo*- σ -alkane complex (See Figure 1.2.3 for *endo/exo* definition). The overall stability of the σ -alkane complex is reflected by the rate at which it decomposes to form the zwitterionic Rh-aryl complex in the solid state. The rate of NBD hydrogenation and composition of product (NBD, NBA or zwitterionic Rh complexes) was determined for each material under a set of standard conditions. The $\text{BAR}^{\text{CF}_3}_4$ material undergoes rapid and complete hydrogenation to give an indefinitely stable NBA σ -alkane complex. Conversely, the BAR^{H}_4 material forms an unstable NBA complex which immediately decomposes to give the zwitterionic Rh complex. Between these extremes are the halide functionalised tetra-aryl borate (BAR^{X}_4 , X= Cl, F) complexes; which undergo hydrogenation at a moderate rate and yield a mixture of predominantly zwitterionic complex with a portion of starting material and σ -alkane complex. Coordinatively unsaturated Rh(I) complexes, including $\text{Rh}(\text{Cy}_2\text{PCH}_2\text{CH}_2\text{PCy}_2)\text{NBA}[\text{BAR}^{\text{CF}_3}_4]$, catalyse the isomerisation of 1-butene to give a mixture of *trans*-2 and *cis*-butene. The stability of the σ -alkane complex in $\text{Rh}(\text{Cy}_2\text{PCH}_2\text{CH}_2\text{PCy}_2)\text{NBA}[\text{BAR}^{\text{CF}_3}_4]$ ensures that the active σ -alkane complex is available throughout the crystal, leading to rapid isomerisation of 1-butene. As expected, the BAR^{H}_4 analogue, in which the σ -alkane complex is completely decomposed to the inactive zwitterionic complex, show no activity towards butene isomerisation. These results demonstrate that the crystalline microenvironment can drastically influence the activity of solid-state catalysts by influencing the stability of active σ -alkane complexes.

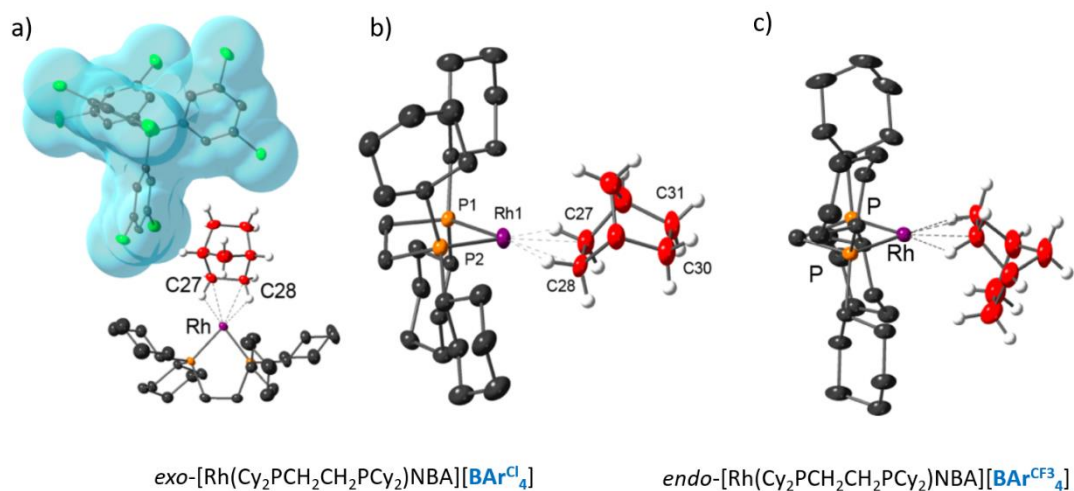


Figure 1.2.3: **a)** X-ray structure of $[\text{Rh}(\text{Cy}_2\text{PCH}_2\text{CH}_2\text{PCy}_2)\text{NBA}][\text{BAR}^{\text{Cl}}_4]$ displaying the packing of the *exo*- σ -alkane complex within the cavity provided by the $[\text{BAR}^{\text{Cl}}_4]^-$ anion. The difference between the *endo*- and *exo*-coordination mode of the σ -alkane complex is depicted in **b)** *exo*- $[\text{Rh}(\text{Cy}_2\text{PCH}_2\text{CH}_2\text{PCy}_2)\text{NBA}][\text{BAR}^{\text{Cl}}_4]$ and **c)** *endo*- $\text{Rh}(\text{Cy}_2\text{PCH}_2\text{CH}_2\text{PCy}_2)\text{NBA}[\text{BAR}^{\text{CF}_3}_4]$. Figure from ref. 40.

1.3 Metal-organic Frameworks: Robust, crystalline reaction matrices

MOFs are composed of metal ions interconnected by organic ligands to produce extended materials with a high degree of porosity and crystallinity.⁵²⁻⁵⁴ The multitude of potential ligand and metal combinations has given rise to a plethora of materials whose properties can be tailored to suit potential applications in gas storage/separation,⁵⁵⁻⁵⁸ catalysis,^{52-53, 59-79} biotechnology,⁸⁰⁻⁸¹ as a crystalline sponge,^{66, 82} for characterization of reactive species⁸³ and microelectronics.⁸⁴⁻⁸⁵ The crystallinity of MOFs allows their structure to be precisely elucidated via single crystal X-ray crystallography (SCXRD). Unlike molecular crystals such as those described by Weller *et al.*, MOF crystals are generally robust towards chemical processing, including the removal of solvent, and possess pores suitable for the transport of large guest molecules. This combination of chemical robustness, porosity and proclivity to remain crystalline makes MOFs an ideal matrix for the study of chemical processes using X-ray crystallography.^{60, 83} The confining environment within MOFs, combined with the ability to tune their structural properties via judicious ligand and metal choice; makes MOFs an ideal platform for the development of heterogeneous catalysts whose structural properties can be tailored at the nanoscale,⁷⁴ informed by the insights of X-ray crystallography.

By anchoring the metal complex to the rigid structure of the MOF, the microenvironment of the catalyst is precisely defined and the metal centre is physically isolated from adjacent complexes that may otherwise combine to form inactive di- or multi-nuclear species. Reactive metal sites can be incorporated in MOFs directly via formation of appropriate metal nodes⁸⁶⁻⁸⁸ or the use of metal functionalised linkers⁸⁹ such as porphyrins,⁹⁰ or post-synthetically via methodologies that will be defined below. The advantage of post-synthetic incorporation of metal complexes is that it permits the integration of metal complexes that are not compatible with the solvothermal synthesis conditions used to prepare MOFs.⁹¹⁻⁹² Metals can be introduced post-synthetically by expansion or exchange of the structural nodes, exchange of the existing linkers for a metal functionalised analogue, or by reaction of a free-binding site within the MOF with a guest metal complex.⁷³ Modification of the structural nodes has been demonstrated in several robust MOFs,⁹³⁻⁹⁷ in one example Ni(NO₃)₂ and was grafted to the Zr₆O₄(OH)₈(H₂O)₄ nodes of PCN-700 via a process of ligand migration. The MOF retained crystallinity, allowing the metallated node to be structurally characterised using X-ray Crystallography.⁹³ Linker exchange has been used extensively in Zr-based MOFs to dope MOF crystals with modified linkers bearing catalytically active complexes,^{68, 98} however the exchange is typically incomplete and the resulting metal sites are therefore not amenable to characterisation by X-ray crystallography. The final

methodology, post-synthetic metalation, is perhaps the most versatile route to introducing active metal complexes. The process involves the reaction between a guest metal complex and a MOF linker bearing a free-coordination sites, often leading to quantitative incorporation of complexes that can be characterised via X-ray Crystallography.⁹²

Numerous examples of post-synthetically metalated MOFs now occupy the literature^{92, 99-105} and employ a variety of coordination sites including arene,^{103, 106-108} bipyridine,^{99, 108-111} phosphine,^{101, 112} porphyrin,¹¹³ bis-pyrazolyl-methane¹⁰⁰ and arsine¹⁰² based donors among others.^{105, 114} An advantage of post-synthetic metalation over ligand exchange is that it can lead to quantitative functionalisation and therefore allows the coordination environment of the included complex to be determined by X-ray crystallography.

The following paragraphs will explore the potential of MOFs in heterogenous catalysis by highlighting the role of site-isolation, tunability, crystallinity and nano-scale control in the development of highly active MOF-based heterogeneous catalysts.

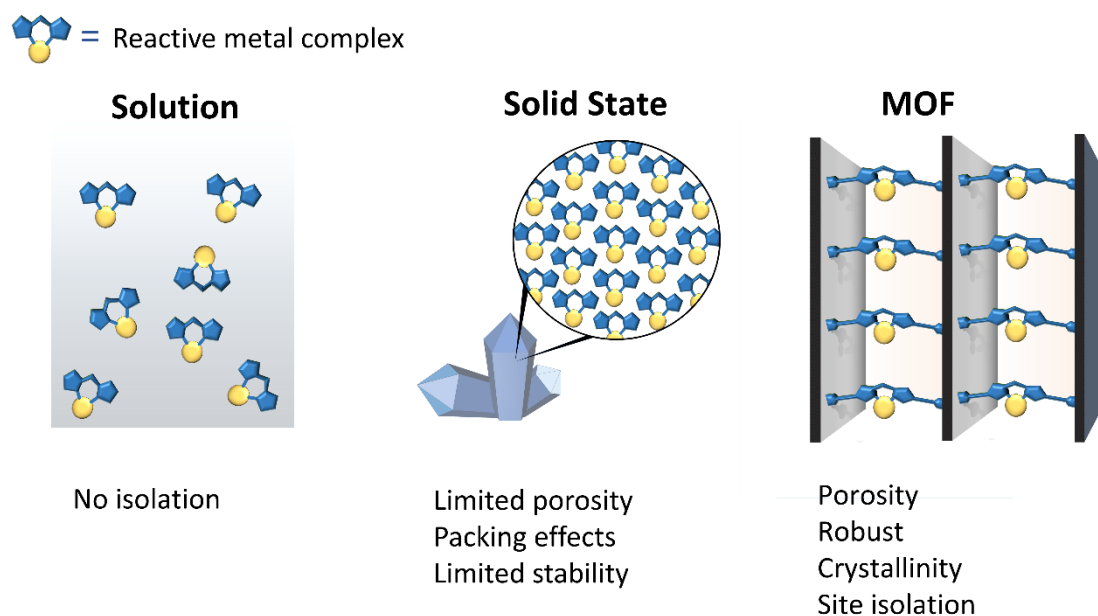


Figure 1.3.1. The formation of reactive metal complexes in solution results in decomposition due to a lack of site-isolation. The site-isolation imposed by the crystalline lattice within a single crystal can allow highly reactive species to be stabilised, however the lack of permanent porosity limits their application in small molecule activation. Metal-organic Frameworks provide a robust, permanently porous matrix within which highly reactive complexes can be generated and studied, including their reactivity with small molecules.

1.4 The case for Metal-organic Frameworks in heterogeneous chemistry

Much like the solid-state examples described above, MOFs have been used as 'crystalline molecular flasks' in which chemical reactions can take place and are monitored by X-ray crystallographic 'snapshots' obtained at different time-points. The advantage of MOFs in this area is their porosity and robust structure. Using this technique, Fujita *et al.* obtained intimate insight into the mechanism of palladium mediated aromatic bromination, which has been proposed to occur via a Pd(II)/Pd(IV) mechanism.¹¹⁵ The precursor [Pd(azatriphenylene)(methylxanthate)] complex was incorporated into a Zn(II) based MOF. The Pd complex is well ordered within the MOF due to π -stacking interactions with the MOF linkers, allowing the precursor to be characterised by X-ray crystallography. By collecting X-ray structure data at different time-points, the reaction between the MOF-bound Pd(II) complex and N-bromosuccinimide was monitored. The results revealed a [Pd(azatriphenylene)(acetonitrile)Br] intermediate, which forms after two hours and slowly converts to form the brominated azatriphenylene product. The authors proposed that the dominant mechanism within the crystalline system is the reductive elimination of the bromo-azatriphenylene from the Pd(II) centre. The square-planar Pd(II) centre observed throughout the experiment confirms that a Pd(IV) intermediate is unlikely to contribute to the mechanism within the crystalline system, casting doubt on the previously proposed mechanism. However, the authors note that the reaction mechanism may be influenced by the porous framework, particularly the stacking of the azatriphenylene moieties which may inhibit the formation of an octahedral Pd(IV) species. However, the time-resolved structural data obtained via the X-ray snapshot technique highlights the extraordinary potential of MOFs as crystalline hosts for short-lived catalytic intermediates.⁸³

Isolation of active sites by incorporation in MOFs has been shown to enhance catalytic activity by preventing the formation of degradation products such as dimers, allowing catalysis to be performed with species that are not accessible in solution.^{68, 94, 116-121} The isolation of metalloporphyrin compounds by incorporation as structural ligands or encapsulation in MOF pores^{113, 122} prevents the formation of inactive μ -oxo dimers that generally inhibit homogenous catalysis. The concept of site isolation is particularly important when considering catalysis with 'base-metals' that are significantly less expensive than the noble metals traditionally reserved for such roles.¹²¹ Such catalysts tend to be unstable in solution, undergoing decomposition via formation of multinuclear species, and are therefore protected with sterically demanding ligands that increase their cost and inhibit their catalytic activity. Several reports have emerged in which active base-metal catalysts have been generated within MOFs and

stabilised by the site-isolation induced by the crystalline framework.^{12, 118, 123} Zhang *et al.* prepared a MOF bearing phenanthroline based cobalt complexes which are active in the hydroboration of alkenes, ketones and aldehydes and arene C-H borylation.¹² The active MOF-Co(THF)₂ catalyst is bound to the phenanthroline based ligand of the MOF framework with its activity garnered from the weakly coordinating THF ligands, producing what can be considered as a ‘coordinatively unsaturated complex’ (Figure 1.4.1). In solution, the equivalent molecular complexes rapidly decompose to form nanoparticles and coordinatively saturated complexes which are catalytically inactive. By maintaining site-isolation of the metal centres within the MOF framework the activity of the Co catalysts is preserved. Similarly, Manna *et al.* prepared a Zr(IV) based MOF in which the μ_2 -OH sites on the Zr₈(μ_2 -O)₈(μ_2 -OH)₄ and Zr₆(μ_3 -O)₄(μ_3 -OH)₄ nodes (Zr₈- and Zr₆-nodes respectively), following deprotonation with ⁿBuLi, can be metallated with CoCl₂ to form the corresponding tridentate complex bound by a μ_2 -O- and two μ -carboxylate oxygen atoms.¹²³ The dichloride complex can be converted into the active hydride species by reaction with NaBEt₃H. Due to the presence of both Zr₈- and Zr₆-nodes in the structure, the hydride complexes exist in two distinct environments with different steric properties; the Zr₈- node is less sterically demanding and produces an open cobalt hydride site. The cobalt hydride is a competent hydrogenation catalyst and is highly stable within the MOF. Intriguingly, previous work had found that a similar cobalt hydride complex formed on the Zr₆(μ_3 -O)₄(μ_3 -OH)₄ node of UiO-68 was not capable of hydrogenating large substrates due to the sterically demanding environment at this node.⁹⁴ However, the cobalt hydride sites in the Zr₈-node in the new material are more accessible and therefore facilitate the hydrogenation of larger substrates. The stability and accessibility of the highly reactive cobalt hydride sites is a testament to the ability of robust crystalline frameworks to maintain site-isolation of active catalysts. Furthermore, the selectivity of such species can be tuned by careful engineering of the steric environment.

The lattice of MOFs has been used to encapsulate and thereby isolate organometallic catalysts. Li *et al.* encapsulated the active catalyst [(^tBuPNP)Ru(CO)HCl] (^tBuPNP = 2,6-bis((di-tert-butylphosphino)methyl)pyridine) within UiO-66 via a novel linker exchange ‘aperture-opening’ method. The Ru complex is too large to fit into the confining pores of the MOF, therefore the MOF was partially ‘dissolved’ (See Figure 1.4.2 for explanation) to provide access for the Ru complex, and subsequently repaired to trap the catalyst within the MOF lattice¹²⁴ (Figure 1.4.2). The resulting material successfully catalysed the hydrogenation of CO₂ to formate and owing to the protective MOF shell, the catalyst could be recycled without decomposition, contrary to the behaviour of the equivalent homogenous system.

This is a further example of how isolation of metal centres within robust crystalline lattice can enhance their durability.

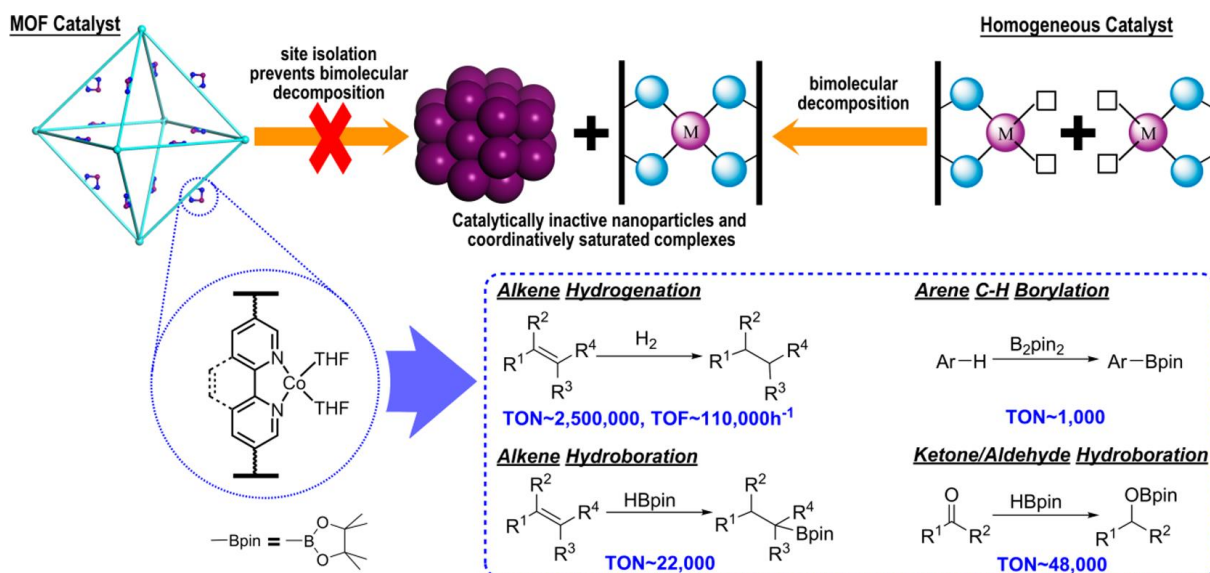


Figure 1.4.1: Catalytically active virtually ‘coordinatively unsaturated’ $[\text{Co}(\text{THF})_2]$ complexes coordinated to phenanthroline based ligands within a Zr(IV) based MOF. Physical isolation of the Co centres prevents unwanted decomposition pathways that are observed in solution and thereby preserves the catalytic activity of the metal centres. Figure adapted from ref. 12.

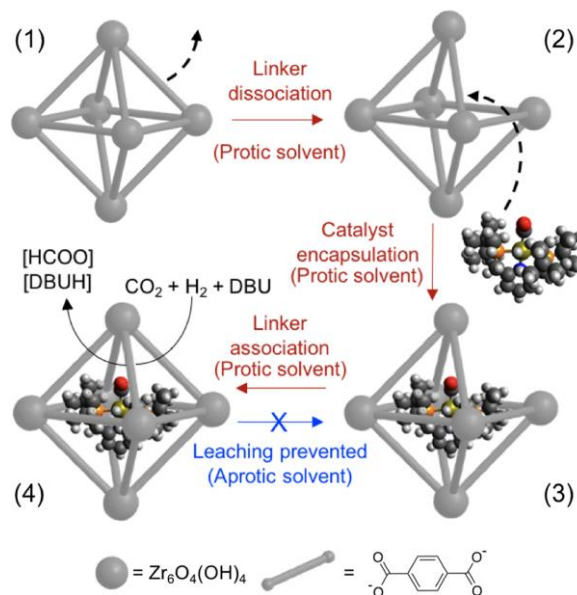


Figure 1.4.2: Encapsulation of the active catalyst $[(\text{t}^{\text{Bu}}\text{PNP})\text{Ru}(\text{CO})\text{-HCl}]$ within UiO-66 via a novel linker exchange method which forms a protective MOF ‘shell’ around the catalyst. The MOF crystals were exposed to the large Ru catalyst in the presence of a polar protic solvent which leads to partial linker dissociation, allowing the catalyst to enter the MOF structure. Repair of the material is accomplished in the presence of excess linker. When the catalyst loaded MOF is placed in an aprotic solvent it resists ligand dissociation, thereby preventing leaching of the Ru catalyst. Image from ref. 124.

The restrictive dimensions of the MOF pore network can promote selective catalysis in which products are discriminated based on size and/or shape. In a novel demonstration of the confining effects of the MOF pore, Zhang *et al.* reported the chemoselective methane borylation using an Ir catalyst embedded in the pores of MOF which catalyses the formation of monoborylated methane from methane and pinacol borane with a selectivity of 99%.¹²⁵ Unlike the encapsulated Ru catalyst described above, the Ir(III) catalyst was grafted to the MOF structure via post-synthetic metalation. The parent MOF is composed of Zr nodes interconnected by a mixture of bipyridine dicarboxylate and 1,10-phenanthroline-3,8-dicarboxylate linkers. The phenanthroline based linker was 'doped' into the structure to provide a bidentate nitrogen donor site that would facilitate the post-synthetic incorporation of transition metal complexes. By reacting the MOF with the precursor $[\text{Ir}(\text{cod})(\mu\text{-Cl})_2]$, the framework was functionalised with the corresponding $[\text{Ir}(\text{cod})\text{Cl}]$ complex which is dispersed throughout the material and able to catalyse the borylation of methane. Conventionally, the reaction between methane and bis(pinacolborane) yields a mixture of mono- and bis-borane products, the latter being favoured thermodynamically due to the increased reactivity of monoborylated methane. The pores within the UiO-67 derivative have a 0.8 nm aperture, while the mono- and bisborylated products have dimensions of 0.73x0.88 and 0.8x1.39 nm respectively. As a result the MOF-bound catalyst favours the formation of the monoborylated methane due to size selective effects, with a selectivity of 15:1 (mono:bisborylated product). Thus the physical restraints imposed on the catalytic cycle by the MOF framework dramatically influence the selectivity of the catalyst because the dimensions of the pore are comparable with the dimensions of the product molecules. This size selective effect has been employed to great effect in the catalytic methylation of toluene using the porous zeolite ZSM-5 to direct the formation of the smaller para-xylene isomer rather than the non-linear ortho- and meta- isomers.¹²⁶ The use of MOFs in size-selective catalysis is a burgeoning field that will benefit from the virtually limitless variety of possible MOFs available to chemists.

In both heterogeneous and homogeneous systems, the chemical properties of a catalyst can be tuned by varying the substituents of the appended ligand. Zhou *et al.* prepared a series of Fe-porphyrin based MOFs in which the β -position of the metalloporphyrin was systematically substituted with Br, Cl, F and ethyl substituents to enhance the activity and selectivity of the Fe porphyrin for the oxygenation of 3-methylpentane to form alcohols and ketones.¹²⁷ However, in a homogeneous system it is difficult to achieve precise tuning of the 3D-environment around a single-site catalyst. The building block approach to MOF synthesis can overcome this issue. One of the unique properties of MOFs is the tunability of the pore environment through systematic variation of the organic linkers, allowing nano-scale control of the

spatial environment around catalyst sites.¹²⁸ Long *et al.* prepared a series of iso-reticular Fe frameworks in which the organic ligand was systematically varied in length and hydrophobicity.¹²⁹ The exposed Fe(II) sites that adorn the framework pores are active in the oxidation of cyclohexane in the presence of a sacrificial oxidant. The alcohol:ketone selectivity and activity of the material was substantially increased by extending the linker length and installing hydrophobic tert-butyl groups. Similarly, Grigoropoulos *et al.* encapsulated the cationic Crabtree's catalyst $[\text{Ir}(\text{cod})(\text{PCy}_3)(\text{pyridine})]\text{PF}_6$ (cod = cyclooctadiene) inside the pores of the sulfonated MIL-101(Cr) MOF via a process of cation exchange.¹³⁰ Crabtree's catalyst promotes the hydrogenation of alkenes, however the use of alkenes bearing alcohol functionality usually results in a mixture of products that arise from both hydrogenation and isomerisation reactions due to the ability of the alcohol group to ligate the Ir centre of the catalyst. When Crabtree's catalyst is immobilised within sulfonated MIL-101(Cr) its reactivity towards olefinic alcohols is influenced by the hydrophilic microenvironment of the MOF pores; the sulfonate and Cr(III) sites adjacent to the Ir centre interact with the alcohol functionality and thereby prevent the isomerisation reaction from taking place. No unwanted isomerisation products were detected when the MOF-encapsulated system was employed, furthermore, the porosity of the MOF facilitates the gas phase hydrogenation of but-1-ene with significantly greater activity than the powdered catalyst. Apart from ordering guest molecules, the microenvironment within MOF pores can influence the reactivity of catalysts immobilized within the porous network. The ability to tune the pore environment of MOFs via judicious ligand design invites the possibility to enhance the activity of metallocatalysts by precisely controlling the microenvironment around the active site, much as nature has perfected the activity of metalloenzymes.

A comparatively more sophisticated pore-space can be generated in multi-component MOFs in which multiple distinct ligands are combined at crystallographically distinct positions within the one framework.¹³¹⁻¹³³ By appending diverse functional groups to each ligand, the pore-space can be engineered to enhance the activity of the adjacent catalytic site.¹³² This strategy is epitomised by Telfer *et al.*'s exemplary studies using the multi-component MOF MUF-77. This material contains three distinct ligands (1,4-benzenedicarboxylate, 4,4'-biphenyldicarboxylate and 5,5',10,10',15,15'-hexamethyltruxene-2,7,12-tricarboxylic acid) to which different functionality can be appended.^{132, 134} In one such study, the catalytic moiety employed was enantiopure (S)-prolinyl, an organic functionality that was installed on the 1,4-benzenedicarboxylate or 4,4'-biphenyldicarboxylate linkers.¹³⁴ The remaining linkers, truxene tricarboxylate and either 4,4'-biphenyldicarboxylate or 1,4-benzenedicarboxylate, were adorned with an array of functional groups which were carefully selected with the aid of molecular simulations. The

simulations were necessary to ensure that the prescribed groups would interact with the catalyst/substrate without blocking access to the catalyst site. The (S)-proline group catalyses the asymmetric aldol transformation of acetone and 4-nitrobenzaldehyde, and in a homogenous setting favours the R-enantiomer. However, when installed in MUF-77 analogues both the R and S- enantiomers can be favoured by changing the substituents on the adjacent linkers or, in the case of the R-enantiomer, by installing the (S)-proline on the 4,4'-biphenyl- rather than 1,4-benzene-dicarboxylate linker. Thus, by engineering the pore-environment the (S)-proline catalyst can be prompted to favour the desired product enantiomer. It is conceivable that this systematic, multicomponent approach to tuning the pore-environment could be applied to other catalytic systems within MOFs, including those based on transition metal catalysts.

By varying the combination of active species present within a MOF framework, a family of distinct MOFs can be generated which specialise in catalysing different reactions. Recently, Cao *et al.* examined the MOF *proto*-LIFM-28, a multivariate MOF in which different ligands can be reversibly exchanged into the material.¹³⁵ By using a single catalytically active ligand, or combining two or more ligands into the material, the MOF provides a platform for performing a wide range of reactions (Figure 1.4.3). The presence of two different length linkers within the structure allows up to two different ligands to be incorporated within the material at specific, well defined locations. This study highlights how a systematic, building block approach to MOF synthesis can generate remarkable interchangeability in catalytic ability.

Finally, the advantages of the 'building-block' aspect of MOF design is exemplified by the success of tandem catalysis reactions in which MOFs act as multifunctional catalysts.^{61-62, 101, 112} The building-block approach to MOF design allows multiple catalytically active components to be assembled with nanoscale precision within the one lattice, wherein they act in tandem to catalyse a multistep transformation. In a distinguished example of this concept, Han *et al.* reported the preparation of a sophisticated MOF bearing a polyoxometalate oxidation catalyst, Zn²⁺ Lewis acid sites, amine appended linkers and a pyrrolidine-2-yl-imidazole organocatalyst moiety within the same framework.¹³⁶ The catalysts work in tandem to produce enantiomerically pure cyclic carbonates from CO₂ and olefins in the presence of *tert*-butylhydroperoxide (TBHP) (Figure 1.4.4). Two MOFs were prepared, each bearing one of the two enantiomers of the pyrrolidine organocatalyst, allowing either enantiomer of the product carbonate to be produced in pure form. Polyoxometallates are well known to catalyse the formation of epoxides from styrene in the presence of peroxides, such as TBHP which was used in this case.¹³⁷ Correspondingly, the

precise placement of the amine functionalised organic struts adjacent to the pyrrolidine moiety aids in the adsorption and activation of CO₂ in a prelude to formation of the carbamate product by coupling with styrene-oxide (Figure 1.4.4). Thus, the building block quality of MOFs permits the precise arrangement of diverse functionalities to accomplish tandem catalysis, critically the spatial arrangement of each component can be elucidated by X-ray crystallography, allowing the resulting reactivity to be rationalised and enhanced iteratively.

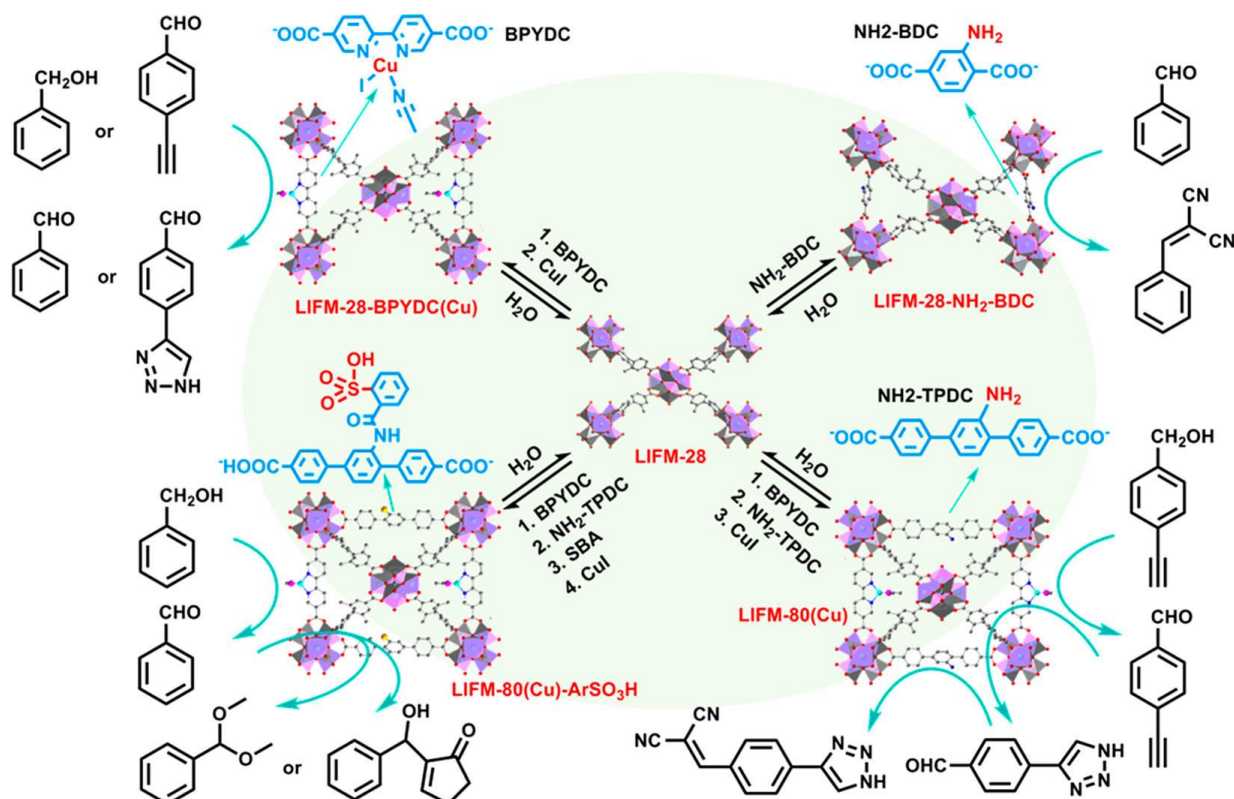


Figure 1.4.3: The multivariate MOF proto-LIFM-28 developed by Cao *et al.* can undergo reversible ligand exchange to incorporate various combinations of catalytically active ligands within the framework, thereby giving rise to a family of MOFs that can catalyse different reactions. Figure from ref. 135.

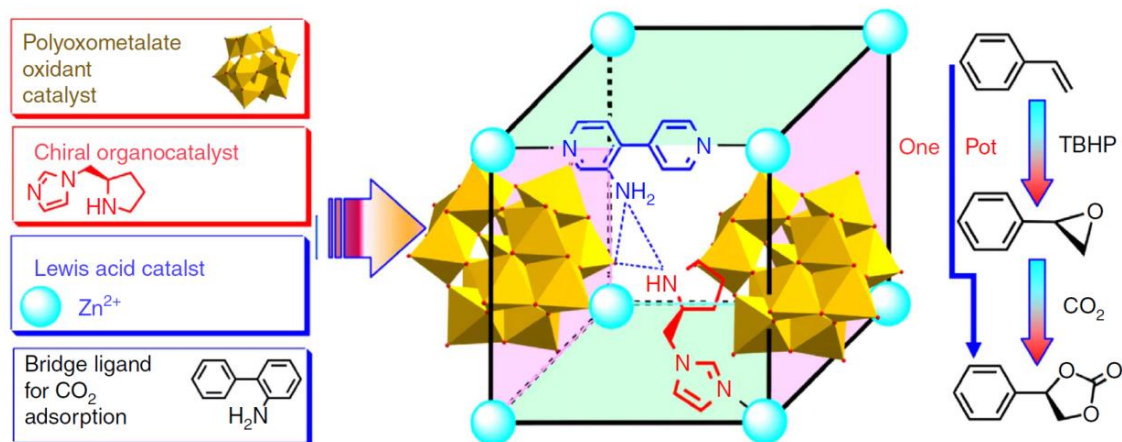


Figure 1.4.4: Tandem catalysis MOF developed by Han *et al.*, for the one-pot conversion of CO₂ into cyclic carbonates. The close proximity of amine and pyrrolidine moieties aids the adsorption and fixing of CO₂. Two MOFs were prepared which each contained one of the enantiomers of the pyrrolidine organocatalyst, allowing enantiomerically pure carbonates to be produced. TBHP = *tert*-butylhydroperoxide. Figure from ref. 136.

1.5 Metal-organic Frameworks: Crystallographic insights into catalysis

The studies discussed above resoundingly validate the role of MOFs as a platform for heterogeneous catalysis by highlighting the role of site-isolation, tunability, crystallinity and nano-scale control in the development of highly active heterogeneous catalysts. The ability to functionalise MOFs with transition metal complexes and systematically tune the chemical environment to enhance catalytic activity invites the development of advanced heterogeneous systems designed at the nanoscale. The use of X-ray crystallography to elucidate the relationships between the MOF microenvironment and reactivity as well as map the structural processes associated with catalysis can provide profound insight into the chemical processes occurring within MOF pores. To date, one of the most useful materials for the X-ray crystallographic study of post-synthetic metalation and chemical reactivity in MOF pores has been a Mn(II) based MOF, **1**, which was developed at the University of Adelaide and is adeptly equipped for post-synthetic metalation.^{100, 104} MOF **1** is based on the organic ligand bis-(4-carboxyphenyl-3,5-dimethylpyrazolyl)methane (L) which forms a 3D network of interconnected Mn(II) trimeric nodes. Importantly, one L moiety bridges two Mn(II) trimers via its carboxylate donors, leaving the bis(3,5-dimethylpyrazolyl)methane component free and accessible to guests via 13 Å channels that penetrate the material (Figure 1.5.1). When crystals of **1** are placed in a solution containing a transition metal

complex, the N,N-chelation sites coordinate to the guest complex in a qualitative fashion. Remarkably, the crystallinity of **1** is retained during metalation and the coordination environment of the added complex can be readily elucidated by X-ray crystallography. A range of transition metal complexes have been incorporated into **1** and structurally characterised. A prime example is cobalt(II) chloride which reacted with **1** in methanol at 65°C to give $\mathbf{1}\cdot[\text{Co}(\text{H}_2\text{O})_4]\cdot\text{Cl}_2$, as determined via single-crystal X-ray crystallography of the pink crystals. Under solvent exchange with distilled acetonitrile or when heated at 50°C in methanol, the material changes colour from pink $\mathbf{1}\cdot[\text{Co}(\text{H}_2\text{O})_4]\cdot\text{Cl}_2$ to bright blue, which is consistent with a change in Co(II) coordination environment from octahedral to tetrahedral. This transition was verified by SCXRD data collected on the blue crystals in acetonitrile, which confirmed the formation of the tetrahedral complex $\mathbf{1}\cdot[\text{CoCl}_2]$. The ability to directly follow the change in coordination sphere using X-ray crystallography highlights the ability of **1** to act as a crystalline host for transition metal chemistry. This ability to study post-synthetic metalation chemistry, particularly chemical processes occurring at the included metal centre; distinguishes **1** from many MOFs. The permanent porosity of **1**, with a BET surface area of $711\text{ m}^2\text{g}^{-1}$ and retention of crystallinity during multistep chemical processing elevates this material above the solid-state materials as a platform for the study of in-situ transition metal chemistry.

The insight into transition metal chemistry garnered from **1** has recently extended to organometallic catalysis. The Monsanto acetic acid synthesis is one of the most significant industrial chemical processes.³ The reaction is performed using homogenous Rh(I) or Ir(I) carbonyl catalysts and revolves around the oxidative addition of MeI to the metal centre, migratory insertion of the methyl fragment into the M-CO bond and reductive elimination of acetyl iodide to regenerate the square planar catalyst. The development of heterogeneous systems that can perform this lucrative reaction have been the focus of recent work.³ **1** was metallated with an organometallic Rh(I) complex, forming $\mathbf{1}\cdot[\text{Rh}(\text{CO})_2]^+\cdot[\text{Rh}(\text{CO})_2\text{Cl}_2]^-$ which was characterised via X-ray crystallography which confirmed the presence of the square planar Rh(I) complex and charge-balancing $[\text{Rh}(\text{CO})_2\text{Cl}_2]^-$ counterion. The Rh(I) metallated material reacts with MeI in acetonitrile to give red-orange crystals suitable for X-ray crystallography, analysis of the electron density map revealed the presence of the octahedral Rh(III) oxidative addition product $\mathbf{1}\cdot[\text{Rh}(\text{CO})(\text{CH}_3\text{CO})(\text{MeCN})]^+$. Intriguingly, the reaction with MeBr produces the oxidative addition product $\mathbf{1}\cdot[\text{Rh}(\text{CH}_3\text{CO})\text{Br}(\text{MeCN})_2]\cdot\text{Br}$ in which the metal centre has undergone reductive elimination of acetyl bromide and a second oxidative addition, thereby consuming both CO ligands.⁶⁰ The disparity between the structures obtained from MeI and MeBr oxidative addition are attributed to the steric demands of the respective halide anions. Following oxidative addition, the acetyl

and halide ligands reside on the axial sites of the Rh complex and must rearrange to give the *cis* complex in order for the reductive elimination of acetyl halide to occur. The smaller bromide anion readily undergoes this rearrangement and therefore undergoes successive oxidative additions and one reductive elimination, while the sterically demanding iodide cannot rearrange to form the *cis* complex and is therefore trapped after the initial oxidative addition step.

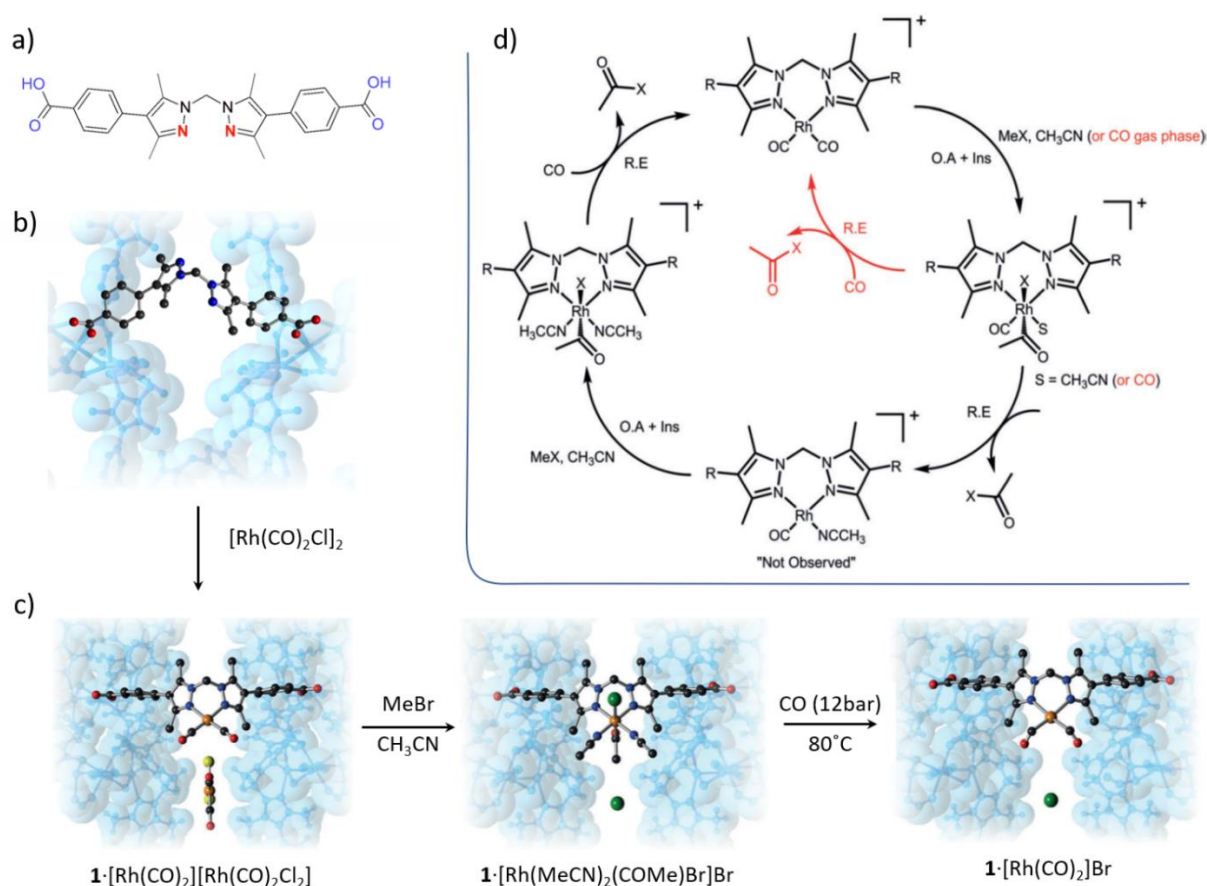


Figure 1.5.1: **a)** The ligand bis(4-carboxyphenyl-3,5-dimethylpyrazolyl)methane (L) from which **1** is produced **b)** the structure of **1** contains a free N,N-chelation site which readily reacts with metal complexes in solution to yield a metallated compound **c)** the metalation process and subsequent chemistry performed at the transition metal site can be elucidated via X-ray crystallography (**b-c**) including the oxidative addition chemistry between Rh(I) and MeX (X= Br, I) **d)** which can be performed in the gas phase to catalytically generate MeCOBr. In **d)** the gas phase reactivity is indicated by the red scheme. The blue blue-surface in **b-c** represent the Van der Waals surface of **1**, with only the ligand bearing the N,N-chelation site shown in detail. Figure adapted from ref. 60.

This remarkable insight obtained via X-ray crystallography was crucial to explaining the catalytic activity of the Rh complex within **1**. In the gas phase, the material catalyses the production of acetyl bromide, albeit at a very slow rate. The slow rate is attributed to the kinetics of the initial oxidative addition step, which is significantly slower for MeBr than MeI. Although MeI undergoes more rapid oxidative addition, the sterically demanding iodo substituent fails to undergo the migration to release $\text{CH}_3(\text{CO})\text{I}$ via reductive elimination, confirmed by the direct observation of $[\text{Rh}(\text{CO})(\text{CH}_3\text{CO})\text{I}(\text{MeCN})]^+$ in the crystal structure. The smaller MeBr undergoes a much slower oxidative addition, but the reduced size of the bromide anion facilitates the necessary migration of bromide to release $\text{CH}_3(\text{CO})\text{Br}$, as revealed by the observation of the complex $[\text{Rh}(\text{CH}_3\text{CO})\text{Br}(\text{MeCN})_2]\text{Br}$ which corresponds to complete consumption of CO. The difference in reactivity between MeI and MeBr can thereby be rationalised based on the structural insights garnered from X-ray crystallography, particularly the observation of key intermediates in the catalytic cycle. These results highlight the power of crystallography in porous crystalline materials as a source of insight into the intricate reactivity of important transition metal catalysts.

The preceding studies involving **1** resoundingly demonstrate that **1** retains its crystallinity throughout multistep chemical reactions including those in the gas phase. X-ray crystallography has provided intricate insight into the chemical processes taking place at post-synthetically incorporated metal sites. The lower symmetry of the N,N-chelation site means that the axial ligands on an included octahedral complex exist in non-equivalent environments due to the 'bent' shape of the methyl hinged ligand. This character produces a very well-defined coordination environment, with the arrangement of different ligands influenced by the steric considerations imposed by the shape of the ligand and local micro-environment of the framework. Several promising avenues remain unexplored, particularly the potential advantages imbued by the site-isolation of metal complexes within **1** which we postulate can be employed to perform site-selective organic transformations and to trap highly reactive metal complexes within the crystalline matrix. The literature discussed in the preceding paragraphs provides precedent for exploring these avenues within **1**.

1.6 Contextual Statement

This thesis outlines work performed with the MOF **1**, aiming to use X-ray crystallography to elucidate the chemistry of transition metal complexes tethered within the MOF lattice. As outlined above, the structural characterisation of reactive transition metal complexes and intermediates is critical for the development of advanced heterogeneous catalysts, for which MOFs provide an ideal medium in lieu of their building block synthesis, crystallinity and porosity.

In line with these goals, Chapter 2 examines the metalation of **1** with a series of first-row transition metal nitrates. The structures of each complex were determined via X-ray crystallography and compared to the structural parameters of solid and solution state analogues. Within **1** (and other MOFs), transition metal complexes are tethered to a crystalline matrix, but remain suspended in void-space, surrounded by solvent molecules that can pass freely through the porous network. Thus, the prevailing environment is dynamic and possess qualities akin to both the solid-state and solution regimes. This work provides crucial insight into the behaviour of simple transition metal complexes within the confining pores of MOFs. When housing molecular catalysts within MOF crystals, it is crucial to establish how those transition metal complexes are likely to behave within their crystalline host. Factors such as solvent choice were found to profoundly influence the coordination sphere of the resulting complex. X-ray crystallography provides the crucial insight required to understand the structural characteristics of the tethered complexes.

The presence of a free N,N-chelation site within the pores of **1** allows quantitative metalation of the material with transition metal complexes. Quantitative metalation is crucial for the structural characterisation of such complexes via X-ray crystallography, which is in-turn important for rationalising and advancing the reactivity of molecular catalysts housed within the framework. However, quantitative metalation can reduce the catalytic activity of MOFs since the large number of metal complexes block the pores and limit transport of products and reagents through the material.¹¹¹ Chapter 3 explores the notion that the parent framework **1** can be engineered by variation of the organic linker (L) or the composition of the structural nodes, thereby providing an avenue to tailor the distribution of metal sites to suit particular practical applications such as catalysis. This was achieved using a mixed linker approach which takes advantage of the fact that the binding site in **1** is derived from the ligand L bridging between the Mn(II) structural nodes via its carboxylate donors, leaving the N,N-chelation site free. The potential binding sites can be diluted by the inclusion of a ligand in the bridging position with no available

coordination site (or a very poor donor). It is demonstrated that a topologically identical MOF can be prepared from a mixture of L and LCF₃ (LCF₃ = bis(4-carboxyphenyl-3,5-trifluoromethylpyrazolyl)methane). Owing to the steric and electronic effects of the trifluoromethyl substituents on LCF₃, the resulting N,N-chelation site does not readily coordinate transition metals and is therefore precluded from participating in the structural nodes of the MOF. Therefore, LCF₃ preferentially occupies the non-coordinated bridging site within the material (which only requires carboxylate coordination) thereby displacing L from this position and diluting the number of available binding sites. The result is a MOF which has the same topology as **1**, however the available coordination sites are reduced by up to 50% due to the inclusion of LCF₃ in predominantly in the bridging position. Thus, it is possible to engineer the structure of **1** to reduce the degree of metalation and promote less crowding of the pore-space. Moreover, the degree of dilution can be controlled between 0 and 50%, allowing the density of metal sites to be tailored to suit specific applications such as catalysis with large/small reagents or products. Furthermore, in a rare example for MOF **1**, it is revealed that the structural nodes can be doped with Fe, offering a new pathway through which to manipulate the composition of **1**.

Chapter 4 advances the case for MOFs as highly tuned heterogeneous reaction vessels and demonstrates the power of X-ray crystallography to provide insight into chemical reactivity at transition metal sites within MOFs. The reaction between **1** and [Mn(CO)₅Br] yields the quantitatively metallated material **1**·[Mn(CO)₃(H₂O)]Br which was revealed by X-ray crystallography to exist as an unusual charged complex with the bromide anion residing in the MOF pore. The formation of this charged complex is peculiar to the MOF pore-space, since the equivalent molecular complexes adopt a neutral [Mn(CO)₃Br] motif. By taking advantage of the fortuitously non-coordinated bromide anion, it is possible to quantitatively exchange bromide for azide, giving **1**·[Mn(CO)₃N₃]. The azide complex readily reacts with small alkynes via the 3+2 Huisgen cycloaddition reaction, with the resulting triazolate complexes were elucidated by X-ray crystallography, highlighting the capacity of **1** to act as a crystalline nano-reactor for successive metal-centred chemical reactions. Via an alkylation strategy, the corresponding alkyne-functionalised triazole is readily liberated from the material while simultaneously regenerating the starting material **1**·[Mn(CO)₃(H₂O)]Br. Furthermore, X-ray crystallography revealed that the azide sites in **1**·[Mn(CO)₃N₃] are physically isolated and separated by 13 Å by virtue of the robust crystalline structure of the parent MOF. As such, the reaction between **1**·[Mn(CO)₃N₃] and small dialkynes that are shorter than the azide-azide separation results in the selective formation of the corresponding alkyne-functionalised triazolate. The un-reacted alkyne is too far from the adjacent azide to undergo a second 'click' reaction, leading to the formation of an alkyne-functionalised triazolate which can be released as the corresponding alkyne-

functionalised triazole via the alkylation strategy outlined above. Thus, the site-isolated nature of the transition metal complexes incorporated within **1** allows site-selective chemo-selective 'click' chemistry to be performed. This novel strategy harnesses the nano-scale precision with which transition metal complexes can be arranged within the three-dimensional, crystalline structure of MOFs. Furthermore, every step of the reaction from metalation to the 'click' reaction is characterised by X-ray crystallography which provides valuable insight into each process.

Finally, Chapter 5 further advances the concept of site-isolation of metal complexes within MOFs, focusing on the role of the MOFs in the stabilisation of reactive metal complexes. The photolysis of metal carbonyl complexes results in the loss of CO ligands, leaving behind coordinatively unsaturated metal complexes which have been implicated as key intermediates in the activation of small molecules. A thorough introduction to this interesting and broad field of chemistry is provided in Chapter 5, particularly to assist in the interpretation of the reported studies. The post-synthetically metallated material **1**·[Mn(CO)₃Br] is an ideal candidate for the study of photochemistry within MOFs because it is sensitive to visible photolysis and the photochemical reactions can be monitored via in-situ X-ray crystallography and IR spectroscopy. The current interest in developing base-metal catalysts has provoked a renaissance in Mn based catalysis, particularly C-H activation chemistry. Photochemistry is a proven method for producing reactive, electron rich metal centres from robust precursor complexes and therefore presents an ideal methodology for developing topical Mn catalysts within MOFs. The reactivity of photochemically generated complexes, whether they be truly coordinatively unsaturated or stabilised by weakly bound solvent molecules, makes them difficult to structurally characterise. By housing these species within a robust crystalline matrix their reactivity can be harnessed without incurring decomposition, while the structural insights garnered from X-ray crystallography can inspire and inform future improvements. Photolysis of **1**·[Mn(CO)₃Br] results in complete loss of CO from the material, which was monitored via IR spectroscopy. Photolysis in the presence of the weakly coordinating solvent THF results in the formation of the corresponding THF adduct, which was directly observed by in-situ X-ray crystallography and supported by IR spectroscopy. This complex is the first example of a structurally characterised THF adduct formed from a Mn(I) complex under photolysis, illustrating the power of in-situ crystallography and the crystalline-matrix strategy to obtain insightful structural information. It is postulated that the photolysis of **1**·[Mn(CO)₃Br] in the presence of more weakly coordinating solvents may produce more reactive complexes that can participate in small molecule activation.

Overall, this thesis validates the role of MOFs in advancing heterogeneous chemical reactivity by revealing the subtle effects of the pore environment on the coordination sphere of metal complexes, the capacity of site-specific ligand doping to engineer the distribution of active metal sites within MOFs and the power of site-isolation to affect highly selective chemical transformations and isolate reactive metal complexes. By harnessing the crystallinity of **1**, X-ray crystallography provides valuable insights into the relevant chemistry throughout each project, confirming that MOFs are indeed a valuable and unique medium within which to explore and harness transition metal chemistry.

1.7 References

- (1) Hutchings, G. J. *ACS Cent. Sci.* **2018**, *4*, 1095.
- (2) Shilov, A. E.; Shul'pin, G. B. *Chem. Rev.* **1997**, *97*, 2879.
- (3) *Industrial Catalysis : A Practical Approach*; Hagen, J., John Wiley & Sons, Incorporated: Berlin, GERMANY, 2015;
- (4) Liu, L.; Corma, A. *Chem. Rev.* **2018**, *118*, 4981.
- (5) Karunadasa, H. I.; Montalvo, E.; Sun, Y.; Majda, M.; Long, J. R.; Chang, C. J. *Science* **2012**, *335*, 698.
- (6) Gonzalez-Rodriguez, C.; Pawley, R. J.; Chaplin, A. B.; Thompson, A. L.; Weller, A. S.; Willis, M. C. *Angew. Chem., Int. Ed. Engl.* **2011**, *50*, 5134.
- (7) Blanckenberg, A.; Malgas-Enus, R. *Catal. Rev.* **2018**, *61*, 27.
- (8) Yoneda, N.; Kusano, S.; Yasui, M.; Pujado, P.; Wilcher, S. *Applied Catalysis A: General* **2001**, *221*, 253.
- (9) Hie, L.; Fine Nathel, N. F.; Shah, T. K.; Baker, E. L.; Hong, X.; Yang, Y. F.; Liu, P.; Houk, K. N.; Garg, N. K. *Nature* **2015**, *524*, 79.
- (10) Morris, R. H. *Chem. Soc. Rev.* **2009**, *38*, 2282.
- (11) Sun, C. L.; Li, B. J.; Shi, Z. J. *Chem. Rev.* **2011**, *111*, 1293.
- (12) Zhang, T.; Manna, K.; Lin, W. J. *Am. Chem. Soc.* **2016**, *138*, 3241.
- (13) Kundu, S.; Choliy, Y.; Zhuo, G.; Ahuja, R.; Emge, T. J.; Warmuth, R.; Brookhart, M.; Krogh-Jespersen, K.; Goldman, A. S. *Organometallics* **2009**, *28*, 5432.
- (14) Pitts, A. L.; Wriglesworth, A.; Sun, X. Z.; Calladine, J. A.; Zaric, S. D.; George, M. W.; Hall, M. B. *J. Am. Chem. Soc.* **2014**, *136*, 8614.
- (15) Labinger, J. A.; Bercaw, J. E. *Nature* **2002**, *417*, 507.
- (16) Jones, W. D. *Inorg. Chem.* **2005**, *44*, 4475.
- (17) Das, A.; Reibenspies, J. H.; Chen, Y. S.; Powers, D. C. *J. Am. Chem. Soc.* **2017**, *139*, 2912.
- (18) Sabenya, G.; Lázaro, L.; Gamba, I.; Martin-Diaconescu, V.; Andris, E.; Weyhermüller, T.; Neese, F.; Roithova, J.; Bill, E.; Lloret-Fillol, J., *et al.* *J. Am. Chem. Soc.* **2017**, *139*, 9168.
- (19) Atienza, C. C. H. A.; Bowman, A. C.; Lobkovsky, E.; Chirik, P. J. *J. Am. Chem. Soc.* **2010**, *132*, 16343.
- (20) Thomson, R. K.; Cantat, T.; Scott, B. L.; Morris, D. E.; Batista, E. R.; Kiplinger, J. L. *Nat. Chem.* **2010**, *2*, 723.
- (21) Scheibel, M. G.; Wu, Y.; Stuckl, A. C.; Krause, L.; Carl, E.; Stalke, D.; de Bruin, B.; Schneider, S. *J. Am. Chem. Soc.* **2013**, *135*, 17719.

- (22) Scheibel, M. G.; Askevold, B.; Heinemann, F. W.; Reijerse, E. J.; de Bruin, B.; Schneider, S. *Nat. Chem.* **2012**, *4*, 552.
- (23) Buschhorn, D.; Pink, M.; Fan, H.; Caulton, K. G. *Inorg. Chem.* **2008**, *47*, 5129.
- (24) Long, A. K. M.; Timmer, G. H.; Pap, J. S.; Snyder, J. L.; Yu, R. P.; Berry, J. F. *J. Am. Chem. Soc.* **2011**, *133*, 13138.
- (25) Kawano, M.; Kobayashi, Y.; Ozeki, T.; Fujita, M. *J. Am. Chem. Soc.* **2006**, *128*, 6558.
- (26) Asplund, M. C.; Snee, P. T.; Yeston, J. S.; Wilkens, M. J.; Payne, C. K.; Yang, H.; Kotz, K. T.; Frei, H.; Bergman, R. G.; Harris, C. B. *J. Am. Chem. Soc.* **2002**, *124*, 10605.
- (27) Asbury, J. B.; Ghosh, H. N.; Yeston, J. S.; Bergman, R. G.; Lian, T. *Organometallics* **1998**, *17*, 3417.
- (28) Bengali, A. A.; Schultz, R. H.; Moore, C. B.; Bergman, R. G. *J. Am. Chem. Soc.* **1994**, *116*, 9585.
- (29) Yang, H.; Kotz, K. T.; Asplund, M. C.; Wilkens, M. J.; Harris, C. B. *Acc. Chem. Res.* **1999**, *32*, 551.
- (30) Wang, X.; Wovchko, E. A. *J. Phys. Chem. B* **2005**, *109*, 16363.
- (31) Hitam, R. B.; Mahmoud, K. A.; Rest, A. J. *Coord. Chem. Rev.* **1984**, *55*, 1.
- (32) Hofmann, P. *Angew. Chem., Int. Ed. Engl.* **1977**, *16*, 536.
- (33) Ward, T. R.; Schafer, O.; Daul, C.; Hofmann, P. *Organometallics* **1997**, *16*, 3207.
- (34) Bianchini, C.; Farnetti, E.; Graziani, M.; Kaspar, J.; Vizza, F. *J. Am. Chem. Soc.* **1993**, *115*, 1753.
- (35) Bianchini, C.; Peruzzini, M.; Zanobini, F. *Organometallics* **1991**, *10*, 3415.
- (36) Siedle, A. R.; Newmark, R. A. *Organometallics* **1989**, *8*, 1442.
- (37) Pike, S. D.; Weller, A. S. *Phil. Trans. R. Soc. A* **2015**, *373*, 20140187.
- (38) Chadwick, F. M.; Kramer, T.; Gutmann, T.; Rees, N. H.; Thompson, A. L.; Edwards, A. J.; Buntkowsky, G.; Macgregor, S. A.; Weller, A. S. *J. Am. Chem. Soc.* **2016**, *138*, 13369.
- (39) Chadwick, F. M.; McKay, A. I.; Martínez-Martínez, A. J.; Rees, N. H.; Kramer, T.; Macgregor, S. A.; Weller, A. S. *Chem. Sci.* **2017**, *8*, 6014.
- (40) McKay, A. I.; Martínez-Martínez, A. J.; Griffiths, H. J.; Rees, N. H.; Waters, J. B.; Weller, A. S.; Krämer, T.; Macgregor, S. A. *Organometallics* **2018**, *37*, 3524.
- (41) Huang, Z.; White, P. S.; Brookhart, M. *Nature* **2010**, 465.
- (42) Cook, P. M.; Dahl, L. F.; Hopgood, D.; Jenkins, R. A. *Dalton Trans.* **1973**, 294.
- (43) Siedle, A. R.; Newmark, R. A.; Sahyun, M. R. V.; Lyon, P. A.; Hunt, S. L.; Skarjune, R. P. *J. Am. Chem. Soc.* **1989**, *111*, 8346.
- (44) Pike, S. D.; Thompson, A. L.; Algarra, A. G.; Apperley, D. C.; Macgregor, S. A.; Weller, A. S. *Science* **2012**, *337*, 1648.

- (45) Yau, H. M.; McKay, A. I.; Hesse, H.; Xu, R.; He, M.; Holt, C. E.; Ball, G. E. *J. Am. Chem. Soc.* **2016**, *138*, 281.
- (46) Calladine, J. A.; Duckett, S. B.; George, M. W.; Matthews, S. L.; Perutz, R. N.; Torres, O.; Vuong, K. Q. *J. Am. Chem. Soc.* **2011**, *133*, 2303.
- (47) Castro-Rodriguez, I.; Nakai, H.; Gantzel, P.; Zakharov, L. N.; Rheingold, A. L.; Meyer, K. *J. Am. Chem. Soc.* **2003**, *125*, 15734.
- (48) Evans, D. R.; Drovetskaya, T.; Bau, R.; Reed, C. A.; Boyd, P. D. W. *J. Am. Chem. Soc.* **1997**, *119*, 3633.
- (49) Chadwick, F. M.; Rees, N. H.; Weller, A. S.; Kramer, T.; Iannuzzi, M.; Macgregor, S. A. *Angew. Chem., Int. Ed. Engl.* **2016**, *55*, 3677.
- (50) Andreychuk, N. R.; Emslie, D. J. *Angew. Chem., Int. Ed. Engl.* **2013**, *52*, 1696.
- (51) Martínez-Martínez, A. J.; Tegner, B. E.; McKay, A. I.; Bukvic, A. J.; Rees, N. H.; Tizzard, G. J.; Coles, S. J.; Warren, M. R.; Macgregor, S. A.; Weller, A. S. *J. Am. Chem. Soc.* **2018**, *140*, 14958.
- (52) Furukawa, H.; Cordova, K. E.; O'Keeffe, M.; Yaghi, O. M. *Science* **2013**, *341*, 974.
- (53) Yaghi, O. M.; O'Keeffe, M.; Ockwig, N. W.; Chae, H. K.; Eddaoudi, M.; Kim, J. *Nature* **2003**, *423*, 705.
- (54) Ricco, R.; Pfeiffer, C.; Sumida, K.; Sumbly, C. J.; Falcaro, P.; Furukawa, S.; Champness, N. R.; Doonan, C. J. *CrystEngComm* **2016**, *18*, 6532.
- (55) Dechnik, J.; Sumbly, C. J.; Janiak, C. *Cryst. Growth Des.* **2017**, *17*, 4467.
- (56) Dechnik, J.; Gascon, J.; Doonan, C. J.; Janiak, C.; Sumbly, C. J. *Angew. Chem., Int. Ed. Engl.* **2017**, *56*, 9292.
- (57) Seoane, B.; Coronas, J.; Gascon, I.; Benavides, M. E.; Karvan, O.; Caro, J.; Kapteijn, F.; Gascon, J. *Chem. Soc. Rev.* **2015**, *44*, 2421.
- (58) Mason, J. A.; Veenstra, M.; Long, J. R. *Chem. Sci.* **2014**, *5*, 32.
- (59) Fortea-Pérez, F. R.; Mon, M.; Ferrando-Soria, J.; Boronat, M.; Leyva-Pérez, A.; Corma, A.; Herrera, J. M.; Osadchii, D.; Gascon, J.; Armentano, D., *et al.* *Nature Mat.* **2017**, *16*, 760.
- (60) Burgun, A.; Coghlan, C. J.; Huang, D. M.; Chen, W.; Horike, S.; Kitagawa, S.; Alvino, J. F.; Metha, G. F.; Sumbly, C. J.; Doonan, C. J. *Angew. Chem., Int. Ed. Engl.* **2017**, *56*, 1.
- (61) Huang, Y. B.; Liang, J.; Wang, X. S.; Cao, R. *Chem. Soc. Rev.* **2016**, *46*, 126.
- (62) Dhakshinamoorthy, A.; Garcia, H. *ChemSusChem.* **2014**, *7*, 2392.
- (63) Dhakshinamoorthy, A.; Asiri, A. M.; Garcia, H. *Angew. Chem., Int. Ed. Engl.* **2016**, *55*, 5414.
- (64) Kitagawa, S.; Kitaura, R.; Noro, S. *Angew. Chem., Int. Ed. Engl.* **2004**, *43*, 2334.
- (65) Ferey, G. *Chem. Soc. Rev.* **2008**, *37*, 191.

- (66) Inokuma, Y.; Yoshioka, S.; Ariyoshi, J.; Arai, T.; Hitora, Y.; Takada, K.; Matsunaga, S.; Rissanen, K.; Fujita, M. *Nature* **2013**, *495*, 461.
- (67) Liu, M.; Wu, J.; Hou, H. *Chemistry* **2018**, *0*.
- (68) Rimoldi, M.; Howarth, A. J.; DeStefano, M. R.; Lin, L.; Goswami, S.; Li, P.; Hupp, J. T.; Farha, O. K. *ACS Catal.* **2016**, *7*, 997.
- (69) Osadchii, D. Y.; Olivos-Suarez, A. I.; Szécsényi, Á.; Li, G.; Nasalevich, M. A.; Dugulan, I. A.; Crespo, P. S.; Hensen, E. J. M.; Veber, S. L.; Fedin, M. V., *et al.* *ACS Catal.* **2018**, *8*, 5542.
- (70) Lee, J.; Farha, O. K.; Roberts, J.; Scheidt, K. A.; Nguyen, S. T.; Hupp, J. T. *Chem. Soc. Rev.* **2009**, *38*, 1450.
- (71) Luz, I.; Llabres i Xamena, F. X.; Corma, A. *J. Catal.* **2010**, *276*, 134.
- (72) Wang, C.; An, B.; Lin, W. *ACS Catal.* **2018**, *9*, 130.
- (73) Cohen, S. M.; Zhang, Z.; Boissonnault, J. A. *Inorg. Chem.* **2016**, *55*, 7281.
- (74) Liu, J.; Ye, J.; Li, Z.; Otake, K. I.; Liao, Y.; Peters, A. W.; Noh, H.; Truhlar, D. G.; Gagliardi, L.; Cramer, C. J., *et al.* *J. Am. Chem. Soc.* **2018**, *140*, 11174.
- (75) Mon, M.; Adam, R.; Ferrando-Soria, J.; Corma, A.; Armentano, D.; Pardo, E.; Leyva-Pérez, A. *ACS Catal.* **2018**, *8*, 10401.
- (76) Dhakshinamoorthy, A.; Asiri, A. M.; Garcia, H. *ACS Catal.* **2018**, *9*, 1081.
- (77) Tejada-Serrano, M.; Mon, M.; Ross, B.; Gonell, F.; Ferrando-Soria, J.; Corma, A.; Leyva-Pérez, A.; Armentano, D.; Pardo, E. *J. Am. Chem. Soc.* **2018**, *140*, 8827.
- (78) Zhu, L.; Liu, X.-Q.; Jiang, H.-L.; Sun, L.-B. *Chem. Rev.* **2017**, *117*, 8129.
- (79) Yang, D.; Gates, B. C. *ACS Catalysis* **2019**.
- (80) Doonan, C.; Riccò, R.; Liang, K.; Bradshaw, D.; Falcaro, P. *Acc. Chem. Res.* **2017**, *50*, 1423.
- (81) Riccò, R.; Liang, W.; Li, S.; Gassensmith, J. J.; Caruso, F.; Doonan, C.; Falcaro, P. *ACS Nano* **2018**, *12*, 13.
- (82) Qiu, Q.-f.; Chen, C.-X.; Wei, Z.-W.; Cao, C.-C.; Zhu, N.-X.; Wang, H.-P.; Wang, D.; Jiang, J.-J.; Su, C.-Y. *Inorg. Chem.* **2018**, *58*, 64.
- (83) Kawamichi, T.; Haneda, T.; Kawano, M.; Fujita, M. *Nature* **2009**, *461*, 633.
- (84) Stassen, I.; Burtch, N.; Talin, A.; Falcaro, P.; Allendorf, M.; Ameloot, R. *Chem. Soc. Rev.* **2017**, *46*, 3185.
- (85) Dou, J.-H.; Sun, L.; Ge, Y.; Li, W.; Hendon, C. H.; Li, J.; Gul, S.; Yano, J.; Stach, E. A.; Dincă, M. *J. Am. Chem. Soc.* **2017**, *139*, 13608.
- (86) Zhou, Z.; He, C.; Yang, L.; Wang, Y.; Liu, T.; Duan, C. *ACS Catalysis* **2017**.

- (87) Wang, L.; Agnew, D. W.; Yu, X.; Figueroa, J. S.; Cohen, S. M. *Angew Chem Int Ed Engl* **2018**, *57*.
- (88) Valvekens, P.; Vermoortele, F.; De Vos, D. *Catalysis Science & Technology* **2013**, *3*.
- (89) Li, J.; Ren, Y.; Yue, C.; Fan, Y.; Qi, C.; Jiang, H. *ACS Appl. Mater. Interfaces* **2018**, *10*, 36047.
- (90) Feng, D.; Chung, W.-C.; Wei, Z.; Gu, Z.-Y.; Jiang, H.-L.; Chen, Y.-P.; Darensbourg, D. J.; Zhou, H.-C. *J. Am. Chem. Soc.* **2013**, *135*, 17105.
- (91) Marshall, R. J.; Forgan, R. S. *Eur. J. Inorg. Chem.* **2016**, *2016*, 4310.
- (92) Evans, J. D.; Sumbly, C. J.; Doonan, C. J. *Chem. Soc. Rev.* **2014**, *43*, 5933.
- (93) Yuan, S.; Chen, Y.-P.; Qin, J.; Lu, W.; Wang, X.; Zhang, Q.; Bosch, M.; Liu, T.-F.; Lian, X.; Zhou, H.-C. *Angew. Chem., Int. Ed. Engl.* **2015**, *54*, 14696.
- (94) Manna, K.; Ji, P.; Lin, Z.; Greene, F. X.; Urban, A.; Thacker, N. C.; Lin, W. *Nat. Commun.* **2016**, *7*, 12610.
- (95) Yang, D.; Odoh, S. O.; Wang, T. C.; Farha, O. K.; Hupp, J. T.; Cramer, C. J.; Gagliardi, L.; Gates, B. C. *J. Am. Chem. Soc.* **2015**, *137*, 7391.
- (96) Bernales, V.; Yang, D.; Yu, J.; Gümüşlü, G.; Cramer, C. J.; Gates, B. C.; Gagliardi, L. *ACS Appl. Mater. Interfaces* **2017**, *9*, 33511.
- (97) Yang, D.; Odoh, S. O.; Borycz, J.; Wang, T. C.; Farha, O. K.; Hupp, J. T.; Cramer, C. J.; Gagliardi, L.; Gates, B. C. *ACS Catal.* **2016**, *6*, 235.
- (98) Pullen, S.; Fei, H.; Orthaber, A.; Cohen, S. M.; Ott, S. *J Am Chem Soc* **2013**, *135*.
- (99) Bloch, E. D.; Britt, D.; Lee, C.; Doonan, C. J.; Uribe-Romo, F. J.; Furukawa, H.; Long, J. R.; Yaghi, O. M. *J. Am. Chem. Soc.* **2010**, *132*, 14382.
- (100) Bloch, W. M.; Burgun, A.; Coghlan, C. J.; Lee, R.; Coote, M. L.; Doonan, C. J.; Sumbly, C. J. *Nat. Chem.* **2014**, *6*, 906.
- (101) Dunning, S. G.; Nandra, G.; Conn, A. D.; Chai, W.; Sikma, R. E.; Lee, J. S.; Kunal, P.; Reynolds, J. E., 3rd; Chang, J. S.; Steiner, A., *et al.* *Angew. Chem., Int. Ed. Engl.* **2018**, *57*, 9295.
- (102) Sikma, R. E.; Kunal, P.; Dunning, S. G.; Reynolds, J. E., 3rd; Lee, J. S.; Chang, J. S.; Humphrey, S. M. *J. Am. Chem. Soc.* **2018**, *140*, 9806.
- (103) Kaye, S. S.; Long, J. R. *J. Am. Chem. Soc.* **2008**, *130*, 806.
- (104) Bloch, W. M.; Burgun, A.; Doonan, C. J.; Sumbly, C. J. *Chem. Commun.* **2015**, *51*, 5486.
- (105) Zhang, Y.; Li, J.; Yang, X.; Zhang, P.; Pang, J.; Li, B.; Zhou, H.-C. *Chem. Commun.* **2019**.
- (106) Afzali, N.; Tangestaninejad, S.; Moghadam, M.; Mirkhani, V.; Mechler, A.; Mohammadpoor-Baltork, I.; Kardanpour, R.; Zadehahmadi, F. *Appl. Organometal Chem.* **2018**, *32*, 1.

- (107) Saito, M.; Toyao, T.; Ueda, K.; Kamegawa, T.; Horiuchi, Y.; Matsuoka, M. *Dalton Trans.* **2013**, *42*, 9444.
- (108) Gonzalez, M. I.; Bloch, E. D.; Mason, J. A.; Teat, S. J.; Long, J. R. *Inorg. Chem.* **2015**, *54*, 2995.
- (109) Gonzalez, M. I.; Oktawiec, J.; Long, J. R. *Faraday Discuss.* **2017**, *201*, 351.
- (110) Carson, F.; Agrawal, S.; Gustafsson, M.; Bartoszewicz, A.; Moraga, F.; Zou, X.; Martin-Matute, B. *Chem. Eur. J.* **2012**, *18*, 15337.
- (111) Manna, K.; Zhang, T.; Greene, F. X.; Lin, W. *J. Am. Chem. Soc.* **2015**, *137*, 2665.
- (112) Prasad, R. R. R.; Dawson, D. M.; Cox, P. A.; Ashbrook, S. E.; Wright, P. A.; Clarke, M. L. *Chemistry* **2018**, *24*, 15309.
- (113) Alkordi, M. H.; Liu, Y.; Larsen, R. W.; Eubank, J. F.; Eddaoudi, M. *J. Am. Chem. Soc.* **2008**, *130*, 12639.
- (114) Sun, C.; Skorupskii, G.; Dou, J. H.; Wright, A. M.; Dinca, M. *J. Am. Chem. Soc.* **2018**, *140*, 17394.
- (115) Ikemoto, K.; Inokuma, Y.; Rissanen, K.; Fujita, M. *J. Am. Chem. Soc.* **2014**, *136*, 6892.
- (116) Fei, H.; Cohen, S. M. *J. Am. Chem. Soc.* **2015**, *137*, 2191.
- (117) Drake, T.; Ji, P.; Lin, W. *Acc. Chem. Res.* **2018**, *51*, 2129.
- (118) Huang, Z.; Liu, D.; Camacho-Bunquin, J.; Zhang, G.; Yang, D.; López-Encarnación, J. M.; Xu, Y.; Ferrandon, M. S.; Niklas, J.; Poluektov, O. G., *et al.* *Organometallics* **2017**, *36*, 3921.
- (119) Goetjen, T. A.; Zhang, X.; Liu, J.; Hupp, J. T.; Farha, O. K. *ACS Sustainable Chem. Eng.* **2019**, *7*, 2553.
- (120) Wang, C. H.; Das, A.; Gao, W. Y.; Powers, D. C. *Angew. Chem., Int. Ed. Engl.* **2018**, *57*, 3676.
- (121) Song, Y.; Li, Z.; Ji, P.; Kaufmann, M.; Feng, X.; Chen, J. S.; Wang, C.; Lin, W. *ACS Catal.* **2019**, *9*, 1578.
- (122) Pereira, C. F.; Simões, M. M. Q.; Tomé, J. P. C.; Almeida Paz, F. A. *Molecules* **2016**, *21*, 1348.
- (123) Ji, P.; Manna, K.; Lin, Z.; Urban, A.; Greene, F. X.; Lan, G.; Lin, W. *J. Am. Chem. Soc.* **2016**, *138*, 12234.
- (124) Li, Z.; Rayder, T. M.; Luo, L.; Byers, J. A.; Tsung, C. K. *J. Am. Chem. Soc.* **2018**, *140*, 8082.
- (125) Zhang, X.; Huang, Z.; Ferrandon, M.; Yang, D.; Robison, L.; Li, P.; Wang, T. C.; Delferro, M.; Farha, O. K. *Nature Catalysis* **2018**, *1*, 356.
- (126) Chen, N. Y.; Kaeding, W. W.; Dwyer, F. G. *J. Am. Chem. Soc.* **1979**, *101*, 6783.
- (127) Huang, N.; Yuan, S.; Drake, H.; Yang, X.; Pang, J.; Qin, J.; Li, J.; Zhang, Y.; Wang, Q.; Jiang, D., *et al.* *J. Am. Chem. Soc.* **2017**, *139*, 18590.
- (128) Li, L.; Yang, Q.; Chen, S.; Hou, X.; Liu, B.; Lu, J.; Jiang, H.-L. *Chem. Commun.* **2017**, *53*, 10026.
- (129) Xiao, D. J.; Oktawiec, J.; Milner, P. J.; Long, J. R. *J. Am. Chem. Soc.* **2016**, *138*, 14371.

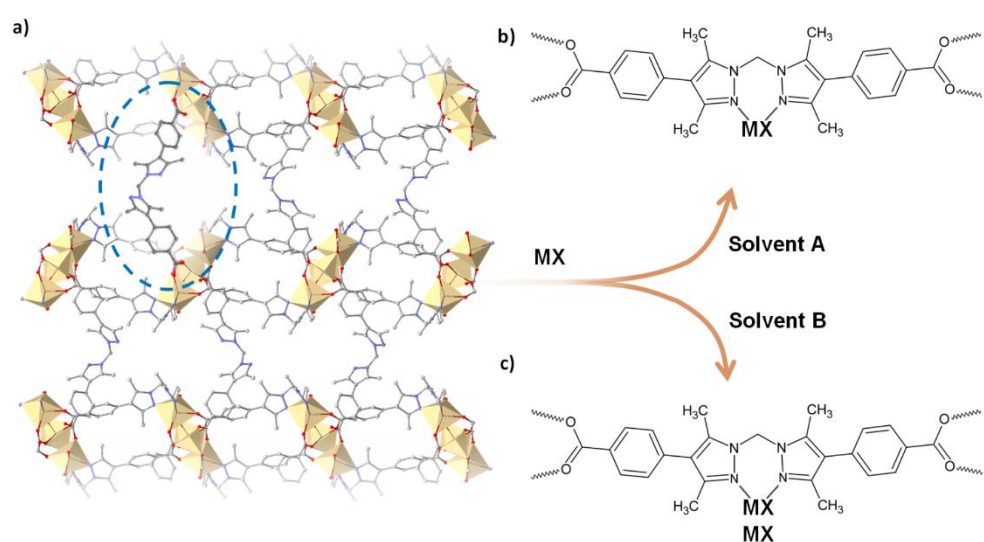
- (130) Grigoropoulos, A.; McKay, A. I.; Katsoulidis, A. P.; Davies, R. P.; Haynes, A.; Brammer, L.; Xiao, J.; Weller, A. S.; Rosseinsky, M. J. *Angew. Chem., Int. Ed. Engl.* **2018**, *57*, 4532.
- (131) Yuan, S.; Qin, J. S.; Li, J.; Huang, L.; Feng, L.; Fang, Y.; Lollar, C.; Pang, J.; Zhang, L.; Sun, D., *et al. Nat. Commun.* **2018**, *9*, 808.
- (132) Zhou, T.-Y.; Auer, B.; Lee, S. J.; Telfer, S. G. *J. Am. Chem. Soc.* **2019**.
- (133) Kirchon, A.; Feng, L.; Drake, H. F.; Joseph, E. A.; Zhou, H.-C. *Chem. Soc. Rev.* **2018**, *47*, 8611.
- (134) Liu, L.; Zhou, T.-Y.; Telfer, S. G. *J. Am. Chem. Soc.* **2017**, *139*, 13936.
- (135) Cao, C.-C.; Chen, C.-X.; Wei, Z.-W.; Qiu, Q.-F.; Zhu, N.-X.; Xiong, Y.-Y.; Jiang, J.-J.; Wang, D.; Su, C.-Y. *J. Am. Chem. Soc.* **2019**.
- (136) Han, Q.; Qi, B.; Ren, W.; He, C.; Niu, J.; Duan, C. *Nat. Commun.* **2015**, *6*, 10007.
- (137) Mizuno, N.; Yamaguchi, K.; Kamata, K. *Coord. Chem. Rev.* **2005**, *249*, 1944.

Chapter 2. X-ray Crystallographic Insights into Post-synthetic Metalation Products in a Metal-organic Framework

Michael T. Huxley, Campbell J. Coghlan, Witold M. Bloch, Alexandre Burgun, Christian J. Doonan* and Christopher J. Sumbly*

*Department of Chemistry and the Centre for Advanced Nanomaterials, School of Physical Sciences,
The University of Adelaide, Adelaide, SA 5005, Australia*


Huxley, M.T., Coghlan, C.J., Bloch, W.M., Burgun, A., Doonan, C.J., Sumbly, C.J., X-ray Crystallographic Insights into Post-synthetic Metalation Products in a Metal-organic Framework, *Phil. Trans. R. Soc. A*, 2017, 375, 28-41



Statement of Authorship

Title of Paper	X-ray crystallographic insights into post-synthetic metalation products in a metal-organic framework
Publication Status	<input checked="" type="checkbox"/> Published <input type="checkbox"/> Accepted for Publication <input type="checkbox"/> Submitted for Publication <input type="checkbox"/> Unpublished and Unsubmitted work written in manuscript style
Publication Details	Huxley, M. T.; Coghlan, C. J.; Bloch, W. M.; Burgun, A.; Doonan, C. J.; Sumbly, C. J. <i>Phil. Trans. R. Soc. A</i> 2017 , 375, 20160028.


Principal Author


Name of Principal Author (Candidate)	Michael Huxley
Contribution to the Paper	Design and development of the project. Preparation of samples and collection of data. Analysis and interpretation of ICP-MS and X-ray crystallography data. Preparation, drafting and final revision of manuscript.
Overall percentage (%)	70%
Certification:	This paper reports on original research I conducted during the period of my Higher Degree by Research candidature and is not subject to any obligations or contractual agreements with a third party that would constrain its inclusion in this thesis. I am the primary author of this paper.
Signature	 Date 25/2/19

Co-Author Contributions

By signing the Statement of Authorship, each author certifies that:

- the candidate's stated contribution to the publication is accurate (as detailed above);
- permission is granted for the candidate to include the publication in the thesis; and
- the sum of all co-author contributions is equal to 100% less the candidate's stated contribution.

Name of Co-Author	Coghlan, C.J.
Contribution to the Paper	Assisted in sample preparation, collection of X-ray crystallography data and drafting of the manuscript.
Signature	 Date 26/2/19

Name of Co-Author	Bloch, W.M.
Contribution to the Paper	Assisted with preparation of preliminary data and data collection.
Signature	 Date 1/03/19

Name of Co-Author	Burgun, A.		
Contribution to the Paper	Assisted with conception of the project and drafting of the manuscript.		
Signature		Date	26/02/2019

Name of Co-Author	Doonan, C.J.		
Contribution to the Paper	Assisted with experiment design and drafting of the manuscript.		
Signature		Date	1/03/2019

Name of Co-Author	Sumbly, C.J.		
Contribution to the Paper	Assisted with experiment design, drafting of manuscript and analysis of X-ray crystallography data.		
Signature		Date	4/3/19

Please cut and paste additional co-author panels here as required.

2.1 Abstract

Post-synthetic modification of metal-organic frameworks (MOFs) facilitates a strategic transformation of potentially inert frameworks into functionalised materials, tailoring them for specific applications. In particular, the post-synthetic incorporation of transition-metal complexes within MOFs, a process known as ‘metalation’, is a particularly promising avenue towards functionalising MOFs. Herein we describe the post-synthetic metalation of a microporous MOF with various transition metal nitrates. The parent framework, **1**, contains free nitrogen donor chelation sites which readily coordinate metal complexes in a single-crystal to single-crystal transformation which, remarkably, can be readily monitored by X-ray crystallography. The presence of an open void surrounding the chelation site in **1** prompted us to investigate the effect of the MOF pore environment on included metal complexes, particularly examining whether void space would induce changes in the coordination sphere of chelated complexes reminiscent of those found in the solution state. To test this hypothesis, we systematically metalated **1** with first-row transition metal nitrates and elucidated the coordination environment of the respective transition metal complexes using X-ray crystallography. Comparison of the coordination sphere parameters of coordinated transition metal complexes in **1** against equivalent solid and solution state species suggests that the void space in **1** does not markedly influence the coordination sphere of chelated species but we show noticeably different post-synthetic metalation outcomes when different solvents are used.

2.2 Introduction

Metal Organic Frameworks (MOFs) have been the subject of extensive recent research activity, owing to the ease with which their porous structures can be modified to suit a range of emerging applications in materials science¹⁻⁴. The broad range of possible ligand and metal combinations available affords an immense variety of potential materials. Although the attractive properties of many MOFs are inherent features of the parent framework, recent developments have seen the emergence of frameworks which can be functionalised post-synthesis to enhance their properties⁵⁻⁸. Post-synthetic modification (PSM) thus provides an avenue towards imbuing porous frameworks with functional moieties that could not otherwise be incorporated into the MOF structure.

A particularly promising avenue for post-synthetic modification is the incorporation of new metal complexes within a framework, a process dubbed post-synthetic metalation (PSMet)⁵. Transition

metal complexes anchored into a porous matrix can instil or enhance the performance of the MOF in applications such as catalysis, sensing and gas storage⁵⁻⁹. However, the crystallographic characterisation of post-synthetically introduced metal complexes has only been reported in rare cases, limiting the systematic study of metalation processes in MOFs and their role in applications.

To enhance our understanding of the benefits of post-synthetic metalation processes, we have developed and previously reported **1**, a Mn(II)-based MOF featuring accessible bidentate bis-(3,5-dimethylpyrazolyl)methane coordination sites¹⁰⁻¹². Our previous work has demonstrated that the reaction of **1** with diverse metal complexes results in the post-synthetic metalation of **1** via the free-bidentate nitrogen donor sites. Metalation is generally quantitative and takes place without significantly compromising crystal quality, thereby facilitating single crystal X-ray diffraction (SCXRD) analysis of the functionalised frameworks. We have previously reported the characterisation of single-crystal to single-crystal transformations within Rh(I) and Co(II) coordinated forms of **1** via X-ray crystallography¹³, highlighting the efficacy of **1** as a platform for the study of bound complexes within the unique environment of the MOF pores.

In MOF **1** the predominant pores extend along the crystallographic *c*-axis, providing a 1-D channel for guest species to access the free-nitrogen donor sites. As the chelating sites project into this open void, they offer an unusual coordination environment for metal complexes in which the close-packing effects associated with discrete solid state structures are somewhat negated. Indeed, the chelation site is typically surrounded by disordered solvent, giving rise to an environment featuring properties akin to the secondary coordination sphere encountered in a solution environment. Our ability to systematically metalate **1** with a diverse range of species and precisely characterise the resulting products, combined with the wealth of discrete bis(pyrazole)methane based complexes¹⁴⁻¹⁷, inspired us to study how the coordination sphere of such metal complexes are influenced by the reaction conditions and the MOF environment. To this end, we have prepared a series of transition metal nitrate functionalised MOF materials, **1**·[Mn(H₂O)₄](NO₃)₂, **1**·[Co(H₂O)₄](NO₃)₂, **1**·[Co(H₂O)₃(NO₃)]NO₃·[Co(MeCN)₄(NO₃)(H₂O)]NO₃, **1**·[Cu(NO₃)₂MeCN]·[Cu(NO₃)(H₂O)₃MeCN]NO₃ and **1**·[Zn(H₂O)₄](NO₃)₂ (henceforth abbreviated: **1**·Mn, **1**·Co, **1**·Co-ACN, **1**·Cu and **1**·Zn respectively), employing a range of analytical techniques to characterise the chemistry of the coordinated moiety and the composition of the bulk material.

2.3 Experimental

Unless otherwise stated, all post-synthetic metalation reactions were carried out in air. The ligand bis(4-(4'-carboxyphenyl)-3,5-dimethylpyrazolyl)methane (H_2L) and MOF **1** were synthesised as previously reported¹⁸. All reagents were sourced from commercial vendors and used as received without further purification.

2.3.1 Metalation Procedures

1·[Co(H₂O)₄](NO₃)₂ (1·Co). Single crystals of **1** (10 mg) were washed with DMF (5×10 mL), then ethanol (5×10 mL) and transferred to a Teflon capped vial. A large excess of Co(NO₃)₂·6H₂O was added, the vial was sealed and heated at 60°C in a preheated oven overnight to yield **1·Co** as pale blue crystals which become pink on cooling. Single crystal X-ray diffraction data was collected on a crystal selected directly from the reaction mixture. IR ν_{max} (neat, cm⁻¹): 1603 (s, C=O), 1550 (C=C), 1506 (C=C), 1468 (C=C), 1405 (s), 1375, 1333, 1302, 1220 (w), 1209 (w), 1179, 1139, 1101.

1·[Zn(H₂O)₄](NO₃)₂ (1·Zn) and 1·[Co(H₂O)₃(NO₃)]NO₃·[Co(MeCN)₄(NO₃)(H₂O)]NO₃ (1·Co-ACN). A general procedure for the synthesis of **1·Zn** and **1·Co-ACN**: Single crystals of **1** (10 mg) were washed with DMF (5×10 mL) followed by acetonitrile (5×10 mL) and transferred to a Teflon capped vial. A large excess of Zn(NO₃)₂·6H₂O or Co(NO₃)₂·6H₂O was added, the vial was sealed and heated at 60°C in a preheated oven overnight to yield **1·Co-ACN** as pale pink crystals and **1·Zn** as colourless crystals. Single crystal X-ray diffraction experiments were performed on the crystals. IR ν_{max} (neat, cm⁻¹) **1·Zn**: 1599 (s, C=O), 1548 (C=C), 1510 (C=C), 1500 (C=C), 1470 (C=C), 1405 (s), 1391, 1379, 1304, 1274, 1177, 1143, 1107; IR ν_{max} (neat, cm⁻¹) **1·Co-ACN**: 1603 (C=O), 1548 (C=C), 1508 (C=C), 1468 (C=C), 1405 (s), 1331, 1302, 1274, 1205, 1179, 1141, 1100.

1·[Cu(NO₃)₂MeCN]·[Cu(NO₃)(H₂O)₃MeCN](NO₃) (1·Cu). Single crystals of **1** (10 mg) were washed with DMF (5×10ml) followed by distilled acetonitrile (5×10 mL) and transferred to a Teflon capped vial under an Ar atmosphere. A large excess of Cu(NO₃)₂·3H₂O was added, the vial was sealed and allowed to stand at room temperature overnight to yield **1·Cu** as green crystals. Single crystal X-ray diffraction data was collected on a crystal selected directly from the reaction mixture. IR ν_{max} (neat, cm⁻¹) **1·Cu**: 1603 (s, C=O), 1550 (C=C), 1508 (C=C), 1498 (C=C), 1468 (C=C), 1405 (s), 1393, 1375, 1306, 1274, 1212, 1175, 1143, 1121, 1103.

1·[Mn(H₂O)₄](NO₃)₂ (1·Mn). Single crystals of **1** (10 mg) were washed with DMF (5×10 mL), then ethanol (5×10 mL) and transferred to a Teflon capped vial. A large excess of Mn(NO₃)₂·H₂O was added, the vial was sealed and heated at 60°C in a preheated oven overnight to yield **1·Mn** as colourless crystals. Single crystal X-ray diffraction data was collected on a crystal selected directly from the reaction mixture. IR ν_{max} (neat, cm⁻¹): 1605 (s, C=O), 1551 (C=C), 1508 (C=C), 1466 (C=C), 1405(s), 1335, 1302, 1280, 1207, 1179, 1145, 1101.

2.3.2 Inductively-coupled plasma mass spectrometry (ICP-MS)

Single crystals of each metalated MOF sample were washed five times in fresh solvent to remove any unreacted metal reagents. The crystals were dried thoroughly under vacuum and soaked in 2% HNO₃ at 65°C overnight, after which the resulting solution was filtered through a 45 μ m filter. The solutions were diluted and the quantity of dissolved metal ions determined using an Agilent 7500cs ICP-MS instrument. Three separate samples were analysed on each occasion to obtain an average.

2.3.3 Single Crystal and Powder X-ray Diffraction Data

Full spheres of diffraction data were collected for single crystals mounted on nylon loops in Paratone-N at 100 K on the MX1 beamline of the Australia Synchrotron using the Blulce software interface,¹⁹ $\lambda = 0.71073$ Å. N_{tot} reflections were merged to N unique (R_{int} quoted) after a multi-scan absorption correction (proprietary software) and used in the full matrix least squares refinements on F^2 , N_o with $F > 4\sigma(F)$ being considered 'observed'. Anisotropic displacement parameter forms were refined for the non-hydrogen atoms; hydrogen atoms were treated with a riding model [weights: $(\sigma^2(F_o)^2 + (aP)^2 + (bP)^2)^{-1}$; $P = (F_o^2 + 2F_c^2)/3$]. Neutral atom complex scattering factors were used; computation used the SHELXL2014 program.²⁰ Pertinent results are given in the manuscript and in Table S7.1.4.1. Powder X-ray diffraction data were collected from capillary mounted samples on a Bruker Advance D8 diffractometer using Cu K α radiation ($\lambda = 1.5418$ Å).

2.4 Results and Discussion

2.4.1 Post-Synthetic Metalation of **1**: Background

We recently reported^{10-11, 13} a MOF, **1**, synthesised from the flexible bis(pyrazole)methane linker, bis(4-(4'-carboxyphenyl)-3,5-dimethyl-pyrazolyl)methane) (H_2L) and $MnCl_2 \cdot 4H_2O$. A linear Mn_3 trimer forms the structural node in **1**, while the carboxylate and pyrazole donors of six L molecules serve to complete the octahedral coordination sphere of each Mn^{2+} ion. Four of the six L molecules involved in binding the Mn_3 trimers coordinate via both their carboxylate and N-donor moieties, the latter chelating each end of the trimer. These fully coordinated L moieties connect to adjacent trimer units via the carboxylate functionality to form a 2D sheet in the crystallographic *ac* plane. The remaining two L molecules, denoted L' , serve to pillar these 2D sheets via their carboxylate donors, leaving their bidentate nitrogen donor sites non-coordinated. This generates a 3D network with open pores running along the crystallographic *c*- and *a*-axes, granting guest molecules access to the free nitrogen donor sites. The combination of an open, porous architecture, flexible sp^3 CH_2 hinge and accessible coordination sites in **1** allows quantitative post-synthetic metalation and single crystal structural identification of the incursive metal ion species and their coordination sphere.

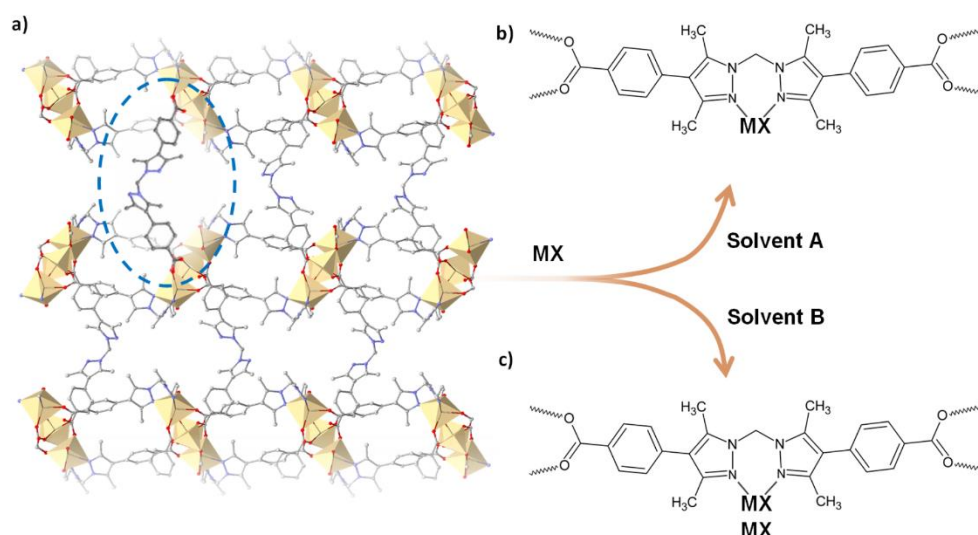


Figure 2.1. a) A perspective view of MOF **1** showing the Mn_3 -trimers bridged by L' molecules, giving rise to a porous network with free-nitrogen donor sites highlighted by a dashed blue oval. Depending on solvent choice, metalation can yield **b**) a structure featuring only a coordinated metal complex, or **c**) a coordinated complex accompanied by a solvated complex residing in the MOF pore.

2.4.2 Metalation of **1** with Transition Metal Nitrates

Given the efficacy of **1** as a host for a broad range of metal complexes,^{10-11,13} we sought to investigate the role of the pore surrounding the chelating site in determining the structure of bound complexes. The ~ 13Å separation between chelation sites along the *c*-axis ensures that coordinated species are held in isolation, an environment which is substantially different to the close-packed structures typically observed in the solid state for discrete metal complexes. Additionally, we hypothesised that the MOF pores, which are typically occupied by disordered solvent molecules, would provide a coordination environment more akin to solution rather than the solid state.

Therefore, we reacted single crystals of MOF **1** with a series of first-row transition metal nitrates (Mn^{2+} , Co^{2+} , Cu^{2+} and Zn^{2+}) using PSMet procedures. The nitrate anion was selected due to the solubility of its derivatives and its ability to act as a monodentate, bidentate or non-coordinating anion. Such diverse coordination modes extend the scope by which the MOF environment can influence the coordination sphere of post-synthetically introduced metal species. We note briefly that analogous reactions with iron salts leads to doping of the Mn^{2+} based trimer with Fe^{2+} .¹⁰

Metalation was performed by soaking single crystals of **1** in a solution of the metalation reagent (in excess), generally with heating to moderate temperatures. In the case of **1·Mn** and **1·Zn** the reaction was performed in acetonitrile at 60°C overnight, while **1·Cu** was synthesised in acetonitrile at room temperature. Metalation with $\text{Co}(\text{NO}_3)_2 \cdot 6\text{H}_2\text{O}$ was found to proceed in both ethanol and acetonitrile at 60°C, giving rise to **1·Co** and **1·Co-ACN** respectively. Intriguingly, the choice of solvent effects the structure of the incorporated Co^{2+} moiety, giving rise to a simple chelated complex in **1·Co** (Figure 2.2) and a chelated/free-solvated Co^{2+} complex pair in **1·Co-ACN** (Figure 2.3) which is discussed in detail below.

The single crystals obtained after PSM were successfully characterised using SCXRD which revealed the coordination environment of each coordinated metal centre (Figure 2.2). Analysis of the samples by Powder X-ray Diffraction (PXRD) confirmed retention of crystallinity in the bulk phase after the reactions with excellent agreement between the theoretical PXRD derived from the respective single-crystal structures and those obtained experimentally (see supporting information). Refinement of the metal site occupancy in the single crystal X-ray structures indicated varying degrees of metalation (Table 2.1). To better assess the degree of metalation achieved in the bulk phase, we performed Inductively Coupled Plasma Mass Spectrometry (ICP-MS) analysis to provide a quantitative measure

of the elemental composition of each sample. Since **1** contains three Mn^{2+} ions per L' chelation site, quantitative metalation is expected to result in a 3:1 Mn:M ratio. This process excludes **1·Mn** from analysis, since chelated Mn^{2+} cannot be distinguished from that in the trimer unit using ICP-MS.¹¹

The results presented in Table 2.1 indicate that a high degree of metalation is achieved in all cases except **1·Co**. The metalation percentage yield determined by ICP-MS for **1·Co** is approximately 40% lower than that determined by X-ray crystallography. We suggest a possible reason for this disparity to be the lability of Co(II) complexes, which likely results in significant leeching of cobalt(II) from the coordination site when the sample is washed with fresh solvent prior to ICP-MS sample preparation. In comparison, as the crystal structures were obtained directly after synthesis, leeching is minimised and thus the site occupancy determined by X-ray crystallography exceeds that observed by ICP-MS. In the case of **1·Co**, leaching is significant after as little as two washes and Co(II) occupancy closely approaches the value reported in Table 2.1 for this species (ICP-MS analysis without washing is precluded as the metalation solution contains a considerable excess of cobalt nitrate that would distort the results). Furthermore, the metalation percentage yields greater than 100% observed for **1·Cu** and **1·Co-ACN** are attributed to the presence of a secondary guest metal complex which resides in the MOF pore and supplements the overall metalation yield observed via ICP-MS. The structural properties of these guest complexes and their extensive interactions with the respective MOF-bound coordinated metal sites is expounded upon below, although we note here that the ICP-MS data largely supports the combined site occupancy observed by X-ray crystallography.

Table 2.1. The metalation percentage yield as determined by ICP-MS (including standard deviations) and refinement of the atom site occupancy in the single crystal X-ray structures. * The first number refers exclusively to the occupancy of the chelating site, the number in brackets refers to metal atom occupancy of solvated complexes in the MOF pores if present (see below).

Sample	ICP-MS	±	X-ray Crystallography*
1·Mn	NA	NA	100
1·Co	57	1	100
1·Co-ACN	120	4	100 (50)
1·Cu	166	4	100 (100)
1·Zn	121.0	3	100

The coordination environment of each MOF bound metal complex is displayed in Figure 2.2. The Mn(II), Co(II) and Zn(II) structures (**1·Mn**, **1·Co** and **1·Zn** respectively) all display an octahedral tetra-aqua ligand environment with an equatorial plane defined by two L' nitrogen atoms and two water molecules. A similar tetra-aqua motif is often observed in the solid state when Mn²⁺, Co²⁺ and Zn²⁺ react with bidentate nitrogen donor ligands²¹⁻²³, and such complexes tend to display strong hydrogen bond interactions between coordinated water and proximate nitrate anions. We also note that complexes featuring bound nitrate anion(s) are occasionally reported in the literature²⁴. In **1·Mn**, **1·Co** and **1·Zn**, disorder of the nitrate anion within the MOF pore prevented its location and refinement, the sole exception being a lone nitrate observed on the L' mirror plane in **1·Mn**. Clearly, the open space surrounding the chelation site in **1** offers a significant degree of freedom, reminiscent of the solution state, for non-coordinated anions.

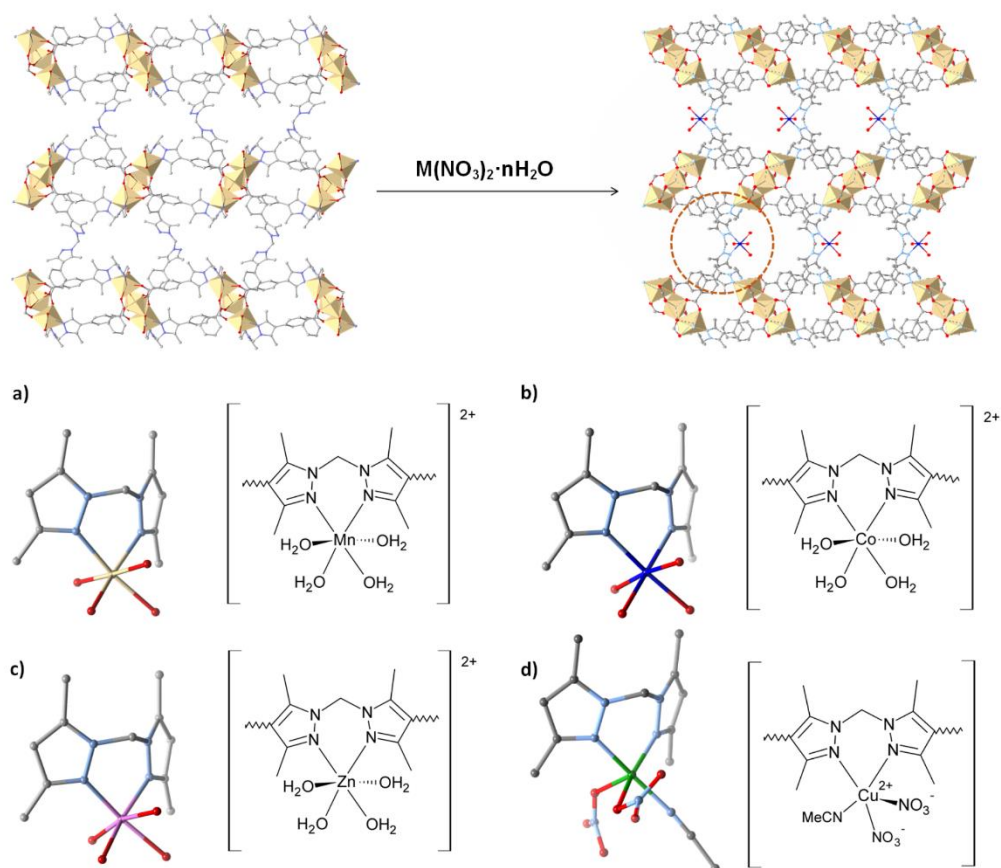


Figure 2.2. Top: A typical outcome of a post-synthetic metalation reaction of MOF **1** with $M(\text{NO}_3)_2 \cdot n\text{H}_2\text{O}$. Bottom: perspective views of the X-ray structures supplemented with chemical diagrams of a) **1·Mn**, b) **1·Cu**, c) **1·Co**, d) **1·Zn** showing the primary coordination sphere of the metal centres bound to the chelating site.

The coordination environment observed in **1·Cu** diverges from the tetra-aqua complexes described above. As expected for a d^9 complex, **1·Cu** displays significant Jahn-Teller distortion, resulting in a distorted tetragonal pyramidal coordination environment with an equatorial plane defined by the L' coordination site, a nitrate anion and N-coordinated acetonitrile. The coordinated axial site is occupied by a monodentate nitrate (Cu-O 2.258(6) Å), while the opposing axial site interacts very weakly with the equatorially bound nitrate anion (Cu-O 2.58(1) Å). The presence of two coordinated nitrate anions and coordinated solvent distinguishes **1·Cu** from the other members of the series. However, we note that a similar Cu^{2+} coordination environment was reported by Lider *et al.* from the reaction of bis(4-iodo-3,5-dimethyl-pyrazolyl)methane (**bidmp**) with copper(II) nitrate²⁵. Although the relative position of the solvent and nitrate anions differs between the two materials, this and other similar discrete metal complex structures²⁶⁻²⁸, confirm the MOF bound copper complex to be in a coordination environment typical for Cu(II).

As described above, the pore surrounding the coordinating site in MOF **1** allows movement of non-coordinated nitrate anions, which is reminiscent of the solution state. To determine whether this extends to modifying the coordination sphere, we compared the metal-water bonding parameters in **1·M(NO₃)₂** to solid state and solution state analogues. Numerous studies employing Extended X-ray Absorption Fine Structure (EXAFS) and X-ray Absorption Spectroscopy (XAS) experiments have been conducted to determine the coordination environment of transition metal complexes in aqueous solution²⁹⁻³². These data have shown that the identity of the anion does not affect the coordination sphere parameters. Of the four transition metal complexes investigated in our study, Mn^{2+} , Co^{2+} and Zn^{2+} are reported to produce octahedral $[\text{M}(\text{H}_2\text{O})_6]^{2+}$ type structures in solution with M-O bond lengths detailed in Table 2.2 below. The final member of the series, Cu^{2+} , forms a Jahn-Teller distorted complex in solution with equatorial and axial bond lengths of ~ 1.94 and ~ 2.38 Å respectively³¹. We hypothesised that the isolated chelation sites in MOF **1**, which are surrounded by pore volume capable of housing solvate molecules, would promote the formation of metal complexes which more closely resemble solution rather than solid state analogues. Comparison of the M-O bond lengths for metalated **1**, solid state discrete metal complexes (for MO_4N_2 type solid state compounds, Cambridge Structural Database [CSD] v1.1, accessed 31/03/16) and hexa-aqua metal complex solution data (Table 2.2) indicates that the complexes in MOF **1** possess a coordination environment that is consistent with both solution and solid state examples.

Table 2.2. Summary of M-O bond lengths (Å) for Mn(II), Co(II), Cu(II) and Zn(II) complexes in solution (EXAFS data), solid state (for MO₄N₂ type solid state compounds, CSD v1.1, accessed 31/03/16), coordinated to **1** or as a guest complex in **1**. * Denotes M-O_{nitrate} bond, all other reported bond lengths are M-O_{water} bonds.

Metal	1-M M-O bond length (MOF-bound)/ Å	1-M M-O bond length (Pore-bound)/ Å	Solvated M-O bond length / Å	Solid state M-O bond length (CSD)/ Å
Mn	2.19(1), 2.31(2), 2.40(2)	N/A	2.20 ³⁰	2.18
Co (EtOH)	2.123(9), 2.132(9), 2.142(8)	N/A	2.08 ³⁰ 2.06 ²⁹	2.09
Co (MeCN)	2.025(9), 2.17(1), 2.23(1)	2.03(1), 2.056(9)*	-	-
Cu	1.996(5)*, 2.258(6)* (axial)	1.963(6), 1.963(5) 1.981(6), 1.980(6)*	1.94, 2.38 ³¹	1.975, 2.35
Zn	2.13(2), 2.15(2), 2.36(3)	N/A	2.08 ³⁰ 2.09 ²⁹	2.11

One notable exception to this observation is **1·Cu** which features two coordinated nitrate anions and thereby possesses a structural motif which resembles the typical solid state complex rather than the aqua complexes which predominate in solution. We postulate this change in the coordination environment to be partly due to the use of acetonitrile as a solvent and the presence of a secondary solvated Cu(II) complex in the MOF pore (see below), with the subsequent reduction in available pore space favouring nitrate coordination. Intriguingly, an analogous MOF bound Co(II) complex formed from a reaction carried out in acetonitrile also features a solvated complex in the MOF pore (see below) and a coordinated nitrate anion. This contrasts with **1·Co** (prepared in ethanol) which has a disordered nitrate anion in the MOF pore. Thus, it is evident that the degree of void space available in MOF **1**, as dictated by the presence or absence of guest complexes, influences the coordination sphere of L' chelated complexes.

2.4.3 Non-Framework Bound Complexes Within MOF 1

Bidentate coordination by the free L' coordination site is not the only mode in which metal complexes can be incorporated within MOF **1**; the pores can also trap metal complexes at well-defined locations within the framework¹¹. The capacity of porous coordination networks to order guest species within their pores has previously been refined and exploited by Inokuma *et al.*³³, among others³⁴⁻³⁶, to facilitate X-ray crystallographic characterisation of large guest molecules without the need for direct crystallisation of the target compound. In **1·Co-ACN** (a derivative of **1·Co**

prepared in acetonitrile rather than ethanol) and **1·Cu**, the combination of framework-anchored coordinating sites and a confined pore environment combine to encourage the ordering of additional discrete metal complexes in the MOF pores, as described below.

The single crystal structures of **1·Cu** and **1·Co-ACN** revealed the presence of a secondary solvated metal complex residing in the MOF pore. In the case of **1·Co-ACN**, the octahedral complex lies on the mirror plane between the L' chelating site and is situated ~ 4.6 Å below the framework-bound complex when viewed along the crystallographic *c*-axis (Figure 2.3a). The equatorial plane of this pore-bound Co(II) complex is constituted by four acetonitrile ligands and the complex is capped by a monodentate nitrate anion. A water molecule occupies the final coordination site, interacting with two non-coordinated nitrate anions (Figure 2.3b). In **1·Cu**, the pore-bound complex possesses an equatorial plane defined by three water molecules and one mono-dentate nitrate ligand. The axial position is occupied by acetonitrile, while charge balance is achieved via a nitrate anion residing nearby in the MOF pore (Figure 2.3c). The pore-bound complex is offset by ~ 2.4 Å from the mirror plane when viewed along the *c*-axis (Figure 2.3d). Refinement of the metal site occupancy of the pore bound complexes in **1·Cu** and **1·Co-ACN** suggested $\sim 100\%$ and 50% occupancy by the solvated complexes respectively, which is consistent with the ICP-MS data obtained. For **1·Co-ACN** this is lower than the occupancy of the coordinated site in the framework and is possibly due to the pores being blocked by excess reagent leading to slower reaction kinetics.

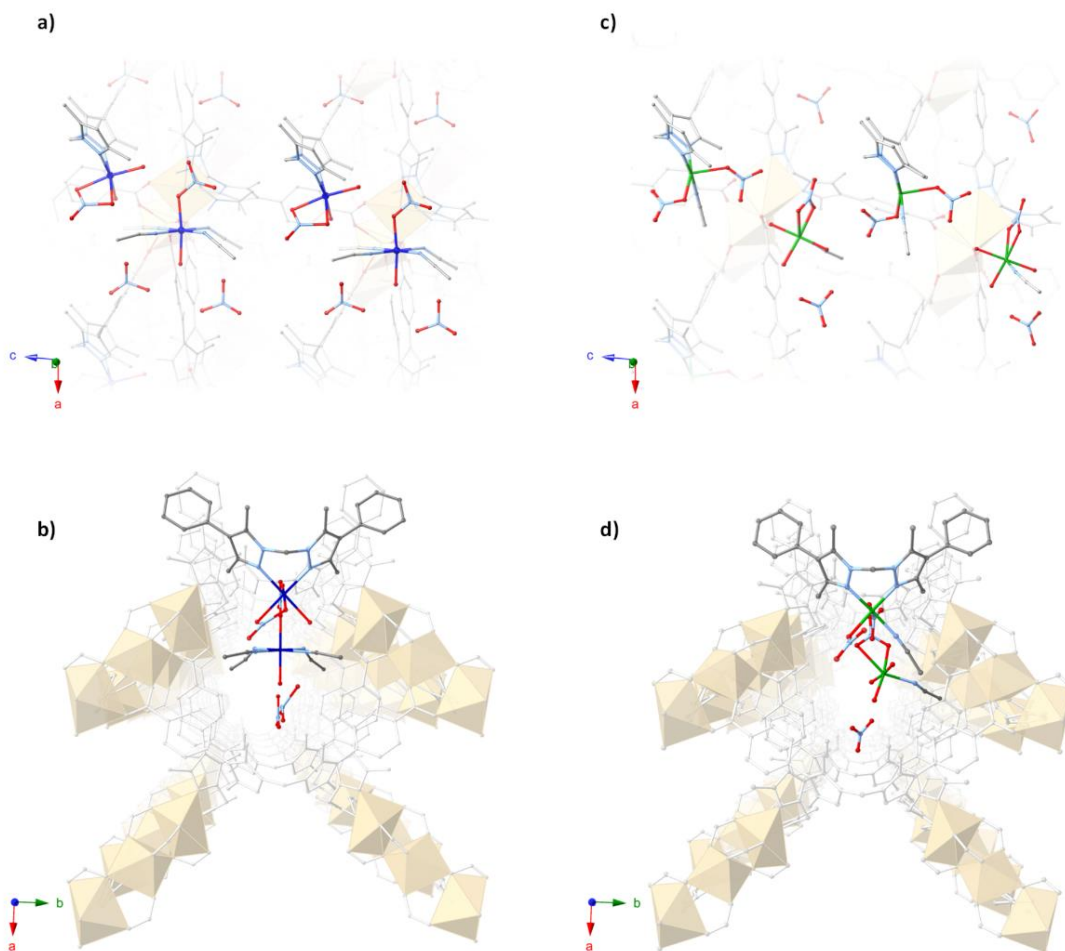


Figure 2.3. **a)** A perspective view displaying the arrangement of chelated and pore-bound Co(II) complexes along the *c*-axis and **b)** the view perpendicular to the *c*-axis pore of **1-Co-ACN**, which highlights the position of the solvated species in the pore space adjacent to the chelation site (adjacent Co(II) complexes have been removed for clarity). The equivalent views of **1-Cu** are displayed in **c)** and **d)** respectively.

The immobilisation of discrete complexes within MOF **1** provides an opportunity to further study the influence of the MOF environment on first row transition metal chemistry although, due to the partial occupancy for the Co example, only general structural comparisons will be discussed. Similar $[\text{Co}(\text{MeCN})_4(\text{X})_2]^{n+}$ (where X are additional acetonitrile ligands or an oxygen donor ligand) complexes have been characterised in solution³⁷ using XAS or the solid state³⁸⁻³⁹. In the later instance, the complex $[\text{Co}(\text{MeCN})_4(\text{H}_2\text{O})_2]^{2+}$ was crystallised as an inclusion complex, with Co-N bond lengths of 2.124 and 2.101 Å that match well with those observed in **1-Co-ACN** (Co-N bond lengths 2.071(8) and 2.115(2) Å). Furthermore, the 2.056 Å Co-O_{water} bond length reported by Willey *et al*³⁸ is consistent with that observed in **1-Co-ACN** (Co-O bond length 2.03(1) Å), being slightly shorter than

reported in typical tetra-aqua solid state or aqueous hexa-aqua solution complexes. In **1·Cu**, the solvated complex possess relatively short Cu-O_{aqua} bond lengths of 1.963(6), 1.963(5) and 1.981(6) Å, although these are comparable to those observed in solution.³¹

Comparing **1·Co-ACN** and **1·Co** reveals that the inclusion of a guest metal complex within the MOF pore modifies the framework bound metal site to include a bidentate chelating nitrate anion in its coordination sphere. While the change in solvent cannot be excluded (ethanol to acetonitrile), the incorporation of a pore-bound complex appears to limit the pore space and favour coordinated as opposed to non-coordinated anions. These confinement affects are also seen in greater ordering of the non-coordinated nitrate anions for both **1·Co-ACN** and **1·Cu**. In both **1·Cu** and **1·Co-ACN**, the coordination spheres of the MOF and pore bound metal species, and adjacent anions, are connected by an extensive network of hydrogen bonding, typical of the well-defined intermolecular interactions between discrete complexes close-packed in the solid state. When the overarching framework of **1** is removed, it is evident that the 1D hydrogen-bonded chains that percolate along the *c* and *a* axes reflect the pore architecture of **1** (Figure 2.3c). At these high metal loadings the confining environment within MOF **1** induces additional inter-complex interactions for the Co(II) and Cu(II) complexes. This behaviour contrasts with the 'isolated' complexes observed in **1·Mn** and **1·Zn** which exhibit minimal defined long-range interactions between complexes, thereby existing in a distinctly different environment to their discrete, solid state analogues.

2.5 Conclusion

We have used a single-crystal to single-crystal PSMet protocol to systematically metalate a microporous metal organic framework with a series of transition metal nitrates. The transformations were examined using single crystal X-ray diffraction which provided detailed insight into the coordination mode of included metal salt guest species. Manganese(II), cobalt(II) and zinc(II) nitrate salts were found to readily form tetraaqua(N,N-chelate) chelated complexes with coordination parameters that compare favourably with solid (MO₄N₂ motif) and solution state (hexa-aqua motif) structures. More complex structures featuring secondary solvated and pore bound Cu(II) or Co(II) complexes were observed when copper(II) or cobalt(II) nitrate were reacted with **1** in acetonitrile. These uncharacteristic pore-bound metal complexes further serve to underline the importance of careful solvent choice and the ability to accurately characterise metalation products following post-synthetic metalation reactions. The inclusion of a free complex within the void space of **1** was found

to induce greater order in non-coordinated nitrate anions (and coordinated ligands), facilitating an improved ability to locate and refine these in the respective X-ray crystal structures. Combined, these results demonstrate further promising attributes of **1** as a candidate for the systematic study of post-synthetic metalation protocols in MOFs, thereby providing opportunities to closely examine metal coordination chemistry in an environment that intersects that seen in both solution and the solid state.

2.6 Additional Information

2.6.1 Acknowledgments

Aspects of this research were undertaken on the MX1 beamline at the Australian Synchrotron, Victoria, Australia. ICP-MS studies were performed at Adelaide Microscopy with supervision and assistance from Aoife McFadden.

2.6.2 Funding Statement

This research is supported by the Science and Industry Endowment Fund (SIEF). CJD and CJS would like to acknowledge the Australian Research Council for funding FT100100400 and FT0991910, respectively.

2.6.3 Data Accessibility

The Supplementary Material contains additional X-ray crystallographic details and powder X-ray diffraction data. CIF data have been deposited with the Cambridge Crystallographic Data Centre, CCDC reference numbers CCDC 1476923-1476927 (**1·Cu**, 1476923; **1·Zn**, 1476924; **1·Mn**, 1476925; **1·Co**, 1476926; **1·Co-ACN**, 1476927).

2.6.4 Competing Interests

We have no competing interests.

2.6.5 Author Contributions

MTH led the conception and design of the experiments and was primarily responsible for interpreting the data, drafting and revising the manuscript. CJC, WMB and AB were involved in the acquisition of data, analysis and interpretation of data obtained. CJD and CJS assisted in the conception and design of the experiments and interpretation of data, and were responsible for critically revising the manuscript and final approval of the version to be published.

2.7 References

- (1) Furukawa, H.; Cordova, K. E.; O'Keeffe, M.; Yaghi, O. M. *Science* **2013**, *341*, 974.
- (2) Kitagawa, S.; Kitaura, R.; Noro, S. *Angew. Chem., Int. Ed. Engl.* **2004**, *43*, 2334.
- (3) Yaghi, O. M.; O'Keeffe, M.; Ockwig, N. W.; Chae, H. K.; Eddaoudi, M.; Kim, J. *Nature* **2003**, *423*, 705.
- (4) Ferey, G. *Chem. Soc. Rev.* **2008**, *37*, 191.
- (5) Evans, J. D.; Sumbly, C. J.; Doonan, C. J. *Chem. Soc. Rev.* **2014**, *43*, 5933.
- (6) Bloch, E. D.; Britt, D.; Lee, C.; Doonan, C. J.; Uribe-Romo, F. J.; Furukawa, H.; Long, J. R.; Yaghi, O. M. *J. Am. Chem. Soc.* **2010**, *132*, 14382.
- (7) Manna, K.; Zhang, T.; Lin, W. *J Am Chem Soc* **2014**, *136*.
- (8) Wang, Z.; Cohen, S. M. *Chem Soc Rev* **2009**, *38*.
- (9) Tanabe, K. K.; Cohen, S. M. *Chem Soc Rev* **2011**, *40*.
- (10) Huxley, M.; Coghlan, C. J.; Burgun, A.; Tarzia, A.; Sumida, K.; Sumbly, C. J.; Doonan, C. J. *Dalton Trans* **2016**, *45*.
- (11) Bloch, W. M.; Burgun, A.; Doonan, C. J.; Sumbly, C. J. *Chem. Commun.* **2015**, *51*, 5486.
- (12) Bloch, W. M.; Champness, N. R.; Doonan, C. J. *Angew. Chem., Int. Ed.* **2015**, *54*, 12860.
- (13) Bloch, W. M.; Burgun, A.; Coghlan, C. J.; Lee, R.; Coote, M. L.; Doonan, C. J.; Sumbly, C. J. *Nat. Chem.* **2014**, *6*, 906.
- (14) Pettinari, C.; Pettinari, R. *Coordination Chemistry Reviews* **2005**, *249*.

- (15) Pettinari, C.; Lorenzotti, A.; Pellei, M.; Santini, C. *Polyhedron* **1997**, *16*, 3435.
- (16) Pettinari, C.; Gioia Lobbia, G.; Lorenzotti, A.; Cingolani, A. *Polyhedron* **1995**, *14*, 793.
- (17) Potapov, A. S.; Domina, G. A.; Petrenko, T. V.; Khlebnikov, A. I. *Polyhedron* **2012**, *33*.
- (18) Bloch, W. M.; Doonan, C. J.; Sumbly, C. J. *CrystEngComm* **2013**, *15*, 9663.
- (19) McPhillips, T.; McPhillips, S.; Chiu, H.; Cohen, A. E.; Deacon, A. M.; Ellis, P. J.; Garman, E.; Gonzalez, A.; Sauter, N. K.; Phizackerley, R. P., *et al.* *J. Synchrotron Rad.* **2002**, *9*, 401.
- (20) Sheldrick, G. M. *Acta Crystallogr. C Struct. Chem.* **2015**, *71*, 3.
- (21) Weguo, W.; Changneng, C.; Qiutian, L. *Acta Cryst. E* **2003**, 908.
- (22) Zhang, C.; Janiak, C. *Journal of Chemical Crystallography* **2001**, *31*, 29.
- (23) Li, Z.; Wang, G.; Niu, J.; Xu, J.; Hu, N. *Acta Cryst. C* **2007**, *C63*, m94.
- (24) Zhang, X.; Huang, D.; Wang, W.; Chen, C.; Liu, Q. *Acta Cryst. C* **2002**, *C58*, m268.
- (25) Lider, E. V.; Peresykina, E. V.; Lavrenova, L. G.; Krivenko, O. L.; Boguslavskii, E. G.; Smolentsev, A. I.; Sheludyakova, L. A.; Vasilevskii, S. F. *Russian Journal of Coordination Chemistry* **2009**, 35.
- (26) Lider, E. V.; Krivenko, O. L.; Peresykina, E. V.; Smolentsev, A. I.; Shvedenkov, Y. G.; Vasilevskii, S. F.; Lavrenova, L. G. *Russian Journal of Coordination Chemistry* **2007**, 33.
- (27) Fujisawa, K.; Kanda, R.; Miyashita, Y.; Okamoto, K.-i. *Polyhedron* **2008**, 27.
- (28) Schuitema, A. M.; Engelen, M.; Koval, I. A.; Gorter, S.; Driessen, W. L.; Reedijk, J. *Inorganica Chimica Acta* **2001**, *324*, 57.
- (29) Bol, W.; Gerrits, G. J. A.; Van Panthaleon Van Eck, C. L. *J. Appl. Cryst.* **1970**, 3.
- (30) Ohtaki, H.; Yamaguchi, T.; Maeda, M. *Bulletin of the Chemical Society of Japan* **1976**, *49*, 701.
- (31) Persson, I. *Pure and Applied Chemistry* **2010**, 82.
- (32) Sham, T. K.; Hastings, M. L.; Perlman, M. L. *J. Am. Chem. Soc.* **1980**, *102*, 5906.
- (33) Inokuma, Y.; Yoshioka, S.; Ariyoshi, J.; Arai, T.; Hitora, Y.; Takada, K.; Matsunaga, S.; Rissanen, K.; Fujita, M. *Nature* **2013**, *495*, 461.
- (34) Inokuma, Y.; Arai, T.; Fujita, M. *Nat Chem* **2010**, 2.

(35) Ohmori, O.; Kawano, M.; Fujita, M. *J Am Chem Soc* **2004**, *126*.

(36) Kawano, M.; Fujita, M. *Coordination Chemistry Reviews* **2007**, *251*.

(37) Diaz-Moreno, S.; Munoz-Paez, A.; Sanchez Marcos, E. *J. Phys. Chem. B* **2000**, *104*, 11794.

(38) Willey, G. R.; Aris, D. R.; Errington, W. *Transition Metal Chemistry* **2000**, *25*.

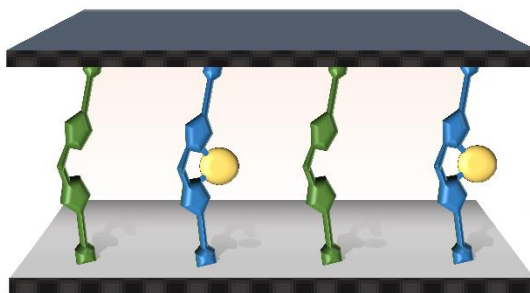
(39) Kopylovich, M. N.; Kukushkin, V. Y.; Guedes da Silva, M. F. C.; Haukka, M.; Fraústo da Silva, J. J. R.; Pombeiro, A. J. L. *Journal of the Chemical Society, Perkin Transactions 1* **2001**.

Chapter 3: Site-Specific Metal and Ligand Substitutions in a Microporous Mn²⁺-Based Metal-Organic Framework

Michael Huxley, Campbell J. Coghlan, Alexandre Burgun, Andrew Tarzia, Kenji Sumida,* Christopher J. Sumby,* and Christian J. Doonan*

*Centre for Advanced Nanomaterials, School of Physical Sciences, University of Adelaide, SA 5005, Australia.

Huxley, M.T., Coghlan, C.J., Burgun, A., Tarzia, A., Sumida, K., Sumby, C.J., Doonan, C.J., Site-specific metal and ligand substitutions in a microporous Mn²⁺-based metal-organic framework, *Dalton Trans.*, 2016, 45, 10, 4431-4438



Statement of Authorship

Title of Paper	Site-specific metal and ligand substitutions in a microporous Mn ²⁺ -based metal-organic framework
Publication Status	<input checked="" type="checkbox"/> Published <input type="checkbox"/> Accepted for Publication <input type="checkbox"/> Submitted for Publication <input type="checkbox"/> Unpublished and Unsubmitted work written in manuscript style
Publication Details	Huxley, M.; Coghlan, C. J.; Burgun, A.; Tarzia, A.; Sumida, K.; Sumbly, C. J.; Doonan, C. J. <i>Dalton Trans</i> 2016 , 45 (10), 4431-4438.

Principal Author

Name of Principal Author (Candidate)	Michael Huxley
Contribution to the Paper	Design and development of the mixed ligand synthesis project. Preparation of samples and collection of NMR and ICP-MS data. Analysis and interpretation of ICP-MS and NMR data. Preparation of manuscript.
Overall percentage (%)	50%
Certification:	This paper reports on original research I conducted during the period of my Higher Degree by Research candidature and is not subject to any obligations or contractual agreements with a third party that would constrain its inclusion in this thesis. I am the primary author of this paper.
Signature	Date 25/2/19

Co-Author Contributions

By signing the Statement of Authorship, each author certifies that:

- i. the candidate's stated contribution to the publication is accurate (as detailed above);
- ii. permission is granted for the candidate to include the publication in the thesis; and
- iii. the sum of all co-author contributions is equal to 100% less the candidate's stated contribution.

Name of Co-Author	Coghlan, C.J.
Contribution to the Paper	Design and development of the Fe metalation component of the project, including the preparation of samples and analysis of data. Assisted with the preparation and drafting of the manuscript.
Signature	Date

Name of Co-Author	Burgun, A.
Contribution to the Paper	Assisted with the conception of the project and drafting of the manuscript.
Signature	Date 26/02/2019

Statement of Authorship

Title of Paper	Site-specific metal and ligand substitutions in a microporous Mn ²⁺ -based metal-organic framework
Publication Status	<input checked="" type="checkbox"/> Published <input type="checkbox"/> Accepted for Publication <input type="checkbox"/> Submitted for Publication <input type="checkbox"/> Unpublished and Unsubmitted work written in manuscript style
Publication Details	Huxley, M.; Coghlan, C. J.; Burgun, A.; Tarzia, A.; Sumida, K.; Sumbly, C. J.; Doonan, C. J. <i>Dalton Trans</i> 2016 , 45 (10), 4431-4438.

Principal Author

Name of Principal Author (Candidate)	Michael Huxley
Contribution to the Paper	Design and development of the mixed ligand synthesis project. Preparation of samples and collection of NMR and ICP-MS data. Analysis and interpretation of ICP-MS and NMR data. Preparation of manuscript.
Overall percentage (%)	50%
Certification:	This paper reports on original research I conducted during the period of my Higher Degree by Research candidature and is not subject to any obligations or contractual agreements with a third party that would constrain its inclusion in this thesis. I am the primary author of this paper.
Signature	Date 25/2/19


Co-Author Contributions


By signing the Statement of Authorship, each author certifies that:


- the candidate's stated contribution to the publication is accurate (as detailed above);
- permission is granted for the candidate to include the publication in the thesis; and
- the sum of all co-author contributions is equal to 100% less the candidate's stated contribution.


Name of Co-Author	Coghlan, C.J.
Contribution to the Paper	Design and development of the Fe metalation component of the project, including the preparation of samples and analysis of data. Assisted with the preparation and drafting of the manuscript.
Signature	Date 26/2/19

Name of Co-Author	Burgun, A.
Contribution to the Paper	Assisted with the conception of the project and drafting of the manuscript.
Signature	Date

Name of Co-Author	Tarzia, A.		
Contribution to the Paper	Performed computational work and assisted with the preparation of the manuscript.		
Signature		Date	26/2/19

Name of Co-Author	Sumida, K.		
Contribution to the Paper	Assisted with the data interpretation and preparation, drafting and final revision of the manuscript.		
Signature		Date	25/2/19

Name of Co-Author	Sumbly, C.J.		
Contribution to the Paper	Assisted with the conception of the project, analysis of data and preparation of the manuscript.		
Signature		Date	4/2/19

Name of Co-Author	Doonan, C.J.		
Contribution to the Paper	Assisted with the conception of the project, analysis of data and preparation of the manuscript.		
Signature		Date	1/03/2019

3.1 Abstract

The precise tuning of the structural and chemical features of microporous metal-organic frameworks (MOFs) is a crucial endeavour for developing materials with properties that are suitable for specific applications. In recent times, techniques for preparing frameworks consisting of mixed-metal or ligand compositions have emerged. However, controlled spatial organisation of the components within these structures at the molecular scale is a difficult challenge, particularly when species possessing similar geometries or chemical properties are used. Here, we describe the synthesis of mixed-metal and ligand variants possessing the Mn_3L_3 (Mn-MOF-1; $H_2L = \text{bis}(4-(4'\text{-carboxyphenyl})-3,5\text{-dimethylpyrazolyl})\text{methane}$) structure type. In the case of mixed-ligand synthesis using a mixture of L and its trifluoromethyl-functionalised derivative ($H_2L' = \text{bis}(4-(4'\text{-carboxyphenyl})-3,5\text{-di(trifluoromethyl)pyrazolyl})\text{methane}$), a mixed-ligand product in which the L' species predominantly occupies the pillar sites lining the pores is obtained. Meanwhile, post-synthetic metal exchange of the parent Mn_3L_3 compound using Fe^{2+} or Fe^{3+} ions results in a degree of cation exchange at the trinuclear carboxylate-based clusters and metalation at the pillar bispyrazolate sites. The results demonstrate the versatility of the Mn_3L_3 structure type toward both metal and ligand substitutions, and the potential utility of site-specific functionalisations in achieving even greater precision in the tuning of MOFs.

3.2 Introduction

Metal-organic frameworks (MOFs)¹ are an emerging class of porous materials that have received intensive investigation in recent years due to their high surface areas, and structural and chemical tunability. These features are attractive for a wide range of applications, including gas storage, molecular separations, heterogeneous catalysis, and their integration within functional devices.² While the large library of MOFs now available to researchers encompass a broad range of properties, there is an increasing need for the development of techniques that facilitate molecular-level manipulations of their framework compositions to engender an even greater degree of control over the properties of the materials.

In the area of mixed-metal and mixed-ligand MOFs, a number of preparative strategies have emerged that afford functionalised variants of existing structure types, and considerable effort has also been

directed toward the discovery of unique structure types that depend on the mixed compositions for their assembly. These synthetic methods can generally be classified into direct synthetic methods that employ mixed-component reaction solutions,³ and post-synthetic modification that induce exchange or insertion at the metal nodes^{4,5} (single ions or clusters) or organic linkers constituting the framework.⁶ These strategies generally lead to statistical mixtures (i.e. solid solutions) of the components throughout the crystals, and in this context, examples of structure types that allow site-specific manipulations have remained rare. Furthermore, expansion of the synthetic scope of such mixed-metal and ligand systems is expected to provide greater insight related to the influence of such modifications on the framework properties.

With this in mind, we selected the microporous Mn_3L_3 (Mn-MOF-1; H_2L = bis(4-(4'-carboxyphenyl)-3,5-dimethylpyrazolyl)methane) compound for investigation as a potentially versatile platform for systematic metal and ligand substitutions.⁷ This material features free bispyrazolate coordination sites that are available for post-synthetic metal insertions, providing the opportunity for the composition of the metal component to be tuned at both the metal node and at the bispyrazolate sites. Moreover, the incorporation of linkers with additional functionalisation at the periphery of the bispyrazolate moieties is also of interest for tuning the metal binding affinity, as well as the dynamic properties of the framework. Herein, we describe the synthesis and characterisation of a series of frameworks in which a trifluoromethyl-functionalised derivative of L (H_2L' = bis(4-(4'-carboxyphenyl)-3,5-di(trifluoromethyl)pyrazolyl)methane) is introduced into the framework. Interestingly, the L' linker is demonstrated to principally occupy just one of the two unique linker positions within the framework, despite the use of a one-pot, mixed-ligand synthetic procedure. Further, the outcomes of post-synthetic metal exchange reactions on the parent Mn_3L_3 compound with Fe^{2+} and Fe^{3+} cations are probed, which are demonstrated to afford mixed-metal compositions while preserving the original framework connectivity. The results serve to demonstrate the versatility of the Mn_3L_3 structure type toward both metal and ligand substitutions, and the potential utility of site-specific functionalisation in preparing MOFs with precisely tuned properties.

3.3 Experimental Section

Unless otherwise stated, all preparations of the organic compounds were performed under an Ar atmosphere using standard Schlenk techniques with dried and degassed solvents. All MOF synthesis

reactions were carried out in the air. All reagents except 4-bromo-bis(3,5-trifluoromethyl)pyrazole⁸ were obtained from commercial vendors and used without further purification. Powder X-ray diffraction data were collected on a Bruker Advance D8 diffractometer equipped with a capillary stage using Cu K α radiation ($\lambda = 1.5418 \text{ \AA}$). NMR spectra were recorded on a Varian 500 MHz spectrometer operating at 23 °C and equipped with a 5 mm probe. Thermogravimetric analysis was performed on a Perkin-Elmer STA-6000 instrument using a nitrogen flow. Adsorption isotherms were collected on a Micromeritics ASAP 2020 instrument using liquid nitrogen (77 K), dry ice/acetone (195 K) and water (298 K) baths for the N₂, CO₂, and H₂O isotherms, respectively.

3.3.1 Synthetic Procedures

Bis(4-bromo-3,5-di(trifluoromethyl)pyrazolyl)methane (1). A previously reported method for the synthesis of bis(3,5-di(trifluoromethyl)pyrazolyl)methane was adapted.⁹ A solution of 4-bromo-3,5-trifluoromethylpyrazole (1.5 g, 5.3 mmol) in anhydrous DMF (3.2 mL) was added dropwise to a vigorously stirred mixture of NaH (0.18 g of a 60% paraffin oil dispersion) in anhydrous DMF (1.6 mL). Diiodomethane (0.32 mL, 3.9 mmol) was then added, and the mixture was heated at 80 °C for 2 days. The mixture was cooled to room temperature, poured into diethyl ether (50 mL), and the organic layer was washed with aqueous K₂CO₃ solution (3 \times 20 mL), brine (1 \times 20 mL), dried over MgSO₄. The solvent was evaporated under a reduced pressure, and the resulting brown oil was cooled in a salted ice-bath to yield crude **1** as a brown solid (1.7 g). This was kept under vacuum for 2 days to remove a diiodomethane impurity to afford the pure product as an off-white solid (1.2 g, 75%). ¹H NMR (CDCl₃): δ (ppm) 6.60 (s, CH₂); ¹⁹F NMR (CDCl₃): δ (ppm) -57.72 (s, CF₃), δ (ppm) -63.18 (s, CF₃).

Bis(4-(4'-ethoxyphenyl)-3,5-di(trifluoromethyl)-pyrazolyl) methane (2). To a mixture of **1** (540 mg, 0.9 mmol), 4-phenylboronic acid ethyl ester (800 mg, 4.1 mmol) and K₂CO₃ (2.48g, 17.9 mmol) in dioxane (30 mL) was added Pd(PPh₃)₄ (170 mg, 0.15 mmol). After degassing the mixture for 20 min, the mixture was heated at 90 °C for 5 days. After cooling to room temperature, the solvent was evaporated to yield a dark brown solid which was dissolved in chloroform. The solution was filtered, and removal of the solvent resulted in crude **2** as a dark brown solid. The pure product was obtained following purification *via* column chromatography (silica gel, dichloromethane) as a white solid (280 mg, 44%). ¹H NMR (CDCl₃):

δ (ppm) 1.43 (t, CH₃, J=7.2 Hz), 4.43 (q, CH₂, J= 7.1 Hz), 6.74 (s, CH₂), 7.42 (d, 2H, Ar-H, J= 8.3Hz), 8.13 (d, 2H, Ar-H, J= 8.6 Hz); ¹⁹F NMR (CDCl₃): δ (ppm) -55.85 (s, CF₃), -60.46 (s, CF₃).

Bis(4-(4'-carboxyphenyl)-3,5-di(trifluoromethyl)pyrazolyl)methane (H₂L'). **2** (180 mg, 0.25 mmol) and aqueous KOH (1.8 mL, 2 M) were combined in methanol (7.2 mL), and the resulting mixture was heated at reflux for 20 h. After cooling to room temperature, the solution was filtered and acidified to pH 1 with concentrated HCl. The resulting precipitate was collected under filtration and washed with water to yield H₂L' as a white solid (160 mg, 96 %). IR ν_{max} (neat, cm⁻¹): 2996 (w, O-H), 2892 (w, O-H), 2674 (w, O-H), 2547 (w, O-H), 1698 (C=O); 1421 (C=C); 1284 (s), 1238 (C-F), 1181 (C-F), 1169 (C-F), 1127 (C-F); ¹H NMR ((CD₃)₂SO): δ (ppm) 7.04 (s, CH₂), 7.49ppm (d, Ar-H, J= 8.1 Hz), 8.04 (d, Ar-H, J= 8.3 Hz), 13.21 (br, OH); ¹⁹F NMR ((CD₃)₂SO): δ (ppm) -59.28 (s, CF₃), -55.46 (s, CF₃); ¹³C NMR ((CD₃)₂SO): δ (ppm) 167.17, 132.13, 131.59, 130.40, 129.73, 127.59, 123.56, 109.7, 66.16, 65.60.

Mixed-ligand frameworks. In a typical synthesis, the ligands L and L' (total quantity: 0.025 mmol) and MnCl₂·4H₂O (8.1mg, 0.040 mmol) were combined in a glass vial. DMF (2.0 mL) and H₂O (1.0 mL) were then added, and the resulting mixture was sonicated for 15 min. The vial was sealed and heated under static conditions at 100 °C in a pre-heated oven for 5 days to yield colorless, block shaped crystals. The solid was isolated and washed with DMF (3 × 20 mL) and methanol (3 × 20 mL), and activation for adsorption experiments was performed by heating at 100 °C *in vacuo* for a period of 24 h. The composition of the solid was deduced by digesting the solid in DCl in (CD₃)₂SO, followed by ¹H and ¹⁹F NMR spectroscopy.

Mixed-metal frameworks. In a typical procedure (described for Fe(acac)₃ as the iron source, acac⁻ = acetylacetonate), the as-synthesised material, Mn₃L₃ (24.0 mg), was firstly solvent-exchanged with dry acetonitrile. The solvent was decanted and replenished five times, each time allowing the crystals to soak for 10 min between each cycle. Then, Fe(acac)₃ (30.0 mg) was added to the vial and the resulting mixture was placed in an oven pre-set at 65 °C for 1, 5 or 10 days. The orange suspension was then allowed to cool to room temperature, and the solvent was exchanged with freshly dried acetonitrile (× 5). The solvent was decanted and the crystals were dried under a dynamic vacuum to afford the Fe-exchanged material. The same exchange procedure was performed for FeCl₂·4H₂O and FeCl₃, using ethanol and acetonitrile as the exchange solvents, respectively. X-ray diffraction data for these compounds were collected at 100(2) K on the MX-1 beamline of the Australian Synchrotron (λ = 0.71073 Å). CCDC accession codes 1443923 and 1443924 contain the structural data associated with the samples

exchanged with FeCl_3 and $\text{FeCl}_2 \cdot 4\text{H}_2\text{O}$, respectively. Further details associated with the data collection and structural refinement are provided in the supporting information (see also Table S7.2.1).

Inductively-coupled plasma mass spectrometry (ICP-MS). Each sample was synthesized separately three times and the bulk dissolved in a 2% HNO_3 sample at 65 °C overnight. The samples were then filtered through a 45 μm filter to remove any ligand and particulate matter. Each sample was then diluted to within the measurement range. The samples were then analysed on an Agilent 7500cs solution ICP-MS instrument to evaluate the molar Fe-to-Mn ratio, and the average of the three samples were tabulated (see below).

3.4 Results and Discussion

Prior to discussing the preparation and characterisation of the new materials, we first briefly review the structural details of the parent Mn_3L_3 structure type⁷ that are relevant to the manipulations in the mixed-component systems.

3.4.1 Mn_3L_3 structure type

The structure of Mn_3L_3 is presented in Figure 3.1A. This material consists of linear Mn_3^{6+} clusters (see Figure 3.1B), wherein adjacent Mn^{2+} centres are bridged by a total of three carboxylate groups of three different ligand molecules: two that are bound in a bridging mode through both oxygen atoms, and one bridging through just one of the oxygen atoms. The central Mn^{2+} centre is in an octahedral ligand environment bound solely by the carboxylate groups, while the terminal centres are bound by four carboxylate oxygen atoms and are further capped by a chelating bispyrazolate moiety to complete the distorted octahedral coordination environment. Two-thirds of the linker molecules in the structure bridge adjacent Mn_3^{6+} clusters in the crystallographic *ac*-plane to form a square grid. The remaining one-third of ligand molecules axially pillar the individual grids to form a microporous three-dimensional network (space group: *C2/c*) with a moderate BET surface area of 700 m^2/g . Note that in the activated form of the Mn_3L_3 framework, the bispyrazolate groups in the pillar ligands are free of coordinated metal

ions, and this has previously been the focus of post-synthetic insertion reactions using a range of metal ions, including Co^{2+} and Rh^+ .⁷

3.4.2 *Mixed-ligand frameworks*

The synthesis of mixed-ligand frameworks was carried out by systematically tuning the composition of the reaction mixture, while holding constant all other reaction conditions employed in the synthesis of the Mn_3L_3 compound. Specifically, the mole ratio of the trifluoromethyl-substituted linker L' was varied with respect to the parent ligand L (see Figure. 3.1C) between 0.00 (all L) to 1.00 (all L'). Crystalline materials were obtained for all reactions, and the powder X-ray diffraction patterns collected for selected samples are shown in Figure. 3.2. The data revealed that the parent Mn_3L_3 structure type was preserved up to a mole ratio of 0.46. Within this range, a gradual shift in the peaks to lower 2θ angles was observed for an increasing content of L' , potentially reflecting a slight expansion in the unit cell parameters due to the bulkier trifluoromethyl substituents present within the L' linker. Interestingly, at 0.50 and higher L' compositions, a new crystalline phase was obtained in high purity up to an L' content of 1.00. Further, observation of the crystal morphology showed that the crystals adopted a rhombus-shaped morphology for the parent Mn_3L_3 phase (Figure. S7.2.1), while at a mole ratio up to 0.46, a uniform, block-shaped morphology was observed (Figure. S7.2.2). At higher proportions of L' , very thin plates not suitable for single-crystal X-ray analysis were obtained (Figure. S7.2.3). These changes in crystal morphology coincide with the L' levels in the reaction mixture that induce changes in the powder X-ray diffraction patterns, providing further evidence for changes in the composition and structure of the resulting frameworks.

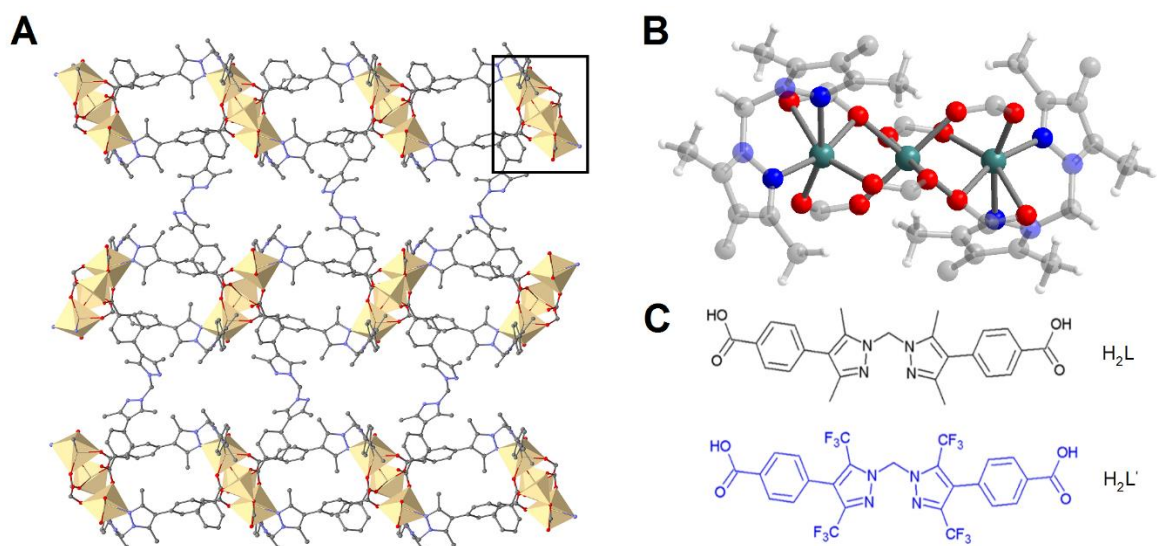


Figure 3.1. (A) A portion of the crystal structure of Mn_3L_3 ,⁷ as observed along the crystallographic c -direction. The structure features square grids in the bc -plane that are bound by axial pillar linkers having bispyrazolate moieties available for metal binding; (B) A view of the trinuclear Mn_3^{6+} cluster enclosed by the black box; and (C) molecular structures of the bis(4-(4'-carboxyphenyl)-3,5-dimethylpyrazolyl)methane (H_2L) and bis(4-(4'-carboxyphenyl)-3,5-di(trifluoromethyl)methane) (H_2L') employed in this work. Teal, grey, blue, red, and white spheres represent Mn, C, N, O, and H atoms, respectively. H atoms are omitted from panel (A) for clarity.

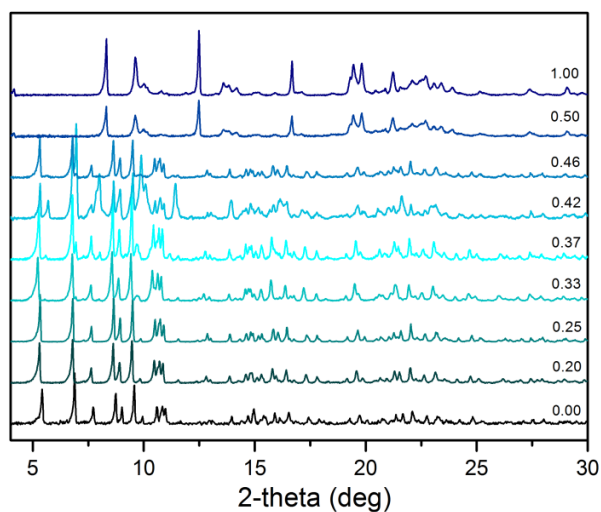


Figure 3.2. Powder X-ray diffraction patterns collected for materials synthesised with varying ratios of the ligands L and L' . The fraction associated with each plot represents the mole ratio of L' in the mixture, which is varied from 0.00 (resulting in pure Mn_3L_3) to 1.00.

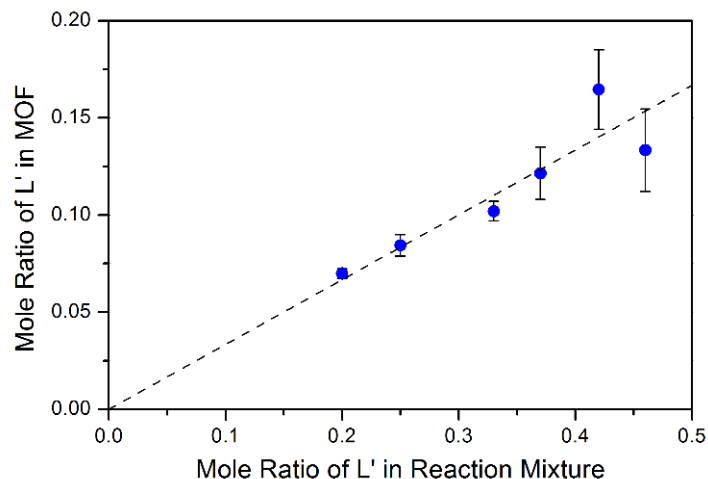


Figure 3.3. A plot of the proportion of the trifluoromethyl-substituted linker (L') within the MOF as calculated from the NMR data as a function of the quantity of L' in the reaction mixture. The dotted line represents the line of best fit to the data, while the error bars represent one standard deviation.

The degree of incorporation of L' into the materials was examined via a combination of ^1H - and ^{19}F -NMR experiments¹⁰ for samples that displayed powder X-ray diffraction data matching that of the parent Mn_3L_3 structure type. Since the methylene bridge of L and L' display distinct ^1H -NMR chemical shifts (δ 6.28 and 7.04 ppm, respectively), the content of L' in the MOF sample could be estimated via integration of the respective methylene signals. Interestingly, analysis of the peak integrals revealed a near-linear relationship between the mole ratio of L' in the framework and the mole ratio within the reaction mixture (see Figure 3.3). A maximum ratio of ca. 0.17 was observed for a reaction mixture containing a mole ratio of 0.42 in L'. Note that the samples obtained using reaction mixtures containing higher levels of L' (i.e. 0.5 and higher) did not exhibit any content of the L linker, indicating the formation of a new phase consisting of only L' linkers.¹¹

Following elucidation of the composition of the samples, the impact of the mixed composition on the metal uptake (i.e. metal insertion at the pillar bispyrazolate binding site) was investigated. Here, each sample was immersed in a methanol solution containing an excess of $\text{CoCl}_2 \cdot 4\text{H}_2\text{O}$, and heated at 65 °C for a period of 16 h. After this time, the products were subjected to energy dispersive X-ray (EDX) and inductively-coupled plasma mass spectrometry (ICP-MS) experiments. Interestingly, the Co^{2+} content linearly decreased with an increasing composition of the L' linker (black dotted line in Figure 3.4). Previous crystallographic investigation of the parent Mn_3L_3 compound metalated with Co^{2+} cations revealed full occupancy of the bispyrazolate binding sites under the same reaction conditions.⁷

Therefore, we surmised that the decrease in Co^{2+} uptake is a result of the L' linker being unable to accommodate metal species at its bispyrazolate moiety under these conditions. Further, the slope of the linear fit in Figure. 3.5 was a close match with the maximum decrease in Co^{2+} metalation that would be observed for a case where all of the L' occupied the pillar site (blue dotted line in Figure. 3.4), suggesting that site-specific substitutions were obtained with the L linkers chiefly occupying the square grid positions in the framework.

In order to elucidate the origin of this observation, we firstly investigated the binding environment around the Mn_3^{6+} cluster of the metal node in more detail. The similarity in powder X-ray diffraction patterns between the parent Mn_3L_3 material and the mixed-ligand frameworks suggested that the ligand environments about the Mn^{2+} ions were structurally similar. Modeling of the substitution of the position of the methyl groups on the 3 and 5 positions of the pyrazolate rings with trifluoromethyl groups (Figure. S7.2.4) resulted in larger van der Waals radii of the substituent groups, which were incompatible with the packing of the ligand groups around the cluster. This further supports the L' linker being directed to the pillar sites of the structure, where only their carboxylate groups (which are unaffected by functionalisations on the pyrazolate rings), participate in binding to the metal clusters.

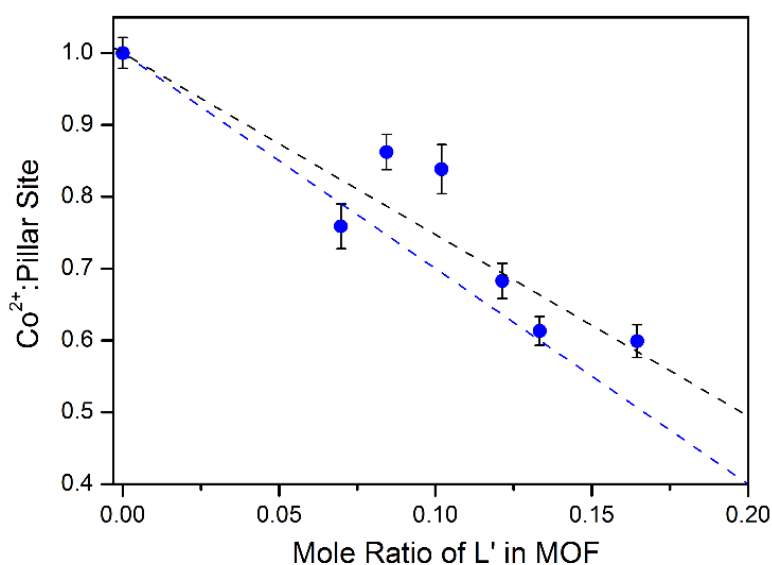


Figure. 3.4. A plot of Co^{2+} uptake per pillar site in the MOF from ICP-MS data as a function of the quantity of trifluoromethyl-substituted linker (L') within the MOF. The black dotted line represents the line of best fit to the data, while the error bars represent one standard deviation. The blue dotted line represents the expected overall population of Co^{2+} ions per pillar site assuming all of the L' linker within the MOF occupies the pillar site, and does not participate in Co^{2+} binding.

Further, DFT calculations were carried out on a truncated portion of the linker in order to probe the absence of Co^{2+} metalation at the bispyrazolate site of the L' linkers when in the pillar position. Firstly, we note that in the Mn_3L_3 compound, the metalation results in a structural change at the pillar linkers necessitating a rotation about the methylene hinge within the L linker (see Figure. S7.2.5, upper panel). We suspected that this rotation was greatly hindered in the L' linker due to the greater steric bulk of the trifluoromethyl groups.¹² Computation of the molecular energy as a function of the dihedral angle between the two pyrazolate rings showed a considerably larger barrier to rotation in L' compared to L (see Figure. S7.2.5, lower panel), which is expected to inhibit access to the conformation necessary to bind metal ions. In addition to this steric factor, the binding of Co^{2+} is also likely to be significantly weaker within L' due to the decreased donor strength of the bispyrazolate groups due to the electron-withdrawing nature of the trifluoromethyl substituents. Thus, from these modelling data, it can be deduced that the L' component favourably occupies the pillar position in the crystal structure, and the trifluoromethyl-substituted bispyrazolate groups are unable to act as binding sites for metal ions, resulting in a lower Co^{2+} uptake as the concentration of L' within the structure is increased.

After elucidation of the composition and structure of the mixed-ligand systems, the material containing the maximum quantity of L' linkers (reaction L' content: 0.42; composition: $\text{Mn}_3\text{L}_{2.49}\text{L}'_{0.51}$) was subjected to gas sorption experiments. The N_2 adsorption isotherm collected at 77 K presented in Figure. S7.2.6 represents a type-I isotherm reflecting the microporous nature of the structure, while the slightly decreased total adsorption capacity reflects the increased steric bulk and mass of the trifluoromethyl groups compared to the methyl groups in the parent compound. Furthermore, as shown in Figure. S7.2.7, the material exhibits a stepped CO_2 adsorption isotherm at 195 K, which is consistent with the dynamic nature of the parent Mn_3L_3 framework. However, the position of the step is located at significantly higher pressures once the L' linker is introduced, presumably due to its larger barrier to rotation about the methylene hinges as described above. Similar observations are observed for the adsorption isotherm for H_2O (293 K; Figure. S7.2.8).

Table 3.1. Metal composition as obtained by ICP-MS for Mn₃L₃ samples after treatment with Fe-containing solutions

Metal source	T (°C)	t (days)	Mn	Fe	±*
FeCl ₂ ·4H ₂ O	25	1	77.5	22.5	3.1
		5	63.6	36.4	0.3
	60	1	71.6	28.4	1.3
		5	71.5	28.5	3.2
FeCl ₃	25	1	75.2	24.8	1.5
		5	77.5	22.5	0.9
	60	1	42.4	57.6	13.0
		5	1.4	98.6	0.6
Fe(acac) ₃	25	1	98.9	1.1	0.4
		5	96.2	3.8	2.9
	60	1	97.1	2.9	1.5
		5	94.9	5.1	0.9

*indicates standard deviation

3.4.3 Mixed-metal frameworks

The ability of the Mn₃L₃ compound to accommodate functionalised linkers prompted the investigation of post-synthetic metal exchange and metalation reactions. Owing to its redox activity and its potential for use in catalytic reactions, several Fe²⁺- and Fe³⁺-containing metal sources, namely FeCl₂·4H₂O, Fe(acac)₃, and FeCl₃ were selected for testing. Here, samples of Mn₃L₃ were suspended in a concentrated solution of the metal salt in an organic solvent at room temperature or under mild heating (60 °C), and the composition of the material was analyzed by ICP-MS after 1 and 5 days (see Table 3.1). As can be clearly observed by the data, the metal source, soaking time, and reaction temperature each significantly influenced the composition of the resulting product.

Metal source. Here, minimal exchange was observed with Fe(acac)₃ compared to the chloride salts, potentially due to the relative stability of the complex in solution, and the bulky nature of the ligands

inhibiting the complex from freely diffusing within the pores. The highest exchange is observed with FeCl_3 , which is expected to diffuse more rapidly due to its smaller molecular size and relatively strong binding of Fe^{3+} within the binding environments found in the metal clusters and at the chelating bispyrazolate moieties.

Reaction time. Higher iron loadings were observed at longer reaction times, particularly for those maintained at room temperature. This can be ascribed to the diffusion of the iron source and the rate of exchange and metalation requiring a longer time to reach an equilibrium at lower temperatures.

Soaking temperature. In addition to the rate of loading, the extent of exchange and metalation was higher at higher temperatures. Interestingly, heating of the FeCl_3 reaction mixture at 60 °C over 5 days resulted in near complete exchange of the metal cations.

3.4.4 Single crystal X-ray structure determinations

Following the characterisation of the chemical composition of each of the iron-exchanged samples, single-crystals of the material following a 5-day exchange reaction at 60°C using $\text{FeCl}_2 \cdot 4\text{H}_2\text{O}$ (iron content: $28.5 \pm 3.2\%$) and FeCl_3 (iron content: $98.6 \pm 0.6\%$) were subjected to X-ray diffraction experiments (see Supporting Information and Table S7.2.1 for further experimental details). These crystalline samples are homogenous in appearance and the crystals were light and dark orange in colour (see Figure. S7.2.9-10), consistent with moderate and high levels of Fe incorporation, respectively. The crystallographic analysis is complicated by competing processes occurring during these metalations, the exchange of metals at the nodes of the MOF, metalation of the well-established metal binding site and possibly a minor contribution from residual metal salts in the pores. Despite this, these structures confirmed the original framework connectivity and provide some further insight into the process of metalation, specifically excluding significant pore loading of Fe^{3+} for $\text{Fe}_3\text{L}_3 \cdot \text{FeCl}_3$.

Structure of $\text{Fe}_3\text{L}_3 \cdot \text{FeCl}_3$. Here, the iron content was established as $98.6 \pm 0.6\%$ indicating that, within the crystals, Fe not only occupies the free coordinating site of Mn_3L_3 but also substitutes for the Mn^{2+} centres of the node. Analysis of the diffraction data was consistent with quantitative exchange of the metals at the metal nodes, as well as a full occupancy at the bispyrazolate binding sites. Importantly, no evidence for significant pore-bound Fe species was observed in the single crystal structure.¹³ The lack of Mn in the

samples led us to model the data with a trinuclear Fe₃ node in the MOF. A detailed examination of the metal-ligand bond distances within the trinuclear clusters revealed only minor differences with those of the parent Mn₃L₃ compound, providing support for the presence of Fe²⁺ as opposed to the reactant Fe³⁺ within the clusters. While the precise mechanism for the reduction of Fe³⁺ to Fe²⁺ upon metal exchange has not yet been established, trinuclear Mn-based clusters have been known to participate in redox chemistry, potentially acting as a sufficiently strong reductant under these conditions to reduce Fe³⁺ ions with a concomitant liberation of a Mn³⁺ ion.¹⁴ Based upon the inductively-coupled plasma mass spectrometry (ICP-MS) data, a very small residual amount of Mn is still present in these crystals but, given the low levels, we did not include this in the model for structure refinement.

While this structure importantly confirms there is no significant electron density in the pores of the MOF, we also examined the ligand-based metalation site within the material. On the basis of the ICP-MS and structural data, metalation at the bispyrazolate site proceeds in high yield but the form of the metalated product is unclear. In our previous work,^{7,13} the identity of the post-synthetic metalation product could be readily discerned from difference electron density maps. To shed light on the structure of the product here, we examined the F_{obs} electron density maps which indicate appreciable disorder of the added metal complex. The metal site is ill-defined, consistent with there being a second complex with a different geometry and/or oxidation state disordered over the site. Specifically, the site has two significant regions of electron density above and below the plane formed by the pyrazole nitrogen atoms and the Fe centre (see Figure. S7.2.11). We have modelled the data as an octahedral Fe³⁺ cation (due to slightly shorter Fe-N bonds of 2.084(8) Å) possessing two inner-sphere chloride ions and a third outer-sphere anion within the pores of the framework (see panel d of Figure. S7.2.11), but the disorder present limits ultimate identification and model refinement. Interestingly, this arrangement of the chloride ions is similar to that observed within iron salts such as FeCl₃·6H₂O, which contains two apical chlorides and four equatorial water molecules, and an outer-sphere chloride ion for charge balance.

Structure of Mn_{3-x}Fe_xL₃·0.4FeCl₂ (x = 0.55). In the case of the FeCl₂-exchanged sample, partial occupancy of ca 0.2 (40% metalation due to the mirror plane) is observed at the bispyrazolate moiety, which was established by trial refinement. This observation coupled with the 28.5 ± 3.2% Fe occupancy in the MOF as determined by ICP-MS leads us to suggest that ca 0.5-0.6 equivalents of Fe occupy the trinuclear node of the MOF. While there is potential for a minor amount of Fe loading into the pores to remain after the washing cycles, the lack of significant electron density in the pores further supports this rationalisation

and the assigned formula $\text{Mn}_{3-x}\text{Fe}_x\text{L}_3$ ($x = 0.55$). Given the similarities between Fe^{2+} and Mn^{2+} cations, the bond lengths and angles around the metal node are relatively unchanged.

The low occupancy Fe centre bound to the bispyrazolate coordinating site is surprisingly well-ordered, and the octahedral coordination environment ($\text{FeN}_2\text{O}_3\text{Cl}$) supports retention of the Fe^{2+} oxidation state based on the longer Fe-N distance of 2.218(9) Å. Given the relatively low occupancy nature of this site and a limited amount of evidence for the anion species in the pores, we have confined the discussion to this observation. The pores of the MOF contain a peak, assigned as a chloride (0.2 occupancy, 40%), to provide charge balance to the octahedral Fe centre that sits in the pocket typically occupied by anions within the MOF structure.^{7,13} There is additional electron density in this site (largest peak = 2.958 e·Å³, unmodeled before application of the SQUEEZE routine of Platon¹⁵), which is potentially ascribable to a partial occupancy of solvent molecules occupying this position in the absence of an anion. Note that the ability of these bispyrazolate moieties to accommodate both Fe^{2+} and Fe^{3+} ions is of interest in catalytic processes involving redox transformations, and studies directed toward understanding the reactivity of these sites is currently underway.

3.5 Summary and Outlook

The foregoing work has described experiments for preparing frameworks of the Mn_3L_3 structure type with compositions having a mixture of organic linkers or metal cations. As discussed, in the case of the use of the trifluoromethyl-substituted L' linker, the substitutions occur solely at the pillar linker site, and metalation does not occur at the bispyrazolate moiety owing to the hindered rotation about its methylene bridge, as well as the weaker binding stemming from the electron-withdrawing nature of the substituents. Although such a dilution of available metalation sites will limit the ability to structurally characterize the coordination sphere of the added metal centres, it may actually offer significant benefit in cases where factors such as catalyst loading, diffusion rates and heat dissipation require tuning in order to maximise the performance of the support. In the case of metal exchange and insertion, the metal source is demonstrated to have the most significant influence on the magnitude and rate of the conversion. Activating these metalated species to afford exposed metal cations, and understanding the reactivity of these metal sites will be a central focus of future studies with an object of developing enhanced MOF-based catalysts.

3.6 Acknowledgements

This research is supported by the Science and Industry Endowment Fund (SIEF). CJD and CJS acknowledge the Australian Research Council (ARC) Future Fellowship scheme for funding under award numbers FT100100400 and FT0991910, respectively. KS acknowledges the ARC for funding DE160100306. We thank the MX-1 beamline at the Australian Synchrotron for instrument time and technical support. We also acknowledge the NCI National Facility (Canberra, Australia) supported by the Australian Commonwealth Government for computational time used for the DFT studies. We thank Lynton for helpful discussions.

3.7 Notes and references

- 1 (a) O. M. Yaghi, M. O'Keeffe, N. W. Ockwing, H. K. Chae, M. Eddaoudi and J. Kim, *Nature*, 2003, **423**, 705; (b) S. Kitagawa, R. Kitaura and S. Noro, *Angew. Chem., Int. Ed.*, 2004, **43**, 2334; (c) G. Férey, *Chem. Soc. Rev.*, 2008, **37**, 191.
- 2 For recent reviews covering the emerging applications of metal-organic frameworks, refer to the special themed issues in *Chem. Rev.*, and more recently *Chem. Soc. Rev.*: (a) H.-C. Zhou, J. R. Long and O. M. Yaghi, *Chem. Rev.* 2012, **112**, 673; (b) H.-C. Zhou and S. Kitagawa, *Chem. Soc. Rev.* 2014, **43**, 5415, and references therein.
- 3 (a) K. Koh, A. G. Wong-Foy and A. J. Matzger, *Angew. Chem., Int. Ed.*, 2007, **47**, 677; (b) H. Deng, C. J. Doonan, H. Furukawa, R. B. Ferreira, J. Towne, C. B. Knobler, B. Wang and O. Yaghi, *Science*, 2010, **327**, 846; (c) S. Marx, W. Kleist, J. Huang, M. Maciejewski and A. Baiker, *Dalton Trans.*, 2010, **39**, 3795; (d) L. Liu, K. Konstas, M. R. Hill and S. G. Telfer, *J. Am. Chem. Soc.*, 2013, **135**, 17731; (e) C. Wang, D. Liu, Z. Xie and W. Lin, *Inorg. Chem.*, 2014, **53**, 1331; (f) A. Sue, R. Mannige, H. Deng, D. Cao, C. Wang, F. Gándara, J. F. Stoddart, S. Whitelam, and O. M. Yaghi, *Proc. Nat. Acad. Sci. U.S.A.*, 2015, **112**, 5591.
- 4 Examples of metal insertion include: (a) E. D. Bloch, D. Britt, C. J. Doonan, F. J. Uribe-Romo, H. Furukawa, J. R. Long and O. M. Yaghi, *J. Am. Chem. Soc.*, **2010**, **132**, 14382; (b) C. Wang, Z. Xie, K. deKrafft and W. Lin, *J. Am. Chem. Soc.*, 2011, **133**, 13445; (c) M. I. Gonzalez, E. D. Bloch, J. A. Mason, S. J. Teat and J. R. Long, *Inorg. Chem.*, **2015**, **54**, 2995; (d) T. Toyao, K. Miyahara, M. Fujiwaki, T.-H. Kim, S. Dohshi, Y. Horiuchi and M. Matsuoka, *J. Phys. Chem. C*, 2015, **119**, 8131.

- 5 Examples of metal ion exchange include: (a) C. K. Brozek and M. Dincă, *Chem. Sci.*, 2012, **3**, 2110; (b) M. Kim, J. F. Cahill, H. Fei, K. A. Prather and S. M. Cohen, *J. Am. Chem. Soc.*, 2012, **134**, 18082; (c) X. Song, T. K. Kim, H. Kim, D. Kim, S. Jeong, H. R. Moon and M. S. Lah, *Chem. Mater.* 2012, **24**, 3065; (d) J.-H. Liao, W.-T. Chen, C.-S. Tsai and C.-C. Wang, *CrystEngComm*, 2013, 3377; (e) C. K. Brozek and M. Dincă, *J. Am. Chem. Soc.*, 2013, **135**, 12886.
- 6 Examples of organic linker exchange include: (a) B. J. Burnett, P. M. Barron, M. Paul, C. Hu and W. Choe, *J. Am. Chem. Soc.*, 2011, **133**, 9984; (b) M. Kim, J. F. Cahill, Y. Su, K. A. Prather and S. M. Cohen, *Chem. Sci.* 2012, **3**, 126; (c) T. Li, M. T. Kozlowski, E. A. Doud, M. N. Blakely and N. L. Rosi, *J. Am. Chem. Soc.* 2013, **135**, 11688; (d) M. B. Lalonde, J. E. Mondloch, P. Deria, A. A. Sarjeant, S. S. Al-Juaid, O. I. Osman, O. K. Farha and J. T. Hupp, *Inorg. Chem.* 2015, **54**, 7142.
- 7 W. M. Bloch, A. Burgun, C. J. Coghlan, R. Lee, M. L. Coote, C. J. Doonan and C. J. Sumby, *Nat. Chem.*, 2014, **6**, 906.
- 8 A. Maspero, G. Giovenzana, D. Monticelli, S. Tagliapietra, G. Palmisano and A. Penoni, *J. Fluorine Chem.*, 2012, **139**, 53.
- 9 G. Pampaloni, R. Pelso, D. Belletti, C. Graiff and A. Tiripicchio, *Organometallics*, 2007, **26**, 4278.
- 10 (a) K. K. Tanabe, Z. Wang and S. M. Cohen, *J. Am. Chem. Soc.*, 2008, **130**, 8508; (b) R. K. Deshpande, J. L. Minnaar and S. G. Telfer, *Angew. Chem., Int. Ed.* 2010, **49**, 4598; (c) H. Deng, C. J. Doonan, H. Furukawa, R. B. Ferreira, J. Towne, C. B. Knobler, B. Wang and O. M. Yaghi, *Science*, 2010, **327**, 849.
- 11 Note that although attempts to obtain crystals suitable for single-crystal X-ray diffraction analysis were unsuccessful, the material is found to be non-porous by adsorption experiments. Thus, full characterisation was performed only on those materials exhibiting the parent Mn_3L_3 structure type.
- 12 Single-crystal X-ray diffraction experiments performed on the mixed-ligand frameworks exhibited significant disorder, precluding conclusive refinement of the trifluoromethyl groups of the L' linker.
- 13 W. M. Bloch, A. Burgun, C. J. Doonan and C. J. Sumby, *Chem. Commun.*, 2015, **51**, 5686.
- 14 F. Birkelbach, T. Weyhermüller, M. Lengen, M. Gerdan, A. X. Trautwein, K. Wieghart and P. Chaudhuri, *J. Chem. Soc., Dalton Trans.*, 1997, 4259.
- 15 (a) A.L. Spek, *Acta Crystallogr.*, 2009, **D65**, 148; (b) A.L. Spek, *Acta Crystallogr.*, 2009, **C71**, 9.

Chapter 4: Protecting-Group-Free Site-Selective Reactions in a Metal–Organic Framework Reaction Vessel

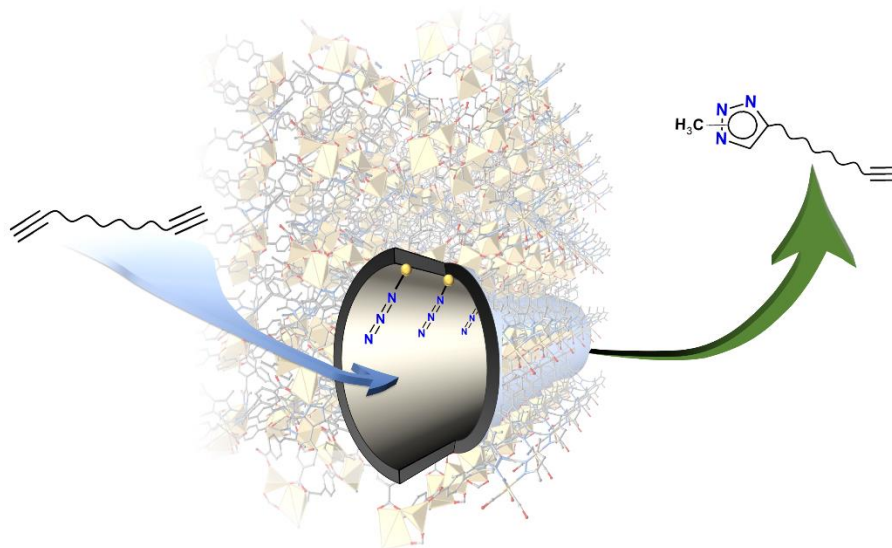
Michael. T. Huxley,^a Alexandre Burgun,^a Hanieh Ghodrati,^{a,b} Campbell J. Coghlan,^a Anthony Lemieux,^a Neil R. Champness,^c David M. Huang,^a Christian J. Doonan*^a and Christopher J. Sumbly*^a

^a Department of Chemistry and Centre for Advanced Nanomaterials, The University of Adelaide, Adelaide, South Australia 5005, Australia; E-mail: christopher.sumbly@adelaide.edu.au; E-mail: christian.doonan@adelaide.edu.au

^b Present address: School of Mechanical Engineering, University of Adelaide, Adelaide, South Australia 5005, Australia

^c Department of Chemistry, University of Nottingham, Nottingham, UK


Huxley, M., Burgun, A., Ghodrati, H., Coghlan, C.J., Lemieux, L., Champness, N.R., Huang, D.M., Doonan C.J., Sumbly, C.J., *Protecting-Group-Free Site-Selective Reactions in a Metal–Organic Framework Reaction Vessel, J. Am. Chem. Soc., 2018, 140, 6416-6425*



Statement of Authorship

Title of Paper	Protecting-Group-Free Site-Selective Reactions in a Metal–Organic Framework Reaction Vessel
Publication Status	<input checked="" type="checkbox"/> Published <input type="checkbox"/> Accepted for Publication <input type="checkbox"/> Submitted for Publication <input type="checkbox"/> Unpublished and Unsubmitted work written in manuscript style
Publication Details	Huxley, M. T.; Burgun, A.; Ghodrati, H.; Coghlan, C. J.; Lemieux, A.; Champness, N. R.; Huang, D. M.; Doonan, C. J.; Sumbly, C. J. <i>J. Am. Chem. Soc.</i> 2018 , <i>140</i> , 6416.

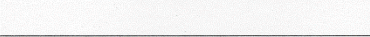
Principal Author

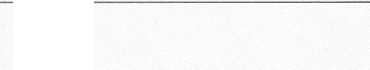
Name of Principal Author (Candidate)	Michael Huxley
Contribution to the Paper	Design and development of the project. Preparation of samples and collection of data. Analysis and interpretation of NMR and X-ray crystallography data. Preparation and drafting of the manuscript. Final revision of the manuscript.
Overall percentage (%)	70%
Certification:	This paper reports on original research I conducted during the period of my Higher Degree by Research candidature and is not subject to any obligations or contractual agreements with a third party that would constrain its inclusion in this thesis. I am the primary author of this paper.
Signature	 Date 25/2/19

Co-Author Contributions

By signing the Statement of Authorship, each author certifies that:

- the candidate's stated contribution to the publication is accurate (as detailed above);
- permission is granted for the candidate to include the publication in the thesis; and
- the sum of all co-author contributions is equal to 100% less the candidate's stated contribution.


Name of Co-Author	Burgun, A.
Contribution to the Paper	Assisted with conception of the project, analysis of the data and drafting of the manuscript.
Signature	 Date

Name of Co-Author	Ghodrati, H.
Contribution to the Paper	Performed computational work to support and explain the experimental results. Contributed to the preparation and drafting of the manuscript.
Signature	 Date 25/02/19

Statement of Authorship

Title of Paper	Protecting-Group-Free Site-Selective Reactions in a Metal–Organic Framework Reaction Vessel
Publication Status	<input checked="" type="checkbox"/> Published <input type="checkbox"/> Accepted for Publication <input type="checkbox"/> Submitted for Publication <input type="checkbox"/> Unpublished and Unsubmitted work written in manuscript style
Publication Details	Huxley, M. T.; Burgun, A.; Ghodrati, H.; Coghlan, C. J.; Lemieux, A.; Champness, N. R.; Huang, D. M.; Doonan, C. J.; Sumbly, C. J. <i>J. Am. Chem. Soc.</i> 2018 , <i>140</i> , 6416.


Principal Author


Name of Principal Author (Candidate)	Michael Huxley
Contribution to the Paper	Design and development of the project. Preparation of samples and collection of data. Analysis and interpretation of NMR and X-ray crystallography data. Preparation and drafting of the manuscript. Final revision of the manuscript.
Overall percentage (%)	70%
Certification:	This paper reports on original research I conducted during the period of my Higher Degree by Research candidature and is not subject to any obligations or contractual agreements with a third party that would constrain its inclusion in this thesis. I am the primary author of this paper.
Signature	 Date 25/2/19

Co-Author Contributions

By signing the Statement of Authorship, each author certifies that:

- the candidate's stated contribution to the publication is accurate (as detailed above);
- permission is granted for the candidate to include the publication in the thesis; and
- the sum of all co-author contributions is equal to 100% less the candidate's stated contribution.

Name of Co-Author	Burgun, A.
Contribution to the Paper	Assisted with conception of the project, analysis of the data and drafting of the manuscript.
Signature	 Date 26/02/2019

Name of Co-Author	Ghodrati, H.
Contribution to the Paper	Performed computational work to support and explain the experimental results. Contributed to the preparation and drafting of the manuscript.
Signature	 Date

Name of Co-Author	Coghlan, C.J.		
Contribution to the Paper	Assisted collection of preliminary data.		
Signature	[Redacted]	Date	26/2/19

Name of Co-Author	Lemieux, A.		
Contribution to the Paper	Assisted with preparation of samples and preparation of manuscript.		
Signature	[Redacted]	Date	

Name of Co-Author	Champness, N.R.		
Contribution to the Paper	Assisted with conception of the project and drafting of the manuscript.		
Signature	[Redacted]	Date	

Name of Co-Author	Huang, D.		
Contribution to the Paper	Assisted with conception of the project and drafting of the manuscript.		
Signature	[Redacted]	Date	1/3/2019

Name of Co-Author	Doonan, C.J.		
Contribution to the Paper	Assisted with experiment design, drafting of manuscript and analysis of data.		
Signature	[Redacted]	Date	1/3/2019

Name of Co-Author	Summy, C.J.		
Contribution to the Paper	Assisted with experiment design, drafting of manuscript and analysis of data.		
Signature	[Redacted]	Date	4/3/19

Name of Co-Author	Coghlan, C.J.		
Contribution to the Paper	Assisted collection of preliminary data.		
Signature		Date	

Name of Co-Author	Lemieux, A.		
Contribution to the Paper	Assisted with preparation of samples and preparation of manuscript.		
Signature		Date	2/7/19

Name of Co-Author	Champness, N.R.		
Contribution to the Paper	Assisted with conception of the project and drafting of the manuscript.		
Signature		Date	28.2.19

Name of Co-Author	Huang, D.		
Contribution to the Paper	Assisted with conception of the project and drafting of the manuscript.		
Signature		Date	

Name of Co-Author	Doonan, C.J.		
Contribution to the Paper	Assisted with experiment design, drafting of manuscript and analysis of data.		
Signature		Date	

Name of Co-Author	Sumbly, C.J.		
Contribution to the Paper	Assisted with experiment design, drafting of manuscript and analysis of data.		
Signature		Date	

4.1 Abstract

Site-selective organic transformations are commonly required in the synthesis of complex molecules. By employing a bespoke metal-organic framework (MOF, **1**·[Mn(CO)₃N₃]), in which coordinated azide anions are precisely positioned within 1D channels, we present a strategy for the site-selective transformation of dialkynes into alkyne-functionalized triazoles. As an illustration of this approach, 1,7-octadiyne-3,6-dione stoichiometrically furnishes the mono-“click” product *N*-methyl-4-hex-5'-ynyl-1',4'-dione-1,2,3-triazole with only trace bis-triazole side-product. Stepwise insights into conversions of the MOF reaction vessel were obtained by X-ray crystallography, demonstrating that the reactive sites are “isolated” from one another. Single-crystal to single-crystal transformations of the Mn(I)-metalated material **1**·[Mn(CO)₃(H₂O)]Br to the corresponding azide species **1**·[Mn(CO)₃N₃] with sodium azide, followed by a series of [3+2] azide-alkyne cycloaddition reactions, are reported. The final liberation of the “click” products from the porous material is achieved by N-alkylation with MeBr, regenerating starting MOF **1**·[Mn(CO)₃(H₂O)]Br, and the organic products characterized by NMR spectroscopy and mass spectrometry. Once the dialkyne length exceeds the azide separation, site selectivity is lost, confirming the critical importance of isolated azide moieties for this strategy. We postulate that carefully designed MOFs can act as physical protecting groups to facilitate other site-selective and chemoselective transformations.

4.2 Introduction

Metal-organic frameworks (MOFs) are a class of porous materials that are synthesized via a ‘building-block’ approach from organic links and metal-based nodes.¹⁻² In recent years, they have been intensely studied for their potential application to catalysis,¹⁻⁸ gas storage/separation,⁹⁻¹² biotechnology¹³⁻¹⁴ and microelectronics.¹⁵⁻¹⁶ A key feature of MOFs is that they can be grown as single crystals, which allows their structures to be elucidated via single-crystal X-ray diffraction (SCXRD). This technique has proved crucial to the development of MOF chemistry by providing molecular-level insight into the nature of gas adsorption,¹⁷⁻¹⁹ chemical reactions within pore networks,²⁰⁻²⁵ catalysis,²⁶⁻²⁷ and the structure of guest molecules.⁸ We recently showed that crystals of the Mn(II)-based MOF **1** (**1** = [Mn₃(**L**)₂(**L'**)]), where H₂**L** = bis(4-(4-carboxyphenyl)-1*H*-3,5-dimethylpyrazolyl)methane and **L'** possesses a non-coordinated bis(3,5-dimethylpyrazol-1-yl)methane moiety) can be employed to structurally characterize the intermediates of a catalytic reaction cycle carried out within the framework pores.^{20, 27} A key feature of **1** is that it is

composed of regularly spaced vacant bis-pyrazolyl groups that are accessible to post-synthetic metalation (PSM)^{20, 28} reactions via *ca.* 13 Å diameter pores.

Typically, PSM chemistry is employed to enhance the performance characteristics of a given framework; however, we hypothesized that the spatial isolation of reactive metal centers could be employed to carry out chemoselective reactions within MOF pores without the need for a traditional protecting group. To realize this concept, we incorporated an azide functionality into the pores of **1** via a two-step process: PSM of **1** with [Mn(CO)₅Br] followed by halide exchange with sodium azide to afford **1**·[Mn(CO)₃N₃], which is primed for further reaction. The azide groups of **1**·[Mn(CO)₃N₃] are located 13 Å apart and thus uniquely poised to selectively carry out an azide-alkyne [3+2] cycloaddition reaction on one of the alkyne moieties of a symmetrical dialkyne (Figure 4.1). Synthetic approaches towards the preparation of compounds that possess both triazole and alkyne functional groups generally proceed via chemical protection of one alkyne or the addition of the alkyne fragment to a pre-formed halogenated triazole derivative via Sonogashira coupling.²⁹⁻³⁰ Direct synthesis of alkyne-substituted triazoles from the corresponding azide and polyalkyne reagents are less common. Tykwinski *et. al.*, however, reported the preparation of triazoles bearing poly-alkyne substituents from non-symmetric poly-alkynes and benzyl azide.³¹ Other studies have reported the synthesis of 5-alkynyl triazoles from poly-alkynes featuring phenyl³² or trimethyl-silyl^{30, 33} terminal groups. However, direct “click”-type synthesis of triazoles bearing unhindered terminal alkyne substituents have not been reported.

Herein we employ SCXRD to demonstrate that reactive-site isolation in a MOF scaffold facilitates site-selective reactions. Single-crystal to single-crystal (SC-SC) transformations of **1**·[Mn(CO)₃(H₂O)]Br to the corresponding azide species **1**·[Mn(CO)₃N₃] with sodium azide, followed by a series of [3+2] azide-alkyne cycloaddition reactions, and final liberation of the “click” products from the porous material by N-alkylation with MeBr to regenerate **1**·[Mn(CO)₃(H₂O)]Br, were examined by SCXRD and IR spectroscopy to reveal the postulated reaction cycle. Five alkynes, namely dimethyl-acetylene dicarboxylate (DMAD), ethyl-propiolate (EPOP), 1,7-octadiyne-3,6-dione (DA1), 1,9-decadiyne-3,8-dione (DA2), and 1,11-dodecadiyne-3,10-dione (DA3) were investigated to test the site isolation hypothesis. For all alkyne substrates, the reactions yield the desired triazoles, and reveal an unexpected N1 binding mode of the triazole in the MOF. In particular, we demonstrate the site-selective conversion of dialkynes into alkyne-substituted triazoles when the structure metrics of the dialkyne are smaller than the azide group spacing in the MOF. This study exemplifies how the inherent crystallinity of MOFs can be exploited to gain a

fundamental understanding of chemical reactivity within their pores. Additionally, it develops the concept of how the modular approach to MOF synthesis can lead to the precise spatial isolation of reactive sites that are poised to bind substrates³⁴ and facilitate site-selective reactions.

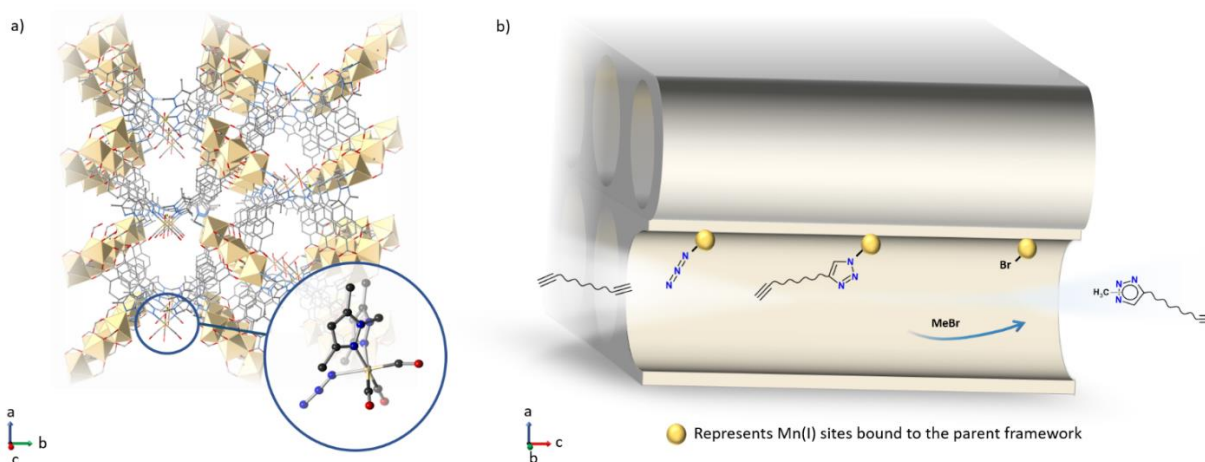


Figure 4.1. **a)** A representation of the spatially isolated azide sites along the 1-D *c*-axis pores of **1** (C, dark grey; N, blue; O, red; Mn, beige; H atoms omitted for clarity). The insert reveals the coordination chemistry about the PSM added Mn(I) center in the MOF, showing the loaded azide reagent in the axial site. **b)** A graphical depiction of the site-isolation strategy using a dialkyne substrate, showing the introduction of the dialkyne, its “click” conversion (the Mn(I) sites are periodically separated by *ca.* 13Å), and then liberation by alkylation with MeBr to produce the desired N-methyl alkynyl triazole.

4.3 Results and Discussion

4.3.1 Azide “loading” of the MOF

We previously showed that the functionality of MOF **1** can be tailored via quantitative metalation of the bis-pyrazole moieties lining its pore network.^{20, 27} The flexible organic linker allows the MOF structure to respond dynamically to the changing coordination environment of the PSM added metal without compromising the integrity of the single crystals. The post-synthetically introduced reactive sites are uniformly distributed within the MOF (*ca.* 13 Å apart), and so we envisaged that they may be employed to carry out site-selective chemical transformations (Figure 4.1). For example, based on collision theory, a homogeneous [3+2] cycloaddition reaction between an inorganic azide and dialkyne would conventionally yield a mixture of triazole products. However, the equivalent reaction employing a derivative of **1** bearing site-isolated inorganic azides should selectively yield the alkyne-functionalized

triazolate complex, owing to the physical separation of the adjacent azides. Accordingly, to explore the potential of MOFs as reaction vessels for site-selective chemistry, we sought to perform selective [3+2] cycloaddition reactions using an azide-functionalized version of **1**.

An azide-functionalized derivative of **1** was prepared by a sequential metalation and anion-exchange strategy. Initially MOF **1** was treated with $[\text{Mn}(\text{CO})_5\text{Br}]$ in ethanol at 50°C . The crystalline product was characterized by synchrotron SCXRD, which elucidated that the N,N-chelation site of **1** was occupied by a manganese tricarbonyl moiety, *fac*-**1**· $[\text{Mn}(\text{CO})_3(\text{H}_2\text{O})]\text{Br}$, with a non-coordinated Br^- counterion. Quantitative metalation was confirmed by energy-dispersive X-ray (EDX) analysis which yielded an Mn:Br ratio of 4:1. We also examined **1**· $[\text{Mn}(\text{CO})_3(\text{H}_2\text{O})]\text{Br}$ by IR spectroscopy, which revealed characteristic $\text{C}\equiv\text{O}$ stretches at 1951, 2040 and 1921 cm^{-1} .³⁵⁻³⁷ Additionally, the phase purity of **1**· $[\text{Mn}(\text{CO})_3(\text{H}_2\text{O})]\text{Br}$ was confirmed by PXRD analysis (Figure S7.3.6.1.).

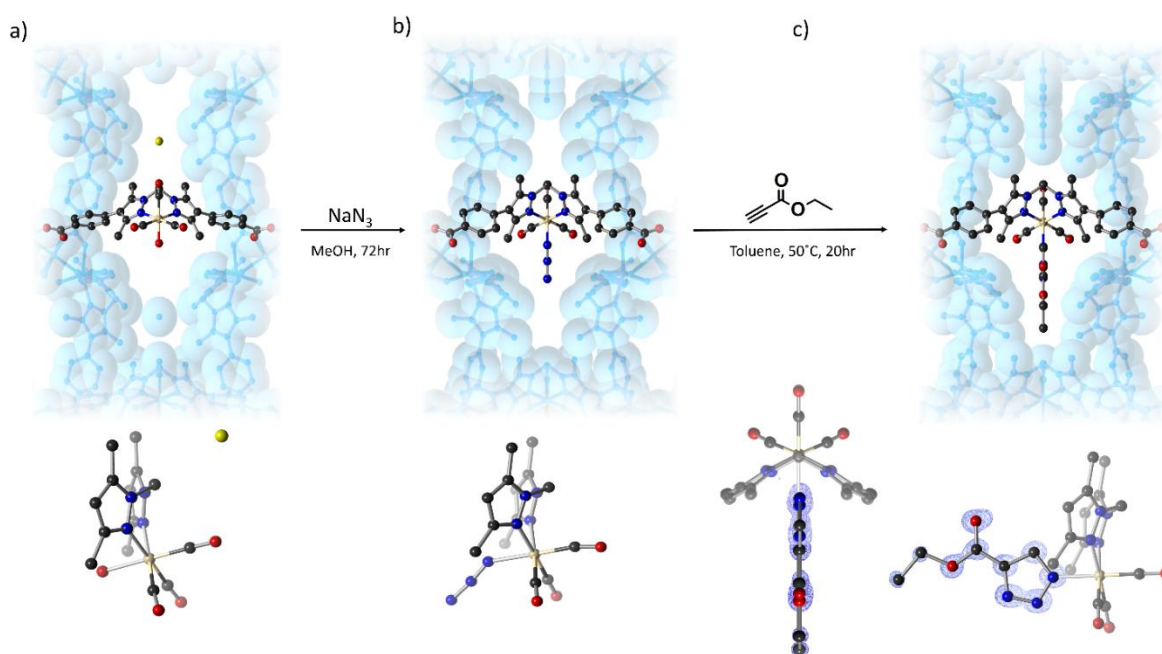


Figure 4.2. Representations of the metalated N,N-chelation site in the pore space of **1** at key steps in the "click" chemistry reaction scheme, with a perspective view of each complex shown below. **a)** **1**· $[\text{Mn}(\text{CO})_3(\text{H}_2\text{O})]\text{Br}$, displaying the facial isomer of the $[\text{Mn}(\text{CO})_3(\text{H}_2\text{O})]$ moiety following post-synthetic metalation, **b)** **1**· $[\text{Mn}(\text{CO})_3\text{N}_3]$, following facile exchange of Br^- for N_3^- ; and **c)** **1**· $[\text{Mn}(\text{CO})_3(\text{ET})]$ (where ET = ethyl-4-carboxy-1,2,3-triazolate), the triazolate complex following reaction of the azide with ethyl-propiolate, including side and top views of the F_{obs} electron density map associated with the triazolate. The parent MOF framework is represented by a translucent, blue van der Waals surface (C, dark grey; N, blue; O, red; Mn, beige; Br, yellow; H atoms omitted for clarity).

Anion-exchange reactions are well known for metal-halide complexes. Thus, we explored the direct exchange of the non-coordinated bromide with azide to decorate the pores of the MOF with azide moieties. Crystals of $\mathbf{1}\cdot[\text{Mn}(\text{CO})_3(\text{H}_2\text{O})]\text{Br}$ were soaked in a methanol solution of sodium azide (NaN_3) for three days to yield $\mathbf{1}\cdot[\text{Mn}(\text{CO})_3\text{N}_3]$. The IR spectrum of $\mathbf{1}\cdot[\text{Mn}(\text{CO})_3\text{N}_3]$ revealed a strong IR stretch at 2070 cm^{-1} that is typical of a metal-coordinated azide,^{35, 37-39} furthermore, the expected $\nu(\text{C}\equiv\text{O})$ bands were observed at 2025 , 1952 , and 1903 cm^{-1} . The elemental composition of $\mathbf{1}\cdot[\text{Mn}(\text{CO})_3\text{N}_3]$ was assessed by EDX analysis to provide insight into the extent of Br^- substitution. Close inspection of the data showed that subsequent to the anion exchange protocol the Mn:Br ratio decreased from 4:1 to 4:0.07. Throughout the anion-exchange process the MOF retained its crystallinity allowing us to collect SCXRD data. These experiments elucidated the presence of an azide anion bound to the axial site of the octahedral Mn(I) complex and retention of the facially coordinated $\text{C}\equiv\text{O}$ ligands. The crystal structure of $\mathbf{1}\cdot[\text{Mn}(\text{CO})_3\text{N}_3]$ obtained using synchrotron radiation also confirmed that the azide anions are site-isolated (ca. 13 \AA apart), well ordered and accessible to guest molecules rendering this MOF an ideal candidate for site-selective “click” chemistry.

4.3.2 “Click” chemistry within the MOF pores

The azide functional group is known to participate in the [3+2] cycloaddition reaction with alkyne moieties to form a triazole (in the case of an organic azide) or triazolate salt (for an inorganic azide complex).⁴⁰⁻⁴² This prototypical “click” reaction is applied in numerous fields of chemistry, such as dendrimer synthesis,⁴³⁻⁴⁴ preparation of pharmaceuticals,⁴⁵⁻⁴⁸ post-synthetic modification of MOFs,⁴⁹⁻⁵¹ and extensively in polymer science.⁵²⁻⁵³ The Cu-catalyzed [3+2] cycloaddition reaction between organic azides and alkynes has been studied in various MOF frameworks⁵⁴⁻⁵⁵ and zeolites.⁵⁶ However, in $\mathbf{1}\cdot[\text{Mn}(\text{CO})_3\text{N}_3]$ the azide source is inorganic and, although such transformations are colloquially termed “click” reactions, the reaction described herein is formally a Huisgen cycloaddition process. Importantly, it is expected that the reaction between $\mathbf{1}\cdot[\text{Mn}(\text{CO})_3\text{N}_3]$ and an alkyne will yield a product in which the triazolate is coordinated to the structurally isolated Mn sites.³⁸ Thus, if a dialkyne is employed the physical separation between the triazolate complex and adjacent azide moiety, imposed by the host framework, would prevent the remaining alkyne from participating in a secondary “click” reaction (Figure 4.1). Furthermore, the N-alkyl organic triazole can be easily liberated via reaction with an alkyl halide.

This chemistry facilitates a novel synthesis strategy for alkyne-functionalized triazoles via step-wise inorganic “click” chemistry and N-alkylation.

We exposed single crystals of $\mathbf{1}\cdot[\text{Mn}(\text{CO})_3\text{N}_3]$ to two electron-deficient alkynes, dimethyl-acetylene dicarboxylate (DMAD) and ethyl-propiolate (EPOP) to afford $\mathbf{1}\cdot[\text{Mn}(\text{CO})_3(\text{DMT})]$ and $\mathbf{1}\cdot[\text{Mn}(\text{CO})_3(\text{ET})]$, respectively (where DMT = dimethyl 4,5-dicarboxy-1,2,3-triazolate and ET = ethyl 4-carboxy-1,2,3-triazolate). Each reaction was performed at 50°C in toluene to promote formation of the corresponding triazolate complex and after 24h the respective samples were examined by FTIR spectroscopy. In both spectra the characteristic azide asymmetric stretch at 2070 cm^{-1} of $\mathbf{1}\cdot[\text{Mn}(\text{CO})_3\text{N}_3]$ was absent, indicating that quantitative conversion of the azide had occurred (Figure 4.3a and Figure S7.3.7.1). Furthermore, the simultaneous growth of a methyl or ethyl ester carbonyl stretch at 1716 and 1711 cm^{-1} respectively, was observed, supporting the presence of a coordinated triazolate moiety.⁵⁷ PXRD experiments performed on the MOF crystals after the “click” reactions indicate that the bulk material retains a high degree of crystallinity (Figure 4.3b, data shown for the EPOP cycle).

Remarkably, subsequent to successive anion exchange and ‘click’ reactions the crystals of $\mathbf{1}\cdot[\text{Mn}(\text{CO})_3(\text{DMT})]$ and $\mathbf{1}\cdot[\text{Mn}(\text{CO})_3(\text{ET})]$ remained suitable for SCXRD. Structure solution and data refinement revealed the presence of an N(1)-bound triazolate product in both $\mathbf{1}\cdot[\text{Mn}(\text{CO})_3(\text{ET})]$ (Figure 4.2c) and $\mathbf{1}\cdot[\text{Mn}(\text{CO})_3(\text{DMT})]$ (Figure S7.3.5.2.3). The structure determinations were further supported by a close match of the structural model to the F_{obs} electron density maps (Figure 4.2c). In both instances, the triazolate resides on the mirror plane bisecting the Mn(I) complex and is coordinated to the axial site formerly occupied by azide in $\mathbf{1}\cdot[\text{Mn}(\text{CO})_3\text{N}_3]$. Close examination of the data indicates preferential formation of an N(1)-bound complex in $\mathbf{1}\cdot[\text{Mn}(\text{CO})_3(\text{DMT})]$ (Figure S7.3.5.2.3). The single ethyl ester substituent in $\mathbf{1}\cdot[\text{Mn}(\text{CO})_3(\text{ET})]$ is appended such that it projects into the MOF pore and, by assigning the largest electron density peaks in the triazole ring system as nitrogen atoms, we also refined the triazolate complex as an N(1)-bound isomer consistent with that observed in $\mathbf{1}\cdot[\text{Mn}(\text{CO})_3(\text{DMT})]$.

4.3.3 Unusual “in MOF” triazolate coordination

N(1)-bound octahedral triazolate complexes, such as $\mathbf{1}\cdot[\text{Mn}(\text{CO})_3(\text{DMT})]$ and $\mathbf{1}\cdot[\text{Mn}(\text{CO})_3(\text{ET})]$, are rare,^{38, 57-59} since steric effects in octahedral complexes usually favor the rearrangement of the complex to form the N(2)-bound isomer.^{35, 39} It is evident from the crystal structures that close contacts between the

coordinated triazolate and adjacent features of the MOF pore would be substantially increased if the triazolate were to bind via the N(2) nitrogen. To confirm that the MOF environment, rather than the primary coordination environment, are responsible for this behavior, we synthesized the molecular counterpart, $[\text{Mn}(\text{bis}(3,5\text{-dimethyl-pyrazolyl})\text{methane})(\text{CO})_3(\text{dimethyl } 4,5\text{-carboxy-1,2,3-triazolate})]$ ($[\text{Mn}(\text{bpm})(\text{CO})_3(\text{DMT})]$), where bpm = bis(3,5-dimethyl-pyrazolyl)methane). SCXRD studies revealed an N(2)-bound triazolate coordinated to a *fac*-Mn(I) tricarbonyl complex (Figure S7.3.5.1.1). Evidently, the MOF environment enforces new steric demands on the triazolate, favoring coordination motifs that reduce steric interactions between the host framework and triazolate. Density functional theory calculations support this hypothesis. Comparison of the calculated energies of the N(1)- and N(2)-bound complexes in $1 \cdot [\text{Mn}(\text{CO})_3(\text{DMT})]$ and molecular species shows that the framework stabilizes the N(1)-bound isomer by 11 kJ/mol with respect to the N(2)-bound isomer. Furthermore, significant steric interactions between the host framework and the methyl substituents on the DMT ligand along the pathway that converts the moiety from an N(1)- to the N(2)-bound complex results in a substantial calculated energy barrier for this process of around 170 kJ/mol. This indicates that it is highly unlikely for the N(1)-bound complex that is initially formed in the “click” reaction³⁸ to transform into the N(2)-bound complex (see Section 7.4 for a detailed description of the computational procedures and results).

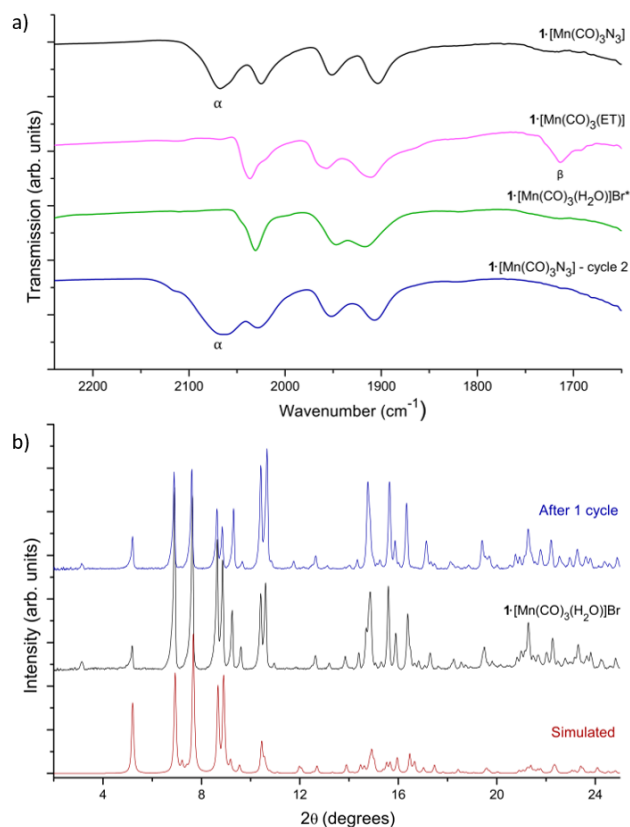


Figure 4.3 a) IR spectra of $1\cdot[\text{Mn}(\text{CO})_3\text{N}_3]$ and the “click”-chemistry product $1\cdot[\text{Mn}(\text{CO})_3(\text{ET})]$, confirming loss of the N_3 stretch (2070 cm^{-1} , indicated by α) and formation of the ethyl ester carbonyl (stretch near 1700 cm^{-1} , indicated by β), which supports the formation of the observed triazolate product. The alkylation of the triazolate is observed as a decrease in the ester stretch in $1\cdot[\text{Mn}(\text{CO})_3(\text{ET})]$, and the resulting bromide complex readily undergoes azide exchange to regenerate $1\cdot[\text{Mn}(\text{CO})_3\text{N}_3]$. **b)** PXRD data obtained from the material after one click cycle using EPOP closely matches the starting material, $1\cdot[\text{Mn}(\text{CO})_3(\text{H}_2\text{O})]\text{Br}$ and the simulated pattern, indicating that the MOF retains crystallinity throughout the cycle.

4.3.4. Triazole release from the MOF platform

For the MOF to act as a functional host for “click” chemistry, the organic product must be liberated and the original framework ‘vessel’ re-generated in suitable condition to perform further reaction cycles. Due to the strong metal–triazolate bond, simple anion exchange with sodium azide is not sufficient to release the triazolate. Fortunately, this issue is overcome by reacting the MOF-bound triazolate complex with MeBr^{57, 60-61} to release the corresponding N-alkylated triazole and regenerate the original host framework, $1\cdot[\text{Mn}(\text{CO})_3(\text{H}_2\text{O})]\text{Br}$. We note that this process also occurs via a SC-SC transition. To monitor the reaction we employed NMR spectroscopy and EDX analysis to assess the formation of the N-alkylated

triazole and the MOF-bound halide complex, respectively. Alkylation was performed by placing crystals of $\mathbf{1}\cdot[\text{Mn}(\text{CO})_3(\text{DMT})]$ in CDCl_3 and heating the mixture at 50°C overnight in the presence of excess MeBr. Following removal of the MOF crystals, the CDCl_3 solution was analyzed via $^1\text{H-NMR}$ spectroscopy and found to contain dimethyl N1-methyl-4,5-dicarboxy-1,2,3-triazole. The position of the methyl group on the triazole ring was confirmed by the presence of two separate methyl ester signals in the $^1\text{H-NMR}$ spectrum, indicating alkylation at N(1).⁵⁷ Notably, PXRD patterns obtained after a full “click” chemistry cycle demonstrated a high degree of crystallinity (Figure 4.3b), as evidenced by the excellent agreement between the patterns of $\mathbf{1}\cdot[\text{Mn}(\text{CO})_3(\text{H}_2\text{O})]\text{Br}$ and $\mathbf{1}\cdot[\text{Mn}(\text{CO})_3(\text{H}_2\text{O})]\text{Br}^*$ (* indicates a MOF that has completed one reaction cycle). Quantitative regeneration of the Mn(I) bromide complex is supported by EDX experiments, which indicate a 4:1 Mn:Br ratio (Table S7.3.2.1) while the IR spectrum of $\mathbf{1}\cdot[\text{Mn}(\text{CO})_3(\text{H}_2\text{O})]\text{Br}^*$ shows analogous $\nu(\text{C}=\text{O})$ bands to $\mathbf{1}\cdot[\text{Mn}(\text{CO})_3(\text{H}_2\text{O})]\text{Br}$. Furthermore, reaction of $\mathbf{1}\cdot[\text{Mn}(\text{CO})_3(\text{ET})]$ with MeBr successfully released ethyl N-methyl-4-carboxy-1,2,3-triazole to regenerate the original framework. ^1H NMR spectroscopy indicated that the liberated product was a mixture of two N-alkylated isomers in a 5:3 ratio. In addition, complete loss of the ester $\nu(\text{C}=\text{O})$ band in the IR spectrum supports the quantitative expulsion of the organic triazole from the MOF (Figure 4.3a). This data supports the successful use of $\mathbf{1}$ as a platform for the complete “click” chemistry cycle.

Buoyed by these results, we subjected the material to a second azide exchange cycle and observed a prominent azide stretch in the IR spectrum, consistent with that observed for $\mathbf{1}\cdot[\text{Mn}(\text{CO})_3\text{N}_3]$ (Figure 4.3a). These results confirm that the material could serve as a platform for “click” chemistry over multiple cycles.

4.3.5. Selective “click” chemistry with dialkynes

Having established the viability of $\mathbf{1}$ as a host for stoichiometric “click” conversions, we turned our attention to carrying out site-selective functionalization on a dialkyne substrate to directly produce the corresponding alkyne-functionalized N-alkylated triazole. We selected a series of terminal dialkynes DA1, DA2 and DA3 with lengths of 10.7, 13.1 and 15.6 Å, respectively. Since the azide separation in $\mathbf{1}\cdot\text{N}_3$ is 13.0 Å, we anticipated that the shortest dialkyne would undergo site-selective “click” chemistry while the longest species would produce a mixture of bis- and mono-triazole products as its length exceeds the azide separation.

We selected the symmetric dialkyne substrates since the well-separated and unhindered terminal alkyne sites pose a challenging profile for selective triazole formation. The inclusion of carbonyl groups adjacent to the alkyne activate them toward “click” chemistry, as seen for DMAD and EPOP, by withdrawing electron density from the triple bond. The “click” reactions were performed in toluene at 50°C and monitored via IR spectroscopy which showed a gradual loss of the asymmetric N_3^- stretch at 2070 cm^{-1} . PXRD analysis after the reaction was complete confirmed that the MOF retained crystallinity (Figure S7.3.6.3-5), while the IR spectrum displayed a C=O stretch at 1690 cm^{-1} consistent with presence of the ketone functionality.

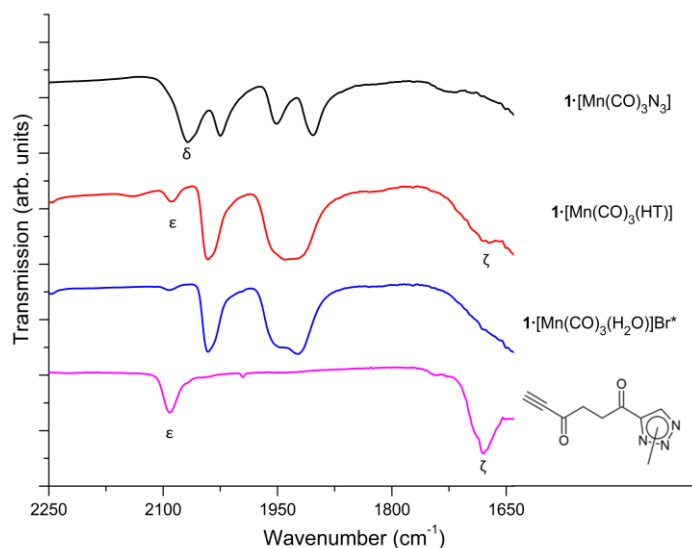


Figure 4.4 IR spectra of Mn(I) metalated forms of **1** displaying characteristic CO stretches, which are retained throughout the “click” chemistry cycle. The progression of the anion exchange, “click” reaction and N-alkylation can be monitored by the appearance and loss of the azide stretch at 2070 cm^{-1} (δ) and concomitant formation of the alkyne and ester stretches at 2090 and 1680 cm^{-1} respectively (ϵ and ζ , respectively). The liberated triazole product displays the same spectroscopic features.

The MOF crystals of $1 \cdot [\text{Mn}(\text{CO})_3(4\text{-hex-5'-ynyl-1',4'-dione-1,2,3-triazolate})]$ ($1 \cdot [\text{Mn}(\text{CO})_3(\text{HT})]$) were found to be suitable for SCXRD studies. Refinement of the structure revealed the presence of a five-membered ring coordinated to the Mn(I) site, which was assigned as an N(1)-bound triazolate. Furthermore, the alkyne functionalized chain can be discerned in the electron density map, bound to C4 of the triazole. Refinement without crystallographic restraints was not possible, but an energy-minimized organic moiety could be modelled in this site and provides a reasonable match to the F_{obs} electron density map (Figure S7.3.5.3.5). In addition, the IR spectrum of ($1 \cdot [\text{Mn}(\text{CO})_3(\text{HT})]$) showed a band at 2090 cm^{-1} , characteristic

of an alkyne $\text{C}\equiv\text{C}$ stretch along with concomitant loss of the azide band at 2070 cm^{-1} (Figure 4.4). Consistent with our hypothesis, this evidence confirms that the shortest dialkyne, DA1, produces the site-selective “click” product, 4-hex-5'-ynl-1',4'-dione-1,2,3-triazolate.

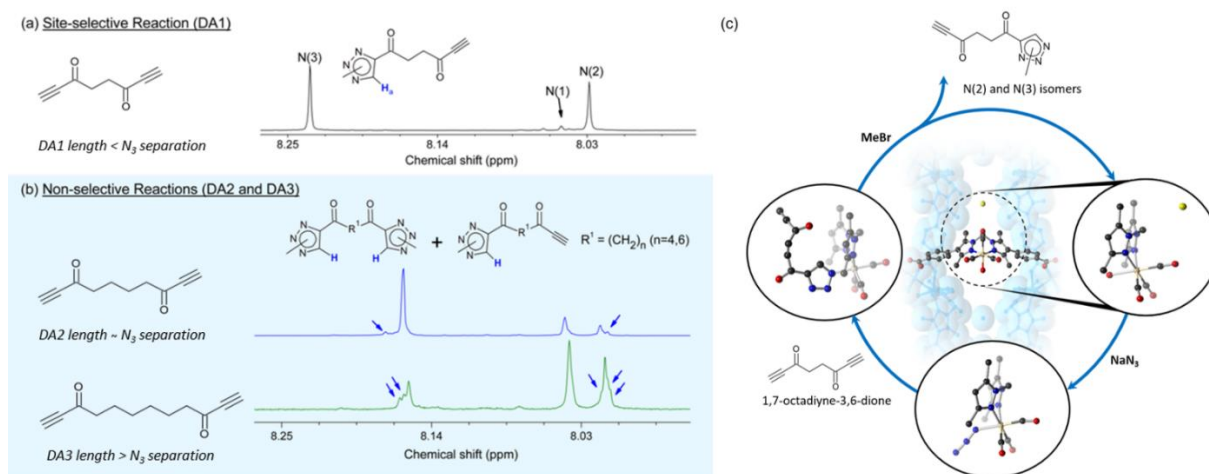


Figure 4.5. (a) The shortest dialkyne, DA1, undergoes site-selective “click” chemistry to yield N-methyl 4-hex-5'-ynl-1',4'-dione-1,2,3-triazole (N(2) and N(3) major isomers), as indicated by consideration of the CH triazole region of the ^1H NMR spectrum, which shows two prominent triazole CH signals (note: the N(1)-methyl isomer is also present in small quantity; see SI Section 7.3). b) Extension of the dialkyne substrate results in a mixture of bis- and mono-“click” products, resulting in multiple triazole CH peaks in the ^1H NMR spectrum; the lower intensity signals are highlighted by a blue arrow. The number of triazole CH signals increases with the dialkyne length, indicating a greater proportion of bis-triazole products and loss of site-selectivity. c) Site-selective “click” chemistry cycle using DA1 proceeding from $1\cdot[\text{Mn}(\text{CO})_3(\text{H}_2\text{O})]\text{Br}$ to $1\cdot[\text{Mn}(\text{CO})_3\text{N}_3]$, formation of the “click” triazolite complex and regeneration of the starting material $1\cdot[\text{Mn}(\text{CO})_3(\text{H}_2\text{O})]\text{Br}$ via alkylation with MeBr .

Each of the DA1-, DA2- and DA3-derived triazolite complexes were reacted with MeBr to yield $1\cdot[\text{Mn}(\text{CO})_3(\text{H}_2\text{O})]\text{Br}$ and the respective N-alkylated triazole product using the alkylation protocol discussed earlier. In all cases the reaction was accompanied by a color change in the crystals from red to a yellow-orange color consistent with re-formation of $1\cdot[\text{Mn}(\text{CO})_3(\text{H}_2\text{O})]\text{Br}$. IR spectroscopy of each MOF sample showed the characteristic $\text{C}\equiv\text{O}$ stretches, confirming the presence of the tricarbonyl moiety and the PXRD patterns obtained after the full “click” chemistry cycle closely matched that of the original framework $1\cdot[\text{Mn}(\text{CO})_3(\text{H}_2\text{O})]\text{Br}$ (Figure S7.3.6.3-5). We characterized the respective triazole products by 1D and 2D NMR experiments and high-resolution mass spectrometry. The NMR analysis of the product obtained from the shortest dialkyne, 1,7-octadiyne-3,8-dione (DA1), confirmed the selective formation of the alkyne functionalized triazole as a mixture of N(3) and N(2)-methyl isomers in a 1:0.8 ratio (a trace of

the N(1)-methyl isomer was also observed) (Figure 4.5a). The alkyne moiety was observed as a singlet in the ^1H NMR (3.27 ppm and 3.32 ppm for the N(2) and N(3) isomers, respectively) and further supported by the IR spectroscopy of the oily product, which displays the characteristic CH stretch at 3249 cm^{-1} and $\text{C}\equiv\text{C}$ stretch at 2091 cm^{-1} . High-resolution mass spectrometry clearly identified the $[\text{M}+\text{H}]^+$ ion at m/z 192.0967 with only traces of the bis-triazole product observed (Figure S7.3.4.1). The combination of NMR and IR spectroscopy, and mass spectrometry overwhelmingly supports the successful site-selective “click” reaction to give the desired alkyne-functionalized triazole product.

As anticipated the NMR and mass spectrometry data reveal a direct relationship between the length of the dialkyne, the azide separation and selectivity obtained. Both longer dialkyne substrates, 1,9-decadiyne-3,8-dione (length $13.1\text{ \AA} \approx \text{N}_3$ separation) and 1,11-dodecadiyne-3,10-dione (length $15.6\text{ \AA} > \text{N}_3$ separation) gave rise to a greater proportion of bis-triazole product (Figure 4.5b), with the longest dialkyne producing at least 8 detectable triazole proton environments. These results confirm that the spatial isolation of the azide moieties achieved in $\mathbf{1}\cdot[\text{Mn}(\text{CO})_3\text{N}_3]$ is integral to the site-selective “click”-chemistry strategy, since the selectivity is compromised once the dialkyne length approaches that of the azide separation. In all cases, PXRD analysis confirmed the parent framework is preserved throughout the “click” chemistry cycle.

4.4. Conclusion

Herein we have demonstrated that the crystalline structure of MOFs can facilitate the angstrom-scale ordering of reactive azide sites to yield a reactive ‘vessel’ that is poised to perform site-selective “click” chemistry. The high degree of crystallinity of the MOF framework allowed us to precisely characterize the precursor azide sites and “click” chemistry triazolone products using SCXRD, providing insight into the effect of the confining pore environment and isolated reactive sites on chemical processes within MOFs. By way of example we performed site-selective “click” chemistry reaction cycles using a series of dialkynes of different structure metrics. These experiments clearly showed that the degree of site selectivity observed was dependent on the length of the dialkyne relative to the distance between the azide moieties. We anticipate that the scope for employing MOFs as site-selective reaction vessels is vast, given their bespoke design and chemical mutability. Indeed, this chemistry could be extended by precisely positioning guest molecules within the framework via specific dynamic covalent, dative, or H-bonding interactions to facilitate highly efficient chemoselective reactions. To this end, the MOF crystal could be considered to function as a novel solid-state protecting group and, accordingly, this strategy may

be broadened to include a wide variety of site-selective and chemoselective transformations that are not easily carried out using a traditional protecting-group strategy.

4.5 Experimental

4.5.1 *Materials and Methods*

Unless otherwise stated, all preparations of the organic compounds were performed under an Ar atmosphere using standard Schlenk techniques with dried and degassed solvents. All MOF synthesis reactions were carried out in air. H_2L (bis(4-(4-carboxyphenyl)-1*H*-3,5-dimethylpyrazolyl)methane), bis(3,5-dimethylpyrazolyl)methane (bpm) and 1,9-decadiyne-3,8-dione (DA2) were synthesized as previously reported.⁶²⁻⁶³⁻⁶⁴ All reagents were obtained from commercial vendors and used without further purification. NMR spectra were recorded on Varian Gemini 500 or 600 MHz spectrometers at 23°C using a 5 mm probe. Energy-dispersive X-ray spectroscopy (EDX) was performed with a Philips XL30 field emission scanning electron microscope. Infrared (IR) spectra were collected on a Perkin-Elmer Spectrum Two, with the sample distributed between two NaCl disks in Nujol. Electrospray ionization (ESI) high-resolution mass spectra (HR-MS) were recorded on Q-TOF mass spectrometer (Agilent 6230). For details regarding the preparation of the dialkynes DA1 and DA3, and the molecular complex [Mn(bpm)(CO)₃(DMT)], please see the Supplementary Information in Sections 7.3 and 7.4.

4.5.2 *Single Crystal and Powder X-ray Diffraction Data*

Single crystals were mounted in paratone-N oil on a nylon loop. Single-crystal X-ray data for $1 \cdot [Mn(CO)_3(H_2O)]Br$, $1 \cdot [Mn(CO)_3N_3]$, $1 \cdot [Mn(CO)_3(ET)]$, $1 \cdot [Mn(CO)_3(DMT)]$ and $1 \cdot [Mn(CO)_3(OT)]$ were collected at 100 K on the MX1 or MX2 beamlines of the Australia Synchrotron using the Blulce software interface,⁶⁵ $\lambda = 0.7108 \text{ \AA}$. Single crystal X-ray data for, [Mn(bpm)(CO)₃Br] and [Mn(bpm)(CO)₃(DMT)] were collected at 150(2) K on an Oxford X-Calibur single crystal diffractometer ($\lambda = 0.71073 \text{ \AA}$). N_{tot} reflections were merged to N unique (R_{int} quoted) after a multi-scan absorption correction (proprietary software) and used in the full matrix least-squares refinements on F_2 . Unless otherwise stated in the additional refinement details, anisotropic displacement parameter forms were refined for the non-hydrogen atoms;

hydrogen atoms were treated with a riding model [weights: $(\sigma^2(F_o)^2 + (aP)^2 + (bP))^{-1}$; $P=(F_o^2 + 2F_c^2)/3$]. Neutral atom complex scattering factors were used; computation used the SHELXL2014 program.⁶⁶ Pertinent results are given in the manuscript, while views of the asymmetric units, additional refinement details, and X-ray experimental and refinement data (Tables S7.3.5.5.1-4) are given in the Supporting Information. Full details of the structure determinations have been deposited with the Cambridge Crystallographic Data Centre as CCDC #s 1826673-1826679 (see Tables S7.3.5.5.1-4 for specific deposit numbers). Copies of this information may be obtained free of charge from The Director, CCDC, 12 Union Street, Cambridge CB2 1EZ, U.K. (fax, +44-1223-336-033; e-mail, deposit@ccdc.cam.ac.uk).

Powder X-ray diffraction data were collected on a Bruker Advance D8 diffractometer equipped with a capillary stage using Cu K α radiation ($\lambda = 1.5418 \text{ \AA}$). Simulated powder X-ray diffraction (PXRD) patterns were produced from the single crystal data using Mercury 3.3.

4.5.3 Synthetic Procedures

1·[Mn(CO)₃(H₂O)]Br. Single crystals of **1** (30 mg) were washed with ethanol (5 × 10 ml) with 30 minutes between each wash. The crystals of **1** were transferred to a 20 ml scintillation vial containing ethanol (15 ml) and excess [Mn(CO)₅Br] (30 mg). The mixture was heated at 50°C for 48 h and the resulting yellow crystals were washed with fresh ethanol (5 × 10 ml) to give **1·[Mn(CO)₃(H₂O)]Br** as yellow single crystals IR ν_{max} (nujol, cm⁻¹): 1951 (s, C=O), 2040 (s, C=O), 1921 (s, C=O), 1608 (C=O), 1553, 1511, 1408, 1306, 1272.

1·[Mn(CO)₃N₃]. Single crystals of **1·[Mn(CO)₃Br]** (30 mg) were washed with methanol (5 × 10 ml) with 30 minutes between each wash and transferred to a 20 ml scintillation vial containing methanol (5 ml). A 2 ml glass vial containing NaN₃ (30 mg) was placed inside the scintillation vial, and methanol was added such that the 2 ml vial was fully submersed within the scintillation vial. The apparatus was left to stand at room temperature for 72 h. The methanol solution was decanted and the MOF crystals washed thoroughly with methanol (5 × 10 ml) to yield **1·[Mn(CO)₃N₃]** as yellow crystals. IR: (nujol, cm⁻¹): 2070 (s, N₃), 2025 (s, CO), 1952 (s, CO), 1903 (s, CO), 1608 (s, C=O), 1555, 1510, 1408, 1303, 1272.

1·[Mn(CO)₃(DMT)]. Single crystals of **1·[Mn(CO)₃N₃]** (30 mg) were washed with toluene (5 × 10 ml) and transferred to a Schlenk tube containing toluene (5 ml) and dimethyl acetylene dicarboxylate (0.1 ml). The mixture was sealed and heated at 50°C for 20 h, after which the solvent was decanted and the MOF

crystals washed with fresh toluene (5 × 10 ml) to yield **1**·[Mn(CO)₃(DMT)] as pale yellow crystals. IR ν_{\max} (nujol, cm⁻¹): 2034 (CO), 1956 (CO), 1909 (CO), 1716 (b, ester), 1608 (s, C=O), 1554 (C=C), 1509 (C=C), 1406, 1376, 1302, 1271, 1169 (w).

1·[Mn(CO)₃(ET)]. Single crystals of **1**·Mn(CO)₃N₃ (30 mg) were washed with toluene (5 × 10 ml) and transferred to a Schlenk tube containing toluene (5 ml) and ethyl propiolate (0.1 ml). The mixture was sealed and heated at 50 °C for 20 h, after which the solvent was decanted and the MOF crystals washed with fresh toluene (5 × 10 ml) to yield **1**·[Mn(CO)₃(ET)] as pale yellow crystals. IR ν_{\max} (nujol, cm⁻¹): 2035 (CO), 1945 (CO), 1922 (CO), 1711 (ester), 1665 (C=O), 1554, 1408, 1303, 1272.

1·[Mn(CO)₃(4-hex-5'-ynyl-1',4'-dione-1,2,3-triazolate)]. Single crystals of **1**·[Mn(CO)₃N₃] (60 mg) were washed with toluene (5 × 10 ml) and transferred to a 8 ml glass vial containing 1,7-octadiyne-3,6-dione (DA1). The mixture was sealed and heated at 50 °C for 20 h, after which the solvent was decanted and the MOF crystals washed with fresh toluene (5 × 5 ml) to yield **1**·[Mn(CO)₃(HT)] as pale yellow crystals. IR ν_{\max} (nujol, cm⁻¹): 2093 (C≡C), 2035 (CO), 1940 (CO), 1928 (CO), 1683 (ketone), 1555, 1458, 1303, 1272.

1·[Mn(CO)₃(4-octa-7'-ynyl-1',6'-dione-1,2,3-triazolate)]. Single crystals of **1**·[Mn(CO)₃N₃] (60 mg) were washed with toluene (5 × 10 ml) and transferred to a 8 ml glass vial containing 1,9-decadiyne-3,8-dione (DA2). The mixture was sealed and heated at 50 °C for 20 h, after which the solvent was decanted and the MOF crystals washed with fresh toluene (5 × 5 ml) to yield **1**·[Mn(CO)₃(OT)] as pale yellow crystals. IR ν_{\max} (nujol, cm⁻¹): 2089 (C≡C), 2034 (CO), 1938 (CO), 1917 (CO), 1671 (ketone), 1554, 1304, 1273.

1·[Mn(CO)₃(4-hex-9'-ynyl-1',8'-dione-1,2,3-triazolate)]. Single crystals of **1**·[Mn(CO)₃N₃] (60 mg) were washed with toluene (5 × 10 ml) and transferred to a 8 ml glass vial containing 1,11-dodecadiyne-3,10-dione (DA3). The mixture was sealed and heated at 50 °C for 20 h, after which the solvent was decanted and the MOF crystals washed with fresh toluene (5 × 5 ml) to yield **1**·[Mn(CO)₃(DT)] as pale yellow crystals. IR ν_{\max} (nujol, cm⁻¹): 2091 (C≡C), 2036 (CO), 1956 (CO), 1903 (CO), 1672 (ketone), 1554, 1509, 1454, 1408, 1302, 1271.

Alkylation of MOF-bound triazolate (general procedure) and re-formation of **1·[Mn(CO)₃(H₂O)]Br.**

Single crystals of **1**·[Mn(CO)₃(DMT)], **1**·[Mn(CO)₃(ET)], **1**·[Mn(CO)₃(HT)], **1**·[Mn(CO)₃(OT)], and **1**·[Mn(CO)₃(DT)] (approx. 60 mg) were washed with toluene (5 × 10 ml) followed by dichloromethane (30 ml) and CDCl₃ (5 ml). The sample was added to CDCl₃ (2 ml) in an 8 ml glass vial with Teflon cap, degassed with Ar and cooled to -10 °C in an ice-salt bath. Simultaneously, MeBr was cooled to -78 °C and an excess poured into the vial containing the MOF under flow of Ar. The vial was sealed and heated to

50°C for 20 h. The sample was cooled to room temperature, the MOF crystals were isolated via filtration and washed with CDCl_3 (5 ml) to yield $1\cdot[\text{Mn}(\text{CO})_3(\text{H}_2\text{O})]\text{Br}$ as yellow single crystals. IR ν_{max} (nujol, cm^{-1}): 2040 (s, CO), 1951 (s, CO), 1921 (s, CO), 1606, 1553, 1510, 1493, 1408, 1305, 1272, 1182.

The filtrate containing N-methylated triazole from the above reaction could be directly analyzed by NMR spectroscopy and mass spectrometry and subsequently evacuated under reduced pressure to yield the triazole compound(s) as oils for IR spectroscopy analysis when possible.

Dimethyl N(1)-methyl-4,5-carboxy-1,2,3-triazole (Me-DMT). ^1H NMR (500 MHz, CDCl_3): 4.28 (s, 3H, N- CH_3), 4.02 (s, 3H, COOCH_3), 3.99 (s, 3H, COOCH_3); ^{13}C NMR (150 MHz, CDCl_3): 163.11 (CO_2 , ester), 161.48 (CO_2 ester), 142.81 (triazole), 132.69 (triazole), 63.15 (CH_3), 56.04 (CH_3 ester), 55.39 (CH_3 ester); IR (Nujol, cm^{-1}): 1733 cm^{-1} (C=O), 1555 cm^{-1} , 1262, 1228, 1179, 1124, 1063; m/z: 199.0590 (calc'd 199.0593).

Ethyl N-methyl-4-carboxy-1,2,3-triazole (Me-ET). Isomers a, b in 5:3 ratio respectively. ^1H NMR (500MHz, CDCl_3): 8.13 (s, 1H, triazole CH (a)), 8.04 (s, 1H, triazole (b)), 4.44 (q, 2H, ester CH_2 (b)), 4.41 (q, 2H, ester CH_2 (a)), 4.34 (s, 3H, CH_3 (a)), 4.28 (s, 3H, CH_3 (b)), 1.42 (t, 3H, ester CH_3 (b)), 1.41 (t, 3H, ester CH_3 (a)).

N-Methyl 4-hex-5'-ynyl-1',4'-dione-1,2,3-triazole. N2 and N3 Isomers in a 1:0.8 ratio respectively.

N2-Methyl-4-hexa-5'-ynyl-1',4'-dione-1,2,3-triazole: ^1H NMR (600MHz, CDCl_3): 8.03 (s, 1H, triazole CH), 4.27 (s, 3H, CH_3), 3.36 (t, 2H, CH_2), 3.27 (s, 1H, $\text{C}\equiv\text{C-H}$), 3.08 (t, 2H, CH_2); ^{13}C NMR (150 MHz, CDCl_3): 191.53 (C=O), 185.16 (C=O), 146.26 (triazole), 135.10 (triazole CH), 81.10 (alkyne), 78.96 (alkyne), 42.25 (CH_3), 38.41(CH_2), 30.05 (CH_2).

N3-Methyl-4-hexa-5'-ynyl-1',4'-dione-1,2,3-triazole: ^1H NMR (600MHz, CDCl_3): 8.23 (s, 1H, triazole CH), 4.31 (s, 3H, CH_3), 3.32 (s, 1H, $\text{C}\equiv\text{C-H}$), 3.25 (t, 2H, CH_2), 3.09 (t, 2H, CH_2); ^{13}C NMR (150 MHz, CDCl_3): 187.69 (C=O), 184.49 (C=O), 137.61 (triazole CH), 132.89 (triazole), 80.88 ($\text{C}\equiv\text{C}$), 79.56 ($\text{C}\equiv\text{C}$), 38.66 (CH_3), 38.04 (CH_2), 34.14 (CH_2).

Analysis of mixture: IR (Nujol, cm^{-1}): 3249 ($\text{C}\equiv\text{C-H}$), 2958 (C-H), 2919 (C-H), 2850 (C-H), 2091 ($\text{C}\equiv\text{C}$), 1680 (C=O), 1608, 1403, 1105; m/z: $[\text{M}+\text{H}]^+$ 192.0967(calc'd $[\text{M}+\text{H}]^+$ 192.0773).

N-Methyl 4-octa-8'-ynyl-1',6'-dione-1,2,3-triazole. Isomers a, b in a 1:0.8 ratio respectively. ^1H NMR (600MHz, CDCl_3): 8.16 (s, triazole), 8.04 (s, triazole), 8.02 (s, triazole), 4.32 (s, CH_3), 4.26 (s, CH_3), 4.17 (s, CH_3), 3.24 (s, $\text{C}\equiv\text{C-H}$), 3.22 (s, $\text{C}\equiv\text{C-H}$), 2.92 (m, CH_2), 2.68 (CH_2), 1.77 (m, CH_2); ^{13}C NMR (150 MHz, CDCl_3): 189.81 (C=O), 186.52 (C=O), 185.57 (C=O), 137.53 (triazole), 135.16 (triazole), 133.55 (triazole), 126.23 (triazole), 81.28 ($\text{C}\equiv\text{C}$), 78.72 ($\text{C}\equiv\text{C}$), 78.67 ($\text{C}\equiv\text{C}$), 78.53 ($\text{C}\equiv\text{C}$), 45.15 (CH_2), 45.01 (CH_2), 44.96 (CH_2), 40.61

(CH₂), 39.23 (CH₂), 38.97 (CH₂), 38.08 (CH₃), 36.99 (CH₃), 23.20 (CH₂), 22.99 (CH₂), 22.92 (CH₂), 22.77 (CH₂); IR (Nujol, cm⁻¹): 3238 (C≡C-H), 2089 (C≡C), 1678 (C=O), 1525, 1448, 1397, 1368, 1261, 1104; m/z: 220.1130 [M+H]⁺ (calc'd [M+H]⁺ 220.1091).

N-Methyl 4-deca-9'-ynyl-1',8'-dione-1,2,3-triazole. Mixture of 8 isomers, signals identified as corresponding to triazole products are listed below. ¹H NMR (600MHz, CDCl₃): 8.16 (three singlet signals, triazole CH), 8.03 (s, triazole CH), 8.01 (three singlet signals, triazole CH), 4.31 (s, CH₃), 4.25 (s, CH₃), 4.15 (s, CH₃), 3.21 (two singlets, C≡C-H), 3.20 (s, C≡C-H), 3.11 (t, CH₂), 2.96 (t, CH₂), 2.87 (m, CH₂), 2.58 (m, CH₂), 1.74 (m, CH₂), 1.69 (m, CH₂), 1.42 (m, CH₂), 1.38 (m, CH₂); IR (Nujol, cm⁻¹): 3249 (C≡C-H), 2089 (C≡C), 1682 (C=O), 1609 (C=O), 1408, 1306; m/z: 248.1421 [M+H]⁺ (calc'd [M+H]⁺ 248.1399).

4.5.4 Computational Methods

Density functional theory (DFT) calculations were carried out with the Gaussian 09 software package (Revision D.01)⁶⁷ using the M06 functional.⁶⁸ Geometry optimizations were carried out in vacuo using the SDD effective core potential⁶⁹ for Mn ions and the 6-31G(d,p) basis set⁷⁰ for all atoms. Single-point energies were also calculated for the optimized geometries with the 6-31+G(d,p) basis set and SMD continuum solvation model⁷¹ with toluene solvent. Calculations were carried out on a 306-atom fragment of **1**·[Mn(CO)₃(DMT)] as a model for the extended MOF structure and on the corresponding molecular species [Mn(bpm)(CO)₃(DMT)]. Geometry optimizations of the MOF fragments were carried out keeping all non-hydrogen atoms in the framework fixed at their positions in the experimental X-ray crystal structure except for the atoms in the immediate vicinity of the Mn(I) ion. The energy barrier to interconvert the N(1)- and N(2)-bound complexes in **1**·[Mn(CO)₃(DMT)] was estimated from the energies of structures obtained by interpolating between the optimized N(1)- and N(2)-bound complexes and then optimizing the geometry with the orientation of the triazolite ring fixed with respect to the rest of the MOF. The computational procedures are described in further detail in the Supporting Information Section 7.4.

4.6 Associated content

Supporting information: characterization data for the MOF samples and related molecular species, characterization of triazole products, details of the SCXRD and tables of crystallographic data collection and refinement parameters, computational results, crystallographic information files (cifs).

4.7 Acknowledgements

CJD, CJS, DMH and NRC gratefully acknowledge the Australian Research Council for funding (DP160103234). Aspects of this research were undertaken on the MX1 and MX2 beamlines at the Australian Synchrotron, part of ANSTO, and made use of the Australian Cancer Research Foundation (ACRF) detector. DMH gratefully acknowledges computational resources provided by the Australian Government through the National Computing Infrastructure under the National Computational Merit Allocation Scheme and by the University of Adelaide's Phoenix High-Performance Computing service. MTH, AL and HG acknowledge the University of Adelaide and the Australian Government for a Research Training Program PhD scholarship.

4.8 References

- (1) Furukawa, H.; Cordova, K. E.; O'Keeffe, M.; Yaghi, O. M. *Science* **2013**, *341*, 974.
- (2) Yaghi, O. M.; O'Keeffe, M.; Ockwig, N. W.; Chae, H. K.; Eddaoudi, M.; Kim, J. *Nature* **2003**, *423*, 705.
- (3) Huang, Y. B.; Liang, J.; Wang, X. S.; Cao, R. *Chem. Soc. Rev.* **2016**, *46*, 126.
- (4) Dhakshinamoorthy, A.; Garcia, H. *ChemSusChem*. **2014**, *7*, 2392.
- (5) Dhakshinamoorthy, A.; Asiri, A. M.; Garcia, H. *Angew. Chem., Int. Ed.* **2016**, *55*, 5414.
- (6) Kitagawa, S.; Kitaura, R.; Noro, S. *Angew. Chem., Int. Ed.* **2004**, *43*, 2334.
- (7) Ferey, G. *Chem. Soc. Rev.* **2008**, *37*, 191.
- (8) Inokuma, Y.; Yoshioka, S.; Ariyoshi, J.; Arai, T.; Hitora, Y.; Takada, K.; Matsunaga, S.; Rissanen, K.; Fujita, M. *Nature* **2013**, *495*, 461.
- (9) Dechnik, J.; Sumbly, C. J.; Janiak, C. *Cryst. Growth Des.* **2017**, *17*, 4467.
- (10) Dechnik, J.; Gascon, J.; Doonan, C. J.; Janiak, C.; Sumbly, C. J. *Angew. Chem., Int. Ed.* **2017**, *56*, 9292.

- (11) Seoane, B.; Coronas, J.; Gascon, I.; Benavides, M. E.; Karvan, O.; Caro, J.; Kapteijn, F.; Gascon, J. *Chem. Soc. Rev.* **2015**, *44*, 2421.
- (12) Mason, J. A.; Veenstra, M.; Long, J. R. *Chem. Sci.* **2014**, *5*, 32.
- (13) Doonan, C.; Riccò, R.; Liang, K.; Bradshaw, D.; Falcaro, P. *Acc. Chem. Res.* **2017**, *50*, 1423.
- (14) Riccò, R.; Liang, W.; Li, S.; Gassensmith, J. J.; Caruso, F.; Doonan, C.; Falcaro, P. *ACS Nano* **2018**, *12*, 13.
- (15) Stassen, I.; Burtch, N.; Talin, A.; Falcaro, P.; Allendorf, M.; Ameloot, R. *Chem. Soc. Rev.* **2017**, *46*, 3185.
- (16) Dou, J.-H.; Sun, L.; Ge, Y.; Li, W.; Hendon, C. H.; Li, J.; Gul, S.; Yano, J.; Stach, E. A.; Dincă, M. *J. Am. Chem. Soc.* **2017**, *139*, 13608.
- (17) Gonzalez, M. I.; Mason, J. A.; Bloch, E. D.; Teat, S. J.; Gagnon, K. J.; Morrison, G. Y.; Queen, W. L.; Long, J. R. *Chem. Sci.* **2017**, *8*, 4387.
- (18) Bloch, E. D.; Queen, W. L.; Krishna, R.; Zadrozny, J. M.; Brown, C. M.; Long, J. R. *Science* **2012**, *335*, 1606.
- (19) Sung Cho, H.; Deng, H.; Miyasaka, K.; Dong, Z.; Cho, M.; Neimark, A. V.; Ku Kang, J.; Yaghi, O. M.; Terasaki, O. *Nature* **2015**, *527*, 503.
- (20) Bloch, W. M.; Burgun, A.; Coghlan, C. J.; Lee, R.; Coote, M. L.; Doonan, C. J.; Sumbly, C. J. *Nat. Chem.* **2014**, *6*, 906.
- (21) Bloch, W. M.; Burgun, A.; Doonan, C. J.; Sumbly, C. J. *Chem. Commun.* **2015**, *51*, 5486.
- (22) Huxley, M. T.; Coghlan, C. J.; Bloch, W. M.; Burgun, A.; Doonan, C. J.; Sumbly, C. J. *Phil. Trans. R. Soc. A* **2017**, *375*, 20160028.
- (23) Bloch, W. M.; Champness, N. R.; Doonan, C. J. *Angew. Chem., Int. Ed.* **2015**, *54*, 12860.
- (24) Duplan, V.; Hoshino, M.; Li, W.; Honda, T.; Fujita, M. *Angew. Chem., Int. Ed.* **2016**, *55*, 4919.
- (25) Ikemoto, K.; Inokuma, Y.; Rissanen, K.; Fujita, M. *J. Am. Chem. Soc.* **2014**, *136*, 6892.
- (26) Fortea-Pérez, F. R.; Mon, M.; Ferrando-Soria, J.; Boronat, M.; Leyva-Pérez, A.; Corma, A.; Herrera, J. M.; Osadchii, D.; Gascon, J.; Armentano, D., *et al.* *Nature Mat.* **2017**, *16*, 760.
- (27) Burgun, A.; Coghlan, C. J.; Huang, D. M.; Chen, W.; Horike, S.; Kitagawa, S.; Alvino, J. F.; Metha, G. F.; Sumbly, C. J.; Doonan, C. J. *Angew. Chem., Int. Ed.* **2017**, *56*, 1.
- (28) Evans, J. D.; Sumbly, C. J.; Doonan, C. J. *Chem. Soc. Rev.* **2014**, *43*, 5933.
- (29) Fiandanese, V.; Maurantonio, S.; Punzi, A.; Rafaschieri, G. G. *Org. Biomol. Chem.* **2012**, *10*, 1186.
- (30) Doak, B. C.; Scanlon, M. J.; Simpson, J. S. *Org. Lett.* **2010**, *13*, 537.
- (31) Luu, T.; McDonald, R.; Tykwinski, R. R. *Org. Lett.* **2006**, *8*, 6035.

- (32) Tang, J.-L.; Ming, L.; Zhao, X.-M. *J. Heterocycl. Chem.* **2016**, *53*, 1367.
- (33) Bettison, R. M.; Hitchcock, P. B.; Walton, D. R. M. *J. Organomet. Chem.* **1987**, *341*, 247.
- (34) Shultz, A. M.; Farha, O. K.; Hupp, J. T.; Nguyen, S. T. *J. Am. Chem. Soc.* **2009**, *131*, 4204.
- (35) Henry, L.; Schneider, C.; Mutzel, B.; Simpson, P. V.; Nagel, C.; Fucke, K.; Schatzschneider, U. *Chem. Commun.* **2014**, *50*, 15692.
- (36) Bravo, J.; Castro, J. A.; Freijanes, E.; García-Fontán, S.; Lamas, E. M.; Rodríguez-Seoane, P. Z. *Anorg. Allg. Chem.* **2005**, *631*, 2067.
- (37) Ault, B. S.; Becker, T. M.; Li, G. Q.; Orchin, M. *Spectrochim. Acta, Part A* **2004**, *60*, 2567.
- (38) Simpson, P. V.; Skelton, B. W.; Raiteri, P.; Massi, M. *New J. Chem.* **2016**, *40*, 5797.
- (39) Bauer, J. A. K.; Becker, T. M.; Orchin, M. *J. Chem. Crystallogr.* **2004**, *34*, 843.
- (40) Totobenazara, J.; Burke, A. J. *Tetrahedron Lett.* **2015**, *56*, 2853.
- (41) Wang, C.; Ikhlef, D.; Kahlal, S.; Saillard, J.-Y.; Astruc, D. *Coord. Chem. Rev.* **2016**, *316*, 1.
- (42) Fehllhammer, W. P.; Beck, W. Z. *Anorg. Allg. Chem.* **2015**, *641*, 1599.
- (43) Astruc, D.; Liang, L.; Rapakousiou, A.; Ruiz, J. *Acc. Chem. Res.* **2012**, *45*, 640.
- (44) Arseneault, M.; Wafer, C.; Morin, J. F. *Molecules* **2015**, *20*, 9263.
- (45) Reck, F.; Zhou, F.; Girardot, M.; Kern, G.; Eyermann, C. J.; Hales, N. J.; Ramsay, R. R.; Gravestock, M. B. *J. Med. Chem.* **2005**, *48*, 499.
- (46) Tron, G. C.; Pirali, T.; Billington, R. A.; Canonico, P. L.; Sorba, G.; Genazzani, A. A. *Med. Res. Rev.* **2008**, *28*, 278.
- (47) Hein, C. D.; Liu, X. M.; Wang, D. *Pharm. Res.* **2008**, *25*, 2216.
- (48) Thirumurugan, P.; Matosiuk, D.; Jozwiak, K. *Chem. Rev.* **2013**, *113*.
- (49) Tuci, G.; Rossin, A.; Xu, X.; Ranocchiaro, M.; van Bokhoven, J. A.; Luconi, L.; Manet, I.; Melucci, M.; Giambastiani, G. *Chem. Mat.* **2013**, *25*, 2297.
- (50) Jiang, H.-L.; Feng, D.; Liu, T.-F.; Li, J.-R.; Zhou, H.-C. *J. Am. Chem. Soc.* **2012**, *134*, 14690.
- (51) Goto, Y.; Sato, H.; Shinkai, S.; Sada, K. *J. Am. Chem. Soc.* **2008**, *130*, 14354.
- (52) Ko, T.; Kim, K.; Jung, B.-K.; Cha, S.-H.; Kim, S.-K.; Lee, J.-C. *Macromolecules* **2015**, *48*, 1104.
- (53) Yigit, S.; Sanyal, R.; Sanyal, A. *Chem. Asian J.* **2011**, *6*, 2648.
- (54) Juan-Alcaniz, J.; Ferrando-Soria, J.; Luz, I.; Serra-Crespo, P.; Skupien, E.; Santos, V. P.; Pardo, E.; F.X, L. i. X.; Kapteijn, F.; Gascon, J. J. *Catal.* **2013**, *307*, 295.
- (55) Luz, I.; Llabres i Xamena, F. X.; Corma, A. *J. Catal.* **2010**, *276*, 134.
- (56) Chassaing, S.; Sani Souna Sido, A.; Alix, A.; Kumarraja, M.; Pale, P.; Sommer, J. *Chem. Eur. J.* **2008**, *14*, 6713.

- (57) Chao-Wan, C.; Gene-Hsiang, L. *Organometallics* **2003**, *22*, 3107.
- (58) Singh, K. S.; Kreisel, K. A.; Yap, G. P. A.; Kollipara, M. R. *J. Organomet. Chem.* **2006**, *691*, 3509.
- (59) Knott, S. A.; Templeton, J. N.; Durham, J. L.; Howard, A. M.; McDonald, R.; Szczepura, L. F. *Dalt. Trans.* **2013**, *42*, 8132.
- (60) Kemmerich, T.; Nelson, J.; Takach, N.; Boehme, H.; Jablonski, B.; Beck, W. *Inorg. Chem.* **1982**, *21*, 1226.
- (61) Chen, C.-K.; Tong, H.-C.; Hsu Chen, C.-Y.; Lee, C.-Y.; Fong, Y. H.; Chuang, Y.-S.; Lo, Y.-H.; Lin, Y.-C.; Wang, Y. *Organometallics* **2009**, *28*, 3358.
- (62) Bloch, W. M.; Doonan, C. J.; Sumbly, C. J. *CrystEngComm* **2013**, *15*, 9663.
- (63) Potapov, A. S.; Khlebnikov, A. I. *Polyhedron* **2006**, *25*, 2683.
- (64) Wilbur, J. M.; Bonner, B. A. *J. Polym. Sci., Part A: Polym. Chem.* **1990**, *28*, 3747.
- (65) McPhillips, T.; McPhillips, S.; Chiu, H.; Cohen, A. E.; Deacon, A. M.; Ellis, P. J.; Garman, E.; Gonzalez, A.; Sauter, N. K.; Phizackerley, R. P., *et al.* *J. Synchrotron Rad.* **2002**, *9*, 401.
- (66) Sheldrick, G. M. *Acta Crystallogr. C Struct. Chem.* **2015**, *71*, 3.
- (67) *Gaussian 09, revision D.01*; Frisch, M. J.; Trucks, G. W.; Schlegel, H. B.; Scuseria, G. E.; Robb, M. A.; Cheeseman, J. R.; Scalmani, G.; Barone, V.; Petersson, G. A.; Nakatsuji, H., *et al.*, Gaussian Inc.: Wallingford CT, 2013;
- (68) Zhao, Y.; Truhlar, D. G. *Theor. Chem. Acc.* **2008**, *120*, 215.
- (69) Andrae, D.; Häußermann, U.; Dolg, M.; Stoll, H.; Preuß, H. *Theor. Chim. Acta* **1990**, *77*, 123.
- (70) *Ab Initio Molecular Orbital Theory*; Hehre, W. J. R., L; Schleyer, P.V.R; Pople, J.A; , Wiley: New York, 1986; 1st ed.
- (71) Marenich, A. V.; Cramer, C. J.; Truhlar, D. G. *J. Phys. Chem. B* **2009**, *113*, 6378.
- (72) Spek, A. L. *Acta Crystallogr D Biol Crystallogr* **2009**, *65*, 148.

Chapter 5: Photochemistry of $1 \cdot [\text{Mn}(\text{CO})_3\text{Br}]$

5.1 Introduction

Transition metal centres bearing vacant coordination sites have seen enduring interest due to their ability to selectively activate small molecules.¹⁻³ A reliable method for producing such species is the photolysis of metal complexes bearing photolabile ligands such as carbon monoxide and dihydrides.⁴⁻⁵ The resulting vacant coordination site(s) formed via photolysis have been implicated in small molecule activation and C-H conversion, a process of intense commercial interest in chemistry. The conversion of abundant but chemically inert alkanes such as methane into valuable commodities such as methanol is a potentially lucrative industry, however the inert nature of C-H bonds necessitates the use of harsh conditions to achieve useful chemical conversions. Typically, alkanes are converted into unsaturated hydrocarbons via energy intensive dehydrogenation, these are subsequently used as feedstock for the production of more valuable commodities such as alcohols, aldehydes and ketones.² Thus, existing routes for the production of valuable chemicals from alkanes are expensive, indirect and energy intensive. As will be discussed, coordinatively unsaturated metal centres have been implicated in facile C-H bond activation (and activation of other X-H bonds X= Si, B, H) and may therefore enable selective, direct conversion of alkanes into valuable chemicals. To take full advantage of these materials the active species must be structurally characterised so that their reactivity can be tailored and fully exploited.

To date, the coordinatively unsaturated metal complexes and the intermediate σ -alkane complexes involved in small molecule activation have been identified and characterised using ultrafast IR spectroscopy.⁶⁻¹⁰ Recently, the coordinatively unsaturated photoproduct $[\text{Mn}(\text{CO})_2\text{Cp}']$ ¹¹ and various σ -alkane complexes¹²⁻¹⁴ were characterised using X-ray crystallography following their in-situ formation within single crystals. MOFs are an ideal medium with which to expand this field, offering a robust, crystalline matrix in which to isolate and study reactive metal complexes generated via photolysis. Other solid supports such as alumina and zeolites have been employed for the isolation of coordinatively unsaturated metal complexes and set a promising precedent for emerging porous media.¹⁵⁻¹⁹ The advantage of MOFs is their crystallinity, which confers greater capacity for insights into the structures and mechanisms behind the reactivity of transition metal complexes. Such insights can inform the development of future systems with improved selectivity and activity.

The goal of the project described in this Chapter is to incorporate a metal carbonyl precursor complex within **1** and employ the site isolation induced by the MOF to trap and harness reactive complexes formed by UV or visible photolysis (Figure 5.1.1). The robust crystallinity of **1** has allowed the products of sequential chemical processes to be studied using crystallography,²⁰⁻²² giving precedent to the goal of studying small molecule activation at tethered transition metal complexes. Since the photochemistry of metal carbonyl complexes is a diverse field that is quite distinct from the topics that have been discussed so far, a comprehensive introduction is presented here. For reasons that will be explained, **1**·[Mn(CO)₃Br] (presented in Chapter 4) has been the focus of the photochemistry work conducted in this project, therefore the ensuing survey of key literature will largely focus on Mn(I) derivatives and is divided into the following key subjects:

- i. The importance of MLCT processes in the photochemistry of Mn(I) complexes
- ii. The incorporation of metal carbonyl complexes in MOFs
- iii. The reactivity of coordinatively unsaturated Mn(I) complexes formed via photolysis, particularly [CpMn(CO)₃] and [TpMn(CO)₃] derivatives.
- iv. Coordinatively unsaturated complexes and the activation of small molecules

Photolysis of Site-isolated Metal Carbonyl inside MOF

Small Molecule Activation

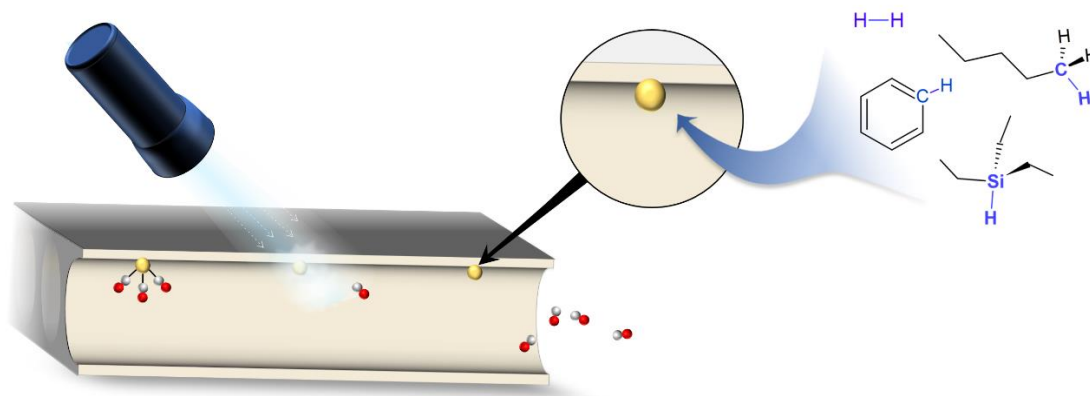


Figure 5.1.1: Schematic depicting the formation of reactive metal complexes within a porous MOF via photolysis. Site-isolation stabilises the highly reactive complexes so that they can be harnessed in the activation of small molecules. The crystallinity of the MOF provides an opportunity to study the photoproduct and its reactivity via X-ray crystallography.

5.1.2 Metal Carbonyl Complexes

Metal carbonyls consist of carbon monoxide ligand(s) bound to low valent (electron rich) transition metal centres²³⁻²⁴ and have been known since 1868 when Schutzenberger prepared $[\text{Pt}(\text{Cl})_2\text{CO}]_2$ and $[\text{Pt}(\text{Cl})_2(\text{CO})_2]$.²⁵ The M-CO bond consists of both a σ -bond contribution in which the CO donates electron density to the metal centre, and π -backdonation in which the metal strengthens the M-CO bond by donating electron density into the π^* -CO orbital (Figure 5.1.2.1). The resulting interaction is extremely robust and produces a strong ligand-field splitting-energy. The backdonation of electron density into the CO antibonding orbital strengthens the metal-ligand bond while weakening the $\text{C}\equiv\text{O}$ bond. As a result, the CO vibrational bands observed via IR spectroscopy are shifted to lower wavenumbers relative to free CO (2140 cm^{-1}), providing a convenient spectroscopic probe. IR spectroscopy has allowed chemical processes that take place at metal carbonyl complexes to be studied at the pico-second time-scale, revealing intricate mechanistic details.

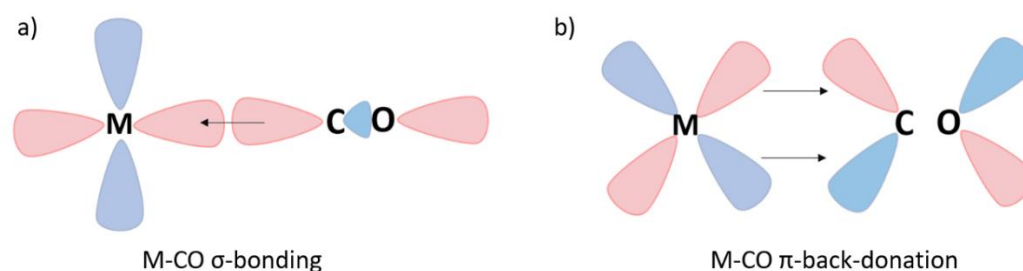


Figure 5.1.2.1: Bonding between a metal and CO ligand involves the formation a σ -bond **a)** as well as backdonation of electron density from the metal centre into the π^* -CO orbital **b)**.

Many metal carbonyl complexes possess interesting photochemical properties, including the loss of their CO ligand(s) upon irradiation with light.²⁶ In most cases, photolysis is only observed under UV irradiation. However, Mn(I) carbonyl complexes can be sensitised to both UV and visible light, typically possess a good quantum yield and are economically favourable due to the abundance of Mn on earth. It is envisaged that the photo-release of CO from **1**· $[\text{Mn}(\text{CO})_3\text{Br}]$ could produce site-isolated coordinatively unsaturated Mn(I) complexes that parallel the reactivity of noble metal complexes containing Rh or Ir.²⁷ With these considerations, attention has been placed on the photochemistry of **1**· $[\text{Mn}(\text{CO})_3\text{Br}]$ while investigations into the photochemistry of Rh(I), Ir(I) and Re(I) derivatives, which require extensive UV photolysis, are also ongoing.

5.1.3 MLCT Processes and the effect of ligand chemistry on Mn(I) carbonyl complexes

Although the photochemistry of Mn(I) carbonyl complexes has been studied since the 1960s, their potential application in the controlled delivery of CO in medicinal applications²⁸ and in the catalytic reduction of CO₂²⁹⁻³³ has prompted a surge in interest. The former topic has spurred the field of 'Photo-releasing Carbon Monoxide Releasing Molecules' (PhotoCORMs), which aims to develop metal carbonyl complexes to deliver controlled doses of CO within the human body.^{28, 34-36} Due to the requirement for non-toxic and visible/near IR photo-sensitive complexes for this application, much of the published research has focused on manganese carbonyl complexes supported by ligands designed to facilitate CO loss under low energy irradiation.³⁵ These complexes are typically brightly coloured due to the presence of a strong Metal to Ligand Charge-transfer (MLCT) band in the visible spectrum. The absorption of light in the MLCT band results in the movement of electron density from a metal centred HOMO orbital to a LUMO orbital which is typically centred on the organic ligand.³⁷ The HOMO orbital includes significant Mn-CO bonding character and the movement of electron density from this orbital to the ligand centred LUMO results in loss of electron density between the Mn and CO, promoting dissociation of CO from the metal centre. Mn(I) tricarbonyl complexes bearing a similar conjugated N-donor/halide motif to $1\cdot[\text{Mn}(\text{CO})_3\text{Br}]$ are particularly well represented in the optically active photoCORMs.

The relative energies of the HOMO and LUMO orbitals dictates the energy of the MLCT band and consequent wavelength required to initiate CO loss. For medicinal applications it is important to red-shift the MLCT transition deep into the visible spectrum, preferably into the near IR, to promote better tissue penetration and preclude the use of damaging UV radiation. This is also beneficial for MOF based small molecule activation in order to improve penetration through the host frameworks which typically contain UV-absorbing aromatic groups such as phenylcarboxylates. By manipulating the coordination sphere of the Mn(I) complex the energy of the HOMO and LUMO can be tuned to affect the required redshift. Typically, a highly conjugated organic ligand is employed to stabilise the LUMO while strong σ -donor ligands simultaneously destabilise the HOMO. The effect is a shift of the MLCT band to lower energy which can be observed via UV-Vis spectroscopy and supported by DFT calculations.

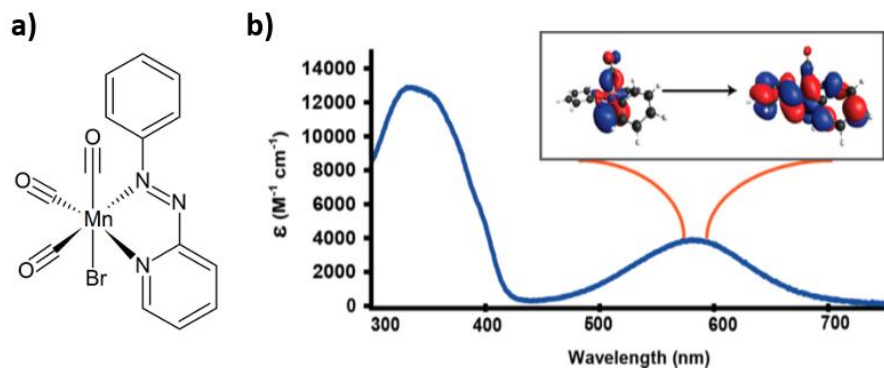


Figure 5.1.3.1: A recently developed photoCORM based on the Mn(I) tricarbonyl bromide motif with a conjugated N-donor ligand. The complex displays a strong MLCT band in the visible spectrum which corresponds to movement of electron density from a HOMO involved in M-CO bonding to a LUMO centred on the conjugated ligand which does not contribute to M-CO bonding. Figure adapted from Chakraborty *et al.*³⁸

Exemplifying this approach, Chakraborty *et al.* designed a series of Mn(I), Re(I) and Ru photoCORMs in which the coordination sphere of the respective metal centre was systematically varied.³⁸ The effect on the HOMO-LUMO gap was determined via UV-Vis spectroscopy and corroborated with DFT calculations. The Mn(I) complexes [Mn(pmtpm)(CO)₃Br], [Mn(qmtpm)(CO)₃Br], [Mn(pmtpm)(CO)₃(MeCN)]ClO₄ and [Mn(pimq)(CO)₃(MeCN)]ClO₄ (See Figure 5.1.3.2 for definitions of pmtpm, qmtpm and pimq) possessed MLCT bands centred at λ_{max} : 500, 535, 390 and 435 nm respectively. The variation in λ_{max} reflects the effect of the N-donor and auxiliary ligands on the energy of the frontier orbitals responsible for the MLCT transition. DFT calculations revealed that the MLCT transition responsible for CO loss involves movement of electron density from the HOMO-2 (significant Mn-CO bonding) to the LUMO (imine and pyridine/quinoline π^* orbitals) (Figure 5.1.3.2), which weakens the Mn-CO bond. The extended conjugation in the N-donor ligand qmtpm stabilises the LUMO orbital while the presence of predominantly σ -donor Br⁻ destabilises the HOMO orbitals, thereby decreasing the HOMO-2/LUMO gap and causing a redshift in the MLCT band. Conversely, the presence of MeCN, a moderate π -acceptor; stabilises the HOMO-2 and thereby blueshifts the MLCT band. Consequently, the bromide complex [Mn(qmtpm)(CO)₃Br] exhibits faster CO loss under visible irradiation than the MeCN analogue.

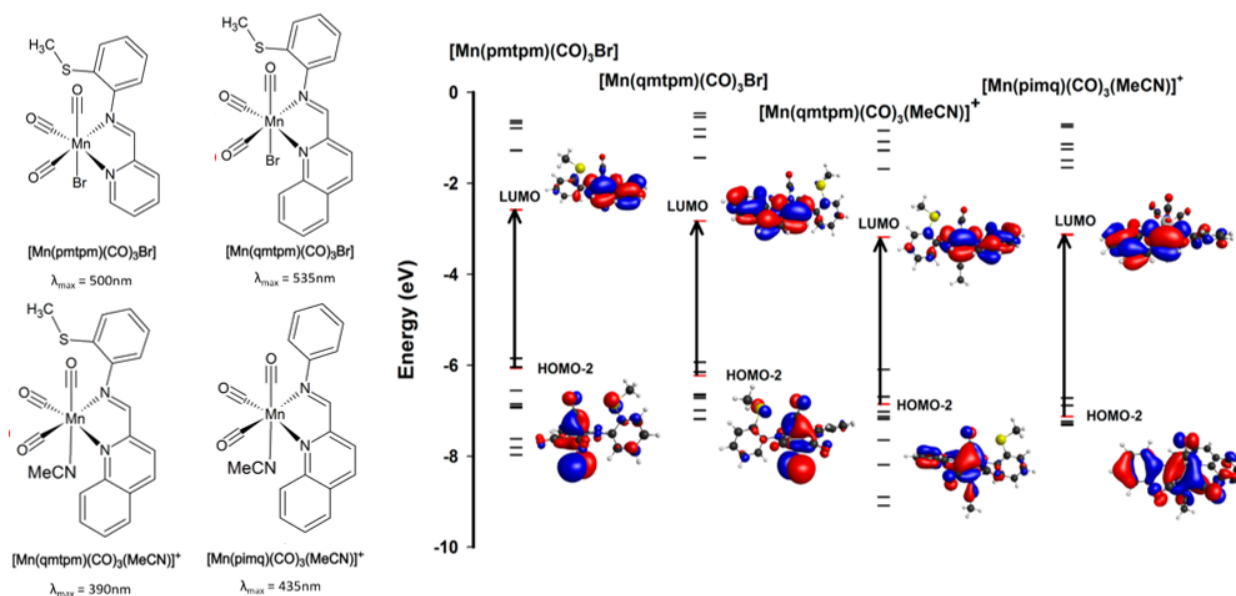


Figure 5.1.3.2: The Mn(I) diimine complexes prepared by Chakraborty *et al.* and the frontier orbitals associated with CO loss for each complex, displaying the effect of conjugation on the position of the LUMO and the ability of Br^- to destabilise the HOMO-2, thereby red-shifting the MLCT band. Pmtpm = 2-pyridyl-N-(2'-methylthiophenyl)methylenimine, qmtpm = 2-quinoline-N-(2'-methylthiophenyl)-methylenimine and pimq = 2-(phenyliminomethyl)quinoline. Figure adapted from Chakraborty *et al.*³⁸

Based on over a decade of research, the systematic engineering of the HOMO-LUMO gap has successfully produced photoCORMs that respond to near-IR light (810 nm)³⁹ and release CO in the solid state under low intensity visible irradiation.⁴⁰ The latter accomplishment is notable because most photoCORMs do not release CO in the solid state due to the close-packed environment. However, the presence of a MLCT band in the visible spectrum does not guarantee that a complex will release CO under visible irradiation. For instance, both Mn(I) and Re(I) complexes based on the azo-imine ligand 1-phenylazopyridine (azpy) possess a MLCT band in the visible spectrum.⁴¹ The MLCT band for the Re(I) complex ($\lambda_{\text{max}} = 540\text{ nm}$) corresponds to the HOMO-1/LUMO transition but does not evoke CO loss. However, UV irradiation corresponding to the HOMO-1 \rightarrow LUMO+1/LUMO+2 transition prompted CO loss due to the transfer of electron density to the LUMO+2 which contains a strong $\pi^*(\text{Re-CO})$ contribution. Absorption by the MLCT only contributes to CO labilisation for the Mn(I) complex because the heavier Re(I) complex is more likely to undergo spin-orbit coupling which allows the complex to dissipate the energy absorbed via non-radiative decay processes that do not contribute to CO loss.⁴¹ For this reason, Re(I) complexes typically do not undergo the facile CO loss observed in equivalent Mn(I) complexes, even when strong MLCT bands exist in the visible region.

Considering the insights from photoCORM research, the carbonyl complex in **1**·[Mn(CO)₃Br] is a promising candidate for photolysis due to the presence of a conjugated N,N'-chelating ligand and σ -donor bromide anion. The coordination motif should respond to visible light induced photolysis, thereby mitigating damage to the material from UV radiation while providing optimal penetration through the optically transparent MOF crystals.

5.1.4 *The Role of Oxidation in CO loss from Mn(I) complexes*

Clearly, absorption of light into the MLCT band plays an important role in the photochemistry of Mn(I) carbonyl complexes, particularly those that respond to visible light and have been recruited as photoCORMs. Other metal carbonyls and Mn(I) carbonyls such as [MnCp(CO)₃] derivatives undergo CO loss only under UV irradiation which typically involves excitation into Ligand Field (LF) states that are strongly dissociative. In some cases, excitation into a MLCT band can allow the complex to access low lying LF states that are dissociative. The interplay between MLCT and LF states and their role in CO loss is complex and varies between complexes.

Another important factor in CO labilisation is oxidation of the metal centre. Low oxidation state metal centres have more electron density with which to contribute towards π -backdonation with CO. When one strongly π -accepting CO ligand is removed via photolysis, the metal centre is consigned with more electron density which renders it more prone to oxidation.⁴² Therefore, di- or monocarbonyl complexes are more sensitive to oxidation which in-turn reduces the electron density of the metal centre and therefore weakens the remaining M-CO bond(s). Several recent reports have suggested that photolysis of photoCORMs only leads to loss of one CO ligand, after which the complex undergoes oxidation and facile loss of the remaining CO ligands.^{35, 43-45} This is an important consideration for **1**·[Mn(CO)₃Br]; if complete CO loss is only possible in conjunction with oxidation, it will be difficult to isolate the desired electron rich, coordinatively unsaturated Mn(I) complex that can participate in small-molecule activation.

One such study involved the UV photolysis of [TpmMn(CO)₃]PF₆ in aqueous buffer, ethanol and ethanol/water mixtures which produced stepwise loss of CO. The complex initially loses one CO ligand to produce a dicarbonyl complex which undergoes oxidation and concomitant release of the remaining CO ligands. IR spectroscopy of the solution revealed complete CO loss, with new Mn(II) and Mn(III)

complexes detected via EPR spectroscopy.³⁵ However, Sachs *et al* reported that the photolysis of $[\text{TpmMn}(\text{CO})_3]\text{PF}_6$ (Tpm = tris(pyrazolyl)methane) in strongly coordinating acetonitrile (as opposed to EtOH/water) initially produces a population of the relatively stable dicarbonyl $[\text{TpmMn}(\text{CO})_2(\text{MeCN})]\text{PF}_6$ (Figure 5.1.4.1).⁴² Under further photolysis the dicarbonyl complex continues to release CO in acetonitrile, however, in the presence of water the photorelease of CO is accompanied by oxidation of the metal centre. Thus, it appears that complete release of CO can be achieved through photolysis in the presence of a strongly coordinating solvent (or absence of water) *or* via concomitant oxidation of the metal centre. The oxidation of the metal centre is therefore relevant in photoCORM research where photolysis is often performed in aqueous buffer to replicate a physiological environment. In a carefully administered anhydrous system it is unlikely that oxidation of the metal centre is required to release CO, which is supported by numerous examples in which up to three CO ligands are exchanged from $[\text{CpMn}(\text{CO})_3]^{46-51}$ or $[\text{TpMn}(\text{CO})_3]$ (Tp = hydridotris(pyrazolyl)borate)⁵² complexes under photolysis without oxidation of the metal centre (Section 5.1.6). The isolated nature of the Mn(I) complexes in $1 \cdot [\text{Mn}(\text{CO})_3\text{Br}]$ and use of anaerobic conditions should inhibit oxidation of the metal centre and preserve the electron-rich Mn(I) photoproduct.

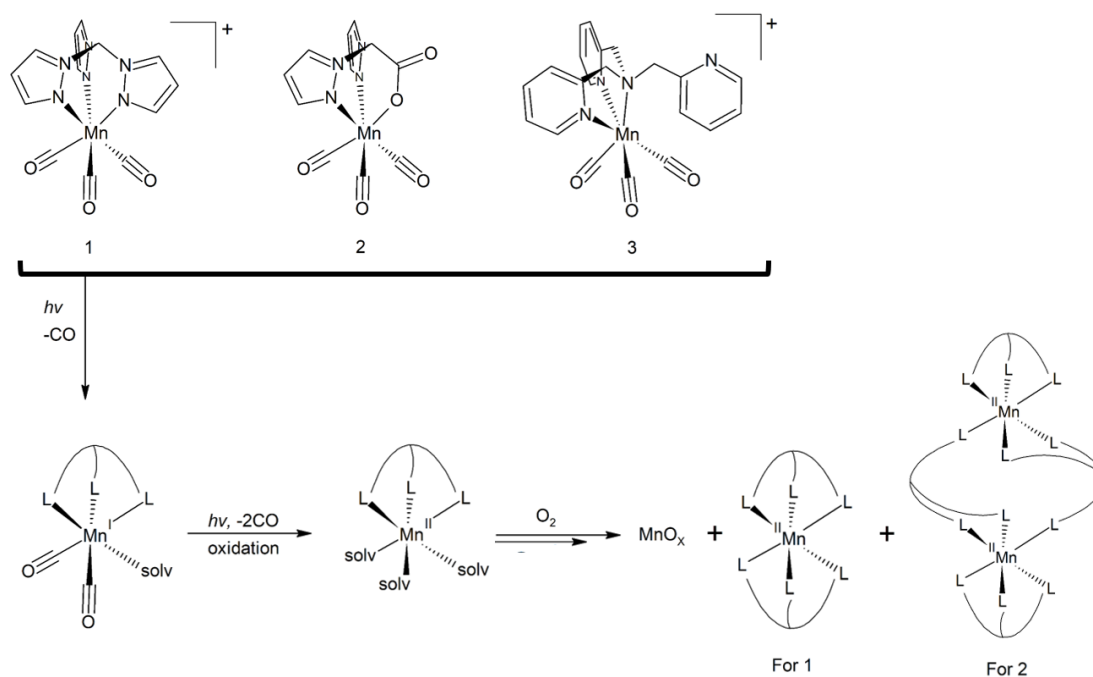


Figure 5.1.4.1: The Mn(I) tricarbonyl complexes bearing tridentate ligands (Tpm, bis(pyrazolyl)acetate and p Tris(2-pyridylmethyl)amine for 1,2 and 3 respectively) prepared by Sachs *et al*. undergo UV photolysis to form dicarbonyl complexes and eventually lose their CO ligands entirely either through photolysis or oxidation in the presence of water or O_2 . The final products are oxidised manganese complexes. Figure adapted from Sachs *et al*. ref. 42.

5.1.5 Metal Carbonyl Complexes in MOFs

Metal carbonyl complexes have been incorporated into MOFs via both post-synthetic metalation and direct synthesis with pre-metallated ligands.⁵³⁻⁶¹ Several early examples involve η^6 -arene complexes of Mo(0) and Cr(0) tricarbonyls which are formed via post-synthetic metalation of MOF linkers with the respective hexacarbonyls.^{53, 60-63} Afzali *et al.* reacted UiO-66 with $[\text{Mo}(\text{CO})_6]$ in refluxing methanol to give UiO-66- η^6 - $[\text{Mo}(\text{CO})_3]$ which was employed in the epoxidation of alkenes and oxidation of sulfides.⁵³ Diverging from the η^6 -arene motif, Long *et al.* reported the post-synthetic metalation of a Zr(IV) based framework (UiO-67-bpy) featuring free bipyridine N,N-chelation sites with a range of transition metal complexes in 2015.⁶⁴ The gas phase reaction between the activated MOF and $\text{Cr}(\text{CO})_6$ vapour produced the corresponding N,N-chelated Cr(0) tricarbonyl complex which was characterised via X-ray crystallography. Similarly, N,N-chelated Mn(I) and Re(I) complexes have been incorporated within MOFs for the photocatalytic reduction of CO_2 ^{55, 65} motivated by the success of analogous molecular complexes.²⁹⁻³³

Recently, MOFs have been posited as solid-state photoCORMs which can negate the shortcomings of conventional photoCORMs such as poor solubility in physiological media^{44, 66} and failure to release CO in the solid state (An exception is described above⁴⁰). Two separate studies have focused on encapsulating $[\text{Mn}(\text{tacn})(\text{CO})_3]\text{Br}$ (tacn = 1,4,7-triazacyclononane)⁶⁷ and $[\text{Mo}(\text{CNCMe}_2\text{CO}_2\text{H})_3(\text{CO})_3]$ ⁶⁸ carbonyl complexes within MOFs as CO releasing therapeutics. Furthermore, Furukawa *et al.* exploited UiO-67-bpy as a solid-state photoCORM by post-synthetically metalating the bipyridine chelation sites with $[\text{Mn}(\text{CO})_5\text{Br}]$ (Figure 5.1.5.1a).⁶⁹ UiO-67-bpy samples comprised of crystals with mean sizes of 260 nm \pm 80 nm and 1200 nm \pm 180 nm were metallated and subjected to photolysis with 460 nm light which corresponds to the observed MLCT band. From IR spectroscopy (Figure 5.1.5.1b) and in-situ monitoring of the CO gas released, the largest crystals were found to release 1.94 CO molecules per Mn(I) site while the smallest crystals released 2.52 CO molecules per site, corresponding to efficiencies of 65 and 85%. The lower efficiency of the largest crystals was attributed to poor penetration of light into the core of the crystals.

In 2008, Kaye *et al.* reported the first instance in which the photochemistry of a MOF-bound metal carbonyl complex and the site-isolation imposed by the framework were synergistically harnessed. The post-synthetic metalation of a 1,4-benzenedicarboxylate based MOF (MOF-5) with $\text{Cr}(\text{CO})_6$ produces isolated arene-chromium tricarbonyl complexes (Figure 5.1.5.2).⁶⁰ Under UV-photolysis the Cr(0)

complex loses a CO ligand to form a coordinatively unsaturated dicarbonyl complex which is stabilised by site-isolation within the crystalline matrix. Both N_2 and H_2 can pass through the material and coordinate to the vacant coordination site. These results parallel those obtained using other porous supports to isolate coordinatively unsaturated metal complexes,^{15, 18-19} validating the role of MOFs in the study of key photoproducts.

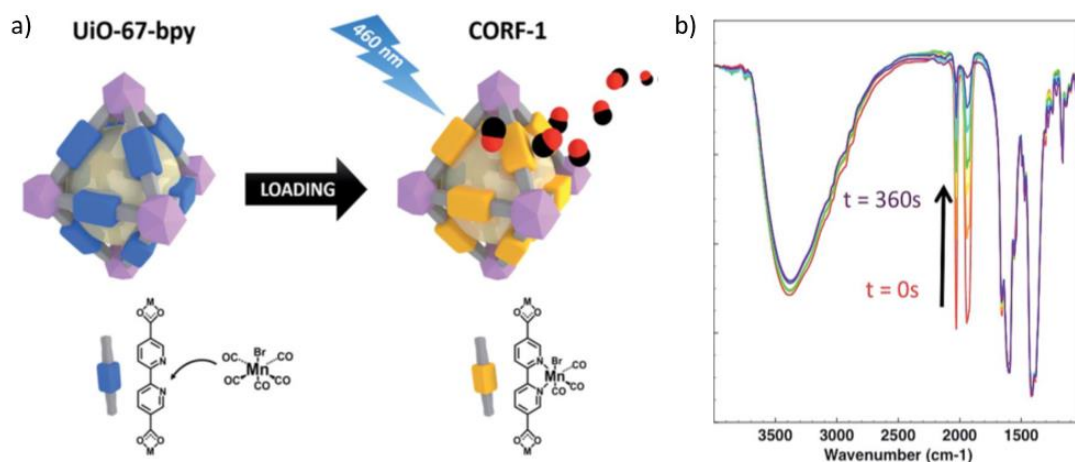


Figure 5.1.5.1: a) Post Synthetic Metalation of a bipyridine-dicarboxylate derivative of UiO-67 with $Mn(CO)_5Br$ to afford the corresponding tricarbonyl bromide complex which readily releases CO gas when irradiated with 460 nm light, as observed via IR spectroscopy b). Figure adapted from ref. 69

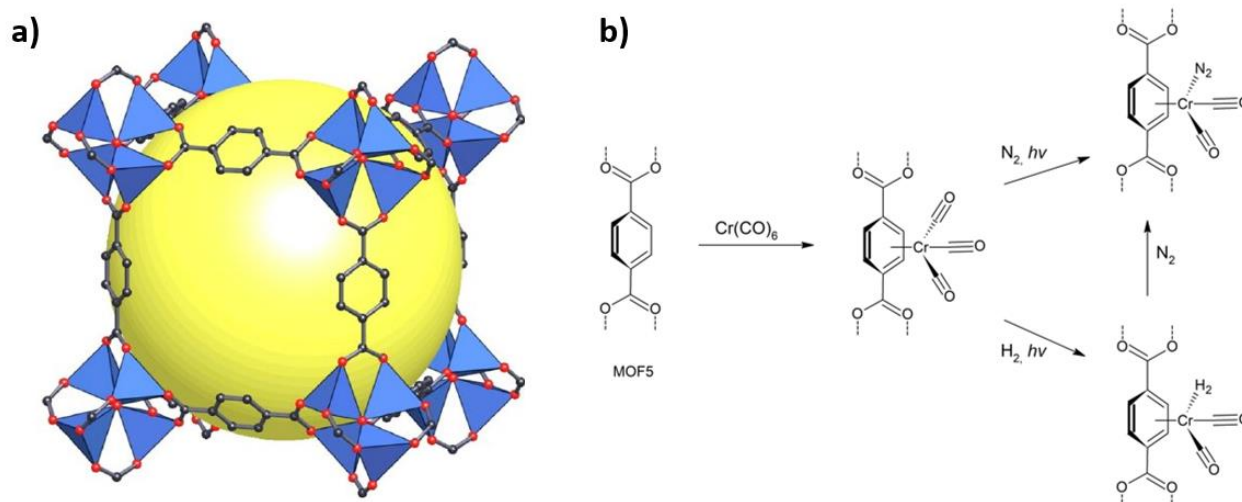


Figure 5.1.5.2: a) MOF-5 composed of benzene dicarboxylate linkers and Zn(II) nodes, undergoes post-synthetic metalation b) of MOF-5 with $Cr(CO)_6$ to produce an η^6 -arene-chromium tricarbonyl complex. Under UV-photolysis the complex loses a CO ligand which is replaced with N_2 or H_2 . Figure adapted from ref. 60

One of the most eminent examples of MOF-based photochemistry are the photocrystallography experiments on MOF bound manganese and rhenium tricarbonyl halide complexes⁵⁶⁻⁵⁹ reported by the Champness group. The MOF developed for these experiments was prepared from the pre-metallated ligand *fac*-[(2,2'-bipyridine-4,4'-dicarboxylate)M(CO)₃X] (M = Mn, X = Cl, Br; M = Re; X = Cl) which was reacted with MnCl₂ or Mn(acetate)₂ to give a 3D, non-porous material (Figure 5.1.5.3a). Both the Re(I) and Mn(I) complexes were determined to exist in a facial geometry via SCXRD. The photochemistry of molecular diimine complexes under both UV and visible irradiation in solution has been studied extensively using ultrafast spectroscopy and DFT calculations to probe the evolution of the coordinatively unsaturated complex that forms upon photolysis.⁷⁰⁻⁷³ The spectroscopy studies have previously revealed that UV or visible photolysis initially labilises an equatorial CO, producing a vacant site that becomes occupied by the migrating chloride anion on the pico-second time-scale. The resulting vacant axial site is temporarily occupied by a solvent molecule until the ejected CO recombines with the metal centre, thereby generating the *mer*-isomer. The photochemistry of the *mer*-isomer is dominated by homolysis of the Mn-Br bond to form a 16e⁻ radical which leads to the formation (in solution) of the dimer [Mn₂(CO)₆(bpy)₂].^{70, 72} The initial loss of CO from the *fac*-isomer is typically attributed to absorption into the MLCT band and transition into a low-lying Ligand Field (LF) state which is highly dissociative for the Mn-CO bond.

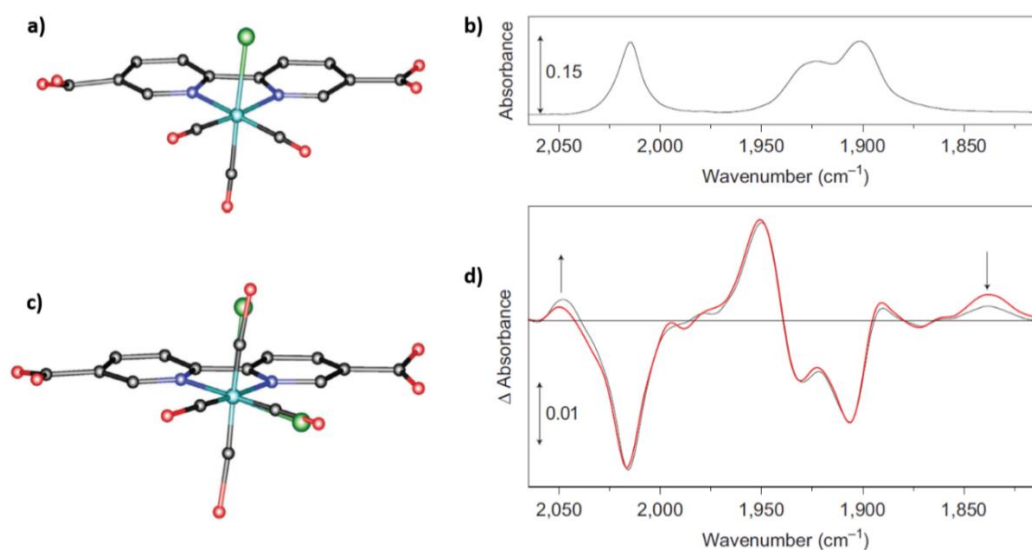


Figure 5.1.5.3: a) The [Mn(4,4'-dicarboxy-2,2'-bipyridine)(CO)₃Cl] within the Mn(II) based MOF reported by Champness *et al.* produces the characteristic IR spectrum b) which changes after 10 seconds of UV irradiation (d, red line) to give the dicarbonyl complex which subsequently decays to the *mer*-isomer (black curve) after 45 seconds of UV irradiation. The *fac*- to *mer*- isomerism was observed via X-ray crystallography which clearly shows the disorder of the chloride anion over both the axial and equatorial positions after photolysis c). Figure from ref. 56.

By housing both the Re and Mn diimine complexes within a crystalline, non-porous MOF, Champness *et al.* successfully followed the UV-photolysis of the complex using ultrafast IR spectroscopy and X-ray crystallography supported by DFT calculations. UV Photolysis at 200 K produces DMF-solvated dicarbonyl products and photo-dissociated CO which remains trapped within the non-porous crystal. Upon warming to 250 K the free CO recombines with the metal centre to give the new *mer*-isomer or reform the original *fac*-isomer. The higher yield of *mer*-photoproduct obtained from the Mn(I) complex (25%) relative to the Re(I) derivative (10%) allowed the photo-isomerism to be discerned crystallographically (Figure 5.1.5.3c). The photochemical reaction takes place within the MOF without damaging the crystallinity of the framework because the Mn(I) complex does not contribute to the structural integrity of the material. This an advantage MOFs possess over discrete molecular systems; their porous, interconnected structure allows metal complexes to undergo substantial rearrangements while preserving crystallinity. Subsequently, changes in the coordination sphere can be revealed by in-situ crystallography rather than requiring recrystallisation of the new complex.

In solution, diimine complexes also undergo photoisomerism and produce solvated dicarbonyl and monocarbonyl complexes that can be detected via IR spectroscopy. Yempally *et al.* investigated the UV photolysis of *fac*-[Mn(bpy)(CO)₃(X)] (X = CPh, Br) and observed that the photoproduct formed on the time-scale of the experiment depends on the solvent (coordinating or weakly coordinating) and X.⁷⁴ In MeCN, photolysis of [Mn(CO)₃(bpy)(Br)] leads to the charged complex [Mn(bpy)(CO)₂(MeCN)₂]Br while the phenylacetylide analogue undergoes *fac*- to *mer*-isomerism to give *mer*-[Mn(bpy)(CO)₃(CPh)]. Photolysis in the relatively weakly coordinating solvent THF, *fac*- to *mer*- isomerism is observed in both complexes with the transient THF complexes observed via IR spectroscopy (Table S7.5.1.1.). The substituted carbonyl complexes, particularly the mono-carbonyl derivatives are unstable have not been isolated.

This project aims to further develop the strategy pioneered by Champness *et al.* by conducting photolysis on Mn(I) complexes inside a porous MOF. This strategy should prevent the recombination of dissociated CO with the parent complex and allow CO-loss products, rather than *fac*-to-*mer* isomerism; to be directly observed using crystallography.

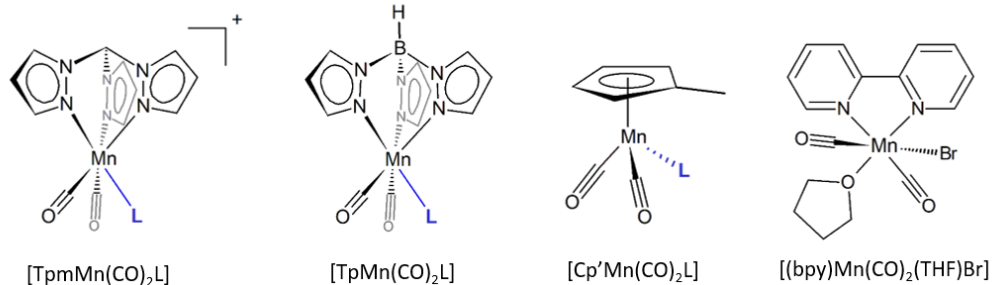
5.1.6 Mn(I) Coordinatively Unsaturated Complexes – Chemistry of $[\text{MnCp}(\text{CO})_3]$

The photolysis of manganese carbonyl complexes in solution has been an area of intense study since the 1960s, well before the emergence of therapeutic photoCORMs. Much of this early work focused on the photolysis of $[\text{MnCp}(\text{CO})_3]$ and the related methyl substituted derivative $[\text{MnCp}'(\text{CO})_3]$ ($\text{Cp}' =$ methylcyclopentadiene) due to the popularity of the latter as an anti-knock fuel additive. Under UV photolysis in solution, the coordinatively unsaturated species $[\text{MnCp}(\text{CO})_2]$ forms and rapidly combines with solvent to give $[\text{MnCp}(\text{CO})_2(\text{solv})]$.⁷⁵ The $[\text{CpMn}(\text{CO})_2]$ moiety is robust and resists further CO loss once photolysis ceases, however the 'solvent' is typically weakly coordinating and acts merely as a 'place-holder ligand' that is readily replaced. The most popular solvent choice is tetrahydrofuran (THF)⁷⁵ which is a weak, purely σ -donor ligand; although diethylether,⁷⁶ benzene and cyclohexane have also been employed for this purpose. Unusually, Strohmeier *et al.* used photolysis in methanol and methanol/water to prepare several substituted complexes.⁷⁷⁻⁷⁹ The solvent can be substituted with an immense variety of ligands (See Figure 5.1.6.1 for examples) including N_2 ,⁷⁵ alkynes,⁸⁰⁻⁸² alkenes,⁸⁰ formaldehyde⁸³ (formed from diethylether complex with Cp'), η^2 -arenes,⁸⁴⁻⁸⁵ pyridine,⁸⁶⁻⁸⁷ THF, alkenes⁸⁸ and phosphines^{50, 89-90} among others.^{50, 87, 91-92} Similar behaviour has been reported for the related η^5 -dimethylpyrrole (DMP) complexes $[\text{Mn}(\eta^5\text{-DMP})(\text{CO})_2\text{L}]$ formed under photolysis.⁹³ In some cases, the substituted complexes have been structurally characterised via X-ray crystallography,^{86, 94} although in most cases characterisation is limited to indirect techniques, particularly IR spectroscopy (Tables 7.5.1.1-5).

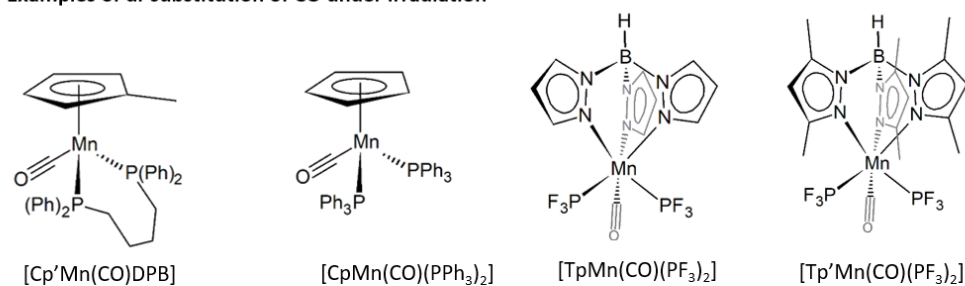
The dicarbonyl complex $[\text{MnCp}(\text{CO})_2\text{L}]$ is resistant to further CO loss without photolysis, even classic chelating ligands such as norbornadiene, diphosphines and bidentate N-donor ligands⁷⁸ (among others) adopt a monodentate coordination mode, sometimes bridging between two $\text{CpMn}(\text{CO})_2$ centres rather than displacing CO.⁹⁵ This stability arises from the exceptional π -acceptor quality of CO; the removal of one CO ligand provides the metal centre with more electron density with which to backdonate to the remaining CO ligands, strengthening these interactions. This effect is highlighted by the vinylidene complex $[\text{CpMn}(\text{CO})_2(\text{C}_2\text{HPh})]$ reported by Nesmeyanov *et al.* which displays unusually high CO stretching frequencies due to the strong π -acceptor ability of the vinylidene ligand. The presence of a competing π -acceptor ligand weakens the remaining Mn-CO bonds sufficiently that the complex reacts with PPh_3 to yield the corresponding monocarbonyl complex $[\text{CpMn}(\text{CO})(\text{PPh}_3)(\text{C}_2\text{HPh})]$.⁹⁶ Thus, it is evident that the

stability of dicarbonyl or monocarbonyl intermediates formed via photolysis is influenced by the electronic properties of the adjacent ligands.

Examples of mono-substitution of CO under irradiation



Examples of di-substitution of CO under irradiation



Examples of tri-substitution of CO under irradiation

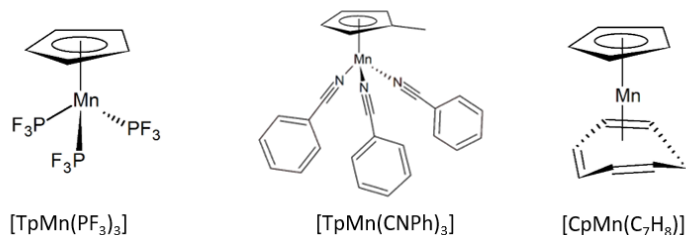


Figure 5.1.6.1: Examples of substitution reactions under photolysis for Mn(I) carbonyl complexes supported by various ligands including Tpm (tris(pyrazolyl)methane), Tp (hydridotris(pyrazolyl)borate), Tp' (hydridotris(3,5-dimethylpyrazolyl)borate), Cp, Cp', bpm (2,2'-bipyridine). Photolysis can lead to loss of one, two or three CO ligands. See text and Tables 7.5.1.1-5 for details.

Extensive UV photolysis in the presence of suitable ligand(s) can result in the additional loss of CO to give mono-carbonyl^{48-49, 97} complexes or eventually, complete removal of CO (Figure 5.1.6.1).^{46-47, 51, 98} Early reports detail the substitution of two CO ligands for one chelating polydentate phosphine^{95, 99} and arsine;^{48, 95} or two monodentate triphenylphosphine,^{50, 89} triphenylarsine,⁵⁰ triphenylantimonate⁵⁰ or dimethylsulfoxide¹⁰⁰ ligands. Beyond simple ligand exchange, photolysis can be used to produce catalytically active monocarbonyl complexes by photo-substitution of CO for non-innocent ligands. UV photolysis of [Cp'Mn(CO)₃] in the presence of free N-heterocyclic carbene (NHC) results in the formation

of the corresponding dicarbonyl complex $[\text{Cp}'\text{Mn}(\text{CO})_2\text{NHC}]$.¹⁰¹⁻¹⁰² These complexes undergo further CO loss under UV irradiation to yield the transient monocarbonyl species which can be stabilised by agostic interactions with the NHC substituents and characterised via TRIR spectroscopy. Zheng *et al.* reported that the $16e^-$ monocarbonyl photoproduct $[\text{CpMn}(\text{CO})\text{NHC}]$ (using Cp rather than Cp') readily catalyses the hydrosilation of ketones and aldehydes.¹⁰¹ Although the mechanism for this reaction has not been elucidated, the involvement of a photo-generated coordinatively unsaturated Mn(I) complex confirms that these species can be active in organic transformations and that the monocarbonyl complex is sufficiently stable (assisted by strong σ -donor NHC ligand) to function as a catalyst.

Direct photo-substitution of all three CO ligands in $[\text{CpMn}(\text{CO})_3]$ has been reported after extensive UV photolysis in the presence of phenylisocyanides,⁴⁶ PF_3 ,⁴⁷ CN^- ¹⁰³ and cycloctrienes (Table 5.1.6.1).^{51, 98} In a fascinating example, Merwin *et al.* reported the photochemical synthesis of the perfluoroalkylphosphine chelated complex $[\text{MnCp}(\text{CO})(\text{dfepe})]$ ($\text{dfepe} = (\text{C}_2\text{F}_5)_2\text{PCH}_2\text{CH}_2\text{P}-(\text{C}_2\text{F}_5)_2$) via photolysis of $[\text{CpMn}(\text{CO})_3]$.⁹⁹ This species underwent further photolysis under N_2 or H_2 purge to produce the corresponding nitrogen or hydrogen complexes $[\text{MnCp}(\text{N}_2)(\text{dfepe})]$ and $[\text{MnCp}(\text{H}_2)(\text{dfepe})]$. The intriguing properties of these species will be discussed in detail in Section 5.1.10 below.

Table 5.1.6.1: Compounds generated by complete substitution of CO under photolysis

Complex	Irradiation Time	Colour
$[\text{CpMn}(\text{Cyclohepta-1,3,5-triene})]$ ⁵¹	-	Red-black
$[\text{Cp}'\text{Mn}(\text{Cyclohepta-1,3,5-triene})]$ ⁹⁸		Red
$[\text{CpMn}(\text{Cyclooctatetraene})]$ ⁵¹		Red
$[\text{CpMn}(\text{Cycloocta-1,3,5-triene})]$ ⁵¹		Red
$[\text{Cp}'\text{Mn}(\text{Phenyl-cyclohepta-1,3,5-triene})]$ ⁵¹		Red
$[\text{CpMn}(\text{benzene})]$ ⁴⁷		Red
$[\text{CpMn}(\text{CH}_3\text{CN})_3]$ ⁴⁶	29hr (100W Hg lamp)	Yellow
$[\text{CpMn}(\text{p-ClC}_6\text{H}_4\text{CN})_3]$ ⁴⁶	96hr (100W Hg lamp)	Yellow
$[\text{CpMn}(\text{C}_6\text{H}_5\text{CN})_3]$ ⁴⁶	48hr (100W Hg lamp)	orange
$[\text{CpMn}(\text{C}_6\text{Cl}_5\text{CN})_3]$ ⁴⁶	27hr (100W Hg lamp)	Red
$[\text{CpMn}(\text{CO})(\text{PF}_3)_2]$ ⁴⁷	-	Yellow

5.1.7 Mn(I) Coordinatively Unsaturated Complexes – Chemistry of $[\text{MnTp}(\text{CO})_3]$

Beyond the prevalent cyclopentadiene derivatives, the photochemistry of Mn(I) carbonyl complexes bearing 'scorpionate' ligands developed in parallel. Early reports document the chemistry of hydridotris(pyrazolyl)borate based complexes^{52, 104} which have analogous properties to the N,N-chelation site in $1 \cdot [\text{Mn}(\text{CO})_3\text{Br}]$. The 3 and 5 positions of the pyrazoles can be substituted with methyl groups to produce the more sterically demanding derivative Tp' ($\text{Tp}' = \text{hydridotris}(3,5\text{-dimethylpyrazolyl})\text{borate}$). The neutral analogues, Tpm and Tpm' ($\text{Tpm} = \text{tris}(\text{pyrazolyl})\text{methane}$, $\text{Tpm}' = \text{tris}(3,5\text{-dimethylpyrazolyl})\text{methane}$), also form the respective complexes $[\text{Mn}(\text{Tpm})(\text{CO})_3]$ and $[\text{Mn}(\text{Tpm}')(\text{CO})_3]$.^{35, 42, 105} The relative electron donating ability of these ligands for Mn(I) complexes are $\text{Cp}' > \text{Cp} \approx \text{Tp}' > \text{Tp} > \text{Tpm}'$, which is reflected in the IR stretches of the corresponding complexes (Table 7.5.1.2-5).¹⁰⁵ The neutrality of the Tpm derivatives means that the metal centre possesses a positive charge and therefore backdonates less electron density to the CO ligands, increasing $\nu(\text{CO})$.¹⁰⁵

Since the early 1970s several reports have detailed the preparation and properties of $[\text{Mn}(\text{Tp})(\text{CO})_3]$ and $[\text{Mn}(\text{Tp}')(\text{CO})_3]$, including the photochemical substitution of one or two CO ligands for various phosphines and phosphites.^{52, 106-107} $[\text{MnTp}(\text{CO})_3]$ undergoes di-substitution with the small monodentate ligands PF_3 , $\text{P}(\text{OC}_6\text{H}_5)_3$ and $\text{P}(\text{OCH}_3)_3$ and mono-substitution with a range of larger phosphines and phosphites. The steric bulk of the larger Tp' ligand prevented di-substitution in all cases, with dicarbonyl complexes formed with less sterically encumbered (small cone-angle) ligands PF_3 , $\text{P}(\text{CH}_3)_3$, $\text{P}(\text{OCH}_3)_3$, $\text{P}(n\text{-C}_4\text{H}_9)_3$ and $\text{P}(\text{OC}_6\text{H}_5)_3$. Thus, it is evident that the steric profile of the supporting ligand influences the degree of photo-substitution.

Apart from steric considerations, the electronic properties of supporting ligand system influence the preferred coordination environment of metal centres following photolysis. The Cp ligand is particularly abiding in this respect due to its relatively small steric profile and its tendency to promote the formation of more diffuse MOs with which the incoming ligand can interact.¹⁰⁴ In this sense, Cp reduces the directionality of the orbitals and thereby facilitates the formation of complexes with less rigid octahedral geometry. Recently, Swennenhuis *et al.* investigated the effect of the Cp ligand on the ligand exchange chemistry of Mn(I) dicarbonyl photoproducts.¹⁰⁴ The Mn(I) complexes $[\text{Mn}(\text{Tp})(\text{CO})_3]$ ($\text{Tp} = \text{hydridotris}(\text{pyrazolyl})\text{borate}$) and $[\text{CpMn}(\text{CO})_3]$ were photolyzed in an alkane solution containing THF and cyclooctene. The formation of the corresponding THF or cyclooctene adducts was observed via time resolved IR spectroscopy. The photolysis of $[\text{Mn}(\text{Tp})(\text{CO})_3]$ in cyclohexane with THF and cyclooctene was

found to produce two new complexes which display IR stretches at 1960/1884 cm^{-1} and 1946/1851 cm^{-1} , these were assigned to $[\text{Mn}(\text{Tp})(\text{CO})_2(\text{cyclooctene})]$ and $[\text{Mn}(\text{Tp})(\text{CO})_2(\text{THF})]$. The $[\text{Mn}(\text{Tp})(\text{CO})_2(\text{cyclooctene})]$ complex is rapidly converted into the THF complex, while in the case of Cp the opposite reactivity is observed, with the cyclooctene complex strongly preferred. The lower stability of $[\text{Mn}(\text{Tp})(\text{CO})_2(\text{cyclooctene})]$ is attributed to the greater steric bulk of the Tp ligand and small size of THF relative to cyclooctene. Furthermore, Cp results in more diffuse electron density in the HOMO and LUMO orbitals of the related Re(I) complexes, which suggests that in the Mn species Cp would produce an orbital manifold with better overlap between the cyclooctene π^* and π orbitals. As a result, the Cp complex is better able to back-donate electron density to cyclooctene, producing a stronger bond.

Thus, the solution-based photo-chemistry of Mn(I) carbonyl complexes is dominated by solvation with weakly binding solvent, followed by ligand exchange chemistry. True coordinative unsaturation is not necessary to imbue metal complexes with desirable reactivity; for example, exchange of the place-holder ligand for small-molecules such as silanes can lead to the formation of a σ -complex and activation of the Si-H bond. This behaviour is promoted by the electron rich metal centre generated by photolysis of metal carbonyl complexes and will now be discussed in detail.

5.1.8 The effect of CO substitution on $\nu(\text{CO})$ and λ_{max}

IR spectroscopy is the preferred technique for tracking the evolution of carbonyl complexes, particularly over ultra-short time-scales. The substitution of CO for new ligand(s) influences both $\nu(\text{CO})$ and the colour of the compound. The IR stretching frequency of coordinated CO is always lower than that of free CO (2140 cm^{-1}) due to the backdonation of electron density from the metal into the $\pi^*(\text{CO})$ orbital, which weakens the CO bond. Thus, since CO is one of the strongest π -acceptor ligands available, the removal of one CO from a tricarbonyl complex results in a redshift of the stretching frequencies of the remaining CO ligands. The extent of this redshift is mediated by the electronic properties of the new ligand; an electron acceptor (e.g. SO_2 , PF_3) will blue-shift the stretching frequency while an electron donor will cause a redshift by providing more electron density for backdonation to CO. For dicarbonyl complexes, frequencies decrease (relative to the corresponding tricarbonyl complex) according to $\text{L} = \text{PF}_3 > \text{P}(\text{OC}_6\text{H}_5)_3 > \text{cyclooctene} \approx \text{P}(\text{OCH}_3)_3 > \text{PR}_3 > \text{pyridine}$ throughout the Cp, Tp and Tp' series. Monocarbonyl compounds typically produce carbonyl stretching frequencies slightly lower than their disubstituted equivalents (often between the symmetric and antisymmetric stretches of the

corresponding dicarbonyl). For example, UV photolysis of $[\text{CpMn}(\text{CO})_3]$ ($\nu(\text{CO})$: 1939, 2024 cm^{-1}) in the presence of the NHC 1,3-bis(2,4,6-trimethylphenyl)imidazol-2-ylidene (IMes) produces the dicarbonyl complex $[\text{CpMn}(\text{CO})_2(\text{IMes})]$ ($\nu(\text{CO})$: 1854 and 1918 cm^{-1}) which undergoes further loss of CO to give a monocarbonyl complex $[\text{CpMn}(\text{CO})(\text{IMes})]$ with $\nu(\text{CO})$ at 1817 cm^{-1} .¹⁰² The systematic redshift in $\nu(\text{CO})$ is consistent with the loss of π -accepting CO and incorporation of the strong σ -donor N-heterocyclic carbene. Similar behaviour is observed in the family of dicarbonyl and monocarbonyl complexes derived from monodentate and chelating bis(dimethylphosphino)alkanes (Figure 5.1.8.1a).⁹⁵

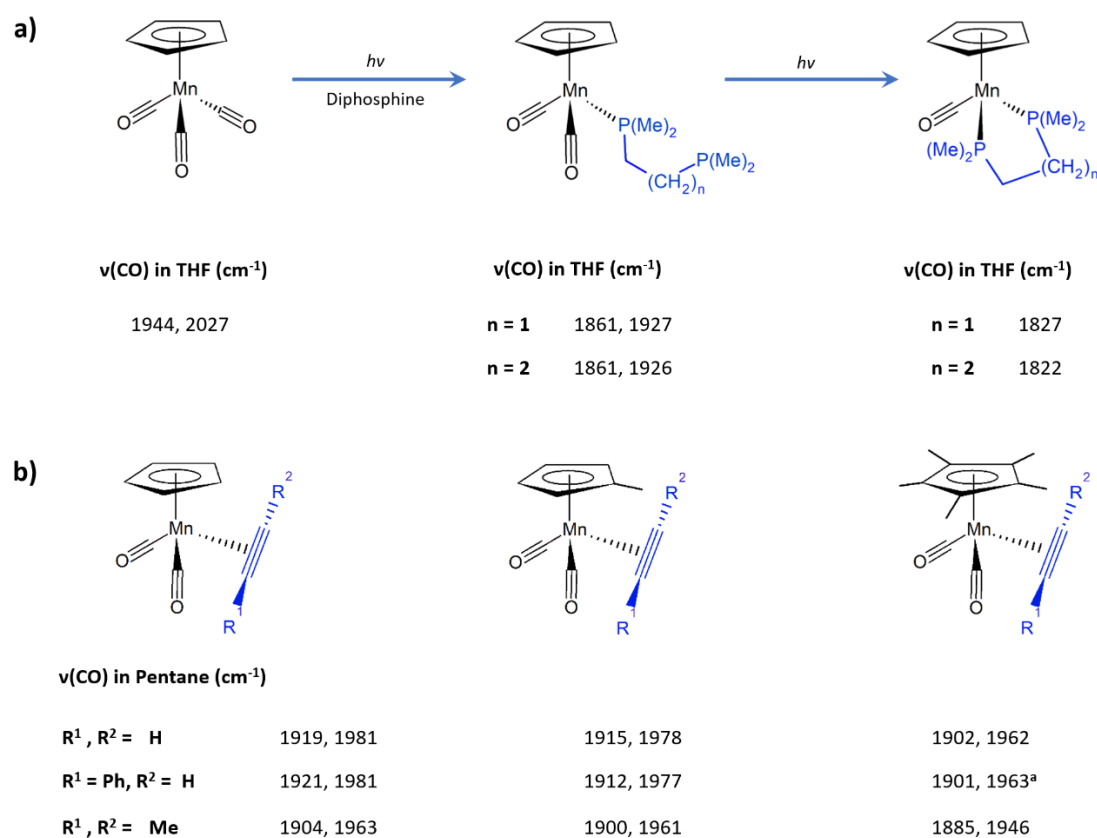


Figure 5.1.8.1: a) Photo-substitution of CO for mono- and bidentate phosphines results in a redshift of $\nu(\text{CO})$. **b)** Similarly, $\nu(\text{CO})$ is redshifted as the electron donating ability of the cyclopentadiene is increased from Cp to Cp'', and as the electron donating ability of the alkyne is increased going from acetylene to dimethyl acetylene. ^a Recorded in cyclohexane. ¹⁰⁸

The conditions under which IR spectroscopy is performed can also affect the energy of CO stretches, this includes the polarity of solvent and the use of solid-state techniques such as Nujol mull or KBr disks

(Tables 5.2-X). For this reason, the stretches observed for metal carbonyl complexes inside a crystalline solid such as a MOF may differ from that observed for the same complex in solution and can be sensitive to the solvent present in the pores of the material.

The same effect is observed when the electronic properties of the supporting ligand are modified. The electron donating power of the substituted cyclopentadienes increase according to $Cp'' > Cp' > Cp$ and this is reflected in the $\nu(CO)$ of the corresponding π -alkyne complexes $[XCp(CO)_2(RC_2R')]$ ($X = Cp, Cp'$ or Cp'' and $R, R' = H, Ph, Me$) (Figure 5.1.8.1b).⁸² The electron donating power of the alkyne ligands is also apparent in the trend towards greater $\nu(CO)$ redshift in going from acetylene to dimethylacetylene. From the data presented in Figure 5.1.8.1 and Tables 7.5.1.1-5, it is evident that the shift in $\nu(CO)$ upon photolysis can be rationalised by considering the electronic properties of the coordination sphere.

Mn(I) tricarbonyl complexes are typically yellow/orange in colour due to the presence of strong-field CO ligands in the coordination sphere. When CO is substituted for a relatively weak-field ligand under photolysis the product is typically red, as reported for $[TpMn(CO)_2(THF)]$,⁵² $[CpMn(CO)_2(THF)]$,⁷⁵ $[CpMn(CO)_2(pyridine)]$ ⁸⁶ and $[Mn(bpy)(CO)_2(MeCN)_2]PF_6$.⁷⁴ The substitution of CO for a relatively strong-field ligand such as phosphines,⁵² phosphites⁵² or NHCs typically results in a yellow/orange complex which is consistent with the preservation of an overall strong-field ligand set.¹⁰² Consistent with this theory, the dicarbonyl complexes $[CpMn(CO)_2(AsPh_3)]$ and $[CpMn(CO)_2(SbPh_3)]$ are pale yellow, while the monocarbonyls $[CpMn(CO)(AsPh_3)_2]$ and $[CpMn(CO)(SbPh_3)_2]$ are dark red.⁵⁰ Intriguingly, Fujita *et al.* describe a colour change from yellow to green-yellow upon UV photolysis of their cage-encapsulated $[Cp'Mn(CO)_3]$ complex, intimating that the coordinatively unsaturated $[Cp'Mn(CO)_2]$ fragment is green rather than red.¹¹

5.1.9 Small Molecule Activation at Coordinatively Unsaturated Metal Centres

The interest in coordinatively unsaturated metal complexes is largely driven by their proven ability to activate small molecules, including the elusive C-H bonds of alkanes. The selective activation of C-H bonds is the ultimate prize in transition metal catalysis due to the valuable commodity chemicals that could be generated from abundant alkane feedstocks. Accordingly, the interaction between coordinatively unsaturated metal complexes and small molecules has been studied extensively. Such reactive metal centres are formed in-situ under matrix isolation in frozen or liquid noble-gas¹⁰⁹ using

laser flash photolysis and studied via ultrafast spectroscopy. Of particular interest are the carbonyl complexes of Rh(I) and Ir(I), which are well known to undergo UV photolysis to form coordinatively unsaturated complexes which can activate C-H bonds.¹⁰⁹⁻¹¹⁹ The presence of CO ligand(s) provides a good spectroscopic handle for studying the ultrafast processes involved in C-H activation at various metal centres.^{7-9, 116-117, 120-122} These studies have mapped small molecule activation over ultrafast time-scales, revealing the conception of the coordinatively unsaturated complex, intermediate noble-gas/ σ -alkane complexes and eventual oxidative addition product(s).

Some of the earliest confirmed cases of C-H activation at a metal centre involved the oxidative addition of a C-H bond across a vacant coordination site generated via photolysis.²⁻³ In 1982, Janowicz *et al.* reported the oxidative addition of cyclohexane across a coordinatively unsaturated Ir(I) complex.¹²³ Photolysis of $[\text{Ir}(\text{Cp}'')(\text{PMe}_3)(\text{H})_2]$ (Cp'' = pentamethylcyclopentadiene) releases H_2 , leaving a vacant coordination site over which various C-H bonds undergo oxidative addition to form the corresponding hydridoalkyl complex. Likewise, Hoyano *et al.* used photolysis of the dicarbonyl complex $[\text{Ir}(\text{Cp}'')(\text{CO})_2]$ to generate a coordinatively unsaturated monocarbonyl complex which successfully activated the C-H bond in neopentane (Figure 5.1.9.1).¹²⁴

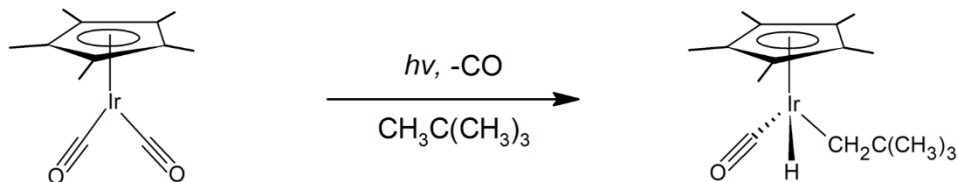


Figure 5.1.9.1: Oxidative addition of the C-H bond in neopentane across the vacant coordination site generated by photolysis of the Ir(I) dicarbonyl complex $[\text{Ir}(\text{Cp}'')(\text{CO})_2]$. Figure from Hoyano *et al.*¹²⁴

IR and NMR spectroscopy has allowed the transient intermediates formed during photolysis and oxidative addition to be identified in the immensely short time-scales over which these transformations take place.^{116, 122, 125} The central role of σ -complexes in the activation of small molecules by transition metal complexes is now well established. The vacant coordination site generated on a metal centre via photolysis can form a σ -complex with a H-H, C-H,^{7-9, 116-117, 120-122} Si-H¹²⁶⁻¹²⁸ or B-H¹²⁹ bond to form a three-centre two-electron complex. The metal centre accepts electron density from the ligand while also donating electron density into the σ^* X-H orbital, which weakens the corresponding X-H bond. In complexes where backdonation is dominant, occupancy of the σ^* X-H orbital and can lead to complete scission of the bond to form an oxidative addition product.^{128, 130-133} As a result, the characterisation of σ -

alkane complexes is of tremendous interest to chemists because they are postulated to be the first step in the activation of C-H bonds at coordinatively unsaturated metal centres.^{3, 110, 130, 132}

Complete oxidative addition is more common among the electron rich, low valent transition metals such as Re, Fe, Ru, Os, Rh, Ir or Pt and requires that the metal (M^{+n}) has a stable 'n+2' oxidation state. The relationship between alkane σ -complexes and C-H activation at coordinatively unsaturated metal centres has been established by numerous IR spectroscopy studies. In one notable example, Bergman *et al.* revealed the complex mechanism behind C-H activation of alkanes during the UV photolysis of $[(Tp')Rh(CO)_2]$ (Figure 5.1.9.2).¹¹⁰ Under photolysis the Rh(I) centre loses one CO ligand to give $\kappa^3-[(Tp')Rh(CO)]$ which forms the σ -alkane complex $\kappa^3-[(Tp')Rh(CO)(R-H)]$ within 20 ps. Within 200 ps one of the pyrazole donors dissociates, forming $\kappa^2-[(Tp')Rh(CO)(R-H)]$ which undergoes oxidative addition within 200ns to give $\kappa^2-[(Tp')Rh(CO)(R)(H)]$ after which the dissociated pyrazole donor recombines with the Rh(I) centre to give the final product $\kappa^3-[(Tp')Rh(CO)(R)(H)]$. Merely observing the final oxidative addition product does not betray the specific processes behind the C-H activation, such as the dissociation/association of the pyrazole N-donor observed by Bergman *et al.* Time-resolved spectroscopy is ideally equipped to probe the intimate mechanistic details of small molecule activation during photolysis.

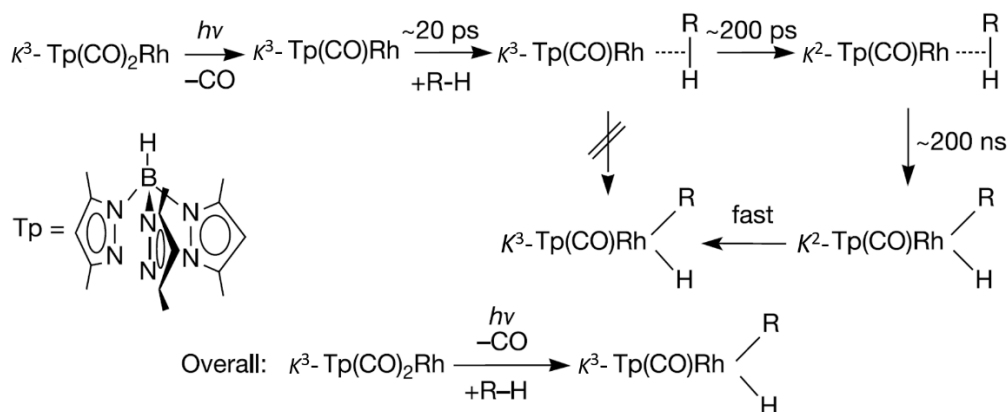


Figure 5.1.9.2: The photolysis of $[TpRh(CO)_2]$ in the presence of alkanes leads to the formation of the corresponding hydridoalkyl complex via a complex mechanism that was deduced by Bergman *et al.* via time-resolved spectroscopy. Figure adapted from Labinger *et al.* (ref. 2)

The role of coordinatively unsaturated metal centres in small molecule activation is clearly established. However, to harness their potential these species must be produced in a robust matrix that maintains

site isolation while facilitating transport of reactant/product molecules. Various solid supports have been employed since the 1980s to support coordinatively unsaturated metal complexes.^{15, 134} For example, zeolites and alumina have been functionalised with Rh(I) dicarbonyl complexes. UV photolysis generates stable Rh(I) monocarbonyls that bind N₂, H₂ and O₂¹⁵ as well as activate alkanes.^{17-19, 135-136} Porosity and mass transport is critical, since slow diffusion of photo-dissociated CO limits the formation of Rh(I) monocarbonyl complexes on alumina supports.¹⁶ Furthermore, high density loading of [Rh(CO)₂] was observed to lead to lower C-H activation of cyclohexane due to the formation of inactive [Rh₂(CO)₃] dimers, highlighting the importance of site isolation in maintaining activity of coordinatively unsaturated metal sites.¹³⁶ In this sense MOFs present a tantalising medium within which to explore small molecule activation due to their exceptional porosity and ability to host well-defined, isolated metal complexes. Furthermore, robust crystallinity offers an opportunity to characterise the structural parameters of reactive metal complexes during photolysis and small molecule activation.

5.1.10 Mn(I) σ -Complexes and Small Molecule Activation

Oxidative addition chemistry is common for complexes of low valent, late transition metals such as Re, Fe, Ru Os, Rh, Ir and Pt but has only been rarely implicated in Mn(I) chemistry. The oxidative addition of an X-H bond across a metal centre requires the presence of a vacant coordination site and that the metal (M⁺ⁿ) possesses an accessible 'n+2' oxidation state. Reassuringly, coordinatively unsaturated Mn(I) complexes are readily generated via photolysis, and Mn(III) is well known (Mn has a particularly broad range of oxidation states from -3 to +7²⁷). However, contrary to the systems described above, the photolysis of [CpMn(CO)₃] in alkane solution results in the formation of the σ -alkane complex [CpMn(CO)₂(R-H)],¹²⁵ with no evidence of the oxidative addition chemistry observed for the Rh, Ir and Re¹²⁰ complexes.

Despite the apparent elusiveness of direct C-H activation with Mn(I), the romance of Mn catalysis has been rekindled. Motivated by the need for cheap, 'earth abundant' transition metal catalysts, the last decade has spawned a plethora of studies detailing C-H activation catalysed by Mn(I), usually in conjunction with acid/base co-catalysis,^{27, 137-140} or mediated by a photo-generated radicals.¹⁴¹⁻¹⁴² Some exceptions exist in which direct C-H activation has been invoked to explain the observed catalytic activity.¹⁴³ Kuninobo *et al.* reported that when a mixture of 1-methyl-2-phenyl-1*H*-imidazole, benzaldehyde, [Mn(CO)₅Br] and triethylsilane was combined with in toluene and heated at 115°C for 24

hr, the corresponding silyl ether was produced (Figure 5.1.10.1).¹⁴³ The authors propose that the reaction proceeds via oxidative addition of the aromatic C-H bond across the manganese centre, followed by aldehyde insertion into the Mn-C bond and silylation of the alkoxy functionality (to yield H₂ and silyl ether product) although no direct evidence of a hydride or Mn(III) intermediate is reported.

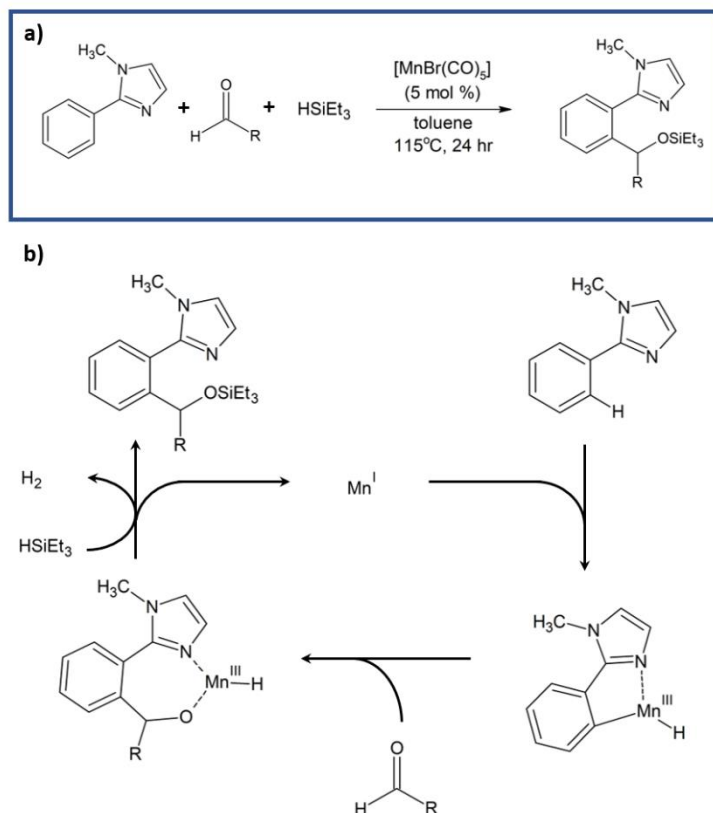


Figure 5.1.10.1: The Mn(I) catalysed silylation reaction and proposed reaction mechanism which includes Mn(I) based C-H activation. Figure adapted from ref. 143.

The second exception was reported by Chen *et al.* in 1999, who used UV photolysis of Mn(I) or Re(I) tricarbonyl methylcyclopentadiene complexes in the presence of pinacol-borane, CO and a alkane substrate to affect selective C-H borylation.¹⁴⁴ Under these conditions the coordinatively unsaturated metal centre produced via photolysis reacts with pinacol borane to give the oxidative addition product [CpMn(CO)₂(Bpin)₂] (Bpin = 4,4,5,5-Tetramethyl-1,3,2-dioxaborane). Although the exact mechanism was not confirmed, Chen *et al.* propose that continued photolysis provides a second vacant coordination site with which the alkane substrate can interact, producing the borylated alkane product either via a C-H oxidative addition product or σ -bond metathesis (Figure 5.1.10.2). Considering the lack of C-H oxidative

addition chemistry observed for Mn complexes, the former mechanism seems unlikely, especially since the oxidative addition would need to occur across a Mn(III) complex. The presence of a CO atmosphere ensures that the starting carbonyl complex is regenerated and the reaction is therefore catalytic, selectively borylating primary C-H bonds and aryl C-H bonds on a variety of substrates. This chemistry presents an ideal target for investigation within **1** because the structural insights obtained via X-ray crystallography may clarify the mechanism. It is possible that this and the chemistry described by Kuninobo *et al.* proceeds via oxidative addition chemistry, however there is no conclusive evidence to support this postulate. It is possible that by performing similar chemistry inside the confining environment of **1** that the reaction mechanism can be elucidated.

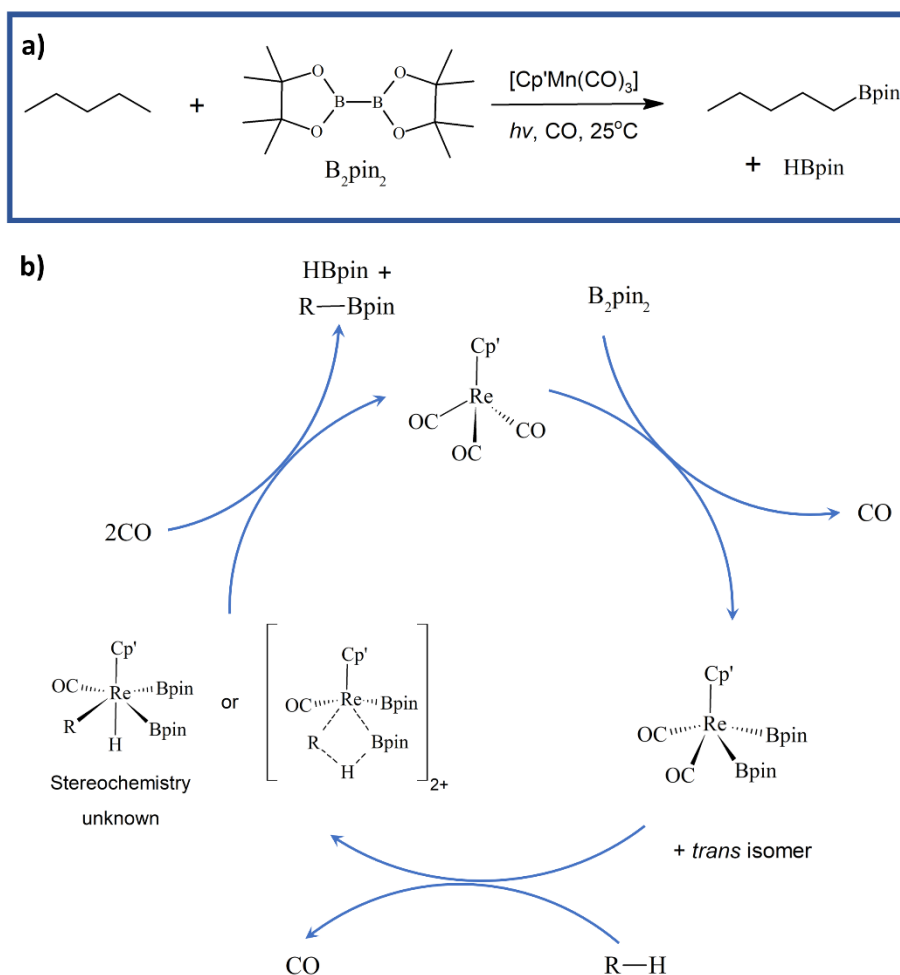


Figure 5.1.10.2: **a)** Selective borylation of alkanes under photolysis using $[\text{Cp}'\text{Mn}(\text{CO})_3]$ and the proposed reaction mechanism **b)** which invokes oxidative addition chemistry. Figure adapted from ref. 144.

Beyond the extreme realm of C-H activation, silanes and boranes are more susceptible to undergoing oxidative addition due to their relatively polar and weak X-H bonds. The reaction between photogenerated Mn(I) complexes and silanes has been studied extensively.^{128, 145-146} Early reports claimed that the photolysis of [CpMn(CO)₃] in the presence of trialkyl silanes resulted in oxidative addition of the Si-H bond across the metal centre. When the metal centre donates electron density into the σ^* Si-H orbital, the Si-H bond-length increases. A Si-H bond length between 1.7-1.8 Å is indicative of a σ -complex, although interactions up to 2.45 Å are still considered to represent a residual Si-H interaction.¹²⁶ Computational studies have investigated the Si-H bond activation of [CpM(CO)₃] (M= Mn, Re) and suggest that Si-H bond extends to 1.9 and 2.35 Å respectively,¹⁴⁷ confirming that the [CpMn(CO)₂] fragment forms σ -complexes with residual Si-H interactions rather than classic oxidative addition products.¹⁰⁴ On the contrary, the analogous Re(I) complexes are considered to form true oxidative addition products, aided by the larger ionic radius of Re(I) compared to Mn(I).¹⁴⁷ Similar interactions occur in Mn(I) σ -(B-H)^{129, 148-150} and σ -(Al-H)¹⁵¹ complexes in which the respective X-H bond is weakened upon coordination.

Although there is little evidence that Mn(I) Silane σ -complexes undergo classic oxidative addition, there are instances in which the coordinated silane is persuaded to react due to significant weakening of the Si-H bond.¹⁵²⁻¹⁵³ Fang *et al.* generated a Mn(I) dichloromethane adduct via halide abstraction, the weakly bound dichloromethane readily exchanges with triethylsilane to form a σ -complex which undergoes silane alcoholysis with phenol to yield PhOSiEt₃ catalytically (Figure 5.1.10.3).¹⁵⁴ The reaction proceeds via the heteroleptic cleavage of the Si-H bond upon coordination to the Mn(I) centre.

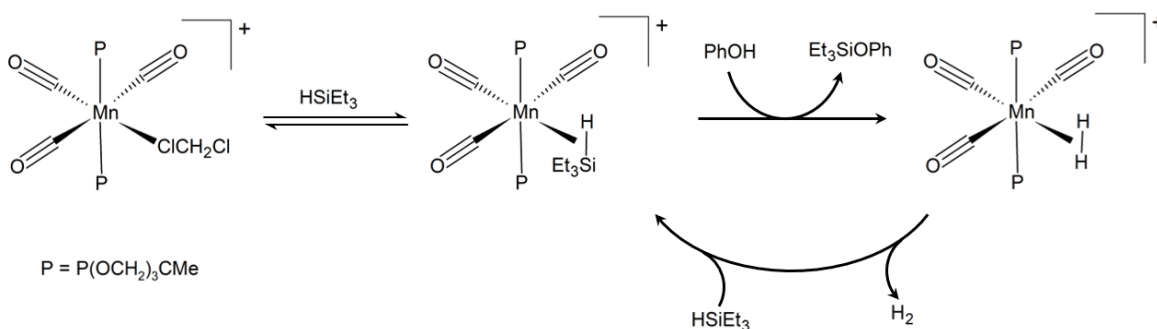


Figure 5.1.10.3: The dichloromethane complex produced by Fang *et al.* via an anion abstraction protocol. The lability of the dichloromethane ligand allows facile exchange with triethylsilane to form the corresponding σ -complex which reacts with phenol via Silane alcoholysis. Figure adapted from ref. 154.

Finally, the last 'X-H' bond activation that will be considered is that of H₂. The formation of a σ-(H-H) complex provides optimal overlap between the σ- and σ*-(H-H) orbitals and the metal d-orbitals. In line with examples described above, adequate backdonation from the metal centre can break the H-H bond to give the corresponding dihydride complex.⁹⁹ Although numerous Mn(I) dihydrogen complexes have been confirmed, including [CpMn(CO)₂(H₂)];¹⁵⁵ in some instances coordinated hydrogen actually undergoes oxidative addition to form the corresponding dihydride.⁹⁹ In 2004, Merwin *et al.* reported the photochemical synthesis of [CpMn(dfepc)(H₂)] which was briefly mentioned in Section 5.1.6.⁹⁹ Immediately after photolysis of [CpMn(dfepc)(CO)] in the presence of H₂, the dihydrogen complex [CpMn(dfepc)(H₂)] is dominant, but undergoes slow conversion to an equilibrium mixture of the dihydride complex [CpMn(dfepc)(H)₂] in solution (Figure 5.1.10.4). Although other dihydrogen complexes of Mn have been reported, this was a unique example of photochemical dihydride/hydrogen conversion and represents an example of oxidative addition chemistry at a vacant Mn(I) coordination site. Reversible cleavage of bound H₂ was also observed by Hulley *et al.* using a 16e⁻ Mn(I) complex generated by halide abstraction rather than photolysis.¹⁵⁶

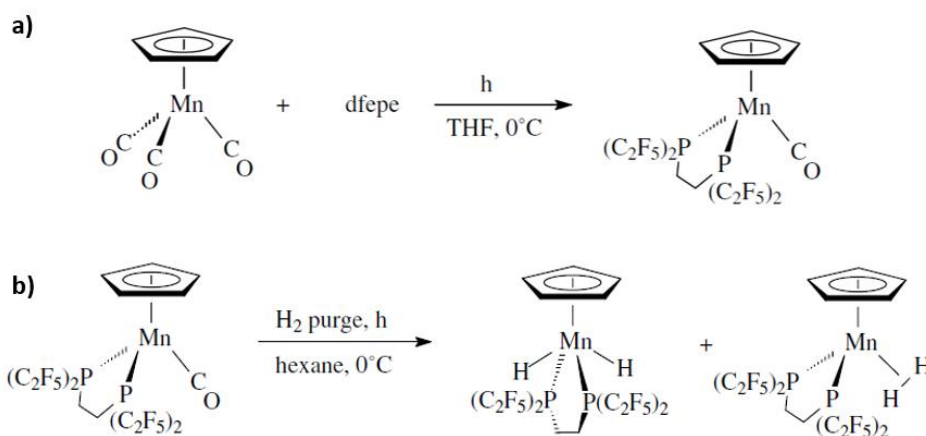


Figure 5.1.10.4: a) Formation of the monacarbonyl complex [MnCp(CO)(dfepc)] via photolysis of [MnCp(CO)₃] which undergoes further CO loss under photolysis and H₂ purge to give a mixture of the σ-H₂ and dihydride complexes b). Figure adapted from ref. 99.

With consideration of the above, it is worth noting that oxidative addition chemistry of R-X (X = H, halide) bonds has been reported under photolysis of [CpRe(CO)₃].^{132, 157} It is possible that a more electron rich Mn(I) centre engendered by complete CO loss may be more capable of activating small molecules than the systems studied so far. Full oxidative addition is not necessarily required, significant weakening upon formation of a σ-complex can be sufficient to activate X-H bonds towards further chemistry. Owing to

the extended conjugation in the ligand system, the photolysis of $\mathbf{1} \cdot [\text{Mn}(\text{CO})_3\text{Br}]$ should result in more rapid CO loss than the Cp analogues, suggesting that more electron rich Mn(I) centres may be accessible due to the loss of more than one CO ligand. If this is true, then the photoproducts generated under photolysis of $\mathbf{1} \cdot [\text{Mn}(\text{CO})_3\text{Br}]$ may be more susceptible to oxidative addition chemistry than the widely studied Cp derivatives.

5.2 Results and Discussion

5.2.1 Formation and Characterisation of $1 \cdot [\text{Mn}(\text{CO})_3\text{Br}]$ via UV-Visible and IR Spectroscopy

As already discussed in Chapter 4, the metalation of **1** with $[\text{Mn}(\text{CO})_5\text{Br}]$ in EtOH results in the formation of $1 \cdot [\text{Mn}(\text{CO})_3(\text{H}_2\text{O})]\text{Br}$ which can be converted to the neutral complex $1 \cdot [\text{Mn}(\text{CO})_3\text{Br}]$ via solvent exchange with either toluene or dry THF. The coordination sphere of the Mn(I) centre in EtOH is well ordered, with water occupying a single axial site and bromide residing nearby in the MOF pore. Upon solvent exchange with toluene or THF, the bromide anion binds to the metal centre to form the corresponding *fac*-tricarbonyl complex $1 \cdot [\text{Mn}(\text{CO})_3\text{Br}]$, as revealed by X-ray crystallography (Figure 5.2.1.1). It is worth noting that the initial formation of a charged complex is unusual, comparable complexes in the literature are neutral.^{44, 158} This suggests that the MOF pore-environment promotes the formation of a charged complex in polar media such as ethanol, perhaps due to the relative proximity (13 Å) of the Mn(I) centres which allows the bromide to reside in the MOF pore between two adjacent Mn(I) centres. Nonetheless, upon solvent exchange with weakly coordinating and non-polar solvents such as THF or toluene, the neutral complex is obtained. This transformation is attributed to the low polarity of these solvents, which destabilises the ion-pair arrangement and thereby promotes the formation of a neutral species. It is worth noting that during the transformation the axial carbonyl ligand undergoes a migration to the opposing coordination site. This behaviour is attributed to the steric demands of the bromide anion which would be better accommodated on the more open face of the complex.

The resulting neutral complex formed in THF possesses a facial geometry with bromide residing in an axial coordination site (Figure 5.2.1.1). The Mn-Br bond length is 2.568(4) Å which is consistent with that observed in other Mn(I) complexes bearing the *fac*- $[\text{Mn}(\text{CO})_3\text{Br}]$ motif. The Mn-CO bond lengths for the equatorial and axial CO ligands are 1.875(14) and 1.82(3) Å respectively which is comparable to those observed in the corresponding neutral complex (1.824(11) and 1.807(13) Å) reported in Chapter 4. Similar results are obtained using toluene, however the structure is more disordered with residual bromide located in the MOF pore. The bond lengths in the complex are comparable to those described above, the Mn-Br bond length is 2.5731(19) Å, while the Mn-CO bonds are 1.827(12) and 1.805(8) Å for the axial and equatorial CO ligands respectively. The residual bromide residing in the pore space adjacent to the Mn(I) centre was refined with an occupancy of 16%, suggesting that the conversion of the ion pair to a neutral complex is not fully complete in toluene. The role of solvent in favouring the ion

pair or the neutral complex is exemplified by the observation that when samples containing toluene are solvent exchanged with ethanol, the original charged (ion pair) complex is regenerated.

Although both charged ($\mathbf{1}\cdot[\text{Mn}(\text{CO})_3(\text{H}_2\text{O})]\text{Br}$) and neutral ($\mathbf{1}\cdot[\text{Mn}(\text{CO})_3\text{Br}]$) Mn(I) complexes can be formed in $\mathbf{1}$, the latter is preferable for photolysis studies due to the coordinated σ -donor bromide which is known to redshift the MLCT transition in similar complexes.³⁸ Furthermore, the retention of water in the coordination sphere of the charged complex would limit the number of possible vacant coordination sites to two, since bromide would be expected to bind to the metal centre following CO loss. Therefore, the photolysis studies described below were conducted using samples that had been washed thoroughly with non-polar solvents that promote the formation of the neutral complex.

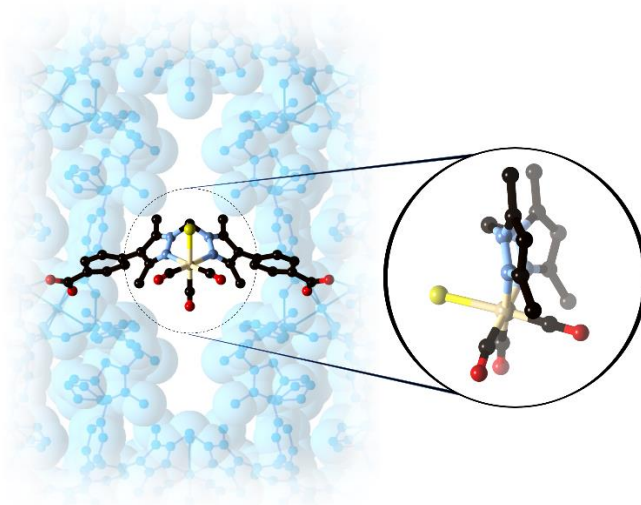


Figure 5.2.1.1. X-ray structure of $\mathbf{1}\cdot[\text{Mn}(\text{CO})_3\text{Br}]$ in dry THF displaying the coordination of the complex at the N,N-chelation site within $\mathbf{1}$, the MOF framework is represented by a blue van der Waals surface. Inset, a perspective view of the Mn(I) coordination sphere clearly illustrates the coordination of the bromide anion to the Mn(I) centre upon solvent exchange with THF or Toluene. Hydrogen atoms have been removed for clarity (C = black, N = purple, Mn = beige, Br = yellow, O = red).

The bright yellow colour of $\mathbf{1}\cdot[\text{Mn}(\text{CO})_3\text{Br}]$ (Figure 5.2.1.2) is typical of Mn(I) tricarbonyl bromide complexes and arises from the presence of strong-field CO ligands. Correspondingly, the UV-Vis spectrum of $\mathbf{1}\cdot[\text{Mn}(\text{CO})_3\text{Br}]$ contains a strong Metal to Ligand Charge-Transfer (MLCT) band centred at 380 nm. The parent MOF, $\mathbf{1}$, only absorbs below 350 nm due to the presence of aromatic substituents in the organic ligand. The MLCT band for $\mathbf{1}\cdot[\text{Mn}(\text{CO})_3\text{Br}]$ is consistent with similar complexes such as $[\text{Mn}(\text{bpy})(\text{CO})_3\text{Br}]$ and $[\text{TpmMn}(\text{CO})_3]^+$ which have MLCT bands centred on $\lambda_{\text{max}} = 430$ nm and 360 nm respectively.³⁴ Although the $\mathbf{1}\cdot[\text{Mn}(\text{CO})_3\text{Br}]$ MLCT band is centred at 380 nm, the absorption extends into

the visible spectrum up to 500 nm which implies that the complex is susceptible to CO loss under both UV and visible irradiation. The latter is preferred because it will limit damage to the material and prevent the host framework from blocking light from reaching Mn(I) sites deep within the crystal.

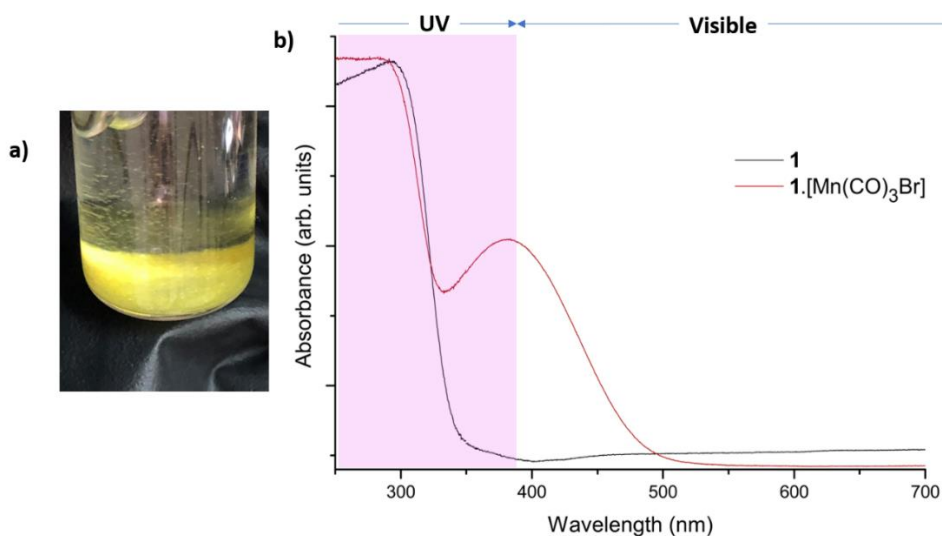


Figure 5.2.1.2: a) The bright yellow crystals of $1 \cdot [\text{Mn}(\text{CO})_3\text{Br}]$ b) Solid state UV-Vis spectra of the parent MOF framework (black curve) and $1 \cdot [\text{Mn}(\text{CO})_3\text{Br}]$ (red curve) showing the strong charge transfer band at 380 nm and absorbance profile of the parent MOF below 350 nm corresponding to the aromatic components of the ligand. The UV LED light emits 365 nm radiation which is well within the charge transfer band of the carbonyl complex.

The N,N-chelation site in $1 \cdot [\text{Mn}(\text{CO})_3\text{Br}]$ features two conjugated 4-phenylcarboxylate-3,5-dimethylpyrazole moieties which are separated by a methylene hinge that inhibits conjugation. Several studies have investigated the photolysis of Mn(I) complexes based on ligands that possess similar methylene or amine bridges between their pyrazolyl or pyridinyl donors.^{44-45, 159-161} Perhaps the closest relative, $[\text{TpmMn}(\text{CO})_3]^+$ possesses a MLCT band at 360 nm and readily releases CO under 365 nm irradiation.³⁴ The complex $[\text{Mn}(\text{CO})_3(\text{N,N,O-2,2-bis}(3,5\text{-dimethylpyrazolyl})\text{ethanol})]\text{Br}$ was proposed as a photoCORM by Mede *et al.* and undergoes complete CO loss under visible irradiation,⁴⁴ as do other related compounds based on the substituted bis(pyrazolyl)methane motif.¹⁶⁰ DFT calculations revealed that for $[\text{Mn}(\text{CO})_3(\text{bis}(\text{pyrazolyl})\text{ethyl}(\text{phenylmethylamine}))]$ complexes (Figure 5.2.1.3), the MLCT transitions correspond to transfer of electron density from the metal centre to $\pi^*(\text{pyrazole})$ orbitals.¹⁶⁰ It is therefore reasonable to expect that photolysis of $1 \cdot [\text{Mn}(\text{CO})_3\text{Br}]$ will lead to a MLCT transition that will correspond to the transfer of electron density to the π^* -pyrazole orbitals which may be delocalised across the phenyl substituents.

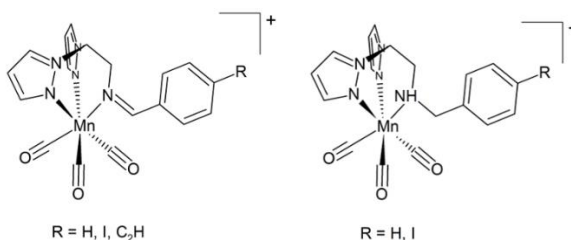


Figure 5.2.1.3: Mn(I) complexes prepared by Pai *et al.* featuring the N,N,N-chelating ligands that contain two pyrazole sites reminiscent of the chelation site in **1**·[Mn(CO)₃Br].

The IR spectrum of **1**·[Mn(CO)₃Br] from THF displays CO stretches at 1906, 1951, 2029 cm⁻¹ characteristic of the [Mn(CO)₃Br] moiety (Figure 5.2.1.4a). It is well established that the three CO stretching bands observed in the IR spectrum of *fac*-[Mn(CO)₃] complexes arise from their symmetric and antisymmetric CO stretching modes.¹⁶² The highest frequency band corresponds to the symmetric stretching mode involving all three CO ligands while the second highest frequency band corresponds to the symmetric stretching mode of the equatorial CO ligands (Figure 5.2.1.4b). The lowest frequency stretching band arises from the antisymmetric stretching mode in which the equatorial CO ligands stretch out of phase with the axial CO ligand. The highest frequency band is particularly sensitive to the environment of the axial CO ligand. IR stretches are also sensitive to analysis conditions such the presence and type of solvent (Tables 5.2 and S7.5.1.1-S7.5.1.5). Nonetheless, IR spectroscopy offers a valuable probe into the processes taking place during photolysis, including ultra-fast processes occurring in the pico-seconds following photolysis. Net CO loss from **1**·[Mn(CO)₃Br] is expected to lead to bleaching of the parent CO stretches and the formation of new features corresponding to mono- and di-carbonyl species (Tables 5.2 and S7.5.1.1-S7.5.1.5), ultimately resolving into a featureless spectrum upon quantitative CO loss.

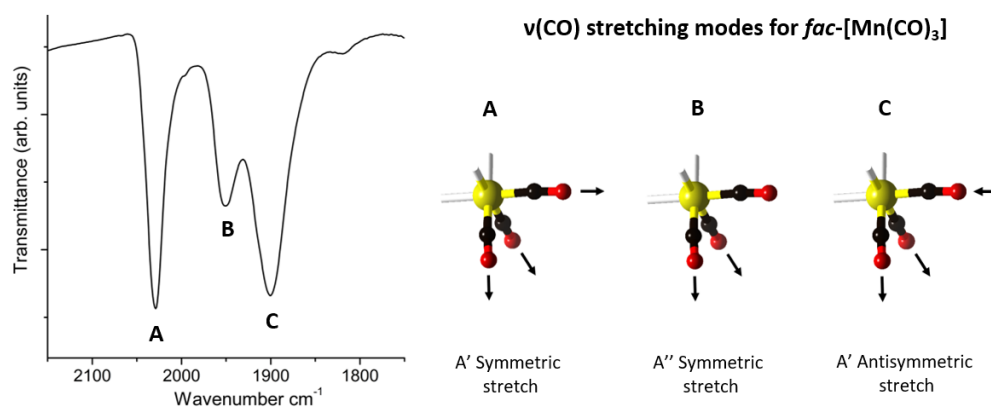


Figure 5.2.1.4. IR spectrum of **1**·*fac*-[Mn(CO)₃Br] displaying three distinct bands which correspond to the symmetric and antisymmetric stretching modes of the CO ligands which are derived from the C_{3v} symmetry considerations.

5.2.2. Photochemistry Experiments with $1 \cdot [\text{Mn}(\text{CO})_3\text{Br}]$

5.2.2.1 Preliminary Results: Monitoring CO loss via IR spectroscopy and Mass Spectrometry

The photochemistry of $1 \cdot [\text{Mn}(\text{CO})_3\text{Br}]$ was investigated by exposing samples to both 365 nm UV and broad-spectrum visible LED light sources. IR spectroscopy of the material post UV photolysis revealed no appreciable CO stretches, confirming that the CO ligands dissociate from the Mn(I) sites during photolysis. The same result is obtained using a broad spectrum visible LED torch to irradiate the crystals, confirming that $1 \cdot [\text{Mn}(\text{CO})_3\text{Br}]$ is susceptible to both UV and visible radiation (Figures 5.2.2.1 and S7.5.3.1). However, the work described below almost exclusively focuses on visible photolysis of $1 \cdot [\text{Mn}(\text{CO})_3\text{Br}]$, UV photolysis will be investigated in more detail in the future.

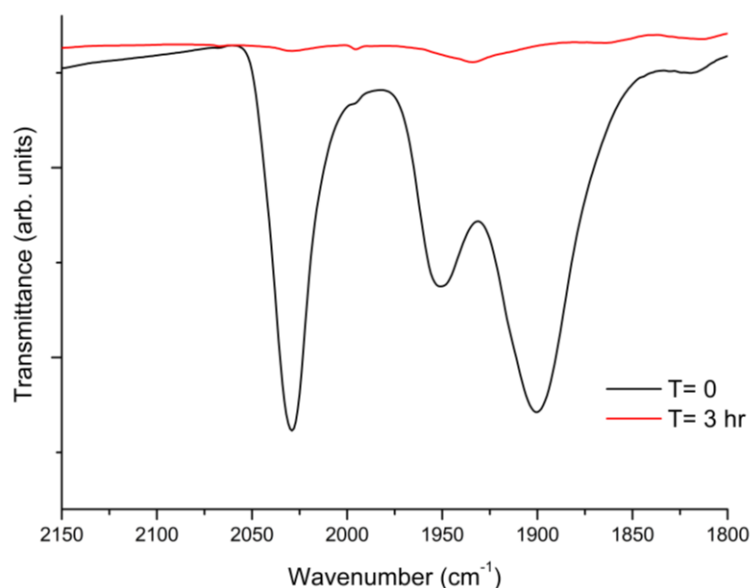


Figure 5.2.2.1. IR spectrum before and after visible photolysis in THF solution under argon degas, demonstrating the quantitative loss of CO from the material. Similar results are obtained after photolysis in toluene and acetonitrile (see section 5.2.3).

To confirm that the CO released from the Mn(I) complex escapes the MOF crystals rather than becoming trapped, we monitored the chemical composition of the reaction vessel headspace during photolysis

using Mass Spectrometry. The sample was initially dried from toluene under vacuum and subsequently photolysed under an argon atmosphere using either visible or UV light. Prior to photolysis the atmosphere contains no CO gas, confirming that the material is stable towards CO loss in the dark. Under visible or UV photolysis the concentration of CO gas immediately increases; plateauing after ~10 minutes. The amount of CO released was quantified and found to be equivalent to approx. 1 CO per Mn(I) site, which does not agree with the apparent quantitative CO loss suggested by IR spectroscopy. One possible explanation for this disparity is the use of a stainless-steel reaction vessel and tubing. Carbon monoxide is known to bind to stainless-steel surfaces, forming Fe, Cr and Ni carbonyl complexes.¹⁶³⁻¹⁶⁴ Considering the small quantities of CO released from the samples, it is possible that the CO gas quantification is underestimated due to the CO coordinating to the steel surfaces within the apparatus. Surface bound CO is readily removed under vacuum at room temperature and therefore each time the apparatus is purged via vacuum/argon, the surface bound CO is diminished.

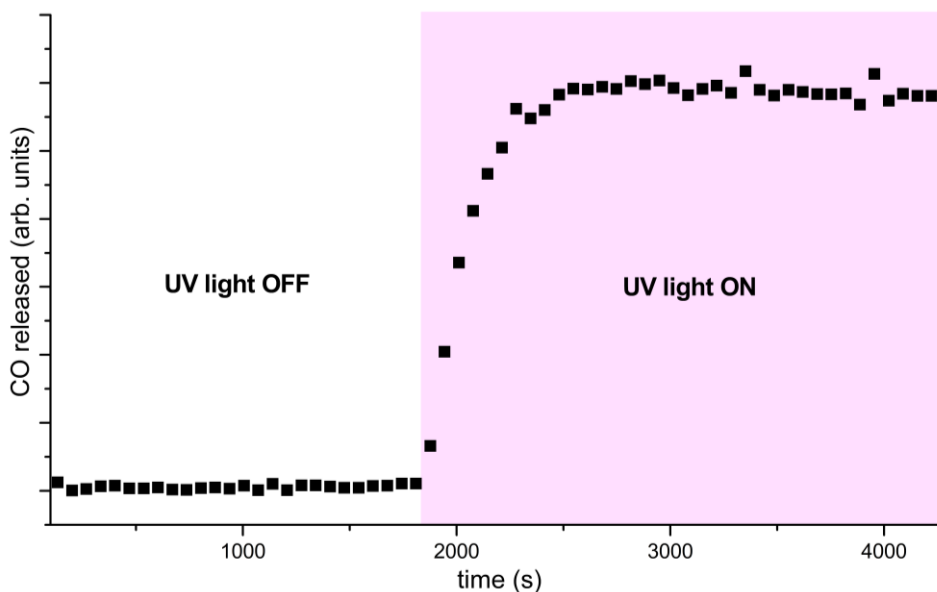


Figure 5.2.2.2: **a)** IR spectra of $1 \cdot [\text{Mn}(\text{CO})_3\text{Br}]$ under UV photolysis displaying quantitative loss of CO from the material after 30 minutes of irradiation. **b)** The concentration of CO in the atmosphere above a sample of $1 \cdot [\text{Mn}(\text{CO})_3\text{Br}]$ rapidly increases when exposed to 365 nm radiation. The same result is observed when visible light is used. The quantity of CO detected plateaus after approx. 10 minutes of irradiation.

An alternative explanation for this behaviour is that only 1 CO molecule is released under photolysis and that the quantitative CO loss observed via IR spectroscopy of the sample is due to oxidation of the sensitive dicarbonyl complex during IR sample preparation. This explanation is unlikely considering the

quantitative loss of CO observed in degassed solution (see below) and the site isolation rendered by the porous matrix. Nonetheless, it is evident that the porosity of **1** allows CO to escape the material during photolysis.

5.2.2.2 Photolysis of 'Activated' Samples of $1 \cdot [\text{Mn}(\text{CO})_3\text{Br}]$

The goal behind utilising **1** as a matrix for photochemically active metal complexes is the formation of truly coordinatively unsaturated metal complexes which are physically isolated within a crystalline matrix. This has been achieved using rhodium and iridium dicarbonyls immobilised on zeolite and alumina supports,¹⁵⁻¹⁷ however these systems do not lend themselves to direct structural characterisation because they do not form large single crystals. The solvent occupying the pores of MOFs can be removed by heating under reduced pressure, a process known as 'activation' and one which is routinely used to characterise **1**.²¹ With solvent removed from the pores, the photolysis of $1 \cdot [\text{Mn}(\text{CO})_3\text{Br}]$ under vacuum or inert atmosphere should create coordinatively unsaturated Mn(I) centres which would be expected to interact with gas molecules (N_2 , CO_2 , H_2 , C_2H_4). Various groups have structurally characterised the interaction between gas molecules and bare metal centres within MOFs using X-ray or Neutron diffraction,¹⁶⁵⁻¹⁶⁸ including the first high spin Mn(II) carbonyl complex, formed by dosing a MOF containing a coordinatively unsaturated Mn(II) site with CO gas.¹⁶⁹ However, the reactive sites are typically generated via removal of solvent from metal nodes under heating, rather than photolysis.

Isotherms are a powerful probe into the interactions between gas molecules and the surfaces of porous materials. A porous material bearing reactive metal sites would be expected to produce an isotherm featuring a steep slope at very low pressure due to a highly enthalpic interaction such as a gas molecule reacting with an open metal site.^{165, 170} The desorption curve should also display hysteresis due to the material resisting removal of strongly coordinated gas molecules. Such interactions between gas molecules and reactive metal sites exhibit temperature dependence from which an enthalpy of adsorption can be calculated. With these considerations in mind a series of isotherms were collected activated samples of $1 \cdot [\text{Mn}(\text{CO})_3\text{Br}]$ both before and after photolysis.

Samples of **1** (including metallated samples) are typically activated by solvent exchanging the sample with methanol and heating at 100°C under dynamic vacuum for 1 hr.²¹ These conditions are not

compatible with $\mathbf{1}\cdot[\text{Mn}(\text{CO})_3\text{Br}]$ due to the thermal lability of the carbonyl complex. Following activation at 100°C , $\mathbf{1}\cdot[\text{Mn}(\text{CO})_3\text{Br}]$ became dark brown and IR spectroscopy revealed a complex set of IR stretches which are different to the starting material, confirming that the material has lost CO during the activation and a mixture of carbonyl complexes persist in the material (Figure S7.5.3.1). To ensure that the carbonyl complexes are preserved during activation, the sample was activated from distilled hexane under dynamic vacuum at 50°C for 20hr. Following this activation protocol, the material retained its bright yellow colour and the IR spectrum was identical to the parent material (Figure S7.5.3.1), confirming the retention of the CO ligands. Thermogravimetric analysis of the activated sample displayed negligible mass loss up to 80°C , between $80\text{--}200^\circ\text{C}$ the TGA trace contains a step in which the material loses 3.6 % of its mass which corresponds well with the 4.9% expected upon loss of three CO ligands from the Mn(I) complex (Figure S7.5.9.2). This observation is consistent with the loss of CO ligands from the material upon activation at 100°C under vacuum. The material maintains crystallinity during activation, as evidenced by the PXRD pattern obtained after activation (Figure S7.6.4.2). To confirm that the activation protocol had successfully removed the solvent from the pores, an N_2 isotherm was measured at 77 K (Figure S7.5.10.1) and gave a BET surface area of $535.6 \pm 5.6 \text{ m}^2\text{g}^{-1}$ which is consistent with other metallated derivatives of $\mathbf{1}$.²¹

To determine if photolysis of activated $\mathbf{1}\cdot[\text{Mn}(\text{CO})_3\text{Br}]$ produces coordinatively unsaturated Mn(I) complexes, activated samples were photolysed with broad spectrum visible light under dynamic vacuum and constant agitation using a vibrating shaft. The pressure in the manifold increased from $\sim 0.004\text{--}0.005$ mbar to ~ 0.3 mbar rapidly when the LED was initially turned on, indicating rapid release of CO. Once the pressure had returned to a satisfactory level, this indicated that photolysis had ceased. IR spectroscopy confirmed that photolysis under these conditions successfully removed CO. Each sample was analysed via gas isotherms, however, despite extensive investigations, none of the room temperature CO_2 , H_2 or N_2 isotherms feature rapid low-pressure uptake or hysteresis that would allude to strong metal-gas interactions (Figure S7.6.4.2). Considering the stability of $[\text{CpMn}(\text{CO})_2\text{N}_2]$,¹⁷¹ a strong interaction with N_2 at 298K may be anticipated, even at low pressure. All isotherms displayed an absorption/desorption profile that is the same as other metallated derivatives of $\mathbf{1}$, confirming that photolysis has no appreciable effect on the properties of the material under these conditions.

Considering these results, it is evident that photolysis of activated $\mathbf{1}\cdot[\text{Mn}(\text{CO})_3\text{Br}]$ does not yield vacant Mn(I) sites that are accessible to gas molecules, despite IR spectroscopy of photolysed samples

confirming that CO had been successfully released. There are several possible explanations for the apparent failure to produce coordinatively unsaturated metal sites. Firstly, the low temperature activation protocol may not remove all the solvent from the pores of the material, especially if the solvent exchange with hexane had not removed traces of water or toluene. In this instance, the coordinatively unsaturated sites would be 'poisoned' by residual solvent molecules. A sample was photolysed under a He atmosphere rather than dynamic vacuum, however the room temperature N₂ isotherm displayed no appreciable hysteresis or rapid uptake at low pressure. It is also conceivable that photolysis under vacuum may generate the desired 'reactive' complexes, but their instability may lead to decomposition.

Considering that the preliminary experiments described above did not provide any evidence for the formation of stabilised coordinatively unsaturated Mn(I) complexes, the photolysis process was investigated in more detail. The characterisation of truly coordinatively unsaturated metal complexes using isotherms is plagued by experimental challenges such as the need to fully activate the sample and prevent contamination of the reactive sites prior to analysis. These issues make it difficult to assess if photolysis process is failing to generate the desired species or whether those sensitive species are compromised prior to analysis. For this reason, the focus has been largely placed on photolysis of **1**·[Mn(CO)₃Br] crystals in the presence of weakly coordinating solvent. These conditions provide ideal circumstances in which to study photo-induced changes in the Mn(I) coordination sphere using in-situ X-ray crystallography and IR spectroscopy. The solvated photoproducts are expected to be more stable and easier to handle than the coordinatively unsaturated complexes formed in activated samples.

5.2.3 Photolysis of Solvated $1\cdot[\text{Mn}(\text{CO})_3\text{Br}]$

5.2.3.1 IR Spectroscopy in THF

The photochemistry of $1\cdot[\text{Mn}(\text{CO})_3\text{Br}]$ was examined by photolyzing crystals of $1\cdot[\text{Mn}(\text{CO})_3\text{Br}]$ with visible light in the presence of different solvents, with a view towards isolating a reactive complex with a 'place-holder' solvent ligand. As outlined in Section 5.1.6-7, solution photolysis of $[\text{LMn}(\text{CO})_3]$ derivatives (L = Cp, Cp', Tp, Tp') leads to well defined products, $[\text{LMn}(\text{CO})_2(\text{solv})]$, with weakly bound solvent ligands. One of the most popular solvents used in this work is THF due to its weak σ -donor character. The weak coordinating ability of THF towards low oxidation state Mn(I) (which prefers ligands with which it can back-bond) is epitomised by the reversible formation of the dinitrogen complex, $[\text{CpMn}(\text{CO})_2\text{N}_2]$, from $[\text{CpMn}(\text{CO})_2\text{THF}]$ under 100bar of N_2 gas.⁷⁵ This remarkably stable N_2 complex can also be formed via the oxidation of the photochemically generated hydrazine complex.¹⁷¹ $[\text{CpMn}(\text{CO})_2\text{N}_2]$ has been employed in the synthesis of MeN_2Me via reaction of coordinated N_2 with MeLi and Me_3O^+ .¹⁷² Other weakly coordinating place-holder ligands that have been installed on Mn(I) complexes include the solvents dichloromethane and diethyl-ether and the anion triflate (CF_3SO_3^-).¹⁷³⁻¹⁷⁴ A dichloromethane complex of Mn(I) was prepared via anion abstraction and structurally characterised by Fang *et al.* As described in Section 5.1.10, the weakly bound dichloromethane ligand is readily displaced by silanes which are activated by the metal centre and undergo alcoholysis.¹⁵⁴ These cases, among other examples,^{75, 172} demonstrate that the place-holder ligand strategy can be used to generate reactive Mn(I) complexes in solution.

However, photochemically generated Mn(I) complexes such as $[\text{CpMn}(\text{CO})_2\text{THF}]$, although used ubiquitously for ligand exchange, have never been isolated or structurally characterised. $1\cdot[\text{Mn}(\text{CO})_3\text{Br}]$ offers a unique opportunity to structurally characterise the solvent complexes formed during photolysis by using the material as a crystalline matrix within which to produce site-isolated complexes that can be studied using in-situ crystallography and IR spectroscopy. The crystalline matrix strategy negates any need to crystallise the photoproduct. Considering its widespread use, THF was selected as the initial target with a view towards eventually exploring photolysis in other solvents such as toluene, diethyl ether, acetonitrile, dichloromethane and cyclohexane. The MOF crystals were washed with toluene prior to exchange with THF to promote the formation of the neutral complex. It is worth noting that when crystals of $1\cdot[\text{Mn}(\text{CO})_3(\text{H}_2\text{O})]\text{Br}$ are solvent exchanged with distilled THF directly from EtOH, an ordered $1\cdot\text{fac-}[\text{Mn}(\text{CO})_3\text{Br}]$ complex is formed, as confirmed via SCXRD.

As a preliminary investigation, bulk samples of $1 \cdot [\text{Mn}(\text{CO})_3\text{Br}]$ were photolysed with broad-spectrum visible light in THF under constant argon degas. The crystals changed colour from bright yellow to green within 10 minutes, after which they became off-white/colourless over the course of 3 hr (Figure 5.2.3.1). The colour change from yellow to green is consistent with the replacement of strong-field CO ligand(s) with weak THF ligand(s), causing a decrease in the crystal field splitting energy. However, Mn(I) complexes typically become red upon loss of CO and coordination of THF, including $[\text{CpMn}(\text{CO})_2(\text{THF})]$ and $[\text{TpMn}(\text{CO})_2(\text{THF})]$.^{52, 75} Red is also commonly observed for other substituted Mn(I) carbonyl compounds (Table 5.1.6.1). A similar green colour was observed by Maekawa *et al.* in a series of Mn(I) halide bridged dimers of the general formula $[\text{Cp}^{\text{tB}}\text{Mn}(\text{I})(\text{THF})(\text{X})]_2$ (Cp^{tB} = 1,3,5-*tert*-butyl cyclopentadiene, X= Cl, Br, I).¹⁷⁵ The only reported green mono-nuclear Mn(I) carbonyl complex is the coordinatively unsaturated fragment $[\text{Cp}'\text{Mn}(\text{CO})_2]$ reported by Fujita *et al.* (Section 1.2).¹¹ This may suggest that the photolysis of $1 \cdot [\text{Mn}(\text{CO})_3\text{Br}]$ produces a Mn(I) complex that possesses a five-coordinate structure, although the five-coordinate Mn(I) complex $[\text{Mn}(\text{CO})_3(\text{S},\text{Se}-\text{C}_6\text{H}_3-\text{CH}_3)]^-$ is reportedly dark purple.¹⁷⁶

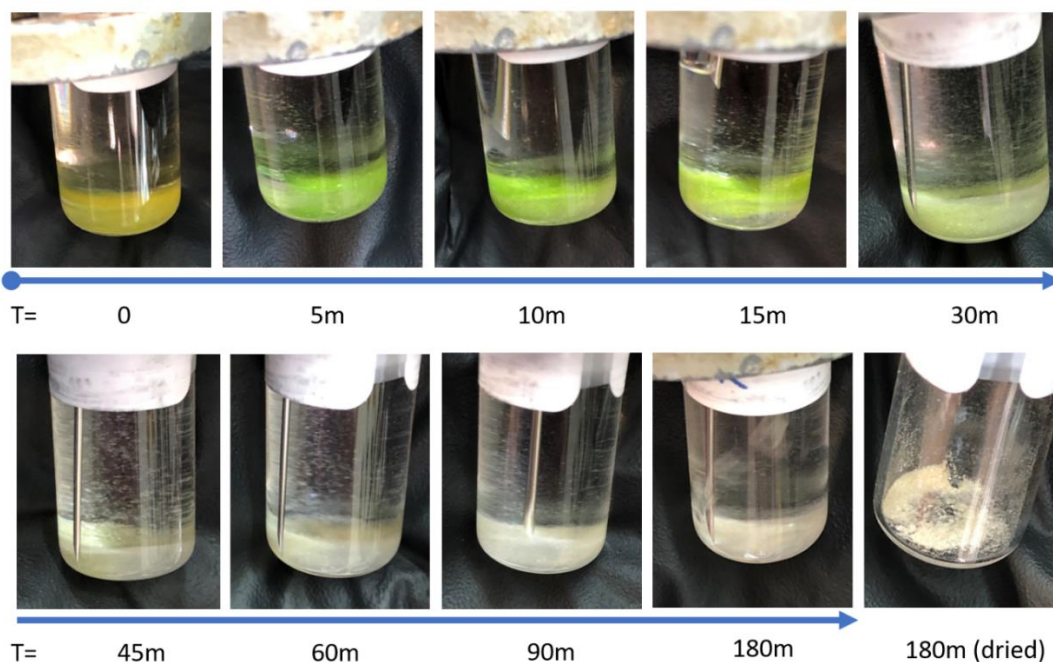


Figure 5.2.3.1: A bulk sample of $1 \cdot [\text{Mn}(\text{CO})_3\text{Br}]$ in freshly distilled THF under an Argon atmosphere shows the bright yellow colour characteristic of the $\text{Mn}(\text{CO})_3\text{Br}$ core. After ten minutes of visible photolysis under Argon delivery (note needle used for gentle Argon delivery) the crystals develop a green colour and eventually become colourless after approx. 3 hr.

Eventually, after 3 hr of photolysis the crystals become colourless and IR spectroscopy reveals negligible intensity in the CO stretching region, confirming quantitative displacement of CO from the coordination sphere (Figure 5.2.2.1). Importantly, the material maintains crystallinity during the photolysis experiment, as evidenced by PXRD (Figure S7.5.4.1).

To probe the chemistry taking place during photolysis, a time-resolved IR spectroscopy experiment was performed in which a sample of $1 \cdot [\text{Mn}(\text{CO})_3\text{Br}]$ in dry THF was dried under argon flow and placed between two NaCl disks with Nujol oil (Figure 5.2.3.3). The sample was irradiated with a visible torch for 20 minutes and the IR spectrum recorded at intermediate times. The duration of the experiment was limited to 20 minutes as the sample is accessible to adventitious water in the Nujol mull and therefore it is expected that the integrity of the photoproducts will be compromised by water, forming a mixture of species that do not reflect of the complexes formed in degassed solution. The IR spectrum of the starting material prior to photolysis shows three bands at 2029 , 1951 and 1906 cm^{-1} which are consistent with the neutral, well ordered $1\text{-fac-}[\text{Mn}(\text{CO})_3\text{Br}]$ complex observed in dry THF. After 10 seconds of irradiation the IR spectrum notably changes, with new bands α , β , γ , δ and ϵ appearing at 2043 cm^{-1} , 1965 cm^{-1} , 1918 cm^{-1} , 1864 cm^{-1} and 1840 cm^{-1} respectively.

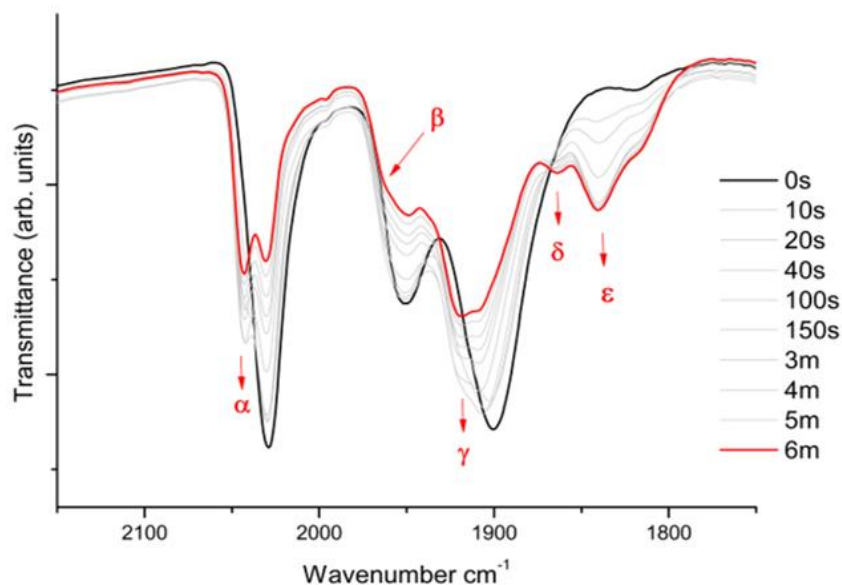


Figure 5.2.3.2. Time resolved IR spectra for $1 \cdot [\text{Mn}(\text{CO})_3\text{Br}]$ recorded at intermediate times during visible photolysis of MOF crystals in a Nujol mull. The intensity of all bands decrease over the course of the experiment, apart from the bands δ and ϵ (1864 and 1840 cm^{-1}) which grow rapidly and stabilise during the time-frame of the experiment.

It should be noted that the mononuclear complex $[\text{Mn}(\text{CO})_3\text{Br}(\text{THF})_2]$ reportedly displays $\nu(\text{CO})$ stretches at 2042 and 1933 cm^{-1} ,¹⁷⁷ which are similar to the α and β bands that appear during photolysis of $1 \cdot [\text{Mn}(\text{CO})_3\text{Br}]$ (c.f. α 2043 and γ 1918 cm^{-1}). However, the formation of a THF-solvated complex by photoinitiated de-chelation from **1** is unlikely since these species would escape the MOF crystals. As discussed below, no decrease in metalation is observed via EDX analysis of photolysed crystals. Rather, the proximity of the new band at 2043 cm^{-1} to that of the parent complex (2029 cm^{-1}) suggests both bands correspond to the respective symmetric stretching modes of two *fac*-tricarbonyl complexes. Two possibilities are worth considering, the first is that the new *fac*-complex originates from axial disorder of bromide, which may arise from recombination of CO with a solvated dicarbonyl complex and would yield a new isomer since the axial sites are not equivalent in $1 \cdot [\text{Mn}(\text{CO})_3\text{Br}]$. This is supported by the observation of axial bromide disorder during photocrystallography experiments (see below, Section 5.2.3.1). The second possibility is that bromide is ejected from the coordination sphere under photolysis, leading to the formation of a charged (solvated) complex (Figure 5.2.3.4) *fac*- $1 \cdot [\text{Mn}(\text{CO})_3(\text{THF})]\text{Br}$. Crystals of $1 \cdot [\text{Mn}(\text{CO})_3(\text{H}_2\text{O})]\text{Br}$ in EtOH (and MeCN), which contain a charged complex, give IR stretches at 2040, 1951, 1921 cm^{-1} and 2041, 1953, 1921 cm^{-1} respectively which closely resemble the new feature at 2043 cm^{-1} . It is possible that photolysis promotes loss of bromide by occupation of orbitals that are antibonding with regard to bromide, leading to ejection of bromide under photolysis, however this cannot be established without further computational and experimental work. It is noted in Section 5.2.3.1 that under photolysis, a bromide anion with occupancy of approximately 20% does appear in the MOF pore. However, at this stage it is not possible to confirm that either of these possibilities is correct; except to say that the new band at 2043 cm^{-1} most likely corresponds to a *fac*-tricarbonyl complex, either charged or neutral.

The appearance of the 2043 cm^{-1} band coincides with that of the new 1918 band, and both ultimately decline in intensity over the course of the experiment. This would suggest that the band at 1918 corresponds to the antisymmetric stretching mode of the new *fac*-tricarbonyl complex. Since the A'' mode does not contain a contribution from the axial CO it should not change significantly between the two facial isomers, the A'' mode of the new *fac*-isomer is therefore observed merely as a shoulder (β). Altogether, the new bands σ , β and γ are assigned to the new *fac*-tricarbonyl complex which arise either from axial disorder of bromide and CO or the ejection of Br from the coordination sphere.

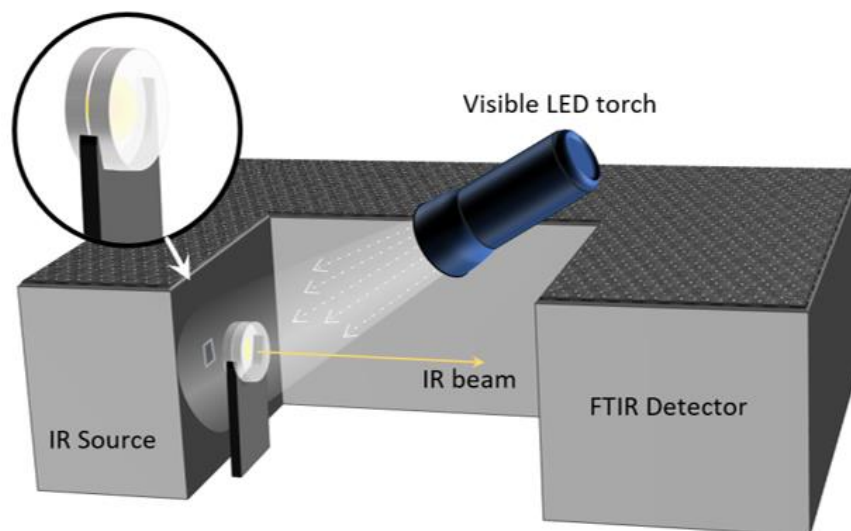


Figure 5.2.3.3: A schematic representation of the apparatus used for in-situ photolysis/IR spectroscopy of $1\cdot[\text{Mn}(\text{CO})_3\text{Br}]$. A sample (yellow) is contained between two NaCl disks in Nujol oil (inset), an IR spectrum is recorded and the sample is irradiated for a period of time prior to the collection of a second IR spectrum. The irradiation/data collection sequence is repeated to obtain a set of spectra.

The new $\nu(\text{CO})$ bands at 1840 and 1864 cm^{-1} are consistent with monocarbonyl or dicarbonyl $\text{Mn}(\text{I})$ photoproducts with coordinated THF such as $[(\text{bpy})\text{Mn}(\text{CO})_2(\text{THF})\text{Br}]$ and $[\text{CpMn}(\text{CO})_2(\text{THF})]$ which give $\nu(\text{CO})$ IR stretches at $1923/1849\text{ cm}^{-1}$ and $1934/1863\text{ cm}^{-1}$.^{70, 104} Monocarbonyl complexes typically produce CO IR stretches at slightly lower frequency than their dicarbonyl equivalents (Tables S7.5.1.1-5). The delayed appearance of the higher frequency band δ may be because it forms from the second *fac*-tricarbonyl complex which needs to be generated photochemically. Although the formation of new red-shifted $\nu(\text{CO})$ stretches is consistent with the formation of distinct CO-loss products under photolysis, it is impossible to conclusively assign these to specific CO-loss products without more extensive IR difference mapping and computational analysis.

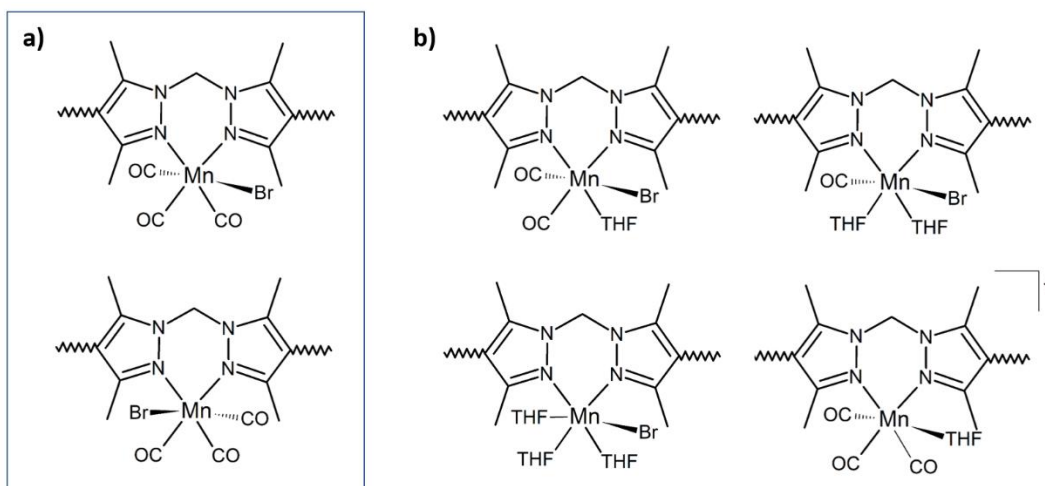


Figure 5.2.3.4: **a)** The isomers of $1\text{-[Mn(CO)}_3\text{Br]}$ arising from axial disorder of bromide **b)** photolysis could generate a range of CO loss products including dicarbonyl or mono-carbonyl intermediates, charged *fac*-tricarbonyl complexes or fully solvated complexes. This set of potential species could be expanded by considering isomers in which the bromide occupies the opposing axial site.

To better understand the origin of the new $\nu(\text{CO})$ bands observed during photolysis, the CO stretching frequencies of the possible products were calculated using DFT (Details are available in section 7.6). The possible compounds considered are the two mono-carbonyl complexes in which THF has replaced two equatorial CO ligands; two isomers arise due to axial disorder of the bromide and CO (Figure 5.2.3.5a and b). The structures used in the calculation contain only the organometallic fragment $[(3,5\text{-dimethylpyrazolyl)methane}]\text{Mn}(\text{CO})(\text{THF})_2\text{Br}$ because $\nu(\text{CO})$ stretching frequencies are sensitive to the immediate coordination environment of the metal centre and are unlikely to be affected by the extended structure of the MOF. To obtain more accurate frequency values, the computational results are scaled by a factor of 0.919 which was determined by comparison of the calculated and experimental stretching frequencies of the parent tricarbonyl complex. The scaling factor 0.919 is similar to that determined for related functionals.¹⁷⁸ Based on the calculations, each monocarbonyl complex produces a single $\nu(\text{CO})$ stretch (Figure 5.2.3.5c) which is redshifted relative to the parent tricarbonyl. Given constraints in the accuracy of computational IR stretches, the computational and experimental results can only be compared in a qualitative fashion. The redshifted $\nu(\text{CO})$ band correspond well with the new bands δ and ϵ that appear during photolysis in THF, supporting the conclusion that these bands correspond to carbonyl-loss products.

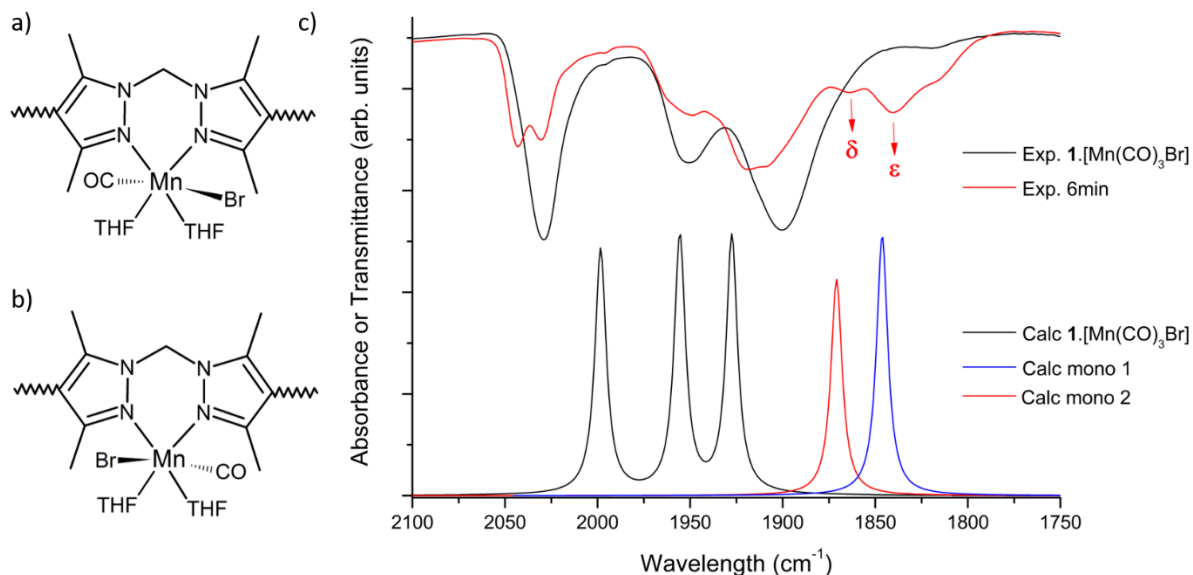


Figure 5.2.3.5: The two mono-carbonyl complexes that arise from Br/CO disorder, mono 1 **a)** and mono 2 **b)** were modelled. **c)** The scaled calculated CO stretches for the parent tricarbonyl and two mono-carbonyl THF complexes (bottom) are plotted against the experimental IR spectra for the parent tricarbonyl complex and a sample after 6 minutes of visible photolysis. The two new bands α and β compare well against the calculated stretches for the mono-carbonyl complexes.

Over the course of the TRIR experiment, the overall intensity of the CO stretches corresponding to the *fac*-tricarbonyl complexes decrease. This suggests that the parent complex as well as the complex responsible for the new band α at 2043 cm^{-1} (assigned to a *fac*-tricarbonyl) are consumed during the photolysis experiment to produce the new bands δ and ϵ which grow and eventually stabilise in intensity. In solution, extended photolysis produces colourless crystals which contain negligible intensity in the CO stretching region of the IR spectrum, which is consistent with the bleaching observed in Figure 5.2.3.2. However, the available TRIR spectroscopy system is limited to the first few minutes of photolysis because adventitious moisture cannot be excluded. To clarify the evolution of the complex under photolysis, the structural characterisation of the material at different time-points during photolysis was investigated using photocrystallography.

5.2.3.2 Photocrystallography using single crystals of $1\cdot[\text{Mn}(\text{CO})_3\text{Br}]$ in THF

Photocrystallography is a powerful technique for characterising highly reactive species using the crystalline matrix strategy. A single crystal is mounted on a diffractometer and a data set is collected

after which the crystal is photolyzed and successive X-ray structure data sets are collected to produce X-ray structure ‘snapshots’ of the photo-process (Figure 5.2.3.6). Photocrystallography has become a prominent technique for obtaining structural information about transient species formed during photolysis, including transition metal nitrides,¹⁷⁹ photo-induced isomerism^{56-57, 180-182} and coordinatively unsaturated metal sites.¹¹ In the context of $\mathbf{1}\cdot[\text{Mn}(\text{CO})_3\text{Br}]$, the goal of photocrystallography experiments is to structurally characterise photo-induced CO loss and concomitant formation of solvated species.

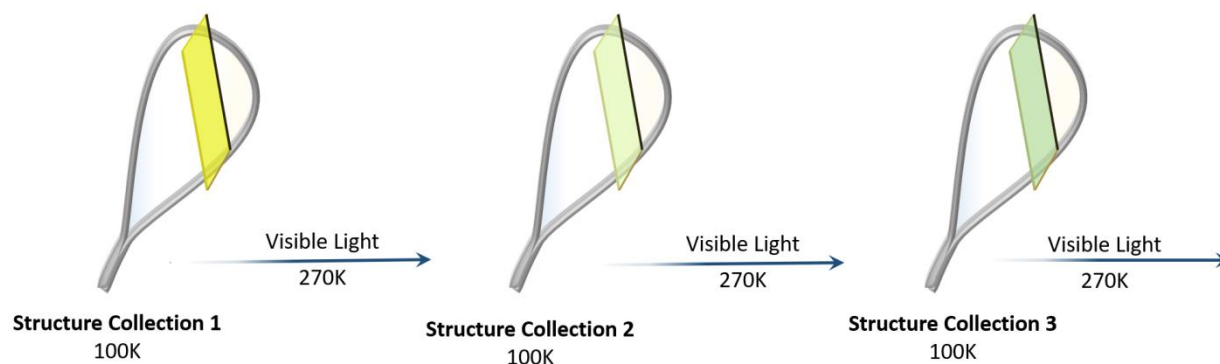


Figure 5.2.3.6: A schematic representation of the photocrystallography technique. A stylised single crystal is mounted on a nylon cryo-loop in Paratone-N oil and cooled to 100 K (150 K for in-house crystallography). An initial structure is collected after which the crystal is warmed to 270 K and irradiated with a visible torch for a period of time after which the light source is terminated and the crystal cooled to 100 K (150 K for in-house crystallography) for a second data-collection. This process is repeated as appropriate to obtain sufficient temporal resolution to observe the photo-induced changes in the coordination sphere.

The focus was initially placed on using photocrystallography to study the photolysis of $\mathbf{1}\cdot[\text{Mn}(\text{CO})_3\text{Br}]$ crystals loaded with distilled THF, although results obtained using other solvent systems will be discussed later. A single crystal of $\mathbf{1}\cdot[\text{Mn}(\text{CO})_3\text{Br}]$ loaded with THF was mounted on a cryo-loop on the Australian Synchrotron macromolecular crystallography beamline. An initial data-set was collected at 100K on the starting material, refinement of the structural model revealed a well-ordered complex with characteristic facial geometry (Figure 5.2.3.7a). The crystal was subsequently warmed to 270 K via a N_2 cryo-stream and photolyzed with a visible LED for a total irradiation time of two hours, with complete data-sets collected at 150 K at intermediate times (See Section 7.5.2 for details). In order to protect the crystal from atmospheric moisture and limit any evaporation of THF from the material due to the N_2 cryostream gas flow, the crystal was kept at or below 270 K throughout the experiment. After three hours of photolysis in solution the material displays negligible intensity in the CO stretching region of the spectrum. However, the time-scale of the bulk scale IR and photocrystallography experiments cannot be

compared directly, since in the latter the single-crystal is entirely exposed to visible radiation throughout the experiment. Therefore, during photocrystallography experiment, structures were collected from the single crystal at intermediate times since the single-crystal should arrive at its final state more rapidly than the two hours required for the bulk sample. During the course of the experiment the single crystal underwent a noticeable change in colour from yellow to colourless (Figure S7.5.6.1) over the course of 120 minutes of photolysis. The grey background in the video-microscope field of view makes it impossible to discern the yellow – green colour change observed for the bulk sample of crystal. Nonetheless, the appearance of a colourless phase after extended photolysis supports the premise that the structural information obtained from the single crystal after 120 minutes of photolysis should correspond to the material obtained after 2-3 hours of photolysis in solution (and characterised via IR spectroscopy).

A total of five data-sets were collected on the single crystal during the two-hour visible photolysis experiment. By refining each structural model against the respective experimental data-set and comparing the respective electron-density maps, the evolution of the complex can be revealed. When overlaid on the structural model, the electron density map obtained from the initial data collection clearly coincides with the *fac*-[Mn(CO)₃Br] complex (Figure 5.2.3.7a). The bromide anion resides on the axial site of the complex which is more open and the equatorial and remaining axial sites are occupied by CO.

The first photolysis dataset was collected after 30 minutes of irradiation, refinement of the electron density map confirmed that the overall MOF structure remains unchanged, however several significant differences are observed in the Mn(I) coordination sphere. The axial bromide and axial CO ligand remained in their original positions on the Mn(I) centre. However, the equatorial coordination sites are now occupied by a mixture of CO and THF ligands, the occupancies of which were refined to be 70 and 30 % respectively. This mixture of CO and THF is clearly evident after inspection of the electron density maps displayed in Figure 5.2.3.7b. This suggests that after 30 minutes of photolysis, a mixture of complexes is present, possibly consisting of a combination of the parent tricarbonyl complex and either di- or mono-carbonyl complexes. Since the X-ray structure provides a snapshot of the average coordination environment at a given time, it is not possible to determine whether the coordinated THF corresponds to a di-carbonyl complex in which both equatorial CO ligands have been replaced with THF or monocarbonyl complex in which only one CO has been replaced with THF (or a mixture of tricarbonyl and THF complexes etc.). The Mn-O(THF) bond length of 2.30(3) Å compares well to Mn(I) THF

complexes reported in the literature. For instance Maekawa *et al.* characterised the Mn(I) dimer $[\text{Cp}^*\text{Mn}(\text{THF})(\mu\text{-I})_2(1,3,5\text{-}t\text{-butyl-cyclopentadiene})]_2$ with a Mn-O(THF) bond length of 2.216(2).¹⁷⁵ A four-coordinate Mn(II) complex $[(\kappa\text{N-PyrtBu}_2\text{Me}_2)(\eta^2\text{-PyrtBu}_2\text{Me}_2)\text{Mn}(\text{THF})]$ (PyrtBu₂Me₂ = 2,5-di(*tert*-butyl)-3,4-dimethyl-pyrrole) was reported by Kreye *et al.* and possessed a Mn-O(THF) bond length of 2.1699(18) Å.¹⁸³ It is worth noting that a second data set was collected on a separate (slightly smaller) crystal after 15 minutes of irradiation and displayed a similar coordination sphere, with the THF and CO occupancies of 46 and 54 % respectively, reflecting the slightly smaller size of the crystal. No further data-sets were collected on this smaller crystal.

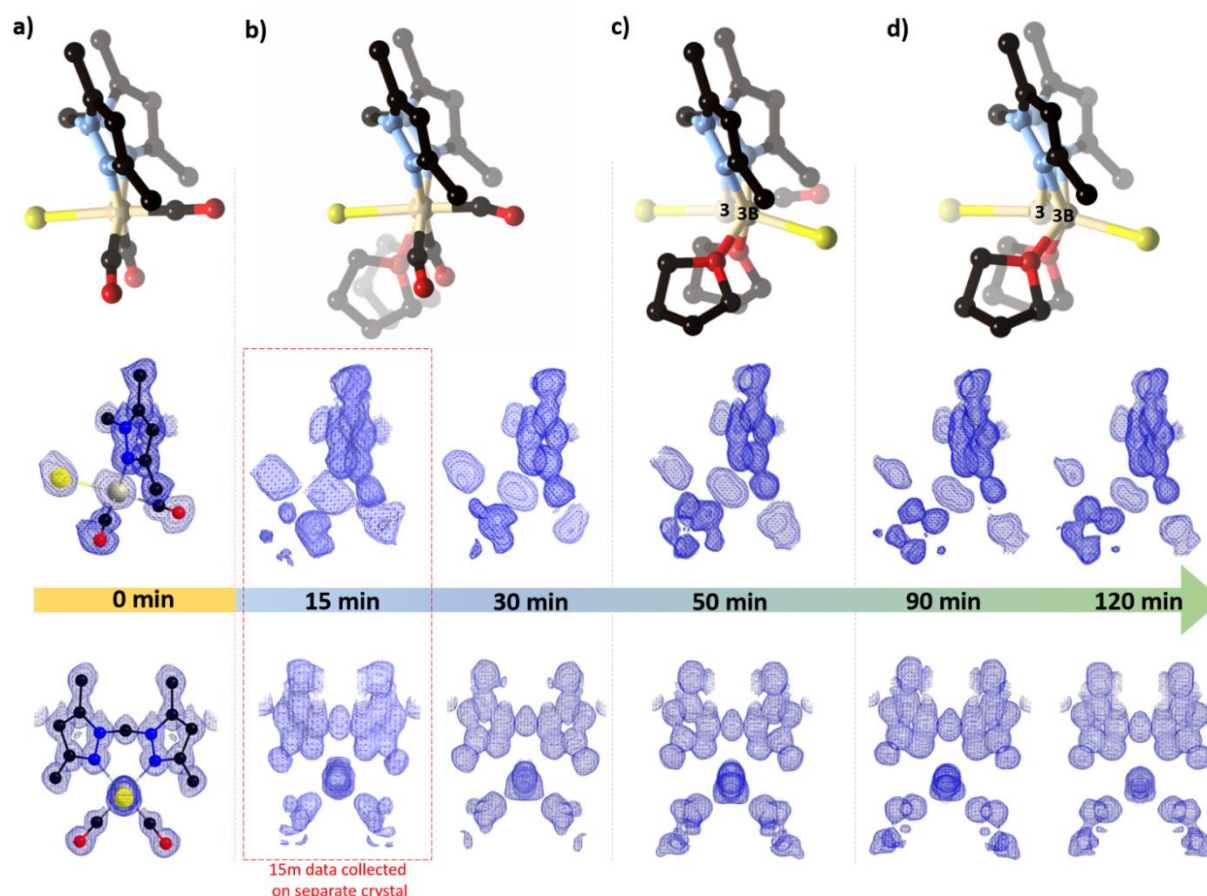


Figure 5.2.3.7. a) Structure and electron density mapping (side and front views) of the initial tricarbonyl complex prior to photolysis b) Structure and electron density mapping of the complex following 15 and 30 minutes of photolysis, displaying a mixture of CO and THF in the equatorial coordination sites. After 50 minutes of photolysis the bromide has become disordered over the two axial sites. Two Mn centres (Mn3 and Mn3B, left and right respectively in c and d) are modelled in the structure with an axial bromide associated with each and an axially bound CO ligand coordinated to Mn3 c), after further photolysis up to 120 minutes, no electron density associated with CO is observed in the electron density map and the occupancy of Mn3B exceeds that of Mn3, suggesting that Mn3B may be a 'final' product of photolysis and Mn3 corresponds to an intermediate carbonyl complex. Hydrogen atoms have been removed for clarity (C = black, N = purple, Mn = beige, Br = yellow, O = red).

However, after 50 minutes of visible irradiation, the electron density map reflects a more disordered coordination sphere. The IR spectroscopy experiments described above suggest that photolysis initially leads to a population of species which includes the parent tricarbonyl complex and CO loss products, eventually leading to the formation of a Mn photoproduct with no CO ligands. The data collection obtained at 50 minutes reflects this situation, it is evident that several complexes are superimposed at the N,N-chelation site. The Mn(I) site was modelled as two distinct Mn(I) centres, 'Mn3' and 'Mn3B' (Figure 5.2.3.7c and Figure 5.2.3.8a) which are displaced by 0.63(3) Å to accommodate their respective coordination spheres (the different backbone ligand environments could not be modelled adequately but there are large thermal ellipsoids for the pyrazole rings which suggest unresolved disorder). EDX analysis of the crystals following 3 hr of photolysis in THF indicated a 4:1 Mn:Br ratio which confirms that the metal centre is retained in the structure. Therefore, the occupancies of Mn3 and Mn3B in the 50 minute collection were allowed to refine against one-another with an overall occupancy of 100%, yielding occupancies of 60 and 40% respectively.

The coordination sphere of Mn3 contains a lone CO ligand in the axial coordination site and a bromide anion in the opposing axial site (Figure 5.2.3.7c and Figure 5.2.3.8a). The occupancy of the bromide anion was modelled as 50% to reflect the presence of a 20% occupied bromide anion in the pore of the MOF (The remaining 30% of bromide required for charge balance was assigned to Mn3B, see below). A THF ligand is observed in the equatorial coordination site although it is not evident whether this ligand is coordinated exclusively to either Mn3 or Mn3B, or present in both complexes. Thus, it is possible that CO is present in the equatorial position(s) of Mn3, perhaps disordered with THF (Figure 5.2.3.8b ii); however the disorder in the structure prevents this from being established with certainty.

Mn3B contains a bromide anion in the axial coordination site on the opposing side to that occupied by bromide in the earlier structures (or Mn3). This intriguing migration of bromide to the opposing axial site could be a result of the steric interactions between the equatorial THF ligands and the methyl substituents on the pyrazole rings which may favour migration of bromide to the less open side of the complex by allowing the equatorial the THF ligands to cant away from the methyl substituents. Interestingly, the occupant of the remaining axial coordination site could not be determined; no electron density corresponding to CO or THF could be discerned in the electron density map. This may be due to disorder in the complex or because the coordination site is truly vacant (Figure 5.2.3.8bv). The steric demands of THF would likely preclude a third THF ligand from occupying the remaining axial site, making

the latter option plausible although computational work is necessary to support these conclusions. Thus, it is evident that after 50 minutes of photolysis, two distinct Mn complexes are present: a complex with at least one carbonyl ligand (Mn3) and a new THF complex in which the bromide anion has migrated to the opposing axial site relative to the earlier structures. Due to the disorder in the structure, it is not possible to ascertain whether other CO/THF ligands are disordered over the coordination spheres of Mn3 or Mn3B.

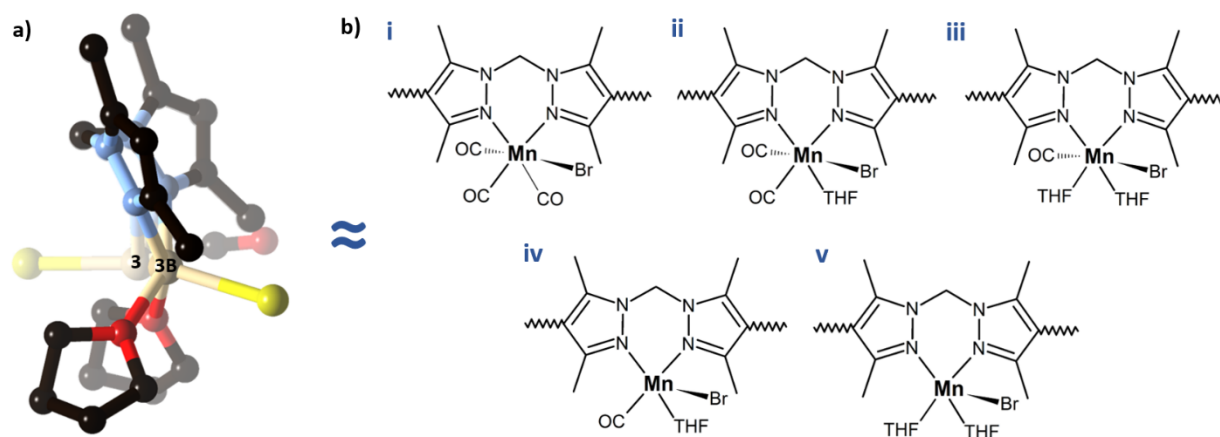


Figure 5.2.3.8. a) The X-ray structure obtained after 50 minutes of irradiation indicates that the MOF contains a mixture of Mn(I) complexes including a THF adduct (Mn3B) and a carbonyl containing complex (Mn3). Although disorder prevents complete elucidation of the coordination sphere, several possible structures can be proposed b) including residual tricarbonyl complex (i), a dicarbonyl THF complex (ii), a monocarbonyl bis-THF complex (iii), a five-coordinate monocarbonyl THF complex (iv) and a five-coordinate bis-THF complex (v). Hydrogen atoms have been removed for clarity (C = black, N = purple, Mn = beige, Br = yellow, O = red).

Over time the occupancy of Mn3 and Mn3B and their respective bromide anions evolves; after 120 minutes the occupancies have reversed such that Mn3 and Mn3B have occupancies of 36 and 64% respectively. Therefore, although the coordination environment of the two complexes Mn3 and Mn3B could not be fully elucidated, the evolution of their populations during photolysis suggests that Mn3B corresponds to a 'final' CO loss product while Mn3 corresponds to an intermediate species with residual CO in the coordination sphere. This conclusion is supported by the presence of CO in the coordination sphere of Mn3 after 50 minutes (Figure 5.2.3.7c). In the later structures (90 and 120 minutes) the occupancy of Mn3 is too low to satisfactorily model CO in this position (Figure 5.2.3.7d), although residual electron density is present in the expected region. The presence of THF in the coordination

sphere of Mn3B is evident in these later structures, supporting the premise that Mn3B is a photoproduct likely containing two equatorial THF ligands in the coordination sphere. Intriguingly, although the occupancy of Mn3B increases to 64%, electron density is still not observed in the remaining 'vacant' axial coordination site, suggesting that this site is either vacant or occupied by a disordered ligand that is concealed beneath the electron density of Mn3 and its associated bromide anion. Several possible structures for Mn3 and Mn3B are proposed in Figure 5.2.3.8b, further experiments are underway to clarify the identity of these species.

The THF ligands are well defined after 50 minutes of irradiation, suggesting that the photolysis process is rapid and that the labilised CO escapes the crystal. The changes observed in the electron density map are supported by the IR spectroscopy experiments described in Section 5.2.3.1. In particular, the bromide disorder observed in the electron density map may correspond with the growth of a new symmetric CO stretch at 2043 cm^{-1} , assigned to a new *fac*-tricarbonyl isomer arising from axial disorder of bromide. It is possible that initial CO loss and recombination could cause a scrambling of the complex, leading to disorder of bromide across the axial sites of the complex observed in the X-ray structure. However, it was also posited that this new IR feature may arise from the formation of a charged solvated complex upon ejection of bromide from the coordination sphere (Figure 5.2.3.4). Thus, without more concrete structural characterisation it is not possible to compare the IR spectroscopy and photocrystallography results in detail, although the eventual formation of a bis-THF complex is consistent with bleaching of the CO stretching bands observed during photolysis in THF. However, as alluded to above, there are some issues that have hampered the interpretation of the data. Firstly, the disordered bromide introduces significant structural disorder and therefore the presence of CO ligand(s), concealed beneath the bromide electron density, cannot be excluded at this point. The complex could therefore be five-coordinate with a vacant axial coordination site, or octahedral with residual carbonyl ligand(s). The presence of mono-carbonyl complex cannot be excluded based on the IR spectroscopy data either, since adventitious water could compromise such a sensitive species during IR sample preparation. Further experiments will employ a custom IR sample chamber to monitor photolysis under an inert atmosphere in order to conclusively characterise the final photoproduct observed via photocrystallography.

It is worth noting that the THF adducts obtained via photolysis of $[\text{CpMn}(\text{CO})_3]$ and $[\text{TpMn}(\text{CO})_3]$ have never been characterised crystallographically or isolated; only the significantly more stable Re derivative $[\text{CpRe}(\text{CO})_2(\text{THF})]$ has been isolated.⁷⁵ By housing the parent tricarbonyl complex inside **1**, the formation

of a likely bis-THF complex was successfully observed using in-situ photocrystallography. This can be achieved because the complex is site-isolated within the MOF matrix and pre-organised within the crystalline lattice, which eliminates the need to crystallise the photoproduct. This set of results builds on the work of Champness *et al.* who observed dicarbonyl intermediates via IR spectroscopy, but only structurally characterised the *fac-to-mer* photo-isomerism because the photodissociated CO was trapped within the non-porous framework. Within $\mathbf{1}\cdot[\text{Mn}(\text{CO})_3\text{Br}]$ however, the intrinsic porosity has clearly facilitated a net loss of CO and the formation of solvated complexes which can be characterised crystallographically. Although the coordination sphere is disordered, this preliminary result verifies that the combination of photocrystallography and a porous crystalline matrix can provide valuable insight into metal complexes that form during photolysis in the presence of weakly coordinating solvent.

5.2.3.3. Photolysis in Acetonitrile and Toluene

Considering the unresolved questions regarding the Mn(I) coordination environment after photolysis in THF, acetonitrile was investigated as a possible alternative solvent with a view towards eliminating disorder in the complex. The relatively small size of acetonitrile compared to THF is expected to allow it to bind to the metal centre to give a well-ordered complex without axial disorder of bromide. A sample of $\mathbf{1}\cdot[\text{Mn}(\text{CO})_3\text{Br}]$ was washed with dry acetonitrile, after which the material retained the bright yellow colour characteristic of the $[\text{Mn}(\text{CO})_3]$ moiety. However, after five days standing in acetonitrile in the dark, the solution developed a pale yellow colour indicating leaching of the Mn(I) centre from the MOF. IR spectroscopy of the yellow MOF crystals reveals a decrease in the intensity of the $\nu(\text{CO})$ stretches, confirming that some of the Mn(I) complexes have been scavenged from the MOF by acetonitrile. This observation is in line with the fact that the reaction between $\mathbf{1}$ and $[\text{Mn}(\text{CO})_5\text{Br}]$ in acetonitrile at 50°C does not yield any metallated product. As a result, the photolysis experiments described below were performed on samples of $\mathbf{1}\cdot[\text{Mn}(\text{CO})_3\text{Br}]$ which had been washed with acetonitrile within 24 hr of the experiment and therefore remained metallated.

Much like the THF experiments described above, initial investigations probed the photochemistry of $\mathbf{1}\cdot[\text{Mn}(\text{CO})_3\text{Br}]$ in dry acetonitrile under constant argon degas. Several key differences are observed between the photolysis of samples in THF and acetonitrile. Firstly, in acetonitrile the material changes colour from yellow to colourless without the green intermediate observed in THF. The colour change is significantly more rapid in acetonitrile, the sample changes from yellow to colourless within the first 20

minutes of photolysis. This is expected since acetonitrile is a significantly stronger ligand than THF, and therefore the acetonitrile adduct would be expected to undergo slower recombination with dissociated CO, leading to more rapid evolution of CO from the material.

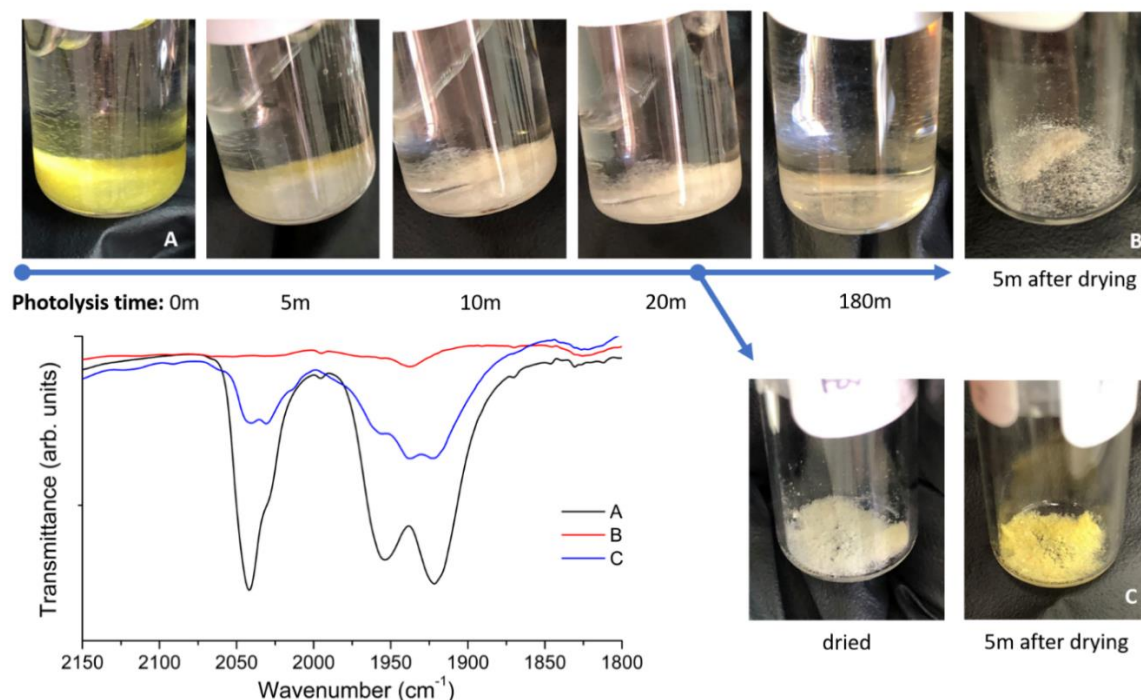


Figure 5.2.3.9: Photolysis of $1\text{-}[\text{Mn}(\text{CO})_3\text{Br}]$ in dry acetonitrile under argon degas results in a rapid colour change from bright yellow to colourless within 20 minutes. When a sample is removed after 20 minutes of photolysis and dried under Argon flow, it recovers the bright yellow colour of the parent material within 5-10 minutes (C), indicating that photo-dissociated CO remains trapped within the crystal lattice and recombines with the Mn(I) centre in the absence of photolysis. Extended photolysis over the course of 3 hours results in complete loss of CO from the material, as evidenced by IR spectroscopy (spectrum B) and the failure of the material to regain its yellow colour upon drying (B).

After 20 minutes of visible photolysis under argon degas, the material appears colourless. After removing the solvent and gently drying the sample under Argon gas flow, the sample recovers its bright yellow colour over the course of 5-10 minutes (Figure 5.2.3.9). This observation indicates that within the first 20 minutes of photolysis, CO dissociates from the Mn(I) centres to give the colourless photoproduct, but the short duration is not sufficient to allow the free CO to escape the crystal lattice. As a result, in the absence of further photolysis the retained CO recombines with the Mn(I) centre to form a yellow

Mn(I) carbonyl complex, as observed after 5 minutes in the dark. IR spectroscopy of the yellow crystals formed in this way revealed relatively strong $\nu(\text{CO})$ stretches that are similar to the parent complex (Figure 5.2.3.9). The conversion of the colourless photoproduct into the yellow carbonyl complex confirms that the colourless complex which forms within the first few minutes of photolysis in acetonitrile is a Mn(I) species, since a Mn(II) or Mn(III) complex could not regenerate a carbonyl complex. Similarly, the green crystals observed during photolysis in THF return to a yellow colour upon drying. The observation that CO remains trapped within the crystal lattice over short periods of photolysis in solution is consistent with the findings of Champness *et al.* who were unsuccessful in permanently removing CO from a densely packed MOF, instead observing rapid recombination of photodissociated CO with a Mn(I) solvent adduct.

Continuous photolysis of $1 \cdot [\text{Mn}(\text{CO})_3\text{Br}]$ in dry acetonitrile for three hours results in complete loss of CO from the material. The crystals appear colourless, as they did after 20 minutes of photolysis, but upon drying under argon flow they do not recover the yellow hue observed previously. This confirms that during extended photolysis the dissociated CO is able to escape the crystal lattice, presumably leaving behind a solvated Mn(I) centre. The material retains crystallinity during the photolysis experiment, as evidenced by PXRD (Figure S7.5.4.1). Work is currently underway to investigate the structure of the Mn(I) complex generated during photolysis in acetonitrile by using photocrystallography.

Photolysis in toluene was investigated because of the possibility of forming Mn(I) π -arene complexes which are of interest in C-H activation chemistry. The photolysis of $[\text{CpMn}(\text{CO})_3]$ in toluene and xylene has been shown to produce the corresponding π -arene complex $[\text{CpMn}(\text{CO})_2(\pi\text{-arene})]$,⁸⁵ while extended photolysis can result in complete CO loss and the formation of the η^6 -benzene complex $[\text{CpMn}(\eta^6\text{-benzene})]$.⁴⁷ Photolysis of $1 \cdot [\text{Mn}(\text{CO})_3\text{Br}]$ in dry toluene under argon degas led to a colour change from yellow to colourless which progressed slowly over the course of three hours (Figure 5.2.3.10a). Unlike in acetonitrile or THF, the material retains a bright yellow colour after 45 minutes of photolysis, suggesting that the rate of CO loss is slower in toluene. This is consistent with the poor coordinating ability of toluene relative to acetonitrile and likely reflects the greater steric demands of toluene relative to THF. Once again, no green colour is observed during photolysis in toluene. IR spectroscopy of the material after three hours of photolysis reveals quantitative loss of CO. EDX analysis of the material after photolysis confirmed the retention of the Mn(I) complex within the material (Table S7.5.5.1), while PXRD confirms that the material retains crystallinity (Figure S7.5.4.1). Work is currently underway to determine the structure of the complex formed during photolysis in toluene.

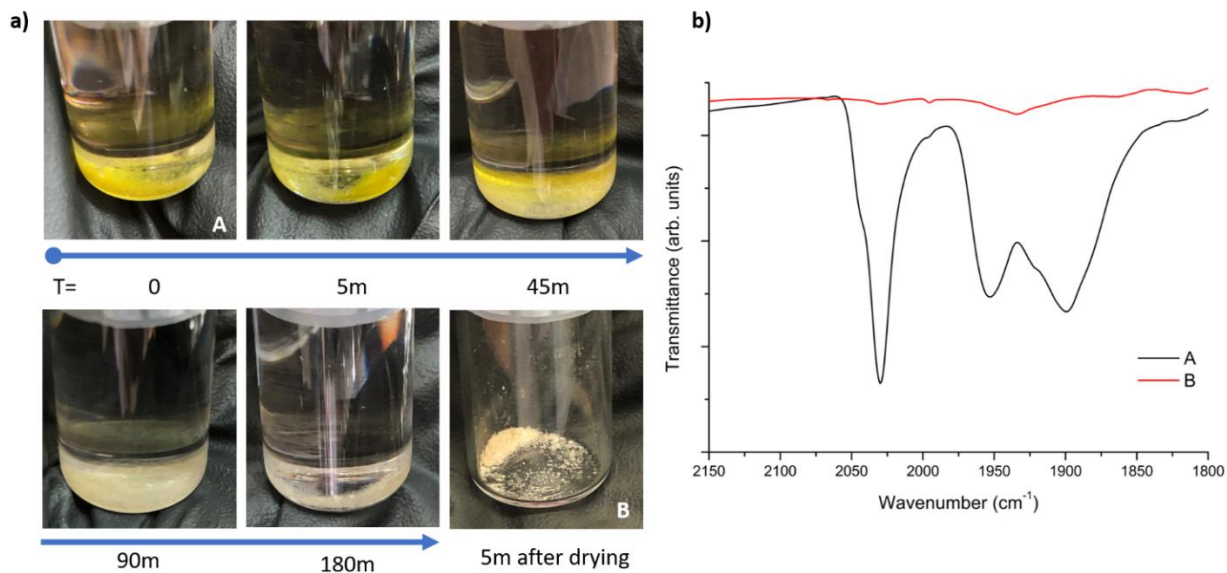


Figure 5.2.3.10: a) Photolysis of $1 \cdot [\text{Mn}(\text{CO})_3\text{Br}]$ in dry toluene under argon degas results in a slow colour change from bright yellow to colourless within 180 minutes. IR spectroscopy reveals complete loss of CO from the material after 180 minutes of photolysis b).

5.3 Conclusions and Future Directions

The exploration of $1 \cdot [\text{Mn}(\text{CO})_3\text{Br}]$ photochemistry was intended to harness the porosity and site-isolation of MOFs to produce site-isolated, coordinatively unsaturated Mn(I) photoproducts that could be structurally characterised and employed in small molecule activation. In line with the properties of similar Mn(I) complexes, the material was found to undergo quantitative CO loss under both UV and visible light. In the presence of dry THF, visible photolysis causes a colour change from bright yellow to green and eventually colourless; indicating a net change in the coordination sphere of the complex. Time-resolved IR spectroscopy experiments revealed that the initial few minutes of photolysis coincide with the appearance of new CO stretches which were proposed to correspond to a mixture of CO-loss products and a new *fac*-tricarbonyl isomer that arises from either disorder of bromide across the axial coordination sites or photodissociation of bromide. These outcomes are supported by photocrystallography experiments in which successive X-ray crystal structures were collected on a single $1 \cdot [\text{Mn}(\text{CO})_3\text{Br}]$ crystal during photolysis. Refinement of each dataset and comparison of the electron density maps revealed that the photolysis is accompanied by displacement of the bromide anion to the other axial site (disorder) and replacement of the equatorial CO ligands with O-bound THF. The disorder of the metal centre complicates the model refinement for the latter datasets and prevents the complete structural characterisation of the photo-process to date, although the formation of a CO-loss product is supported by IR spectroscopy.

The disorder of bromide across both axial sites during photolysis makes it difficult to fully elucidate the coordination sphere. One potential solution to this issue is the elimination of bromide via ligand exchange with a non-coordinating anion such as hexafluorophosphate. Presumably the remaining coordination site would be occupied by solvent, although there is precedent for replacing this with a fourth CO ligand by reaction with CO gas in solution.¹⁸⁴ This would generate a tetracarbonyl complex, $1 \cdot [\text{Mn}(\text{CO})_4]\text{X}$ ($\text{X} = \text{Br}^-$, PF_6^- , BF_4^-). A potential downside to this approach is that the absence of bromide in the coordination sphere would blue-shift the MLCT band and possibly reduce the photoreactivity of $1 \cdot [\text{Mn}(\text{CO})_3\text{Br}]$ towards visible light.⁴¹

A second avenue worth exploring is the reaction between $1 \cdot [\text{Mn}(\text{CO})_3\text{Br}]$ and imidazole. Based on the work of Strinitz *et al.*, imidazole will displace bromide to give $1 \cdot [\text{Mn}(\text{CO})_3(\text{imidazole})]\text{Br}^-$ which presents an alternative path to the exclusion of bromide from the coordination sphere.¹⁵⁹ Mn(I) complexes containing substituted imidazole possess interesting photochemical behaviour centred around ejection

of imidazole from the coordination sphere.¹⁸⁵ Similar behaviour has been observed for substituted pyridine complexes.⁷⁶ Thus, $\mathbf{1}\cdot[\text{Mn}(\text{CO})_3(\text{imidazole})]\text{Br}$ may provide access to new photochemistry and a less disordered photoproduct.

Considering the apparent stability of $[\text{CpMn}(\text{CO})_2(\text{N}_2)]$, the photolysis of $\mathbf{1}\cdot[\text{Mn}(\text{CO})_3\text{Br}]$ in the presence of a N_2 rich solution is of tremendous interest. Coordinated N_2 is easily discerned by IR spectroscopy which mitigates the issue of discerning CO/N_2 via X-ray crystallography, and it would serve as a good placeholder ligand as well as being a novel species.

A custom IR spectroscopy cell which will facilitate in-situ IR spectroscopy during photolysis under an inert atmosphere or vacuum is being developed and will allow more conclusive study of the photo-process. This will allow the photolysis process to be observed in its entirety without the sample becoming compromised by adventitious water (an issue with the present experimental design). Furthermore, picosecond TRIR spectroscopy studies are underway at the University of Nottingham, under the supervision of Prof. Michael George and Prof. Neil Champness. These experiments will develop a detailed understanding of the photolysis process on the ultra-fast time-scale, potentially identifying transient species that provide insight into the photoproducts observed via photocystallography. The existing IR spectroscopy studies have focused on the formation of photo-products such as solvent adducts that form over the course of minutes to hours of photolysis. Ultra-fast spectroscopy complements these experiments by illuminating the transient species that lead to the observed final photoproducts. Computational chemistry is key to this aspect of the project because it provides scaffold with which to interpret the experimental results.

From the photocystallography and IR spectroscopy evidence gathered so far, it is evident that photolysis of $\mathbf{1}\cdot[\text{Mn}(\text{CO})_3\text{Br}]$ in solution gives rise to new complexes bearing THF ligands. Although these species have been used ubiquitously as intermediates in ligand exchange chemistry, they have never been isolated. The observation of a THF-adduct in the pores of $\mathbf{1}$ following photolysis validates the crystalline matrix strategy as a powerful tool for studying photochemistry and the chemistry of reactive metal complexes. Building on this set of results, we aim to fully characterise the THF-adduct described above while also expanding this work to include more weakly binding solvents such as diethylether, dichloromethane and alkanes. The use of THF adducts for ligand exchange chemistry is well established and we intend to use the bis-THF complex as a reagent in the future.

Small molecule activation using reactive Mn(I) complexes generated via photochemistry remains the ultimate goal of this project. The structural characterisation of Mn(I) photoproducts bearing placeholder ligands such as THF is an important step towards the ultimate goal of studying the interaction between such complexes and small molecules. Preliminary experiments will focus on studying ligand exchange chemistry, such as the replacement of THF with cyclooctadiene or norbornadiene, which has been studied extensively in the literature. If this pursuit is successful, the incorporation of more reactive species into the coordination sphere will be investigated. Silanes such as triethyl silane represent a good starting point to investigate the reactivity of Mn(I) photoproducts. The alkane borylation reaction described in Section 5.1.10 is another interesting example because it is postulated to occur via an oxidative addition mechanism under mild conditions. The relatively small nature of the reagents and unconfirmed, topical mechanism makes this an ideal target for study within the pores of **1**.

Finally, the crystalline matrix strategy can be applied to other photo-active metal complexes within **1**, such as Rh(I), Ir(I) and Re(I) carbonyl complexes which have already been incorporated within the framework. Finally, the azide complex described in Chapter 4, **1**·[Mn(CO)₃N₃], is a promising target for photochemistry owing to the presence of the azide anion. Photolysis of azide complexes can generate the corresponding nitride via evolution of N₂ gas, the structural characterisation of which would be of great interest due to the immense reactivity of nitrenes.

In conclusion, the preliminary work on photochemistry inside **1**·[Mn(CO)₃Br] has been successful in obtaining the first structural characterisation of the solvent adduct formed immediately after photolysis in solution. Building on this work, it is intended that full characterise this and several new solvent adducts using in-situ photocrystallography and custom made IR spectroscopy cells will be achieved. There is broad scope and precedent for future work using different solvent systems and Mn(I) complexes bearing different anions and supporting ligands such as imidazole. This project will also expand to accommodate Rh(I), Ir(I), W(0), Cr(0), Mo(0) and Re(I) metal carbonyl complexes which also have a well-developed photochemistry.

5.4 References

- (1) Wrighton, M. S.; Ginley, D. S.; Schroeder, M. A.; Morse, D. L. *pac* **1975**, *41*, 671.
- (2) Labinger, J. A.; Bercaw, J. E. *Nature* **2002**, *417*, 507.
- (3) Shilov, A. E.; Shul'pin, G. B. *Chem. Rev.* **1997**, *97*, 2879.
- (4) Perutz, R. N.; Procacci, B. *Chem. Rev.* **2016**, *116*, 8506.
- (5) Perutz, R. N. *pac* **1998**, *70*, 2211.
- (6) Weiller, B. H.; Wasserman, E. P.; Bergman, R. G.; Moore, C. B.; Pimentel, G. C. *J. Am. Chem. Soc.* **1989**, *111*, 8288.
- (7) Asbury, J. B.; Ghosh, H. N.; Yeston, J. S.; Bergman, R. G.; Lian, T. *Organometallics* **1998**, *17*, 3417.
- (8) Lian, T.; Bromberg, S. E.; Yang, H.; Proulx, G.; Bergman, R. G.; Harris, C. B. *J. Am. Chem. Soc.* **1996**, *118*, 3769.
- (9) McNamara, B. K.; Yeston, J. S.; Bergman, R. G.; Moore, C. B. *J. Am. Chem. Soc.* **1999**, *121*, 6437.
- (10) Bengali, A. A.; Schultz, R. H.; Moore, C. B.; Bergman, R. G. *J. Am. Chem. Soc.* **1994**, *116*, 9585.
- (11) Kawano, M.; Kobayashi, Y.; Ozeki, T.; Fujita, M. *J. Am. Chem. Soc.* **2006**, *128*, 6558.
- (12) Chadwick, F. M.; Rees, N. H.; Weller, A. S.; Kramer, T.; Iannuzzi, M.; Macgregor, S. A. *Angew. Chem., Int. Ed. Engl.* **2016**, *55*, 3677.
- (13) Chadwick, F. M.; Kramer, T.; Gutmann, T.; Rees, N. H.; Thompson, A. L.; Edwards, A. J.; Buntkowsky, G.; Macgregor, S. A.; Weller, A. S. *J. Am. Chem. Soc.* **2016**, *138*, 13369.
- (14) Pike, S. D.; Thompson, A. L.; Algarra, A. G.; Apperley, D. C.; Macgregor, S. A.; Weller, A. S. *Science* **2012**, *337*, 1648.
- (15) Wang, X.; Wovchko, E. A. *J. Phys. Chem. B* **2005**, *109*, 16363.
- (16) Wovchko, E. A.; Zubkov, T. S.; Yates, J. T. *J. Phys. Chem. B* **1998**, *102*, 10535.
- (17) Wovchko, E. A.; Yates, J. T. *Langmuir* **1999**, *15*, 3506.
- (18) Ballinger, T. H.; Yates, J. T. *J. Phys. Chem.* **1992**, *96*, 9979.
- (19) Ballinger, T. H.; Yates, J. T. *J. Am. Chem. Soc.* **1992**, *114*, 10074.
- (20) Huxley, M. T.; Burgun, A.; Ghodrati, H.; Coghlan, C. J.; Lemieux, A.; Champness, N. R.; Huang, D. M.; Doonan, C. J.; Sumbly, C. J. *J. Am. Chem. Soc.* **2018**, *140*, 6416.
- (21) Bloch, W. M.; Burgun, A.; Coghlan, C. J.; Lee, R.; Coote, M. L.; Doonan, C. J.; Sumbly, C. J. *Nat. Chem.* **2014**, *6*, 906.
- (22) Burgun, A.; Coghlan, C. J.; Huang, D. M.; Chen, W.; Horike, S.; Kitagawa, S.; Alvino, J. F.; Metha, G. F.; Sumbly, C. J.; Doonan, C. J. *Angew. Chem., Int. Ed. Engl.* **2017**, *56*, 1.

- (23) Bhatt, V., Chapter 8 - Metal Carbonyls. In *Essentials of Coordination Chemistry*, Bhatt, V., Ed. Academic Press: 2016; pp 191-236.
- (24) Abel, E. W.; Stone, F. G. A. *Quarterly Reviews, Chemical Society* **1969**, *23*, 325.
- (25) Schutzenberger, P. *Journal of the Chemical Society* **1871**, *24*, 994.
- (26) Kumar, A.; Sun, S.; Lees, A. J. *Top Organomet Chem* **2009**, *29*, 1.
- (27) Gandeepan, P.; Müller, T.; Zell, D.; Cera, G.; Warratz, S.; Ackermann, L. *Chem. Rev.* **2018**.
- (28) Kottelat, E.; Fabio, Z. *Inorganics* **2017**, *5*, 24.
- (29) Bourrez, M.; Molton, F.; Chardon-Noblat, S.; Deronzier, A. *Angew. Chem., Int. Ed. Engl.* **2011**, *50*, 9903.
- (30) Agarwal, J.; Shaw, T. W.; Schaefer, H. F.; Bocarsly, A. B. *Inorg. Chem.* **2015**, *54*, 5285.
- (31) Sampson, M. D.; Nguyen, A. D.; Grice, K. A.; Moore, C. E.; Rheingold, A. L.; Kubiak, C. P. *J. Am. Chem. Soc.* **2014**, *136*, 5460.
- (32) Walsh, J. J.; Neri, G.; Smith, C. L.; Cowan, A. J. *Organometallics* **2018**.
- (33) Francke, R.; Schille, B.; Roemelt, M. *Chem. Rev.* **2018**, *118*, 4631.
- (34) Schatzschneider, U. *Inorganica Chimica Acta* **2011**, *374*, 19.
- (35) Berends, H.-M.; Kurz, P. *Inorganica Chimica Acta* **2012**, *380*, 141.
- (36) Rimmer, R. D.; Pierri, A. E.; Ford, P. C. *Coord. Chem. Rev.* **2012**, *256*, 1509.
- (37) Vlček, A. n. *Coord. Chem. Rev.* **1998**, *177*, 219.
- (38) Chakraborty, I.; Carrington, S. J.; Mascharak, P. K. *Acc. Chem. Res.* **2014**, *47*, 2603.
- (39) Kottelat, E.; Ruggi, A.; Zobi, F. *Dalton. Trans.* **2016**, *45*, 6920.
- (40) Carrington, S. J.; Chakraborty, I.; Mascharak, P. K. *Dalton. Trans.* **2015**, *44*, 13828.
- (41) Chakraborty, I.; Carrington, S. J.; Mascharak, P. K. *ChemMedChem* **2014**, *9*, 1266.
- (42) Sachs, U.; Schaper, G.; Winkler, D.; Kratzert, D.; Kurz, P. *Dalt. Trans.* **2016**, *45*, 17464.
- (43) Rimmer, R. D.; Richter, H.; Ford, P. C. *Inorg. Chem.* **2010**, *49*, 1180.
- (44) Mede, R.; Traber, J.; Klein, M.; Górls, H.; Gessner, G.; Hoffmann, P.; Schmitt, M.; Popp, J.; Heinemann, S. H.; Neugebauer, U., *et al.* *Dalton. Trans.* **2017**, *46*, 1684.
- (45) Nagel, C.; McLean, S.; Poole, R. K.; Braunschweig, H.; Kramer, T.; Schatzschneider, U. *Dalton. Trans.* **2014**, *43*, 9986.
- (46) Treichel, P. M.; Mueh, H. J. *Inorganica Chimica Acta* **1977**, *22*, 265.
- (47) Kruck, T.; Krause, V. *Naturforsch.*, **1972**, *27B*, 302.
- (48) Sandhu, S. S.; Mehta, A. K. *Inorg. Nucl. Chem. Letters* **1971**, *7*, 891.
- (49) Butler, I. S.; Coville, N. J. *J. Organomet. Chem.* **1974**, *80*, 235.

- (50) Barbeau, C. *Canadian Journal of Chemistry* **1967**, *45*, 161.
- (51) Paulson, P. L.; Segal, J. A. *J.C.S Dalton* **1975**, 2387-2392.
- (52) Schoenberg, A. R.; Anderson, W. P. *Inorg. Chem.* **1972**, *11*, 85.
- (53) Afzali, N.; Tangestaninejad, S.; Moghadam, M.; Mirkhani, V.; Mechler, A.; Mohammadpoor-Baltork, I.; Kardanpour, R.; Zadehahmadi, F. *Appl. Organometal Chem.* **2018**, *32*, 1.
- (54) Oh, M.; Carpenter, G. B.; Sweigart, D. A. *Acc. Chem. Res.* **2004**, *37*, 1.
- (55) Choi, K. M.; Kim, D.; Rungtaweivoranit, B.; Trickett, C. A.; Barmanbek, J. T. D.; Alshammari, A. S.; Yang, P.; Yaghi, O. M. *J. Am. Chem. Soc.* **2017**, *139*, 356.
- (56) Blake, A. J.; Champness, N. R.; Easun, T. L.; Allan, D. R.; Nowell, H.; George, M. W.; Jia, J.; Sun, X. Z. *Nat. Chem.* **2010**, *2*, 688.
- (57) Easun, T. L.; Jia, J.; Calladine, J. A.; Blackmore, D. L.; Stapleton, C. S.; Vuong, K. Q.; Champness, N. R.; George, M. W. *Inorg. Chem.* **2014**, *53*, 2606.
- (58) Easun, T. L.; Jia, J.; Reade, T. J.; Sun, X.-Z.; Davies, E. S.; Blake, A. J.; George, M. W.; Champness, N. R. *Chem. Sci.* **2014**, *5*, 539.
- (59) Reade, T. J.; Murphy, T. S.; Calladine, J. A.; Horvath, R.; Clark, I. P.; Greetham, G. M.; Towrie, M.; Lewis, W.; George, M. W.; Champness, N. R. *Phil. Trans. R. Soc. A* **2017**, *375*, 20160033.
- (60) Kaye, S. S.; Long, J. R. *J. Am. Chem. Soc.* **2008**, *130*, 806.
- (61) Chavan, S.; Vitillo, J. G.; Larabi, C.; Alessandra Quadrelli, E.; Dietzel, P. D. C.; Bordiga, S. *Microporous and Mesoporous Materials* **2012**, *157*, 56.
- (62) Vitillo, J. G.; Groppo, E.; Bordiga, S.; Chavan, S.; Ricchiardi, G.; Zecchina, A. *Inorg. Chem.* **2009**, *48*, 5439.
- (63) Chavan, S.; Vitillo, J. G.; Uddin, M. J.; Bonino, F.; Lamberti, C.; Groppo, E.; Lillerud, K.-P.; Bordiga, S. *Chem. Mat.* **2010**, *22*, 4602.
- (64) Gonzalez, M. I.; Bloch, E. D.; Mason, J. A.; Teat, S. J.; Long, J. R. *Inorg. Chem.* **2015**, *54*, 2995.
- (65) Fei, H.; Sampson, M. D.; Lee, Y.; Kubiak, C. P.; Cohen, S. M. *Inorg. Chem.* **2015**, *54*, 6821.
- (66) Mede, R.; Klein, M.; Claus, R. A.; Kriek, S.; Quickert, S.; Görls, H.; Neugebauer, U.; Schmitt, M.; Gessner, G.; Heinemann, S. H., *et al.* *Inorg. Chem.* **2016**, *55*, 104.
- (67) Carmona, F. J.; Rojas, S.; Sanchez, P.; Jeremias, H.; Marques, A. R.; Romao, C. C.; Choquesillo-Lazarte, D.; Navarro, J. A.; Maldonado, C. R.; Barea, E. *Inorg. Chem.* **2016**, *55*, 6525.
- (68) Carmona, F. J.; Rojas, S.; Romão, C. C.; Navarro, J. A. R.; Barea, E.; Maldonado, C. R. *Chem. Commun.* **2017**, *53*, 6581.

- (69) Diring, S.; Carne-Sanchez, A.; Zhang, J.; Ikemura, S.; Kim, C.; Inaba, H.; Kitagawa, S.; Furukawa, S. *Chem. Sci.* **2017**, *8*, 2381.
- (70) Stor, G. J.; Morrison, S. L.; Stufkens, D. J.; Oskam, A. *Organometallics* **1994**, *13*, 2641.
- (71) Rosa, A.; Ricciardi, G.; Baerends, E. J.; Stufkens, D. J. *J. Phys. Chem.* **1996**, *100*, 15346.
- (72) Rosa, A.; Ricciardi, G.; Baerends, E. J.; Stufkens, D. J. *Inorg. Chem.* **1998**, *37*, 6244.
- (73) Kleverlaan, C. J.; Hartl, F.; Stufkens, D. J. *Journal of Photochemistry and Photobiology A: Chemistry* **1997**, *103*, 231.
- (74) Yempally, V.; Moncho, S.; Hasanayn, F.; Fan, W. Y.; Brothers, E. N.; Bengali, A. A. *Inorg. Chem.* **2017**, *56*, 11244.
- (75) Caulton, K. G. *Coord. Chem. Rev.* **1981**, *38*, 1.
- (76) Giordano, P. J.; Wrighton, M. S. *Inorg. Chem.* **1977**, *16*, 160.
- (77) Strohmeier, W.; Guttenberger, J. F.; Hellmann, H. *znb* **1964**, *19*, 353.
- (78) Strohmeier, W.; Guttenberger, J. F. *Chemische Berichte* **1963**, *96*, 2112.
- (79) Strohmeier, W.; Guttenberger, J. F. *Chemische Berichte* **1964**, *97*, 1256.
- (80) Strohmeier, W.; Hellmann, H. *Chemische Berichte* **1965**, *98*, 1598.
- (81) Strohmeier, W.; Hobe, D. V. *znb* **1961**, *16*, 402.
- (82) Alt, H. G.; Engelhardt, H. E. *J. Organomet. Chem.* **1988**, *342*, 235.
- (83) Birk, R.; Berke, H.; Hund, H.-U.; Evertz, K.; Huttner, G.; Zsolnai, L. *J. Organomet. Chem.* **1988**, *342*, 67.
- (84) Bengali, A. A. *Organometallics* **2000**, *19*, 4000.
- (85) Bengali, A. A.; Fan, W. Y.; Abdulrazak, K. T. *Organometallics* **2009**, *28*, 3123.
- (86) Crocock, B.; Long, C. *Acta Cryst. C* **1991**, *C48*, 1004.
- (87) Kee, J. W.; Fan, W. Y. *J. Organomet. Chem.* **2013**, *729*, 14.
- (88) Fritz, H. P.; Keller, H. J. *Chemische Berichte* **1963**, *96*, 1676.
- (89) Teixeira, G.; Avilés, T.; Dias, A. R.; Pina, F. *J. Organomet. Chem.* **1988**, *353*, 83.
- (90) Orama, O. *J. Organomet. Chem.* **1986**, *314*, 273.
- (91) Strohmeier, W.; Guttenberger, J. F. *Chemische Berichte* **1964**, *97*, 1871.
- (92) Anderson, W. P.; Brill, T. B.; Schoenberg, A. R.; Stanger, C. W. *J. Organomet. Chem.* **1972**, *44*, 161.
- (93) Swennenhuis, B. H.; Poland, R.; Fan, W. Y.; Darensbourg, D. J.; Bengali, A. A. *Inorg. Chem.* **2010**, *49*, 7597.
- (94) Kelbysheva, E. S.; Ezernitskaya, M. G.; Strelkova, T. V.; Borisov, Y. A.; Smol'yakov, A. F.; Starikova, Z. A.; Dolgushin, F. M.; Rodionov, A. N.; Lokshin, B. V.; Loim, N. M. *Organometallics* **2011**, *30*, 4342.
- (95) Sorensen, A. A.; Yang, G. K. *J. Am. Chem. Soc.* **1991**, *113*, 7061.

- (96) Antonova, A. B.; Kolobova, N. E.; Petrovsky, P. V.; Lokshin, B. V.; Obezyuk, N. S. *J. Organomet. Chem.* **1977**, *137*, 55.
- (97) Le Moigne, F.; Dabard, R. *J. Organomet. Chem.* **1973**, *60*, C14.
- (98) Pauson, P. L.; Segal, J. A. *J. Organomet. Chem.* **1973**, *63*, C13.
- (99) Merwin, R. K.; Ontko, A. C.; Houlis, J. F.; Roddick, D. M. *Polyhedron* **2004**, *23*, 2873.
- (100) Strohmeier, W.; Guttenberger, J. F. *znb* **1963**, *18*, 667.
- (101) Zheng, J.; Elangovan, S.; Valyaev, D. A.; Brousses, R.; César, V.; Sortais, J. B.; Darcel, C.; Luga, N.; Lavigne, G. *Adv. Synth. Catal.* **2014**, *356*, 1093.
- (102) Batool, M.; Martin, T. A.; Algarra, A. G.; George, M. W.; Macgregor, S. A.; Mahon, M. F.; Whittlesey, M. K. *Organometallics* **2012**, *31*, 4971.
- (103) Dineen, J. A.; Pauson, P. L. *J. Organomet. Chem.* **1974**, *71*, 91.
- (104) Swennenhuis, B. H. G.; Poland, R.; DeYonker, N. J.; Webster, C. E.; Darensbourg, D. J.; Bengali, A. A. *Organometallics* **2011**, *30*, 3054.
- (105) Hallett, A. J.; Angharad Baber, R.; Guy Orpen, A.; Ward, B. D. *Dalt. Trans.* **2011**, *40*, 9276.
- (106) Schoenberg, A. R.; Anderson, W. P. *Inorg. Chem.* **1974**, *13*, 465.
- (107) Joachim, J. E.; Apostolidis, C.; Kanellakopoulos, B.; Meyer, D.; Nuber, B.; Raptis, K.; Rebizant, J.; Ziegler, M. L. *J. Organomet. Chem.* **1995**, *492*, 199.
- (108) Nesmeyanov, A. N.; Aleksandrov, G. G.; Antonova, A. B.; Anisimov, K. N.; Kolobova, N. E.; Struchkov, Y., T. *J. Organomet. Chem.* **1976**, *110*, C36.
- (109) Bengali, A. A.; Arndtsen, B. A.; Burger, P. M.; Schultz, R. H.; Weiller, B. H.; Kyle, K. R.; Moore, C. B.; Bergman, R. G. *pac* **1995**, *67*, 281.
- (110) Bromberg, S. E.; Haw Yang, M. C.; Asplund, T. L.; McNamara, B. K.; Kotz, K. T.; Yeston, J. S.; Wilkens, M.; Frei, H.; Bergman, R. G.; Harris, C. B. *Science* **1997**, *278*, 260.
- (111) Jones, W. D. *Inorg. Chem.* **2005**, *44*, 4475.
- (112) Hauser, S. A.; Emerson-King, J.; Habershon, S.; Chaplin, A. B. *Chem. Commun.* **2017**, *53*, 3634.
- (113) Purwoko, A. A.; Lees, A. J. *Inorg. Chem.* **1996**, *35*, 675.
- (114) Purwoko, A. A.; Tibensky, S. D.; Lees, A. J. *Inorg. Chem.* **1996**, *35*, 7049.
- (115) McKeown, B. A.; Lee, J. P.; Mei, J.; Cundari, T. R.; Gunnoe, T. B. *Eur. J. Inorg. Chem.* **2016**, *2016*, 2296.
- (116) Blake, A. J.; George, M. W.; Hall, M. B.; McMaster, J.; Portius, P.; Sun, X. Z.; Towrie, M.; Webster, C. E.; Wilson, C.; Zarić, S. D. *Organometallics* **2008**, *27*, 189.

- (117) Asplund, M. C.; Snee, P. T.; Yeston, J. S.; Wilkens, M. J.; Payne, C. K.; Yang, H.; Kotz, K. T.; Frei, H.; Bergman, R. G.; Harris, C. B. *J. Am. Chem. Soc.* **2002**, *124*, 10605.
- (118) Dunwoody, N.; Lees, A. J. *Organometallics* **1997**, *16*, 5770.
- (119) Lees, A. J. *J. Organomet. Chem.* **1998**, *554*, 1.
- (120) Ball, G. E.; Brookes, C. M.; Cowan, A. J.; Darwish, T. A.; George, M. W.; Kawanami, H. K.; Portius, P.; Rourke, J. P. *Proceedings of the National Academy of Sciences* **2007**, *104*, 6927.
- (121) Asplund, M. C.; Yang, H.; Kotz, K. T.; Bromberg, S. E.; Wilkens, M. J.; Harris, C. B. *Laser Chem.* **1999**, *19*, 253.
- (122) Yang, H.; Kotz, K. T.; Asplund, M. C.; Wilkens, M. J.; Harris, C. B. *Acc. Chem. Res.* **1999**, *32*, 551.
- (123) Janowicz, A. H.; Bergman, R. G. *J. Am. Chem. Soc.* **1982**, *104*, 352.
- (124) Hoyano, J. K.; Graham, W. A. G. *J. Am. Chem. Soc.* **1982**, *104*, 3723.
- (125) Calladine, J. A.; Duckett, S. B.; George, M. W.; Matthews, S. L.; Perutz, R. N.; Torres, O.; Vuong, K. Q. *J. Am. Chem. Soc.* **2011**, *133*, 2303.
- (126) Corey, J. Y. *Chem. Rev.* **2011**, *111*, 863.
- (127) Jetz, W.; Graham, W. A. G. *Inorg. Chem.* **1971**, *10*, 4.
- (128) Hester, D. M.; Sun, J.; Harper, A. W.; Yang, G. K. *J. Am. Chem. Soc.* **1992**, *114*, 5234.
- (129) Pandey, K. K. *Coord. Chem. Rev.* **2009**, *253*, 37.
- (130) Young, R. D. *Chemistry* **2014**, *20*, 12704.
- (131) Weller, A. S.; Chadwick, F. M.; McKay, A. I. *Adv. Organometallic Chem.* **2016**, *66*, 223.
- (132) Cobar, E. A.; Khaliullin, R. Z.; Bergman, R. G.; Head-Gordon, M. *Proceedings of the National Academy of Sciences* **2007**, *104*, 6963.
- (133) Crabtree, R. H., Sigma Bonds as Ligand Donor Groups in Transition Metal Complexes. In *The Chemical Bond III: 100 years old and getting stronger*, Mingos, D. M. P., Ed. Springer International Publishing: Cham, 2017; pp 63-77.
- (134) Siedle, A. R.; Newmark, R. A.; Gleason, W. B.; Skarjune, R. P.; Hodgson, K. O.; Roe, A. L.; Day, V. W. *Solid State Ionics* **1988**, *26*, 109.
- (135) Wong, J. C. S.; Yates, J. T. *J. Phys. Chem.* **1995**, *99*, 12640.
- (136) Wong, J. C. S.; Yates, J. T. *J. Am. Chem. Soc.* **1994**, *116*, 1610.
- (137) Ma, X.; Dang, Y. *J. Org. Chem.* **2019**.
- (138) Hu, Y.; Zhou, B.; Wang, C. *Acc. Chem. Res.* **2018**, *51*, 816.
- (139) Liu, W.; Ackermann, L. *ACS Catal.* **2016**, *6*, 3743.

- (140) Tzouras, N. V.; Stamatopoulos, I. K.; Papastavrou, A. T.; Liori, A. A.; Vougioukalakis, G. C. *Coord. Chem. Rev.* **2017**, *343*, 25.
- (141) Nuhant, P.; Oderinde, M. S.; Genovino, J.; Juneau, A.; Gagné, Y.; Allais, C.; Chinigo, G. M.; Choi, C.; Sach, N. W.; Bernier, L., *et al.* *Angew. Chem., Int. Ed. Engl.* **2017**, *56*, 15309.
- (142) Liang, Y.-F.; Steinbock, R.; Yang, L.; Ackermann, L. *Angew. Chem., Int. Ed. Engl.* **2018**, *57*, 10625.
- (143) Kuninobu, Y.; Nishina, Y.; Takeuchi, T.; Takai, K. *Angew. Chem., Int. Ed. Engl.* **2007**, *46*, 6518.
- (144) CHen, H.; Hartwig, J. F. *Angew. Chem., Int. Ed. Engl.* **1999**, *38*, 3391.
- (145) Komuro, T.; Okawara, S.; Furuyama, K.; Tobita, H. *Chem. Lett.* **2012**, *41*, 774.
- (146) Zhang, Z.-F.; Su, M.-D. *RSC Adv.* **2018**, *8*, 10987.
- (147) Yang, H.; Asplund, M. C.; Kotz, K. T.; Wilkens, M. J.; Frei, H.; Harris, C. B. *J. Am. Chem. Soc.* **1998**, *120*, 10154.
- (148) Schlecht, S.; Hartwig, J. F. *J. Am. Chem. Soc.* **2000**, *122*, 9435.
- (149) Kawano, Y.; Yamaguchi, K.; Miyake, S. y.; Kakizawa, T.; Shimoi, M. *Chem. Eur. J.* **2007**, *13*, 6920.
- (150) Pandey, K. K. *J. Organomet. Chem.* **2007**, *692*, 1997.
- (151) Riddlestone, I. M.; Edmonds, S.; Kaufman, P. A.; Urbano, J.; Bates, J. I.; Kelly, M. J.; Thompson, A. L.; Taylor, R.; Aldridge, S. *J. Am. Chem. Soc.* **2012**, *134*, 2551.
- (152) Braunschweig, H.; Ganter, B. *J. Organomet. Chem.* **1997**, *545-546*, 163.
- (153) Chatterton, N. P.; Guilera, G.; McGrady, G. S. *Organometallics* **2004**, *23*, 1165.
- (154) Fang, X.; Huhmann-Vincent, J.; Scott, B. L.; Kubas, G. J. *J. Organomet. Chem.* **2000**, *609*, 95.
- (155) Banister, J. A.; Lee, P. D.; Poliakov, M. *Organometallics* **1995**, *14*, 3876.
- (156) Hulley, E. B.; Welch, K. D.; Appel, A. M.; DuBois, D. L.; Bullock, R. M. *J. Am. Chem. Soc.* **2013**, *135*, 11736.
- (157) Zhu, B.; Huang, X.; Hao, X. *Eur. J. Inorg. Chem.* **2014**, *2014*, 5932.
- (158) Spall, S. J. P.; Keane, T.; Tory, J.; Cocker, D. C.; Adams, H.; Fowler, H.; Meijer, A. J. H. M.; Hartl, F.; Weinstein, J. A. *Inorganic Chemistry* **2016**, *55*.
- (159) Strinitz, F.; Trautner, P.; Pfeiffer, H.; Schatzschneider, U.; Burzlaff, N. *Tetrahedron* **2015**, *71*, 2951.
- (160) Pai, S.; Hafftlang, M.; Atongo, G.; Nagel, C.; Niesel, J.; Botov, S.; Schmalz, H. G.; Yard, B.; Schatzschneider, U. *Dalton. Trans.* **2014**, *43*, 8664.
- (161) Gonzalez, M. A.; Yim, M. A.; Cheng, S.; Moyes, A.; Hobbs, A. J.; Mascharak, P. K. *Inorg. Chem.* **2012**, *51*, 601.
- (162) Ault, B. S.; Becker, T. M.; Li, G. Q.; Orchin, M. *Spectrochim. Acta, Part A* **2004**, *60*, 2567.
- (163) Ludlum, K. H.; Eischens, R. P. *Surface Science* **1973**, *40*, 397.

- (164) Armbruster, M. H. *J. Am. Chem. Soc.* **1948**, *70*, 1734.
- (165) Bloch, E. D.; Queen, W. L.; Krishna, R.; Zadrozny, J. M.; Brown, C. M.; Long, J. R. *Science* **2012**, *335*, 1606.
- (166) Gonzalez, M. I.; Mason, J. A.; Bloch, E. D.; Teat, S. J.; Gagnon, K. J.; Morrison, G. Y.; Queen, W. L.; Long, J. R. *Chem. Sci.* **2017**, *8*, 4387.
- (167) Runcevski, T.; Kapelewski, M. T.; Torres-Gavosto, R. M.; Tarver, J. D.; Brown, C. M.; Long, J. R. *Chem. Commun.* **2016**, *52*, 8251.
- (168) Queen, W. L.; Hudson, M. R.; Bloch, E. D.; Mason, J. A.; Gonzalez, M. I.; Lee, J. S.; Gygi, D.; Howe, J. D.; Lee, K.; Darwish, T. A., *et al.* *Chem. Sci.* **2014**, *5*, 4569.
- (169) Bloch, E. D.; Hudson, M. R.; Mason, J. A.; Chavan, S.; Crocella, V.; Howe, J. D.; Lee, K.; Dzubak, A. L.; Queen, W. L.; Zadrozny, J. M., *et al.* *J. Am. Chem. Soc.* **2014**, *136*, 10752.
- (170) Liao, Y.; Zhang, L.; Weston, M. H.; Morris, W.; Hupp, J. T.; Farha, O. K. *Chemical Communications* **2017**, *53*.
- (171) Sellmann, D. *Angew. Chem., Int. Ed. Engl.* **1971**, *10*, 919.
- (172) Sellmann, D.; Weiss, W. *Angew. Chem.* **1977**, *89*, 918.
- (173) Cipot, J.; Wechsler, D.; McDonald, R.; Ferguson, M. J.; Stradiotto, M. *Organometallics* **2005**, *24*, 1737.
- (174) Agnew, D. W.; Moore, C. E.; Rheingold, A. L.; Figueroa, J. S. *Organometallics* **2016**, *36*, 363.
- (175) Maekawa, M.; Römel, M.; Daniliuc, C. G.; Jones, P. G.; White, P. S.; Neese, F.; Walter, M. D. *Chem. Sci.* **2012**, *3*, 2972.
- (176) Chen, C.-H.; Hung, S.-H.; Du, W.-T.; Hsieh, C.-H. *Res. Chem. Intermed.* **2017**, *43*, 3621.
- (177) Hieber, W.; Stanner, F. *Chemische Berichte* **1969**, *102*, 2930.
- (178) Kashinski, D. O.; Chase, G. M.; Nelson, R. G.; Di Nallo, O. E.; Scales, A. N.; VanderLey, D. L.; Byrd, E. F. J. *Phys. Chem. A* **2017**, *121*, 2265.
- (179) Das, A.; Reibenspies, J. H.; Chen, Y. S.; Powers, D. C. *J. Am. Chem. Soc.* **2017**, *139*, 2912.
- (180) Hatcher, L. E. *CrystEngComm* **2018**, *20*, 5990.
- (181) Rodenbough, P. P.; Karothu, D. P.; Gjorgjieva, T.; Commins, P.; Hara, H.; Naumov, P. *Cryst. Growth Des.* **2018**, *18*, 1293.
- (182) Casaretto, N.; Fournier, B.; Pillet, S.; Bendeif, E. E.; Schaniel, D.; Gallien, A. K. E.; Klüfers, P.; Woike, T. *CrystEngComm* **2016**, *18*, 7260.
- (183) Kreye, M.; Freytag, M.; Daniliuc, C. G.; Jones, P. G.; Walter, M. D. *Z. Anorg. Allg. Chem.* **2015**, *641*, 2109.

- (184) Yempally, V.; Kyran, S. J.; Raju, R. K.; Fan, W. Y.; Brothers, E. N.; Darensbourg, D. J.; Bengali, A. A. *Inorg. Chem.* **2014**, *53*, 4081.
- (185) Carlos, R. M.; Neto, B. S. L.; Neumann, M. G. *Photochemistry and Photobiology* **2004**, *80*, 203.
- (186) King, R. B.; Raghuveer, K. S. *Inorg. Chem.* **1984**, *23*, 2482.
- (187) McPhillips, T.; McPhillips, S.; Chiu, H.; Cohen, A. E.; Deacon, A. M.; Ellis, P. J.; Garman, E.; Gonzalez, A.; Sauter, N. K.; Phizackerley, R. P., *et al.* *J. Synchrotron Rad.* **2002**, *9*, 401.
- (188) Sheldrick, G. M. *Acta Crystallogr. C Struct. Chem.* **2015**, *71*, 3.
- (189) Spek, A. L. *Acta Crystallogr C Struct Chem* **2015**, *71*.

Chapter 6: Conclusion and Future Outlook

This thesis has confirmed the role of MOFs in the development of advanced heterogeneous catalysts. MOF **1** is well poised to facilitate exploration of the coordination chemistry of included metal complexes because of its propensity to maintain crystallinity throughout multi-step chemical transformations. This has allowed the structure of diverse, post-synthetically included metal complexes to be determined via X-ray crystallography, revealing the role of the MOF pore environment and site-isolation in the ensuing chemistry.

The MOF pore environment presents an unusual combination of properties; metal complexes are anchored to a robust crystalline structure while suspended in a solvent-filled void. The series of transition metal nitrate complexes reported in chapter 2 revealed how the solid/solution hybrid environment within the pores of **1** influences the coordination sphere of the metal complexes. Solvent played an important role in determining the type of complex obtained after metalation. Furthermore, in Chapter 4 and 5 it was revealed that the metalation of **1** with $[\text{Mn}(\text{CO})_5\text{Br}]$ produces the unusual charged complex $\mathbf{1}\cdot[\text{Mn}(\text{CO})_3(\text{H}_2\text{O})]\text{Br}$ which readily converts to the corresponding neutral complex $\mathbf{1}\cdot[\text{Mn}(\text{CO})_3\text{Br}]$ in non-polar solvents (Chapters 4 and 5). The presence of a non-coordinated bromide anion, which resides in the MOF pores in $\mathbf{1}\cdot[\text{Mn}(\text{CO})_3(\text{H}_2\text{O})]\text{Br}$, allowed facile anion exchange with N_3^- to give $\mathbf{1}\cdot[\text{Mn}(\text{CO})_3\text{N}_3]$ which was employed as a platform for site-selective chemo-selective click-chemistry. Remarkably, the triazolate complexes formed via click chemistry are influenced by the confining environment within **1**, forming unusual N(1) coordinated triazolate complexes. This was contrasted against the N(2) complex obtained for the molecular complex, and the disparity is attributed to the encroaching MOF structure which prevents rotation of the triazolate to form the preferred N(2) isomer. Thus, it is evident that the MOF structure plays a subtle but important role in the coordination chemistry occurring within **1**. Remarkably, these effects were elucidated using X-ray crystallography, demonstrating the power of crystalline matrices such as MOFs to pre-order and isolate metal complexes.

A leading attribute of MOFs is their building block design which can allow their structure to be precisely tailored to suit specific applications. Although quantitative metalation of **1** is key to obtaining crystallographic insight into the coordination sphere of metal complexes tethered to the MOF structure, the pores of the material can become blocked and this is detrimental to mass transport in

heterogeneous catalysis. In Chapter 3 a mixed ligand synthesis strategy was employed to prepare a series of materials with the same topology as **1** but with a reduced density of available binding sites for transition metals. Using this strategy it is possible to reduce the degree of metalation by 50%, however control of the spatial distribution of metal centres within the crystal is not possible with this strategy.

Site isolation is crucial to the development of heterogeneous catalysts because it negates the need to use expensive sterically demanding ligands to protect the sensitive reactive sites from decomposition. The formation and characterisation of σ -alkane complexes and coordinatively unsaturated metal complexes in single crystals validates the role of site-isolation and crystallinity in the structural characterisation of key intermediates in small molecule activation. The site-isolation of metal complexes within **1**·[Mn(CO)₃Br] has been harnessed for two key applications; site-selective click chemistry and the trapping reactive photoproducts. The former is a novel application for the remarkable angstrom-scale precision with which metal complexes are distributed throughout **1**·[Mn(CO)₃Br]. Each step of the click-chemistry cycle, from anion exchange to the formation of the triazolite complex, was characterised by X-ray crystallography. This is a testament to the propensity of MOFs to act as crystalline nano-flasks in which chemical transformations can be performed and directly observed using X-ray Crystallography, without the need for recrystallisation at each step. This precedent will be applied in the study of other metal-centred chemical transformations within **1**, especially the formation of reactive metal complexes via photolysis of **1**·[Mn(CO)₃Br]. This latter concept is an advancement of earlier work in which coordinatively unsaturated metal complexes were generated and stabilised on solid supports such as zeolites and alumina. The advantage conferred by MOFs over such solid supports or molecular crystals is the combination of crystallinity and permanent porosity. The latter is particularly relevant for the transport of reagents and products to and from the isolated reaction sites, the density of which can be increased by their angstrom-scale spacing within high-surface area media such as MOFs.

MOF **1**·[Mn(CO)₃Br] readily undergoes visible photolysis which leads to complete loss of CO due the permanent porosity of the material. This contrasts the observations of Champness *et al.* in which photoisomerism was found to be the dominant process in a non-porous MOF. Incidentally, quantitative loss of CO from solvated **1**·[Mn(CO)₃Br] results in the formation of (partially) solvated Mn(I) complexes. Earlier work has shown that such complexes can participate in a range of ligand exchange chemistry and have been implicated in small molecule activation. By combining in-situ X-ray crystallography with visible photolysis, the solvated complexes can be structurally characterised as they form. In the presence of THF, this crystalline matrix strategy revealed the formation of a THF adduct upon CO loss. Further

characterisation is required to fully elucidate the full coordination sphere; however these preliminary experiments demonstrate the capacity of this strategy to provide structural insight into reactive metal complexes. It is worth noting that the ubiquitous THF adduct formed by photolysis of $[\text{CpMn}(\text{CO})_3]$ has never been structurally characterised, which further emphasises the importance of the preliminary observation of a Mn(I) photoproduct bearing THF ligands within **1**.

IR spectroscopy is central to the study of metal carbonyl photolysis both in **1** and more conventional media. Pico-second time resolved IR spectroscopy has successfully identified the transient intermediates involved in C-H activation at coordinatively unsaturated Rh(I) complexes. Photocrystallography on the other hand, provides structural insights into the reaction products such as coordinatively unsaturated metal centres or solvated complexes. Only by combining the ultra-fast time-scales of IR spectroscopy with the structural insights obtained by X-ray crystallography of the 'final' products can a complete understanding of this chemistry be obtained. Time-resolved IR spectroscopy experiments are currently underway and will resolve the behaviour of the Mn(I) complex in the initial moments of photolysis, providing insight into the origin of the structures observed via X-ray crystallography. For instance, time-resolved spectroscopy in conjunction with computational work may resolve why the bromide anion becomes disordered across the Mn(I) axial coordination sites during photolysis.

Future experiments will aim to generate and characterise adducts with other weakly binding solvents such as diethyl ether, dichloromethane or cyclohexane, which would be stabilised by site-isolation within the framework. It is possible that such complexes could activate small molecules such as silanes and boranes, presenting an ideal opportunity to harness the porosity of **1** for heterogeneous catalysis. The reaction between triethylsilane and weakly solvated Mn(I) complexes could result in the formation of a σ -(Si-H) complex; structural analysis of the Si-H bond length (using neutron diffraction) of such species inside **1** would provide insight into the degree of bond activation by Mn(I). As outlined in Section 5.1.10, several studies have implicated direct oxidative addition in Mn(I) catalysis. The selective borylation of alkanes by $[\text{CpMn}(\text{CO})_3]$ under photolysis was attributed to oxidative addition of pinacolodiboron across Mn(I), followed by oxidative addition or σ -bond metathesis of the alkane C-H bond and subsequent reductive elimination to yield the borylated alkane product. Since this mechanism was never confirmed, it presents an ideal candidate for study using **1**· $[\text{Mn}(\text{CO})_3\text{Br}]$ due to the potential to obtain structural insight from X-ray crystallography. Time-resolved IR spectroscopy would also be crucial to this endeavour, by providing evidence for transient intermediates that would not be observed via X-ray crystallography.

The ability to metalate **1** with a range of transition metal complexes has led to the synthesis of other metal carbonyl complexes such as $\mathbf{1}\cdot[\text{Re}(\text{CO})_3\text{Cl}]$, $\mathbf{1}\cdot[\text{Rh}(\text{CO})_2][\text{Rh}(\text{CO})_2(\text{Cl})_2]$ and $\mathbf{1}\cdot[\text{Ir}(\text{CO})_2][\text{Ir}(\text{CO})_2(\text{Cl})_2]$. Previous studies have demonstrated that Rh(I), Ir(I) and Re(I) carbonyl complexes lose CO under UV photolysis to form electron rich, coordinatively unsaturated complexes that readily activate C-H bonds. The study of their photochemistry within **1** is an ongoing project which aims to obtain structural insight into the coordinatively unsaturated complexes formed upon photolysis and their subsequent reactivity towards C-H bonds. The metalation of **1** with other metal carbonyls, particularly $\text{Cr}(\text{CO})_6$, $\text{Mo}(\text{CO})_6$, $\text{W}(\text{CO})_6$ and $\text{Fe}(\text{CO})_5$ is also of interest. New targets for photolysis can be envisaged through modification of the existing $\mathbf{1}\cdot[\text{Mn}(\text{CO})_3\text{Br}]$ complex by incorporation of imidazole, CO, azide or non-coordinating anions in the structure. The azide complex $\mathbf{1}\cdot[\text{Mn}(\text{CO})_3\text{N}_3]$ is an interesting target for photolysis because of the possibility of forming a reactive nitride via loss of N_2 from the azide. Nitrides are well established as reactive intermediates in organic synthesis, but their reactivity generally precludes their structural characterisation. The recent example of an X-ray crystallographically characterised nitride, stabilised within a single crystal at low temperature (see Chapter 1) sets a promising precedent for the study of such species within **1**. The advantage conferred by the MOF system over the molecular crystal used in this previous work is permanent porosity which could allow the nitride to be employed in chemical reactions.

The work described in this thesis has established **1** as a promising medium within which to study coordination chemistry, including multi-step reactions. The confining effect of MOF pores fortuitously influences the coordination sphere of $\mathbf{1}\cdot[\text{Mn}(\text{CO})_3\text{Br}]$, providing access to both charged and neutral Mn(I) complexes that have facilitated novel 'click' chemistry and photolysis studies. The site-isolation engendered by the crystalline lattice of **1** has been harnessed to perform site-selective click chemistry and isolate a photo-generated THF-adduct. Both of these endeavours are novel demonstrations of MOF based chemistry which support the premise that the porosity, robust crystallinity and building block design inherent to MOFs can be employed to develop advanced heterogeneous catalysts.

Chapter 7: Appendices

7.1: Supplementary Information for Chapter 2

7.1.1 PXRD Data

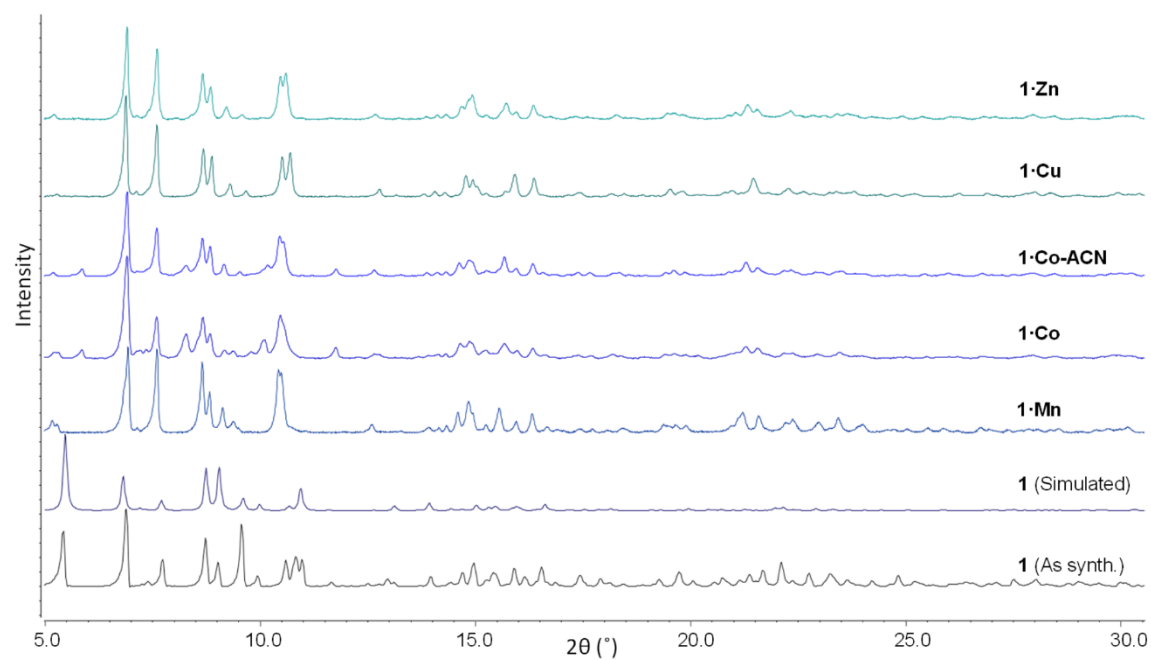


Figure S7.1. Experimental and simulated powder X-ray diffraction data for **1** and the metalated versions of **1** reported in this contribution.

7.1.2 Additional refinement details for the single crystal X-ray structures

Crystals of all five metalated MOF samples (**1•M**) have solvent accessible voids which contained a number of diffuse electron density peaks that could not be adequately identified and refined as solvent. The SQUEEZE routine of PLATON⁴⁰ was applied to the collected data, resulting in significant reductions in R_1 , ωR_2 and an improvement in the goodness of fit (GOF) in all cases.

1•Mn: The minimum (negative) residual density hole is adjacent the post-synthetically added Mn atom (Mn3). The hole possibly arises due to some disorder of this Mn moiety and its associated chelating ligand. The occupancy of this centre was set at the maximum (50% occupied, mirror plane) but as this example is metalated with Mn independent verification of the occupancy could not be obtained from EDX or ICP analysis. The hydrogen atoms on the coordinated water molecules and the nitrate anions could not be located in the difference map but these were included in the formula reported.

1•Zn: The hydrogen atoms on the coordinated water molecules and the nitrate anions could not be located in the difference map but these were included in the formula reported.

1•Cu: Crystals of this compound showed some additional disorder of the post-synthetically added metal species and the ligands associated with this. Weak high angle diffraction data limited the extent to which the model could be refined. Seven restraints were used in the refinement (DFIX restraints on an CN bond of an acetonitrile and an ISOR restraint on the methyl carbon atom).

1•Co-ACN: A disordered nitrate anion is bound to the main residue and two of the nitrate anions in the structure were refined with AFIX 2 restraints on the nitrogen atoms and DFIX restraints on the N-O bond lengths. The MOF-bound metalation site was found to be at full occupancy but secondary site was refined at 50% occupancy (via trial refinement).

The hydrogen atoms on the coordinated water molecules could not be located in the difference map but these were included in the formula reported.

1•Co: The hydrogen atoms on the coordinated water molecules and the nitrate anions could not be located in the difference map but these were included in the formula reported.

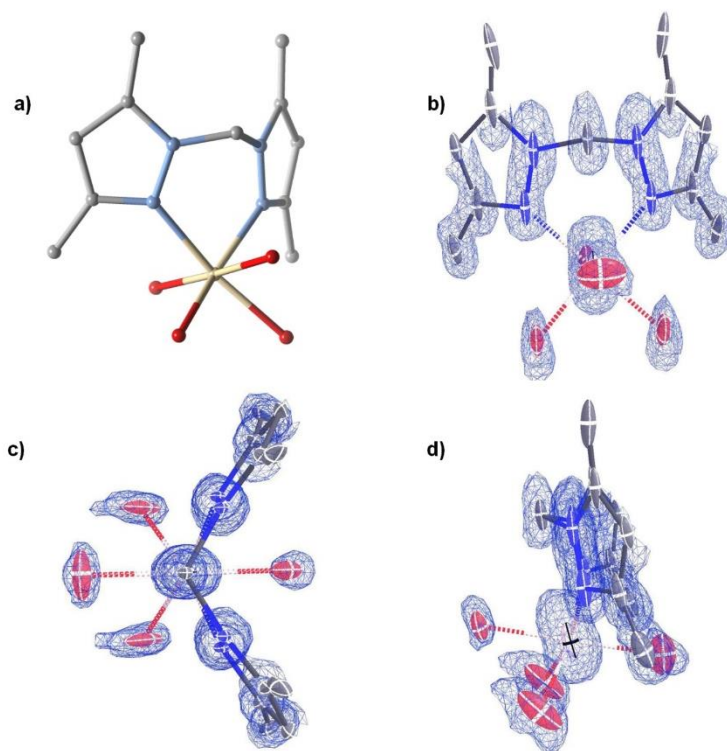
7.1.3 F_{obs} electron density maps

Figure S7.2: The crystal structure presented in a) is supported by the observed electron density map (F_o) surrounding the chelated Mn^{2+} centre in **1·Mn**, which is displayed from three perspectives (b-d). The observed electron density map matches the structural model presented in a).

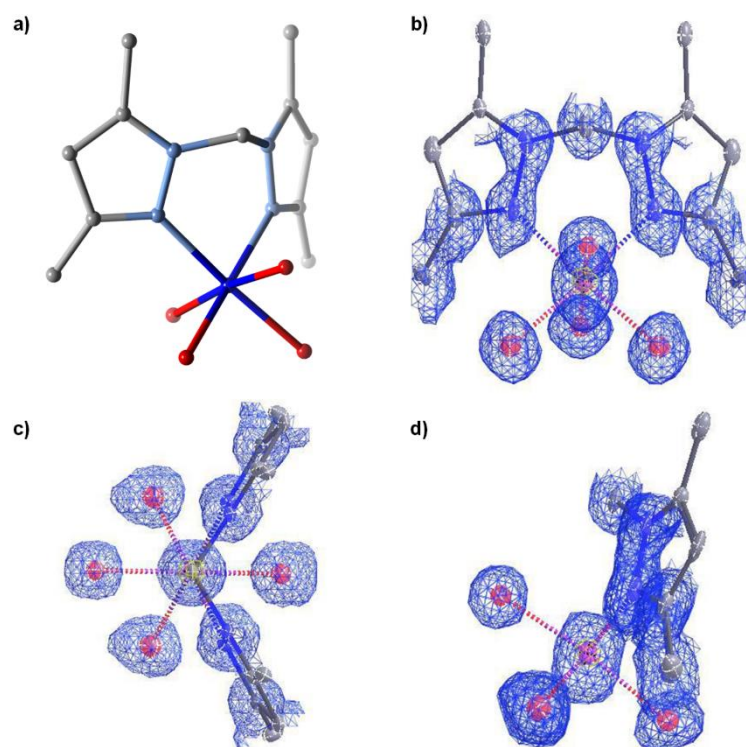


Figure S7.3: The crystal structure presented in a) is supported by the observed electron density map (F_o) surrounding the chelated Co^{2+} centre in **1·Co**, which is displayed from three perspectives (b-d). The observed electron density map matches the structural model presented in a).

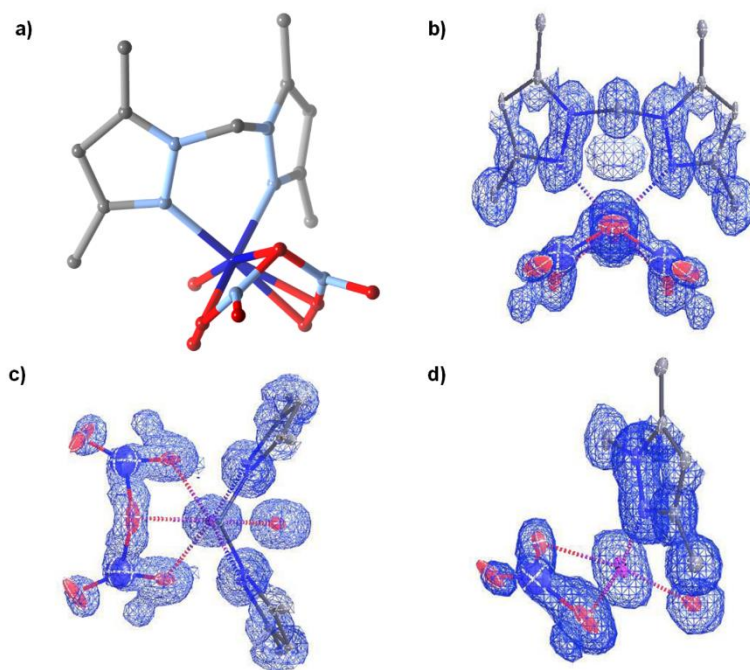


Figure S7.4: The crystal structure presented in a) is supported by the observed electron density map (F_o) surrounding the chelated Co^{2+} centre in $\mathbf{1}\cdot\text{Co}\cdot\text{ACN}$, which is displayed from three perspectives (b-d). The observed electron density map matches the structural model presented in a). We note that the structural model features disordered nitrate/water moieties, as depicted in a).

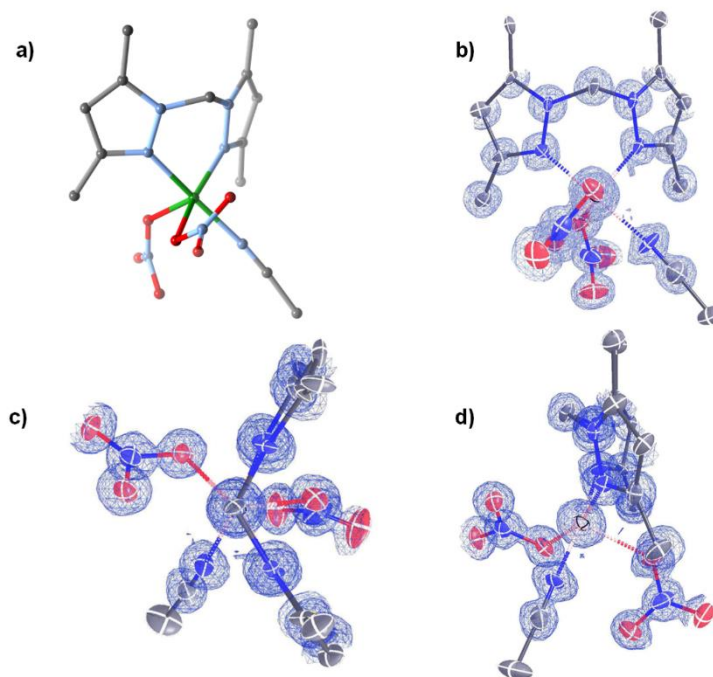


Figure S7.5: The crystal structure presented in a) is supported by the observed electron density map (F_o) surrounding the chelated Cu^{2+} centre in **1**·Cu, which is displayed from three perspectives (b-d). The observed electron density map in the vicinity of the Cu^{2+} site matches the structural model presented in a), note that the electron density map was truncated to avoid inclusion of electron density from the adjacent MOF framework and solvated complex, as a result the electron density map does not include the methyl carbon on the coordinated acetonitrile ligand.

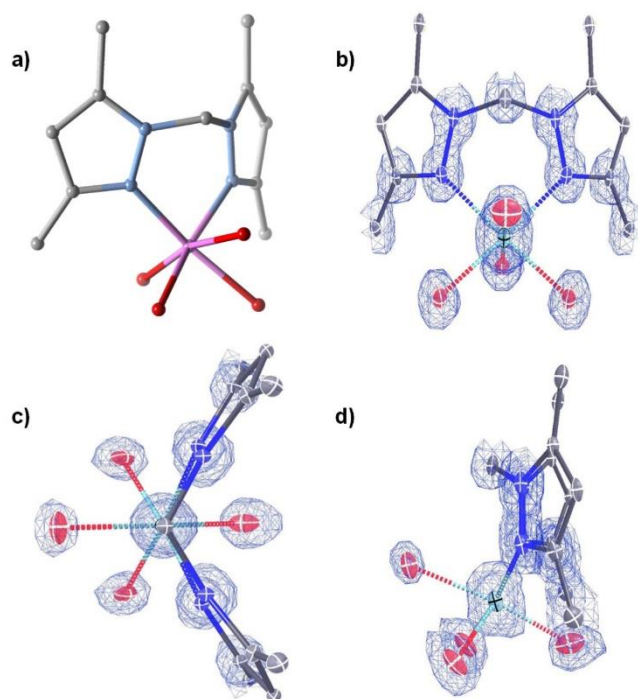


Figure S7.6: The crystal structure presented in a) is supported by the observed electron density map (F_o) surrounding the chelated Zn^{2+} centre in **1·Zn**, which is displayed from three perspectives (b-d). The observed electron density map matches the structural model presented in a).

7.1.4 Crystallographic Parameters

Table S7.1.4.1: Crystallographic parameters for the crystal structures of metalated forms of **1**.

Sample	1·Mn	1·Co	1·Co-ACN
Crystallographic Parameter			
Formula	C ₇₅ H ₇₄ Mn ₄ N ₁₄ O ₂₂	C ₇₅ H ₇₄ CoMn ₃ N ₁₄ O ₂₂	C ₈₃ H ₈₃ Co _{1.5} Mn ₃ N ₂₀ O _{24.5}
FW	1743.24	1747.23	2005.90
T, K	100(2)	100(2)	100(2)
Wavelength, Å	0.71073	0.71073	0.71073
Crystal system, space group	Monoclinic, P2 ₁ /m	Monoclinic, P2 ₁ /m	Monoclinic, P2 ₁ /m
Z	2	2	2
a, Å	12.379(3)	12.457(3)	12.428(3)
b, Å	33.055(7)	34.265(7)	33.163(7)
c, Å	12.878(3)	12.888(3)	12.896(3)
β, °	96.93(3)	100.61(3)	95.40(3)
V, Å ³	5231.0(19)	5407(2)	5291.5(19)
d _{calc} , g/cm ³	1.107	1.073	1.259
Absorption coefficient, mm ⁻¹	0.534	0.554	0.653
F(000)	1796.0	1800.0	2065.0
Crystal size, mm ³	0.20 × 0.10 × 0.10	0.40 × 0.10 × 0.02	0.20 × 0.10 × 0.10
Theta range for data collection	1.232-27.500	1.663-27.500	1.228-27.499
Index range	-15 ≤ h ≤ 15, -42 ≤ k ≤ 42, -16 ≤ l ≤ 16	-16 ≤ h ≤ 16, -44 ≤ k ≤ 44, -16 ≤ l ≤ 16	-15 ≤ h ≤ 15, -43 ≤ k ≤ 43, -16 ≤ l ≤ 16
Reflections collected	84806	85806	86047
Independent reflections	11515	12222	12037
Data/restraints/parameters	11515/0/497	12222/0/497	12037/22/633
GOF on F ²	1.063	1.720	1.070
Largest diff. peak and hole, e ⁻ Å ⁻³	2.02/-5.01	1.84/-1.02	1.89/-1.26
R ₁ , [I > 2σ(I)]	0.1056	0.1328	0.0890
R ₁ (wR ₂) ^a , all data	0.3142	0.3957	0.2577
CCDC Number	1476925	1476926	1476927

$$^a R_1 = \frac{\sum ||F_o| - |F_c||}{\sum |F_o|}, wR_2 = \left(\frac{\sum [w(F_o^2 - F_c^2)^2]}{\sum [w(F_o^2)^2]} \right)^{1/2}$$

Table S7.2: Crystallographic parameters for the crystal structures of metalated forms of **1**.

Sample	1 ·Cu	1 ·Zn
Crystallographic Parameter		
Formula	C ₇₉ H ₇₈ Cu ₂ Mn ₃ N ₁₈ O ₂₇	C ₇₅ H ₇₄ Mn ₃ N ₁₄ O ₂₂ Zn
FW	2003.49	1753.67
T,K	150(2)	100(2)
Wavelength, Å	0.71073	0.71073
Crystal system, space group	Monoclinic, P2 ₁ /c	Monoclinic, P2 ₁ /m
Z	4	2
a, Å	12.4161(4)	12.344(3)
b, Å	33.3880(10)	33.115(7)
c, Å	25.6925(6)	12.899(3)
β, °	95.474(3)	97.39(3)
V, Å ³	10602.2(5)	5228.9(19)
<i>d</i> _{calc} , g/cm ³	1.255	1.114
Absorption coefficient, mm ⁻¹	0.815	0.643
<i>F</i> (000)	4108	1806.0
Crystal size, mm ³	0.30 × 0.20 × 0.01	0.25 × 0.12 × 0.02
Theta range for data collection	2.498-25.035	1.707-27.489
Index range	-14 ≤ <i>h</i> ≤ 14, -39 ≤ <i>k</i> ≤ 39, -30 ≤ <i>l</i> ≤ 30	-15 ≤ <i>h</i> ≤ 15, -42 ≤ <i>k</i> ≤ 42, -16 ≤ <i>l</i> ≤ 16
Reflections collected	63554	83352
Independent reflections	18726	11638
Data/restraints/parameters	18726/7/1177	11638/2/503
GOF on <i>F</i> ²	0.988	1.019
Largest diff. peak and hole, e·Å ⁻³	2.09/-1.89	1.11/-1.62
<i>R</i> ₁ , [<i>I</i> > 2σ(<i>I</i>)]	0.0952	0.0943
<i>R</i> ₁ (<i>wR</i> ₂) ^a , all data	0.2895	0.2841
CCDC Number	1476923	1476924

$$^a R_1 = \frac{\sum ||F_o| - |F_c||}{\sum |F_o|}, wR_2 = \left(\frac{\sum [w(F_o^2 - F_c^2)^2]}{\sum [w(F_o^2)]} \right)^{1/2}$$

7.2: Supplementary Information for Chapter 3

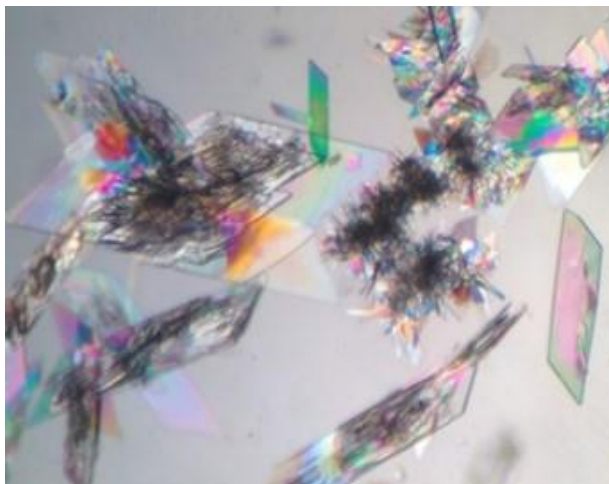
Optical Microscope Images of Mn_3L_3 based materials

Figure. S7.2.1 An optical image showing the as-synthesized form of the parent Mn_3L_3 (L-based) material synthesized using a ratio of L:L' of 1:0.

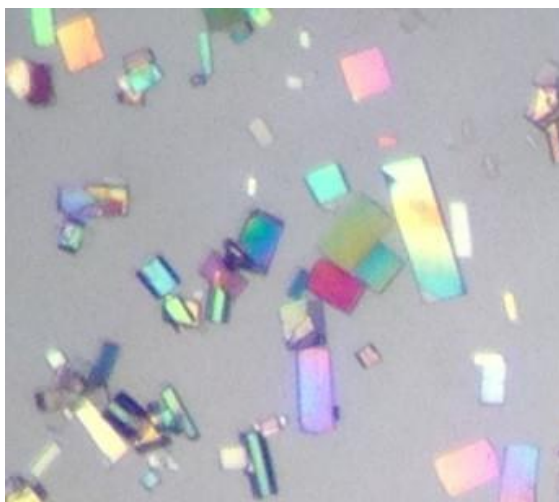


Figure. S7.2.2 An optical image showing the as-synthesized form of the mixed-linker material synthesized using a ratio of L:L' of 0.54:0.46.

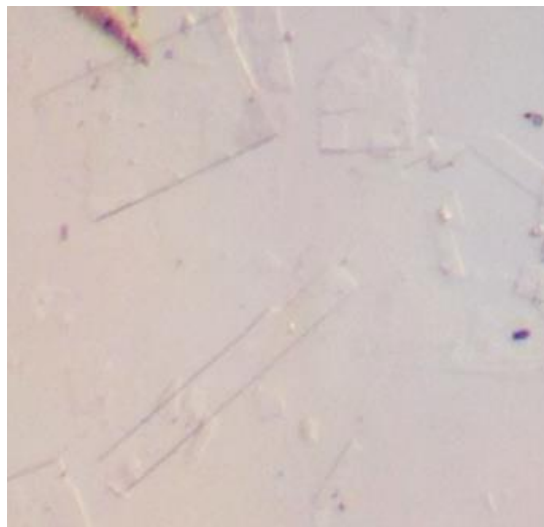


Figure. S7.2.3 An optical image showing the as-synthesized form of the L'-based material synthesized using a ratio of L:L' of 0:1.

Computational Details

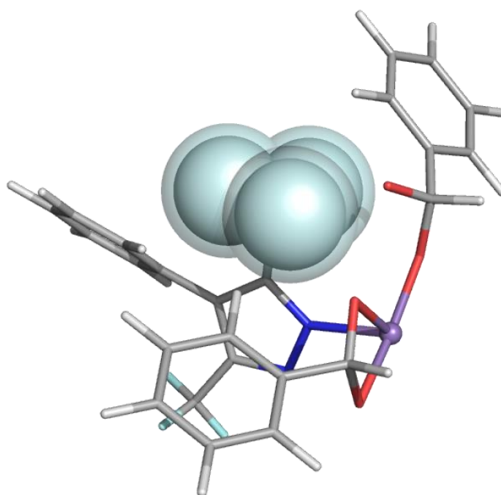


Figure. S7.2.4 An enlarged view of the methyl substituent located in the vicinity of the terminal Mn²⁺ ion of the trinuclear Mn₃⁶⁺ cluster. Upon substitution of the hydrogen atoms (solid spheres; Van der Waals radius: 120 pm) with fluorine (transparent spheres; 135 pm), an unfavorable steric overlap occurs with the surrounding atoms, leading to the trifluoromethyl-substituted linker being predominantly located at the pillar linker sites. Purple spheres, grey, blue, and red nodes represent Mn, C, N, and O, respectively, while H atoms except on the trifluoromethyl substituent have been omitted for clarity.

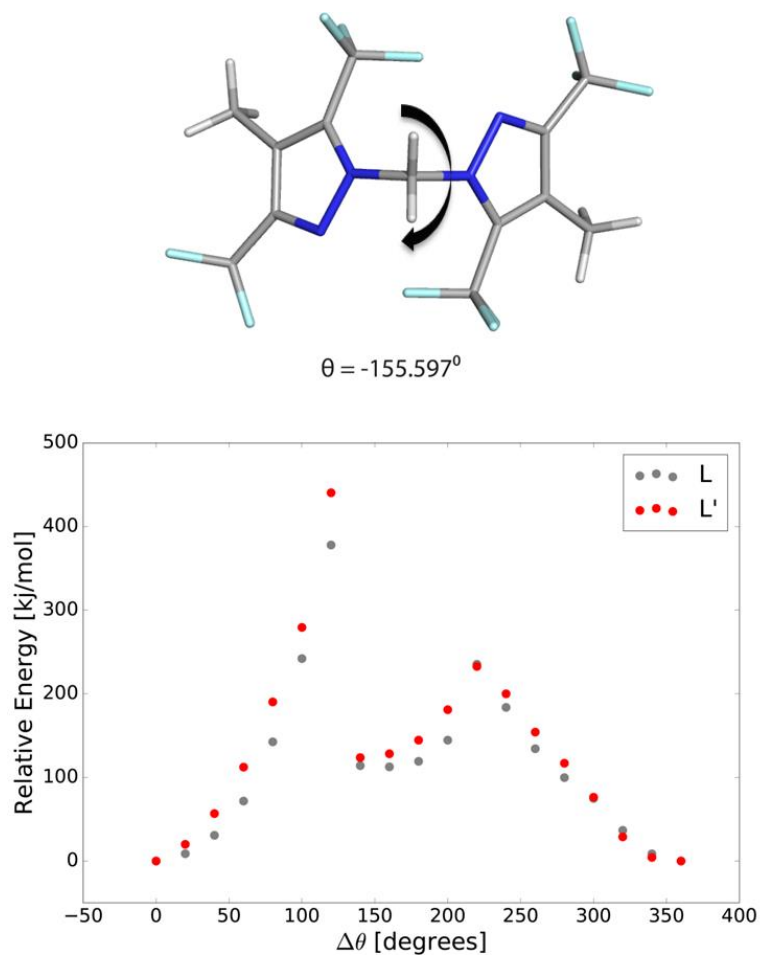


Figure. S7.2.5 A view of the truncated trifluoromethyl-substituted bispyrazolate moiety as modelled by density functional theory at the m06/6-311G++ (d,p) level of theory (upper); and relative energies of the molecule at different angles of rotation about the methylene spacer (lower). Here, the energies are computed for a full, 360° rotation of θ (formed by the four nitrogen atoms of the pyrazolate functionalities), calculating the energies every 20° . For the molecular system, the crystallographically-observed angle ($\theta_0 = -155.6^\circ$, $\Delta\theta = 0^\circ$) in the closed structure is found to be the most favorable conformation, with a local minimum observed for $\Delta\theta$ in the range of 140 - 160° as observed in the open structure. The rotational barrier is significantly greater in the case of the trifluoromethyl-substituted L' linker, which is consistent with the higher pressures at which the structural reorganization is observed in the adsorption isotherms.

Isotherm Data

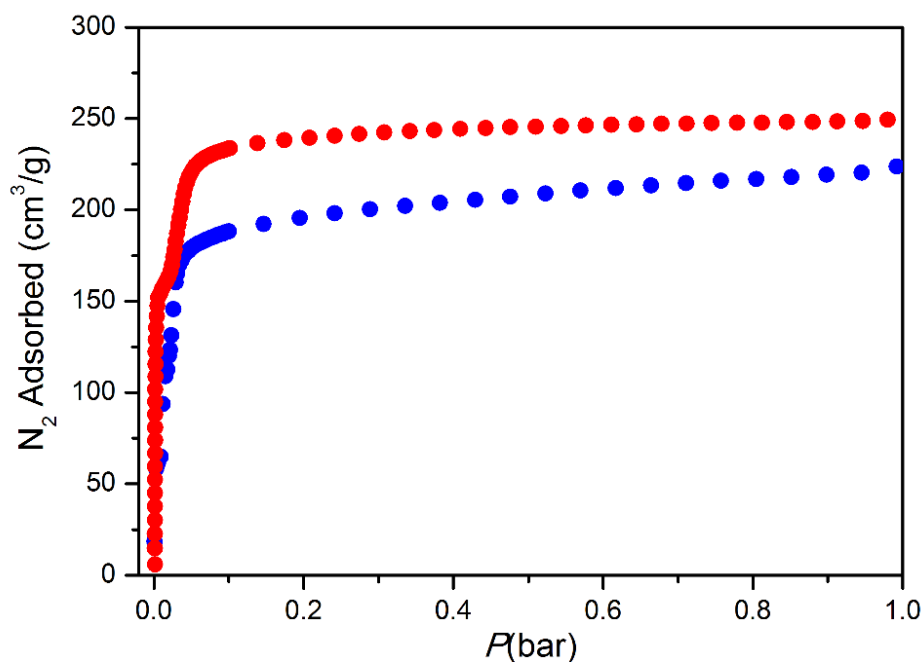


Figure. S7.2.6 N_2 adsorption isotherms recorded at 77 K for Mn_3L_3 (red) and $Mn_3L_{2.49}L'_{0.51}$ (blue).

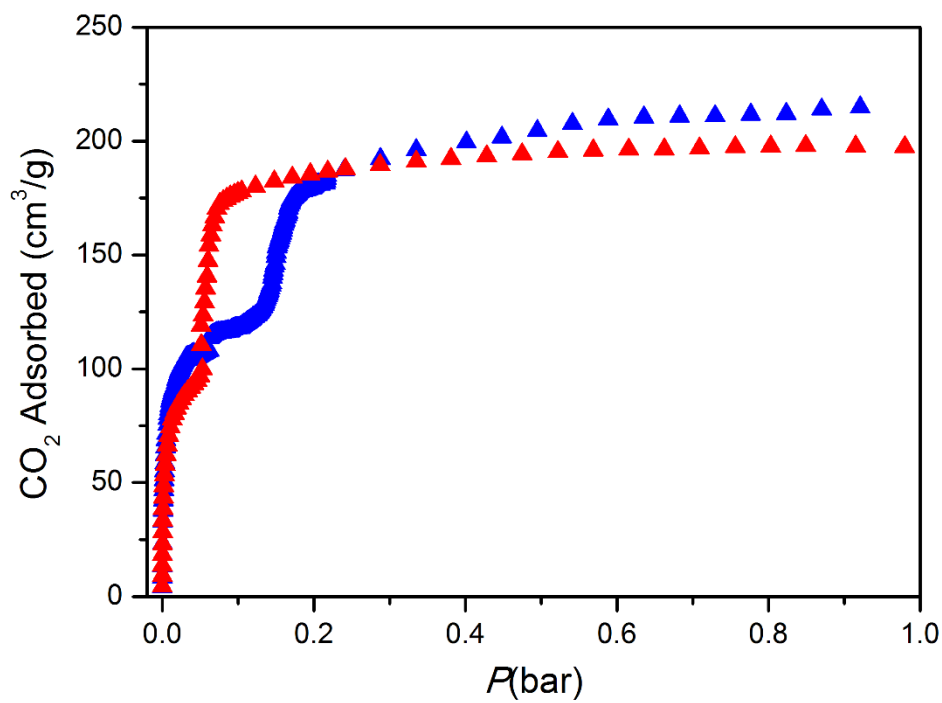


Figure. S7.2.7 CO_2 adsorption isotherms recorded at 195 K for Mn_3L_3 (red) and $Mn_3L_{2.49}L'_{0.51}$ (blue).

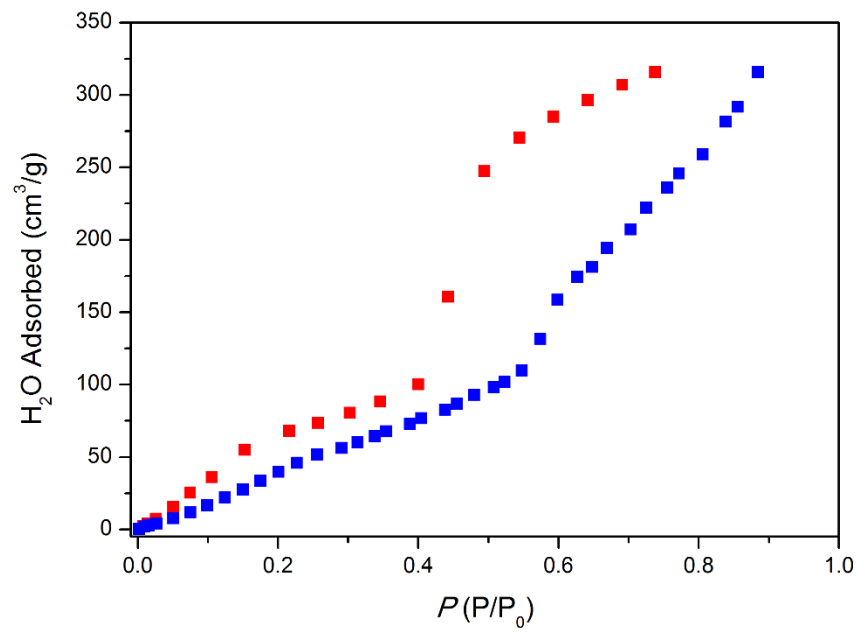


Figure. S7.2.8 H₂O adsorption isotherms recorded at 298 K for Mn₃L₃ (red) and Mn₃L_{2.49}L'_{0.51} (blue).

Optical Microscope Images of Mn_3L_3 based materials after exchange with Iron complexes

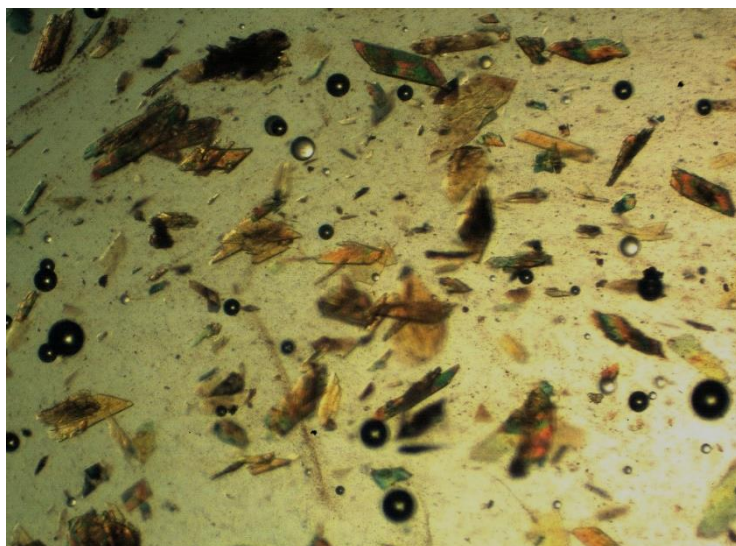


Figure. S7.2.9 An optical image of crystals of the Mn_3L_3 framework following metal exchange with $FeCl_2 \cdot 4H_2O$.

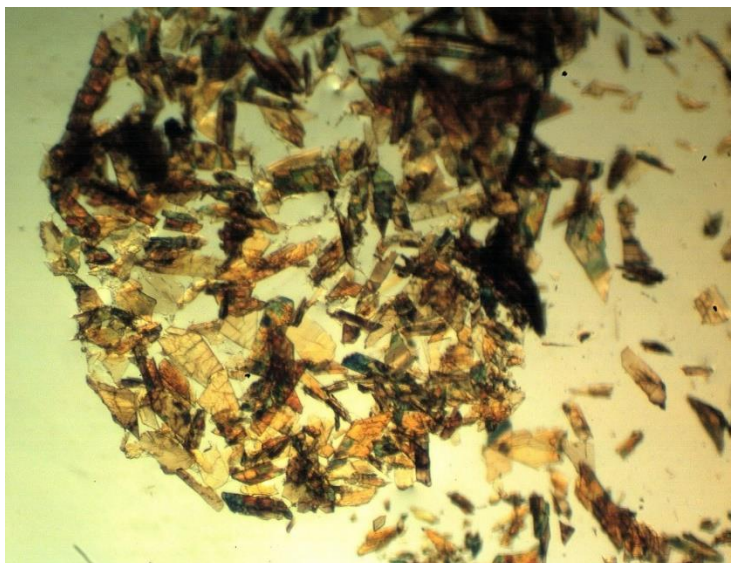


Figure. S7.2.10 An optical image of crystals of the Mn_3L_3 framework following metal exchange with $FeCl_3$.

Single crystal X-ray structure determinations on Fe-exchanged Mn₃L₃ samples

Full spheres of diffraction data were collected for single crystals mounted on nylon loops in Paratone-N at 100 K on the MX1 beamline of the Australia Synchrotron, $\lambda = 0.71073 \text{ \AA}$. [1] N_{tot} reflections were merged to N unique (R_{int} quoted) after 'empirical'/multiscan absorption correction (proprietary software) and used in the full matrix least squares refinements on F^2 , N_o with $F > 4\sigma(F)$ being considered 'observed'. Anisotropic displacement parameter forms were refined for the non-hydrogen atoms; hydrogen atoms were treated with a riding model [weights: $(\sigma^2(F_o)^2 + (aP)^2 + (bP)^2)^{-1}$; $P = (F_o^2 + 2F_c^2)/3$]. Neutral atom complex scattering factors were used; computation used the *SHELXL2013* program. [2] Pertinent results are given in the manuscript and in Table S1. CIF data have been deposited with the Cambridge Crystallographic Data Centre, CCDC reference numbers 1443923 ($[\text{Fe}_3(\text{L}_3)]\text{-FeCl}_3$) and 1443924 ($[\text{Mn}_{3-x}\text{Fe}_x(\text{L}_3)]\text{-FeCl}_2$, $x = 0.55$).

Variata. In the crystal structure of $[\text{Fe}_3(\text{L}_3)]\text{-FeCl}_3$ the metal node of the MOF was refined with an Fe₃ composition (with no allowance made in the refinement for the residual amount of Mn potentially remaining in the node). The MOF structure itself is well behaved with only limited disorder; the commonly encountered disorder of one of the phenyl rings of one of the ligand molecules (not the ligand that is metalated post-synthetically) in the asymmetric unit was refined with two major orientations (0.65:0.35 ratio). The post-synthetically added metal centre is not clearly resolved in this structure as F_{obs} maps reveal (see Figure S11). The metal site itself shows a region of diffuse electron density bounded by two additional regions of electron density in the 'axial' positions of a possible octahedral metal complex and a third region of electron density not on the mirror plane. As noted, we have modelled the electron density as an octahedral Fe³⁺ cation (due to slightly shorter Fe-N bonds of 2.084(8) Å) possessing two inner-sphere chloride ions and a third outer-sphere anion within the pores of the framework (see Fig. S11 below) but the disorder present limits ultimate confirmation and complete refinement. Residual electron density is located adjacent Fe(3) and Cl(1) with an unreasonably long Fe-Cl distance as a consequence of the apparent disorder. Two moderate peaks in the electron density different map located in the positions normally reserved for non-coordinated anions were refined as sites for the outer-sphere chloride ion with 0.2 occupancy each (both on a mirror plane); no additional positions were identified for the remaining 0.1 occupancy chloride to achieve charge balance.

In the refinement of $[\text{Mn}_{3-x}\text{Fe}_x(\text{L}_3)] \cdot 0.4\text{FeCl}_2$ ($x = 0.55$) the Fe occupancy of the metalation site was established by trial refinement and determined to be 0.2 (40% occupancy). Using this data and the Fe:Mn ratio for the material, established from inductively-coupled plasma mass spectrometry (ICP-MS), the composition of the metal node was set as $\text{Mn}_{2.45}\text{Fe}_{0.55}$ and refined with fixed occupancy. Due to the metal occupancy of the bis-pyrazole metalation site only being 40%, meaning that 60% of the ligand does not have a metal centre, there is considerable disorder of the ligand. In other structures of this MOF (without metalation but in DMF and CH_3CN)[3] we see distinct conformations for the non-coordinated ligand. Thus, for this structure, the low occupancy of the metal results in disorder for the bis-pyrazole binding site and the surrounding phenyl ring but the data was not of sufficient quality to allow this disorder to be modelled. Disorder of one of the phenyl rings of the other ligand molecule in the asymmetric unit was refined with two major orientations (0.77:0.23 ratio). The pores of the MOF contain a number of isolated peaks that could not be modelled as solvent (ethanol due to sample preparation). A peak, assigned as a chloride (0.2 occupancy, 40%) to provide charge balance to added octahedral Fe centre, sits in the pocket typically occupied by anions within the MOF structure.[3] There is additional electron density in this 'anion binding' site (largest peak = $2.958 \text{ e}\text{\AA}^3$ before application of the SQUEEZE routine of Platon) but that data is not of sufficient quality for us to build a reasonable structural model for refinement. The SQUEEZE routine of Platon[4] was applied to the data to account for this residual electron density bringing about significant improvements in R_1 , wR_2 and GOF.

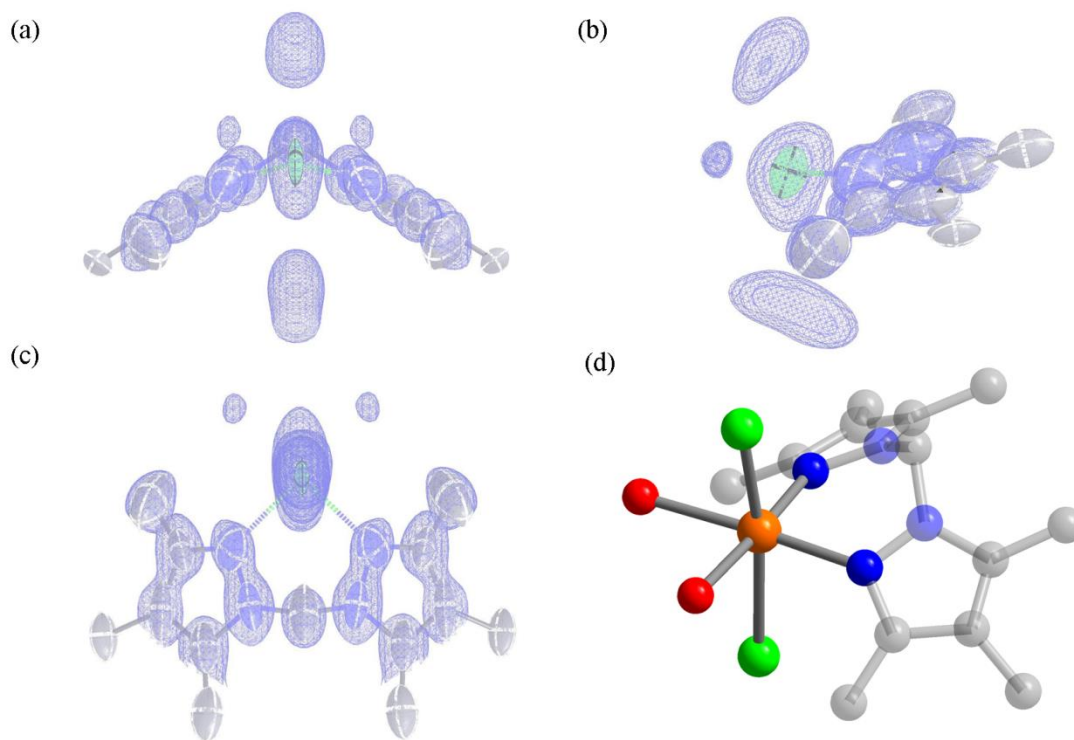


Figure S7.2.11. F_{obs} electron density maps showing the electron density in the vicinity of the post-synthetic metalation site in (a) front, (b) side and (c) top views, and (d) an image showing a perspective view of the major occupancy site. The coordination of the Fe consists of two inner-sphere chloride ions, with an outer sphere chloride ion (not shown) for charge compensation. Orange, green, grey, blue, and red spheres represent Fe, Cl, C, N, and O, respectively. H atoms have been omitted for clarity.

Table S7.2.1. Crystallographic parameters for the crystal structures of Fe-exchanged Mn₃L₃ samples.

Sample	Fe ₃ L ₃ ·FeCl ₃	Mn _{3-x} Fe _x (L ₃)·0.4FeCl ₂ (x=0.55)
Exchange Conditions	FeCl ₃ , acetonitrile, 60 °C, 5 days	FeCl ₂ ·4H ₂ O, ethanol, 60 °C, 5 days
Crystallographic Parameter		
Formula	C ₇₅ H ₆₆ Cl _{2.8} Fe ₄ N ₁₂ O ₁₄	C ₇₅ H ₆₆ Cl _{0.80} Fe _{0.95} Mn _{2.45} N ₁₂ O _{13.2}
FW	1682.05	1562.61
T, K	100(2)	100(2)
Wavelength, Å	0.71073	0.71073
Crystal system, space group	Monoclinic, <i>P2₁/m</i>	Monoclinic, <i>P2₁/m</i>
Z	2	2
a, Å	12.398 (3)	12.345 (3)
b, Å	33.496 (7)	33.257 (7)
c, Å	12.868 (3)	12.934 (3)
β, °	96.64 (3)	96.66 (3)
V, Å ³	5308.0 (19)	5274.4 (19)
d _{calc} , g/cm ³	1.052	0.984
Absorption coefficient, mm ⁻¹	0.658	0.486
F(000)	1727	1610
Crystal size, mm ³	0.20 × 0.10 × 0.05	0.30 × 0.10 × 0.05
Theta range for data collection	1.22 - 27.0	1.66 - 27.0
Index range	-14 ≤ h ≤ 14, -40 ≤ k ≤ 40, -15 ≤ l ≤ 15	-16 ≤ h ≤ 16, -43 ≤ k ≤ 43, -16 ≤ l ≤ 16
Reflections collected	71745	86249
Independent reflections	9914	11740
Data/restraints/parameters	9914 / 1 / 539	11740 / 0 / 539
GOF on F ²	1.301	1.051
Largest diff. peak and hole, e·Å ⁻³	3.02 and -0.81	1.54 and -1.07
R ₁ , [I > 2σ(I)]	0.1077	0.1036
R ₁ (wR ₂) ^a , all data	0.1288 (0.3279)	0.1147 (0.2994)
CCDC Number	1443923	1443924

$$^a R_1 = \sum ||F_o| - |F_c|| / \sum |F_o|, wR_2 = \{\sum [w(F_o^2 - F_c^2)^2] / \sum [w(F_o^2)^2]\}^{1/2}$$

References

- (1) T. M. McPhillips, S. E. McPhillips, H. J. Chiu, A. E. Cohen, A. M. Deacon, P. J. Ellis, E. Garman, A. Gonzalez, N. K. Sauter, R. P. Phizackerley, S. M. Soltis and P. Kuhn, *J. Synchrotron Rad.*, 2002, **9**, 401.
- (2) G.M. Sheldrick, Univ. Gottingen, Gottingen, Germany, 2013; *Acta Crystallogr.*, 2008, **A64**, 112; *Acta Crystallogr.* 2015, **C71**, 3.
- (3) (a) W. M. Bloch, A. Burgun, C. J. Coghlan, R. Lee, M. L. Coote, C. J. Doonan and C. J. Sumby, *Nat. Chem.*, 2014, **6**, 906. (b) W. M. Bloch, A. Burgun, C. J. Doonan and C. J. Sumby, *Chem. Commun.*, 2015, **51**, 5486.
- (4) (a) A.L. Spek, *Acta Crystallogr.*, 2009, **D65**, 148; (b) A.L. Spek, *Acta Crystallogr.* 2009, **C71**, 9.

7.3 Supplementary Information for Chapter 4

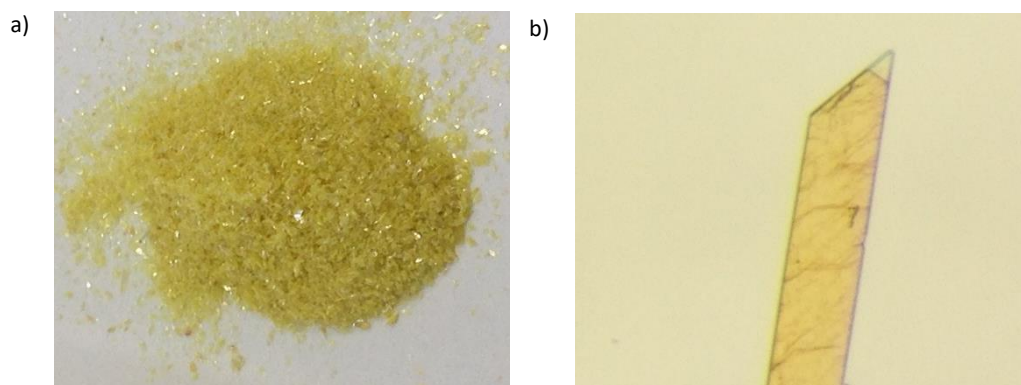
7.3.1 Optical images of metalated samples of **1**.

Figure S7.3.1. (a) A photograph of **1**·[Mn(CO)₃(H₂O)]Br after one click chemistry cycle displaying characteristic yellow coloration of the [Mn(CO)₃]⁺ moiety and (b) an optical microscope image of a single crystal of **1**·[Mn(CO)₃(H₂O)]Br after one click chemistry cycle.

7.3.2 Scanning electron microscopy (SEM) images and energy dispersive X-ray analysis (EDX) of metalated samples of **1**

Table S7.3.2.1: Bromide anion occupancy determined via measurement of the Mn:Br ratio using EDX analysis.

Sample	Bromide occupancy (%) ^{a,b}	Std error (%)
1 ·[Mn(CO) ₃ (H ₂ O)]Br	98	1.2
1 ·[Mn(CO) ₃ N ₃]	7	1.5
1 ·[Mn(CO) ₃ OT] ^c	130	4.1
1 ·[Mn(CO) ₃ DMT] ^c	115	3.3

^a Average atomic% obtained from three crystals.

^b Relative to full occupancy of the free chelation sites in **1**.

^c Following alkylation with MeBr to regenerate **1**·[Mn(CO)₃(H₂O)]Br.

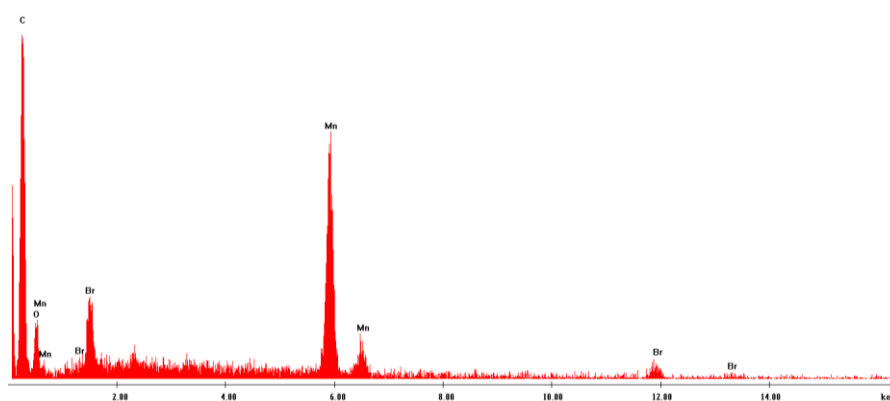


Figure S7.3.2.2. Representative raw EDX spectra for **1**·[Mn(CO)₃(H₂O)]Br.

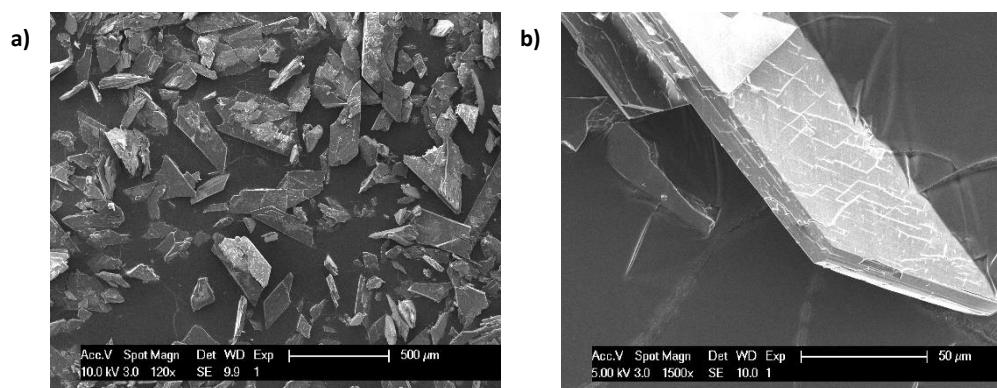


Figure S7.3.2.1. SEM images of metalated **1** following click chemistry showing (a) a group of crystals and (b) an example of a single crystal.

7.3.3. NMR spectroscopy of the triazole products

7.3.3.1 NMR spectra of N-methyl 4-hex-5'-ynyl-1',4'-dione-1,2,3-triazole

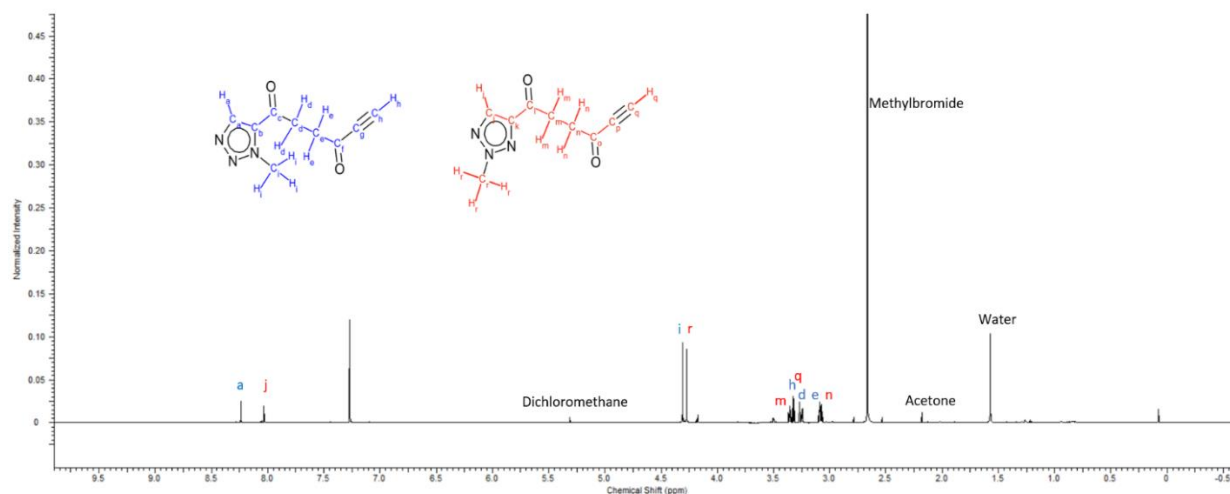


Figure S7.3.3.1. ^1H NMR spectrum (CDCl_3) of the reaction solution containing N-methyl 4-hex-5'-ynyl-1',4'-dione-1,2,3-triazole. Signals corresponding to the major N(2)- and N(3)-methylated isomers, are labelled.

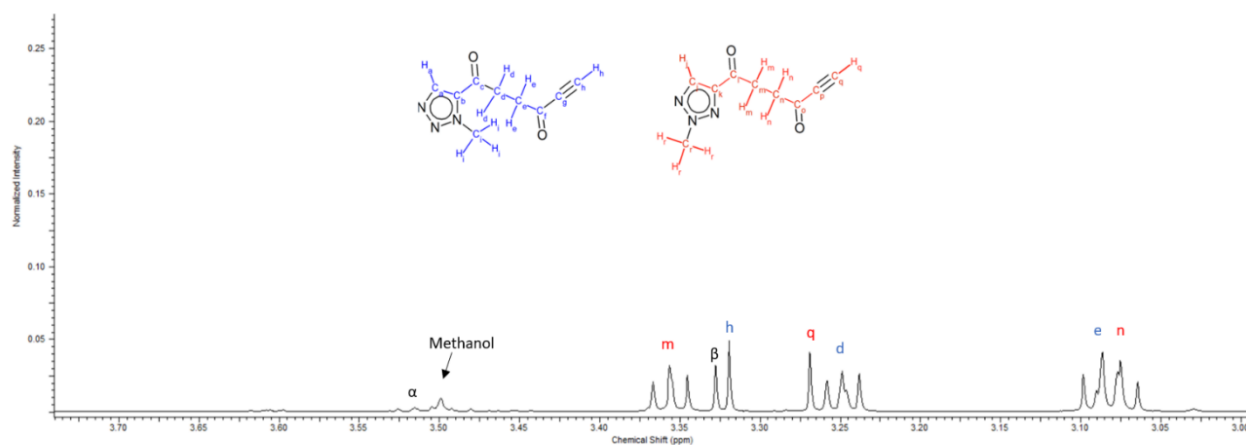


Figure S7.3.3.2. Magnified view of the ^1H NMR spectrum (CDCl_3) of the reaction solution containing N-Methyl 4-hex-5'-ynyl-1',4'-dione-1,2,3-triazole. Signals corresponding to the major N(2)- and N(3)-methylated isomers, are labelled. The signal at 3.49 ppm corresponds to methanol, which originates from the MeBr; adjacent to the methanol signal is a small triplet signal (α), which corresponds to the minor N(1)-methylated isomer (see SI section 3.2 for discussion of this minor isomer). The singlet signal β at 3.33 ppm is a contaminant and shows coupling to a carbon signal at 60.5 ppm (see SI Figure S3.1.4).

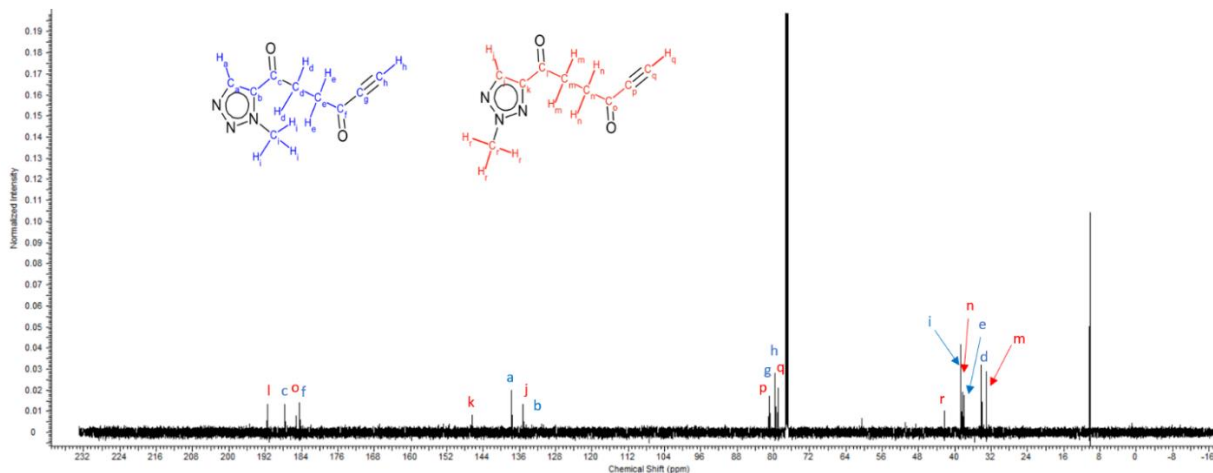


Figure S7.3.3. ^{13}C NMR spectrum (CDCl_3) of the reaction solution containing N-methyl 4-hex-5'-ynyl-1',4'-dione-1,2,3-triazole. A magnified view of the region of interest is shown below (SI Figure S3.1.4).

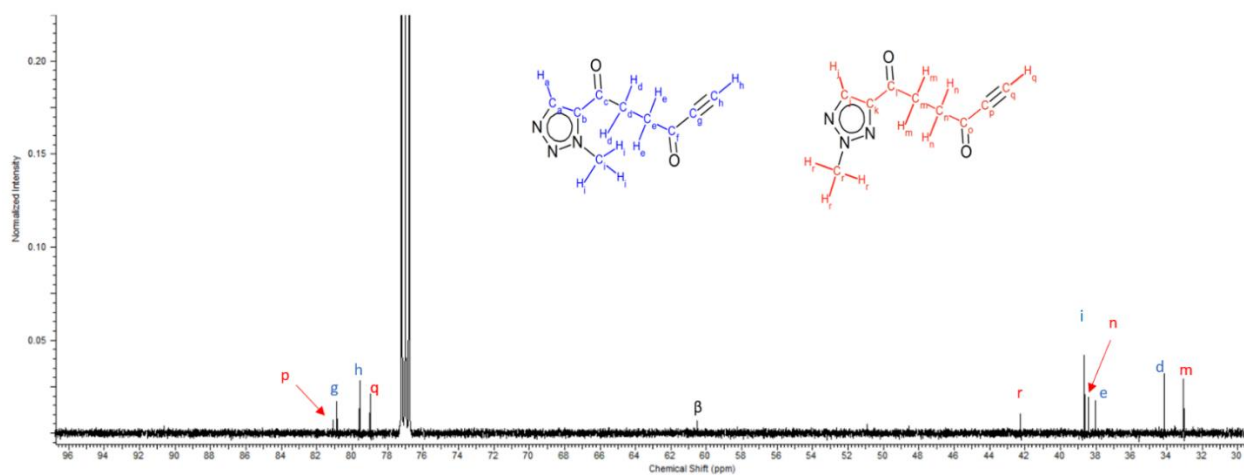


Figure S7.3.4. Magnified view of the ^{13}C NMR spectrum (CDCl_3) of the reaction solution containing N-methyl 4-hex-5'-ynyl-1',4'-dione-1,2,3-triazole. The signal β at 60.5 ppm is a contaminant and is coupled to a singlet proton signal at 3.33 ppm (see SI Figure S3.1.2).

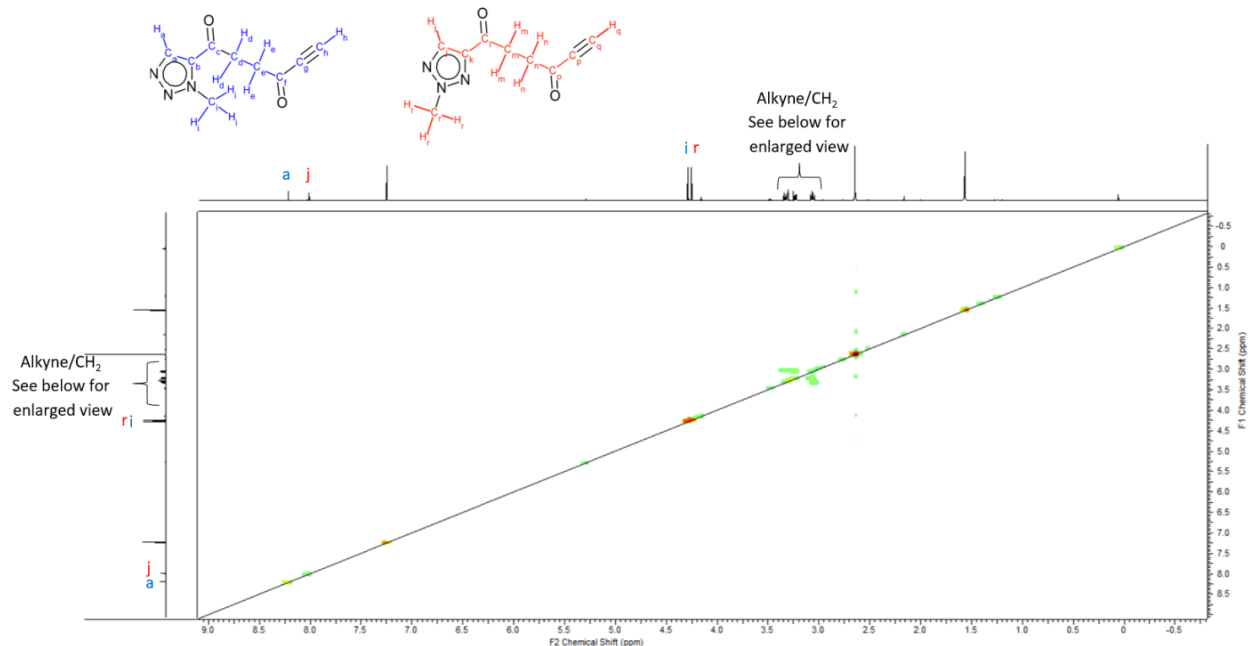


Figure S7.3.3.5. COSY NMR spectrum (CDCl₃) of the reaction solution containing N-methyl 4-hex-5'-ynyl-1',4'-dione-1,2,3-triazole. A magnified view of the region of interest is shown below (SI Figure S3.1.6).

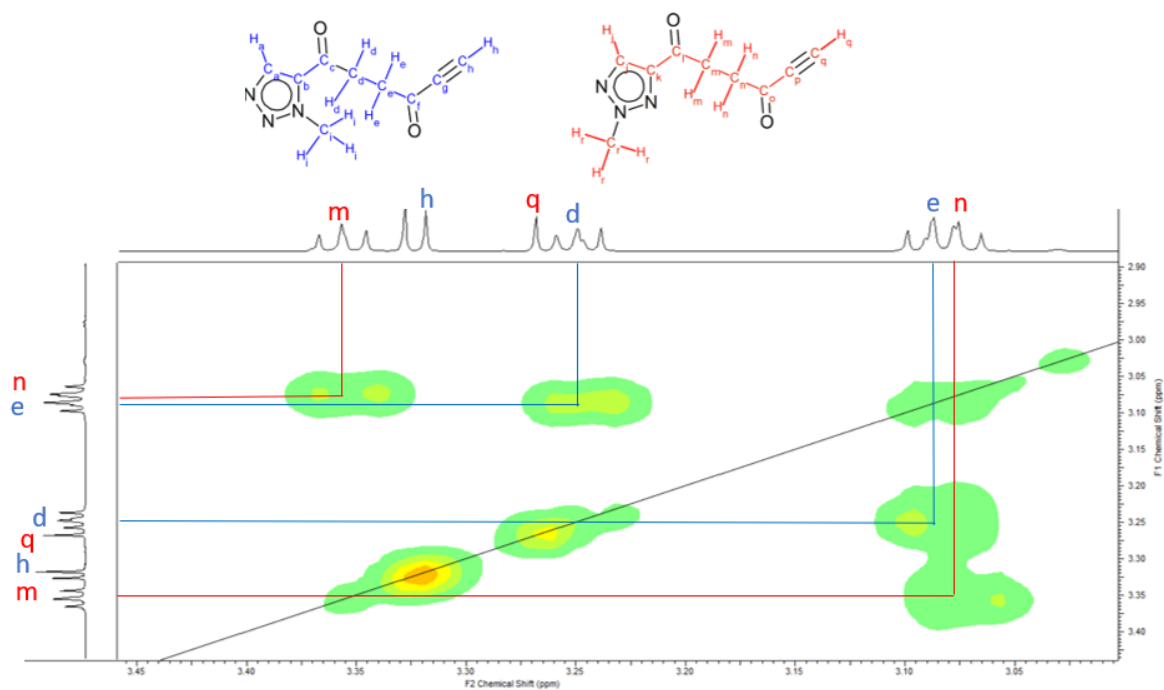


Figure S7.3.3.6. Magnified view of the COSY NMR spectrum (CDCl₃) of the reaction solution containing N-methyl 4-hex-5'-ynyl-1',4'-dione-1,2,3-triazole. Signals corresponding to the major isomers, N(2) and N(3), are labelled.

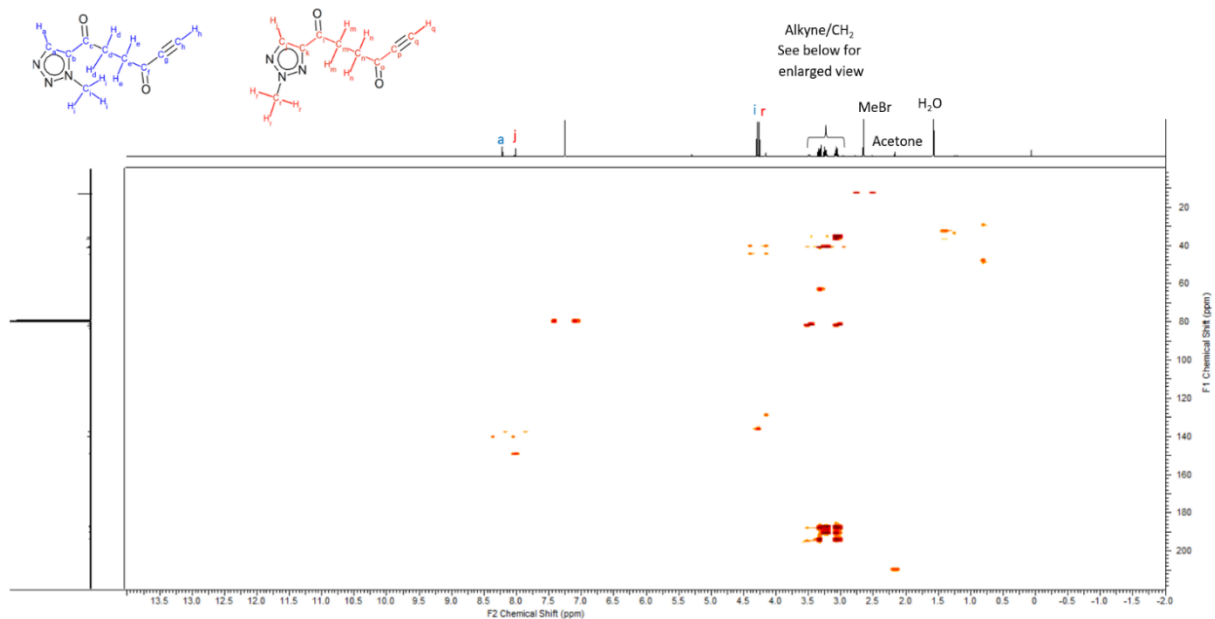


Figure S7.3.3.7. HMBC NMR spectrum (CDCl_3) of the reaction solution containing N-methyl 4-hex-5'-ynyl-1',4'-dione-1,2,3-triazole. Magnified views showing the regions of interest are given below.

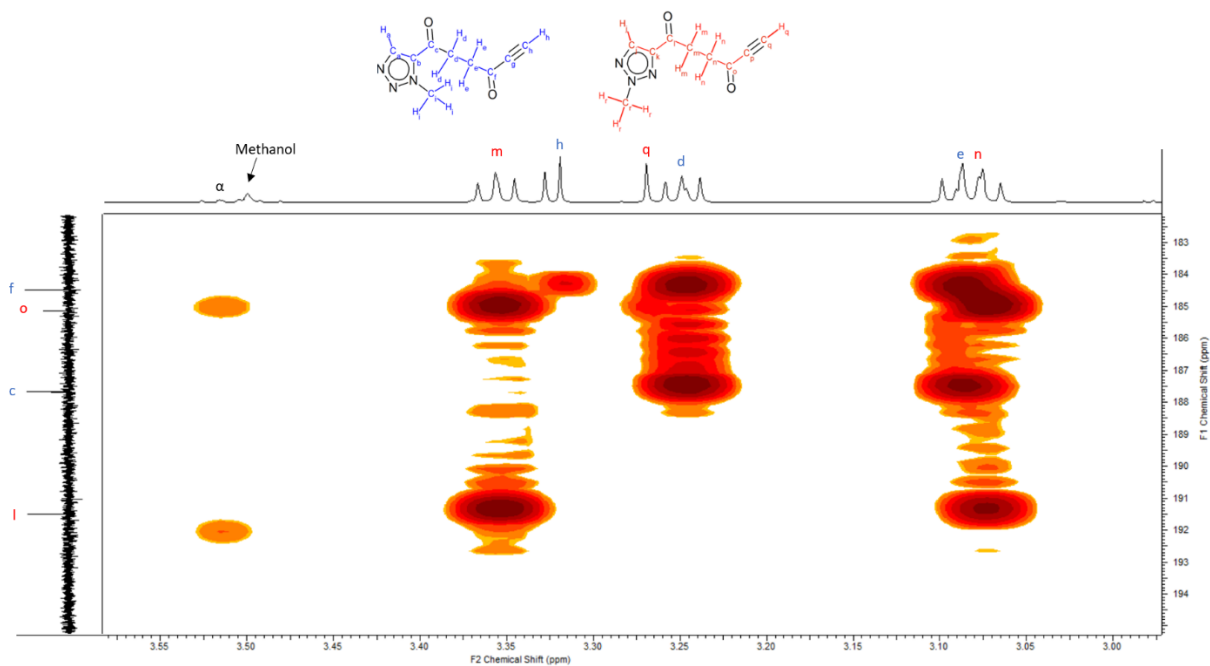


Figure S7.3.3.8. HMBC NMR spectrum (CDCl_3) of the reaction solution containing N-methyl 4-hex-5'-ynyl-1',4'-dione-1,2,3-triazole. This view contains the carbonyl region of the spectrum, highlighting long-range interactions between the alkyne and CH_2 protons and ketone carbons. **NOTE:** the two smaller signals on the far left indicate a minor N(1) isomer (see SI Figure S3.2.2).

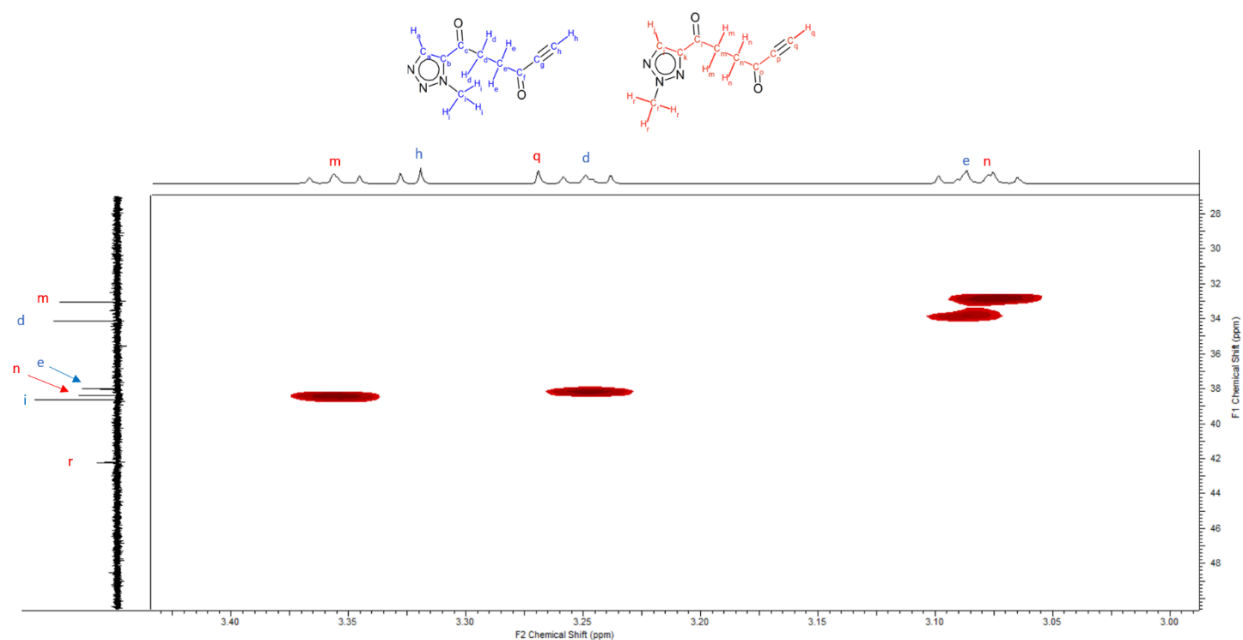


Figure S7.3.3.9. HMBC NMR spectrum (CDCl_3) of the reaction solution containing N-methyl 4-hex-5'-ynyl-1',4'-dione-1,2,3-triazole. This view contains the alkyl region of the spectrum, highlighting long-range interactions between the CH_2 protons and adjacent carbons.

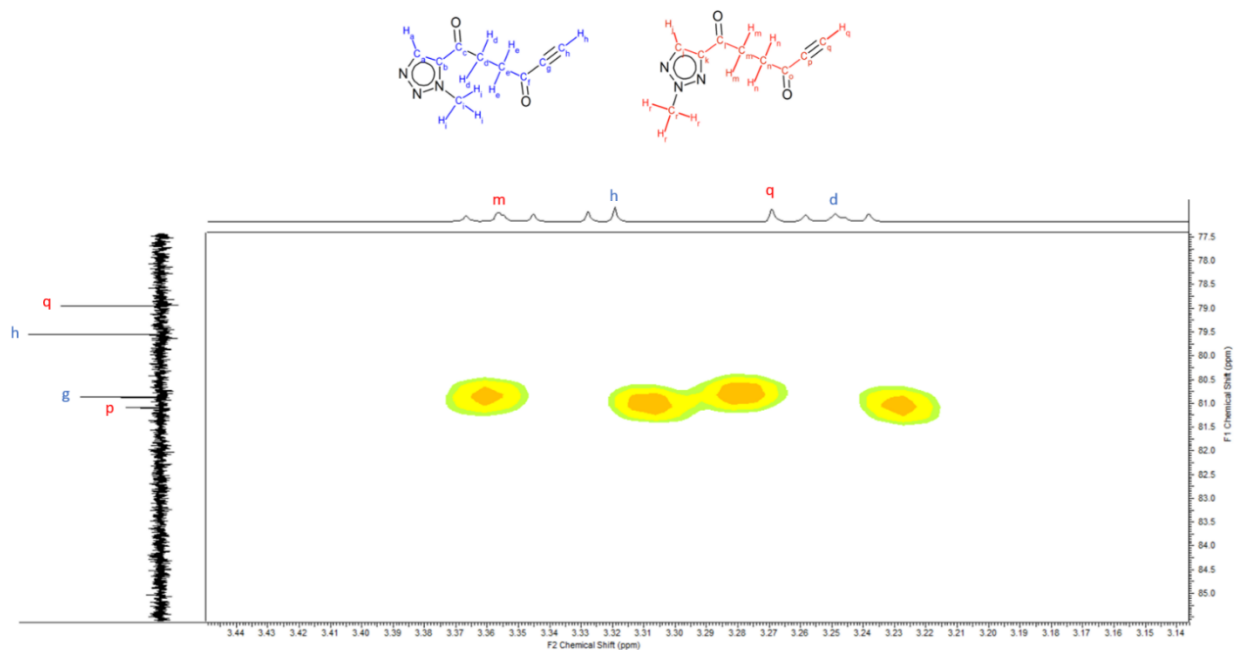


Figure S7.3.3.10. HMBC NMR spectrum (CDCl_3) of the reaction solution containing N-methyl 4-hex-5'-ynyl-1',4'-dione-1,2,3-triazole. This view contains the alkyne region of the ^{13}C NMR spectrum, highlighting long-range interactions between the alkyne and CH_2 protons and internal alkyne carbon (C_g and C_p).

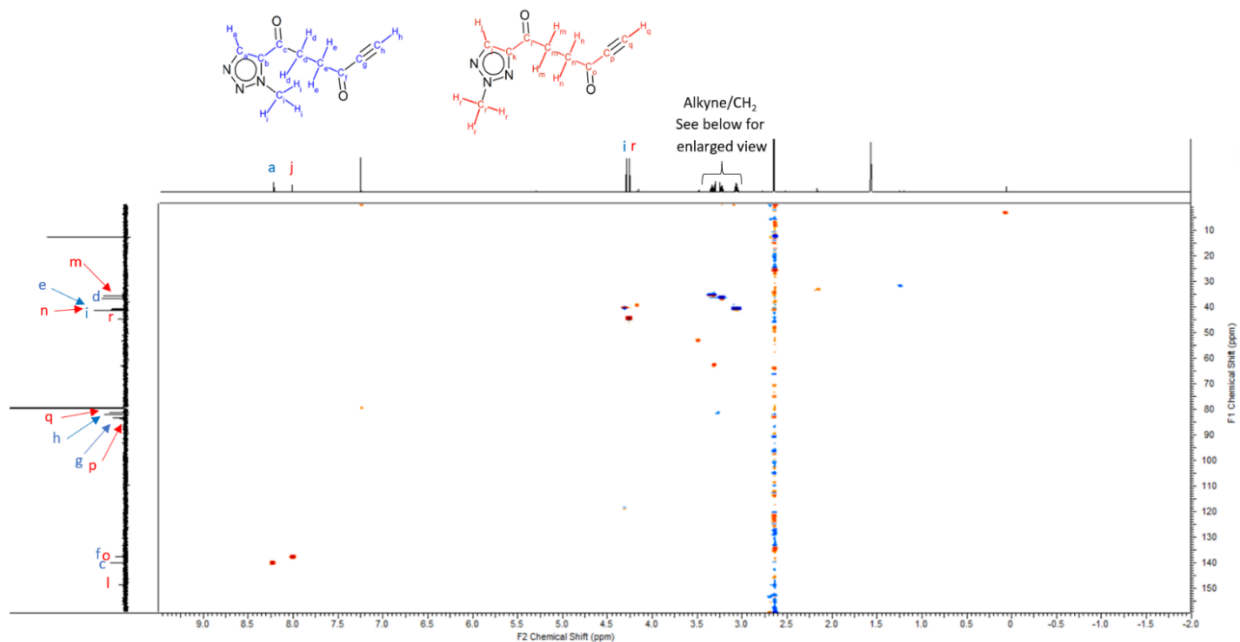


Figure S7.3.3.11. HSQC NMR spectrum (CDCl_3) of the reaction solution containing N-methyl 4-hex-5'-ynyl-1',4'-dione-1,2,3-triazole. A magnified view showing the alkyne and alkyl group regions is given below.

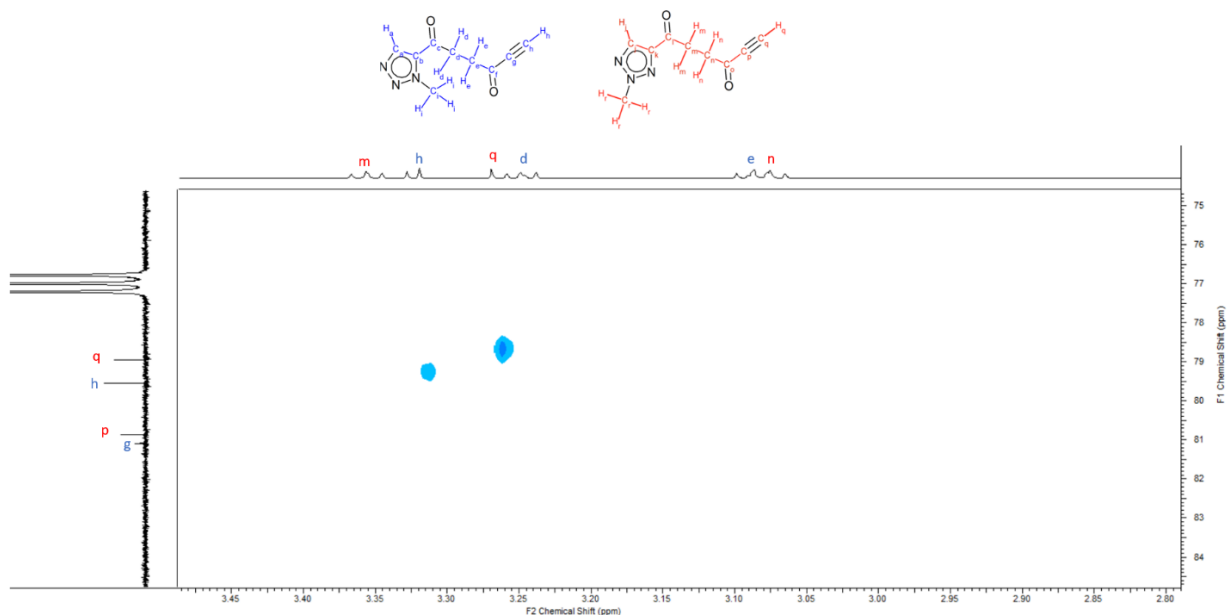


Figure S7.3.3.12. HSQC NMR spectrum (CDCl_3) of the reaction solution containing N-methyl 4-hex-5'-ynyl-1',4'-dione-1,2,3-triazole, highlighting the correlation between the alkyne proton and carbon signals (C_h and C_q for the N(3)- and N(2)-methyl isomers, respectively).

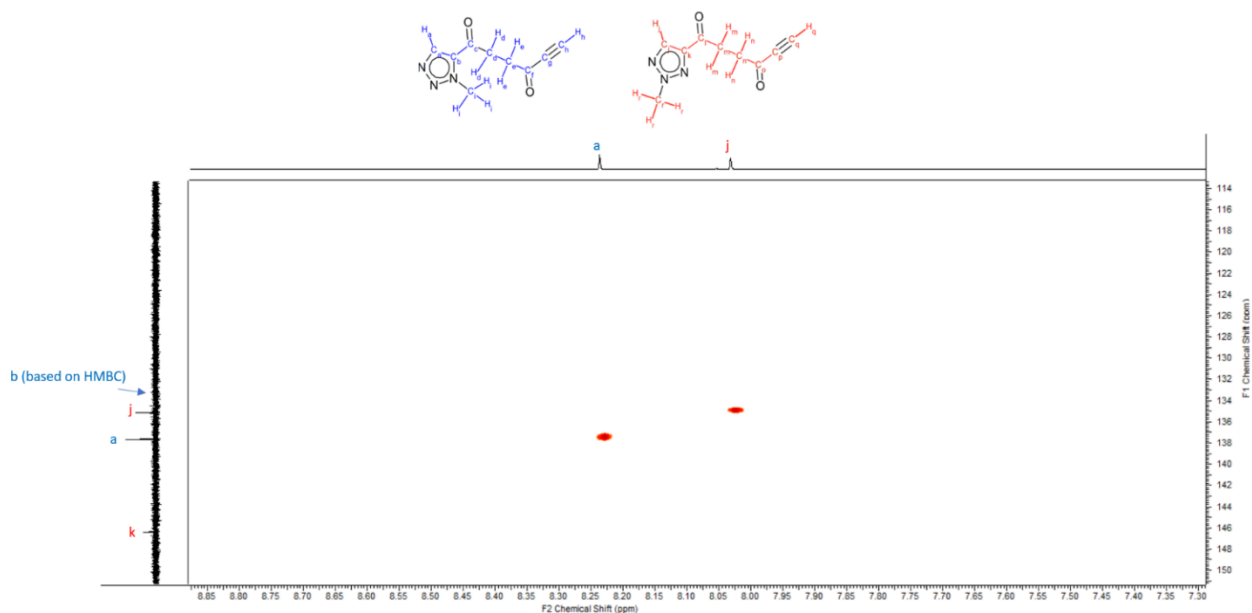


Figure S7.3.3.13. HSQC NMR spectrum (CDCl_3) of the reaction solution containing N-methyl 4-hex-5'-ynyl-1',4'-dione-1,2,3-triazole, highlighting the correlation between the triazole 'CH' proton and carbon signals (C_a and C_j for the N(3)- and N(2)-methyl isomers, respectively).

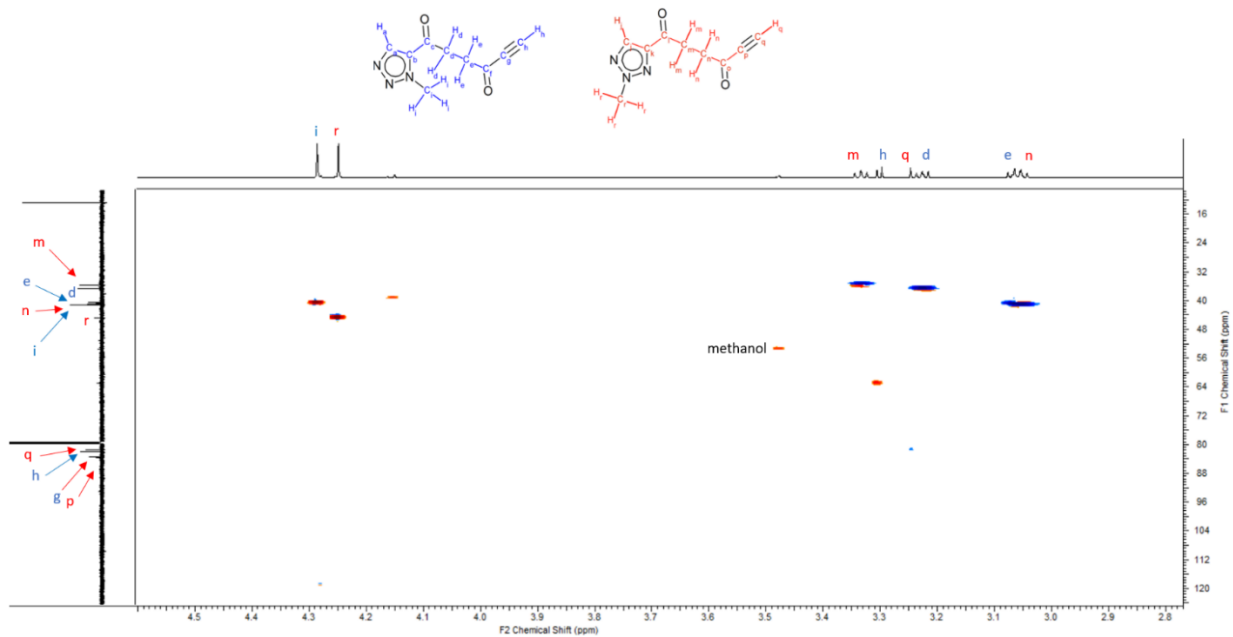


Figure S7.3.3.14. HSQC NMR spectrum (CDCl_3) of the reaction solution containing N-methyl 4-hex-5'-ynyl-1',4'-dione-1,2,3-triazole, highlighting the triazole N-methyl, alkyne and alkane regions of the spectrum.

7.3.3.2 Evidence for the presence of N(1)-methyl 4-hex-5'-ynyl-1',4'-dione-1,2,3-triazole as a minor isomer

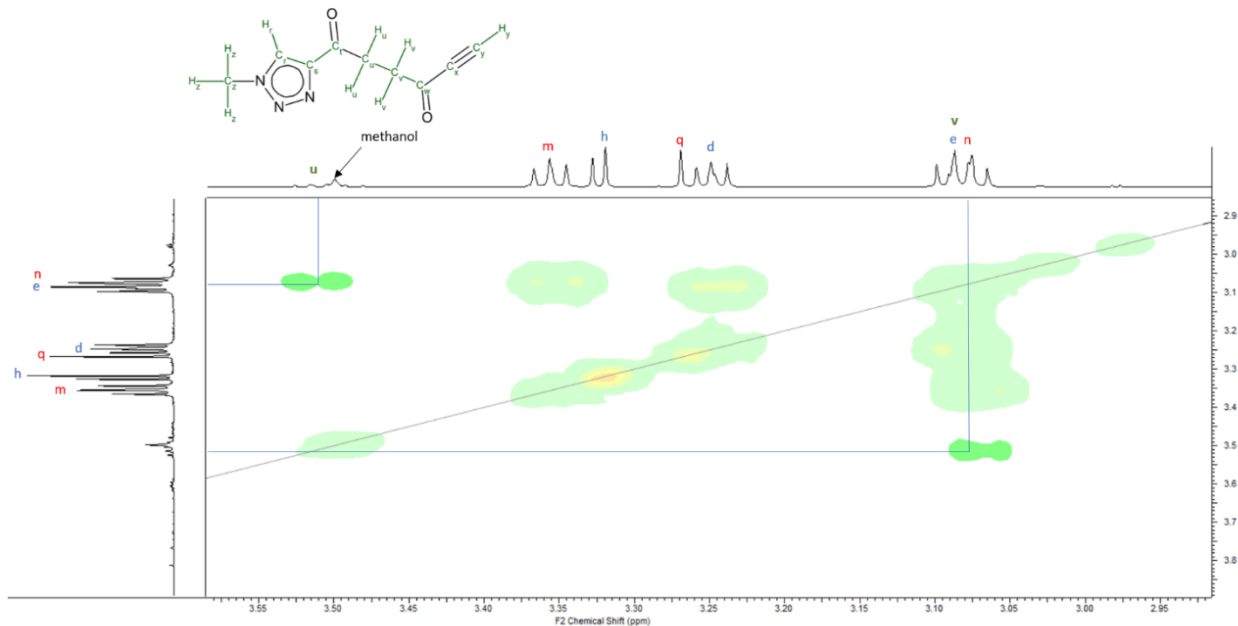


Figure S7.3.3.2.1. The COSY NMR shows cross-peaks between a triplet signal at 3.52 (adjacent to the methanol signal) in the minor N(1) methylated isomer and the overlapping triplets corresponding to protons H_e and H_n in the major N(3) and N(2) methylated isomers (adjacent COSY cross-peaks corresponding to the major isomers have been faded for clarity). Considering that the CH₂ protons in the ethyl bridge of both the major isomers follow a pattern in which the CH₂ protons closest to the triazole group are shifted downfield, the relative position of the COSY cross-peaks suggests that the signal at 3.52 ppm corresponds to the 'u' protons near the triazole moiety in the N(1) isomer, while the signal near 3.06 ppm corresponds to the 'v' protons. *This is consistent with a mono-triazole N(1)-methylated product rather than the bis-triazole, in which both CH₂ groups would be expected to be shifted downfield.* The triazole CH proton signal is observed at 8.05 ppm (see main text, Figure 5) while the N-methyl signal is observed at 4.17 ppm (see SI Figure S3.1.11). The alkyne CH signal for the N(1) isomer cannot be conclusively identified. A correlation is observed between the CH₂ proton signal at 3.52 ppm and two carbon signals in the carbonyl region (see Figure S3.2.2 below).

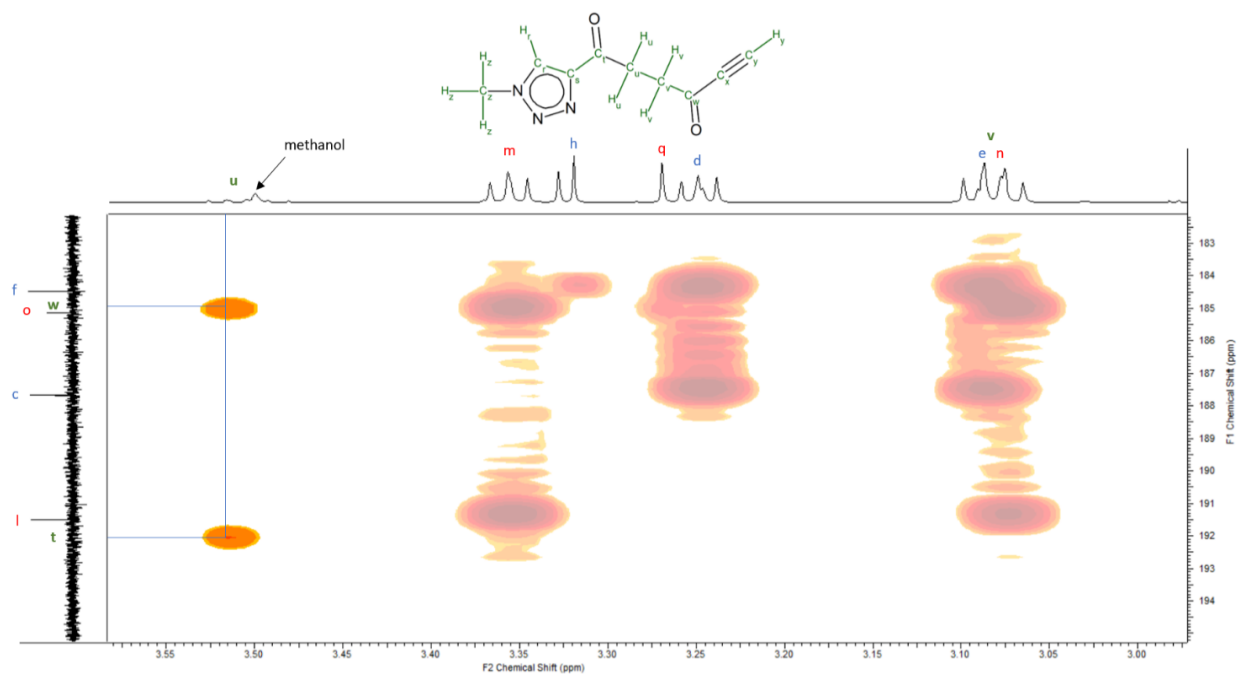


Figure S7.3.3.2.2. HMBC NMR spectrum of the carbonyl region, showing correlation between two carbonyl ¹³C NMR signals and the CH₂ triplet (u) signal at 3.52 ppm. This is consistent with the adjacent signals observed for the corresponding moieties in the N(2) and N(3) isomers. Taking into consideration the assignment of the major isomers, the cross-peaks can be assigned to carbonyl carbons C_w and C_t.

7.3.3.3 NMR spectroscopy of N-methyl 4-octa-8'-ynyl-1',6'-dione-1,2,3-triazole

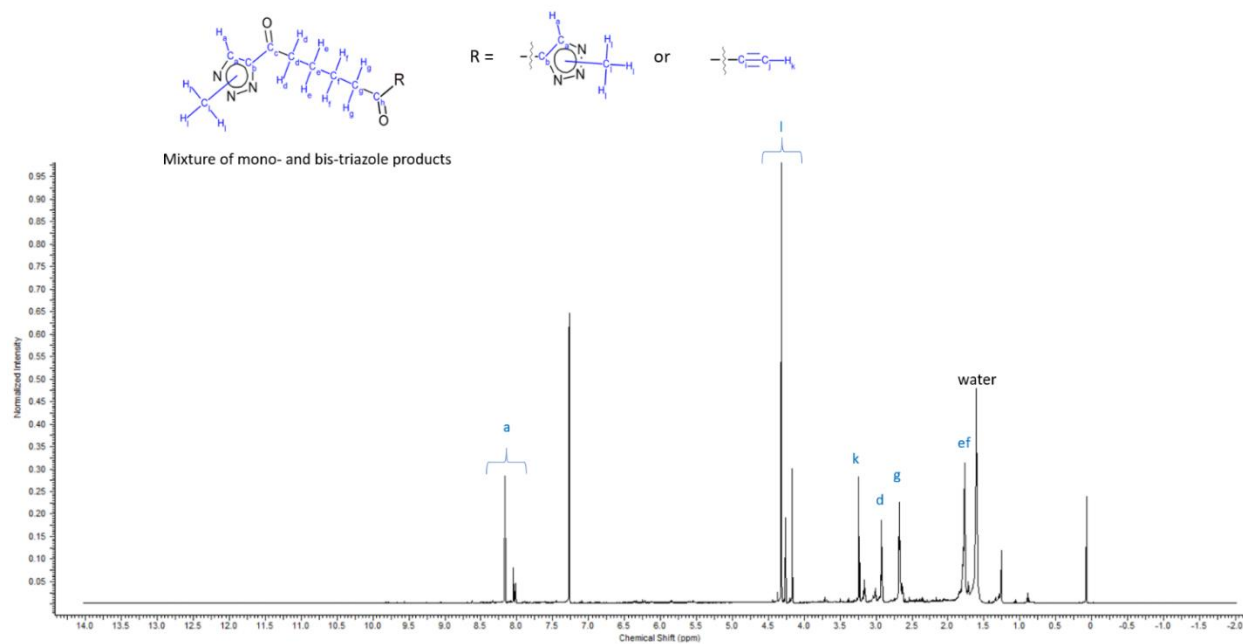


Figure S7.3.3.1. ^1H NMR spectrum (CDCl_3) of the reaction solution containing N-methyl 4-octa-8'-ynyl-1',6'-dione-1,2,3-triazole.

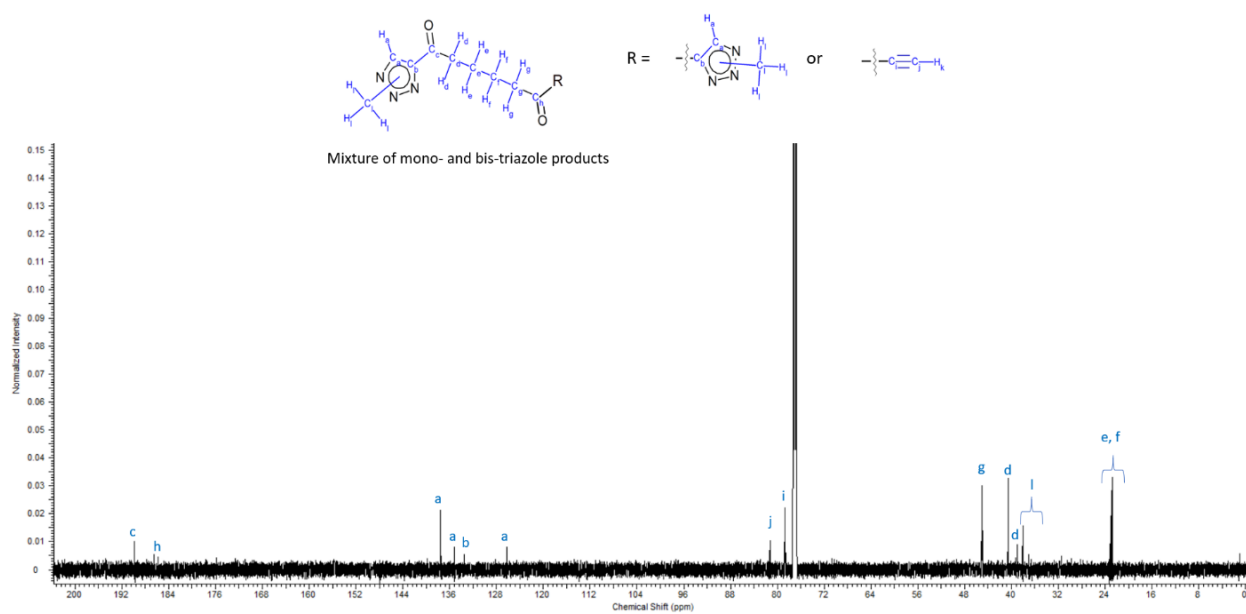


Figure S7.3.3.2. ^{13}C NMR spectrum (CDCl_3) of the reaction solution containing N-methyl 4-octa-8'-ynyl-1',6'-dione-1,2,3-triazole.

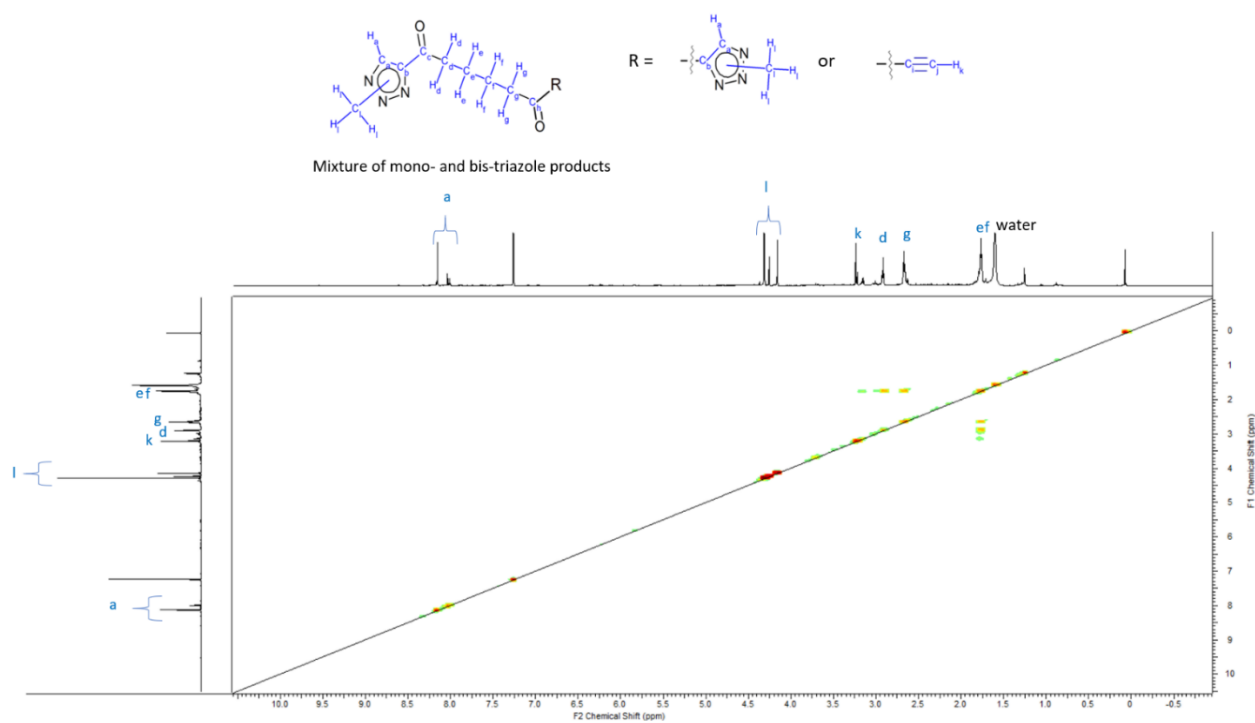


Figure S7.3.3.3. COSY NMR Spectrum (CDCl_3) of the reaction solution containing N-methyl 4-octa-8'-ynyl-1',6'-dione-1,2,3-triazole. A magnified view of the region of interest is given below (SI Figure S3.3.4).

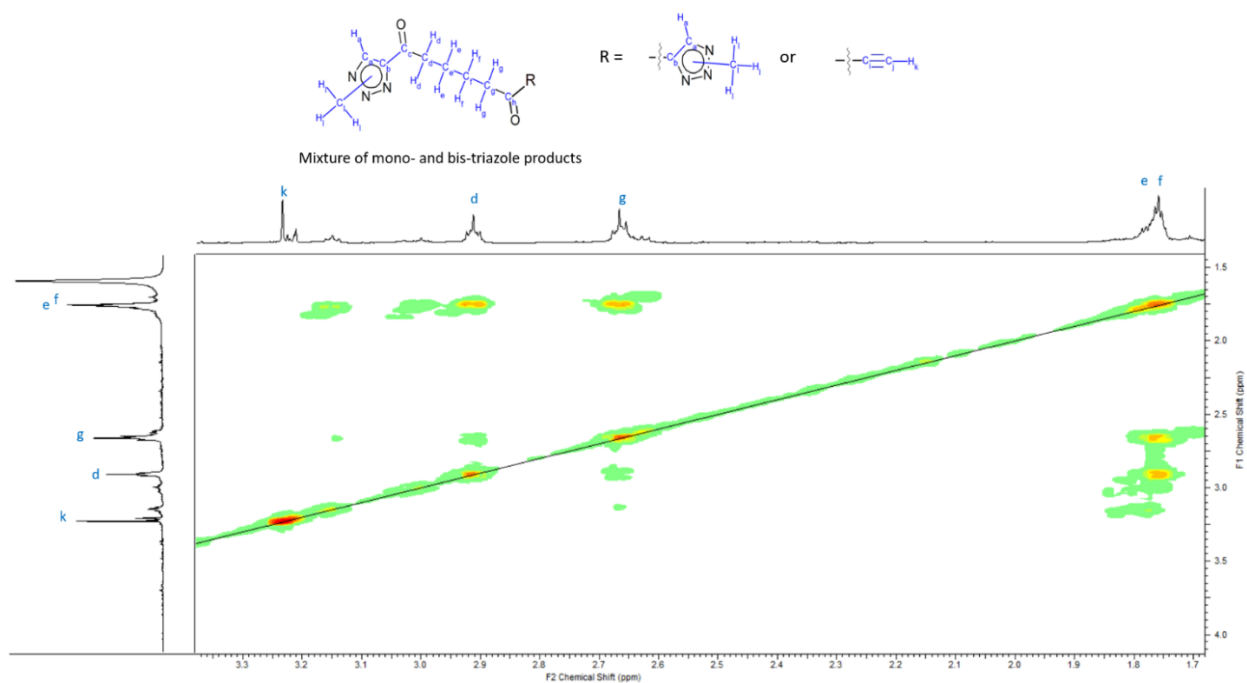


Figure S7.3.3.4. COSY NMR spectrum (CDCl_3) of the reaction solution containing N-methyl 4-octa-8'-ynyl-1',6'-dione-1,2,3-triazole.

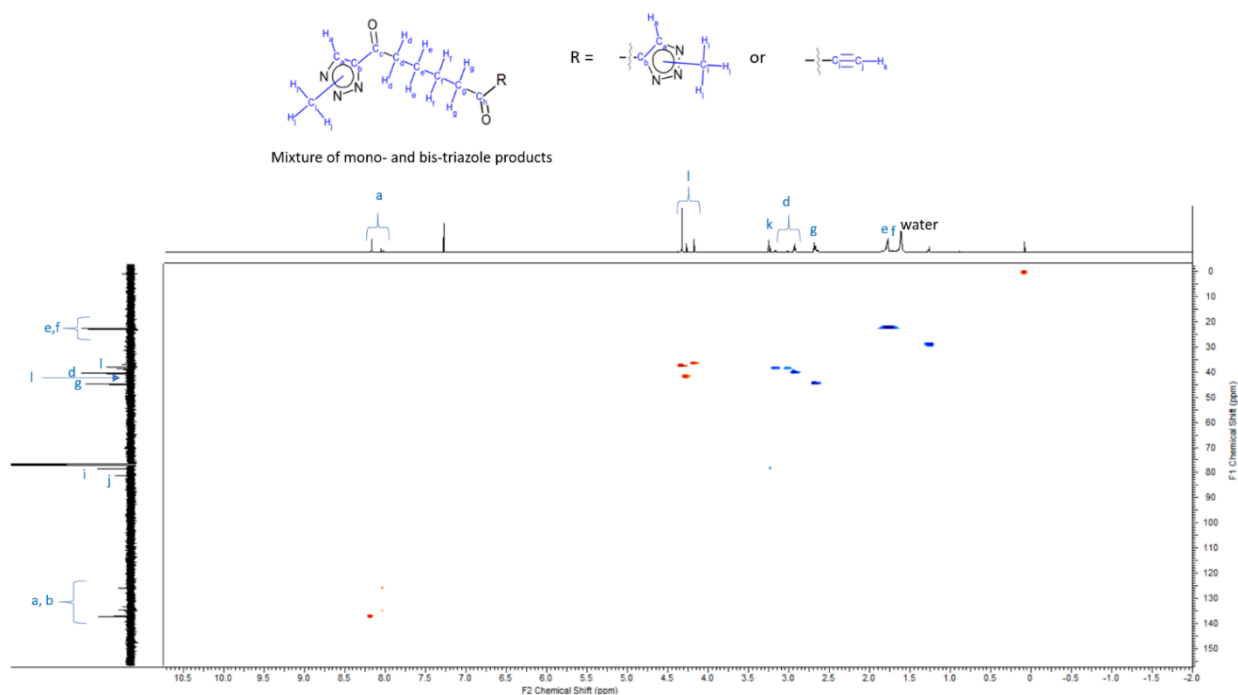


Figure S7.3.3.5. COSY NMR spectrum (CDCl_3) of the reaction solution containing N-methyl 4-octa-8'-ynyl-1',6'-dione-1,2,3-triazole. A magnified view of the region of interest is given below (SI Figure S3.3.6).

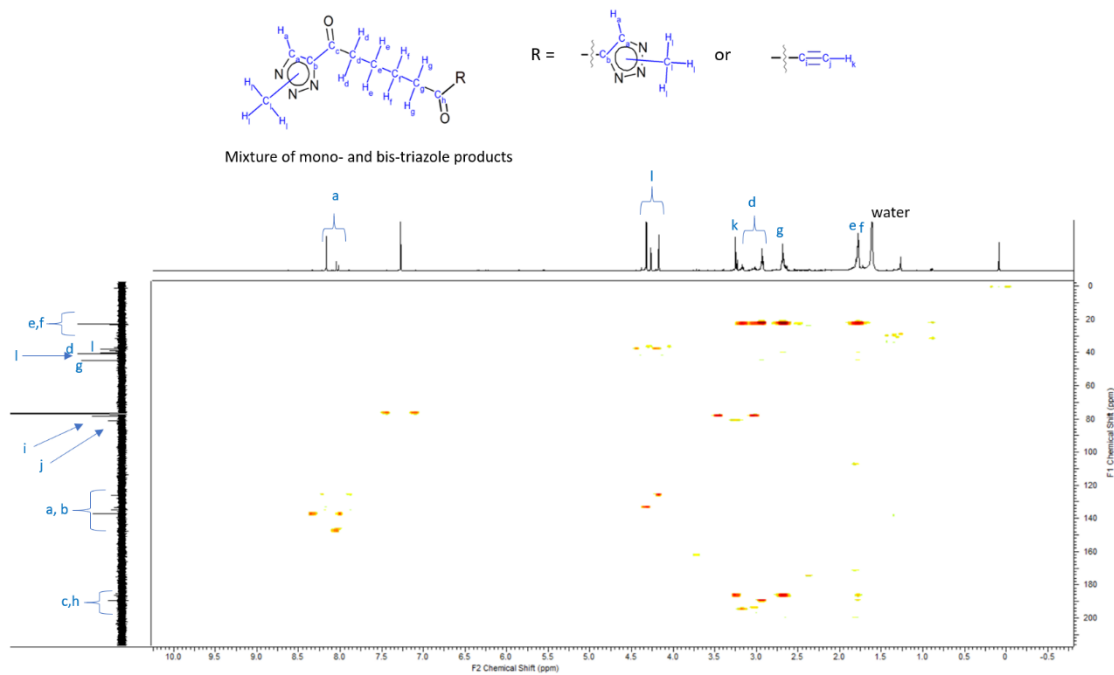


Figure S7.3.3.6. HMBC NMR spectrum (CDCl_3) of the reaction solution containing N-methyl 4-octa-8'-ynyl-1',6'-dione-1,2,3-triazole. The spectrum contains cross-peaks between the ^{13}C satellite signals in the proton NMR and the associated ^{13}C peak.

7.3.3.4 NMR spectroscopy of N-methyl 4-deca-9'-ynyl-1',8'-dione-1,2,3-triazole

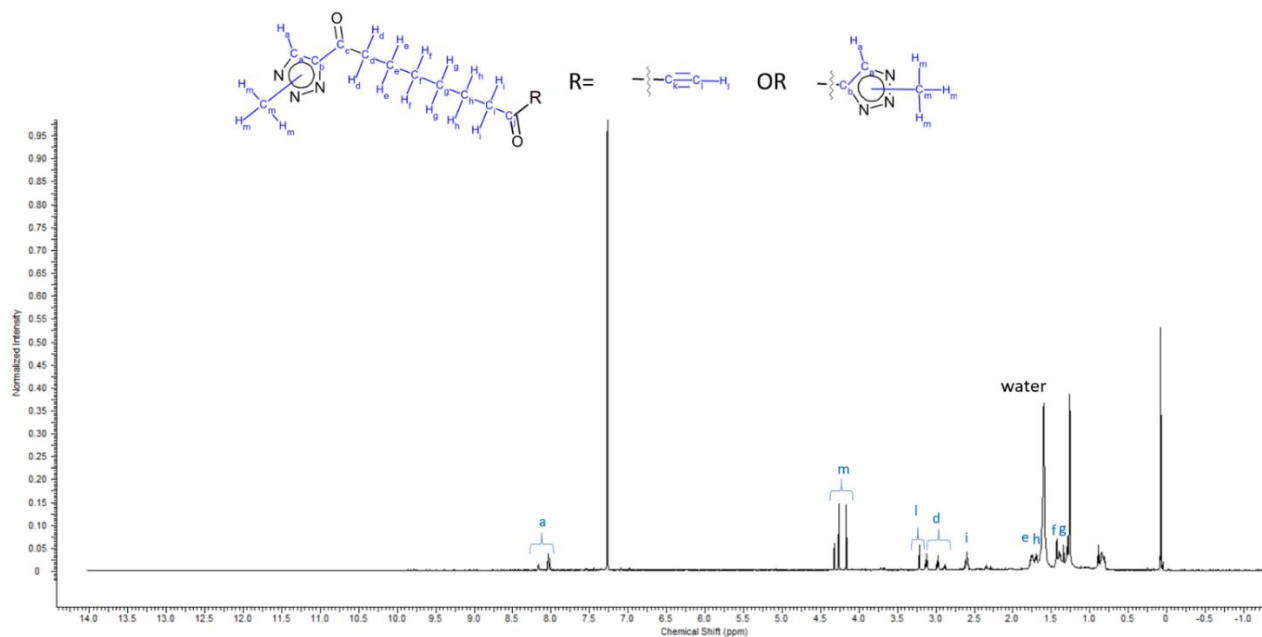


Figure S7.3.3.4.1. ^1H NMR spectrum (CDCl_3) of the reaction solution containing N-methyl 4-deca-9'-ynyl-1',8'-dione-1,2,3-triazole. The product is obtained as a mixture of mono- and bis- "click" products; the key features of the spectrum are labelled.

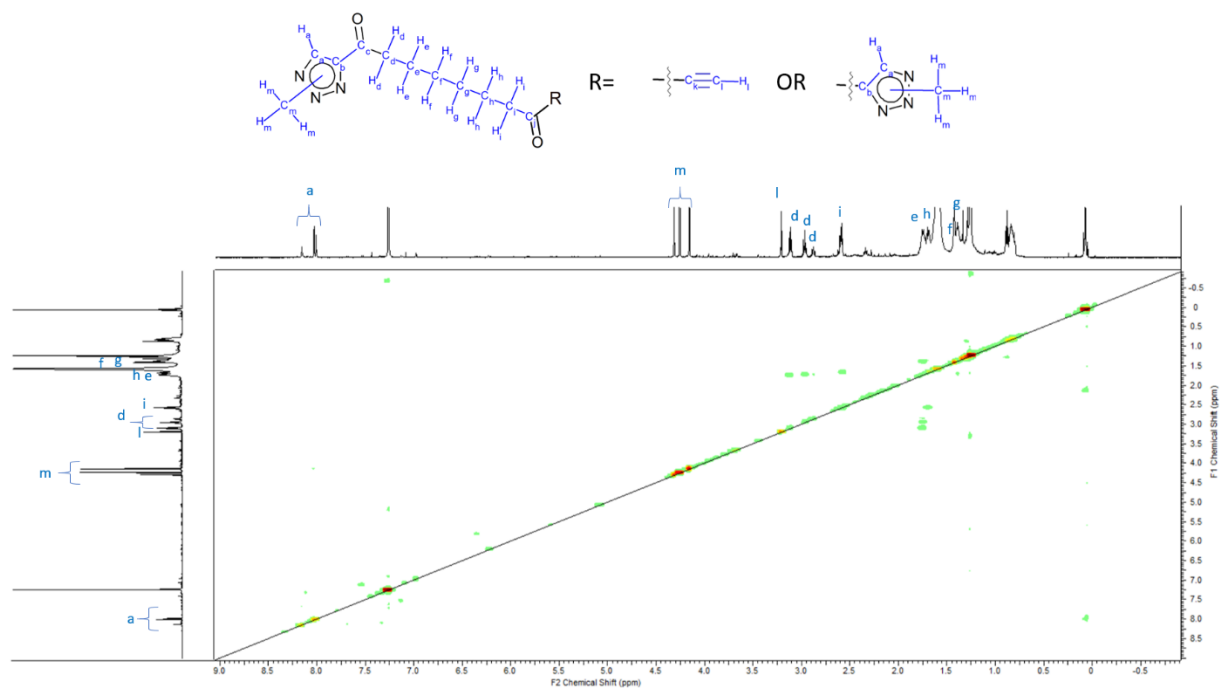


Figure S7.3.3.4.2. COSY NMR spectrum (CDCl_3) of the reaction solution containing N-methyl 4-deca-9'-ynyl-1',8'-dione-1,2,3-triazole. A magnified view of the region of interest is given below (SI Figure S3.4.3).

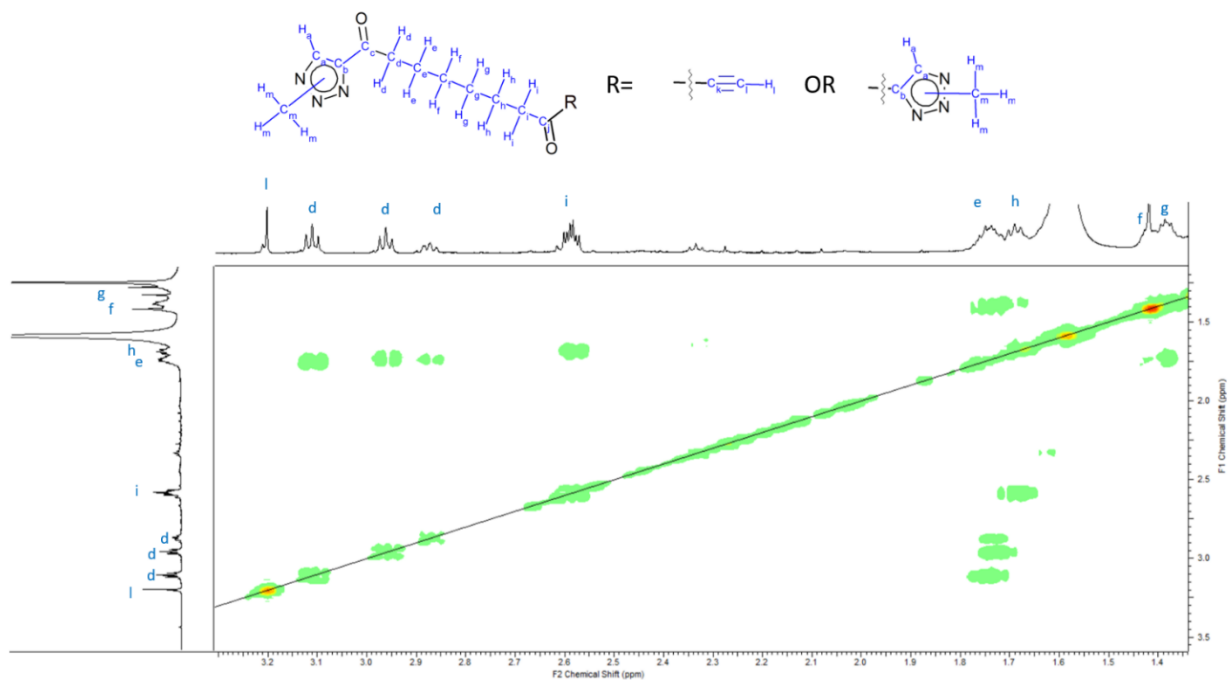


Figure S7.3.3.4.3. COSY NMR spectrum (CDCl_3) of the reaction solution containing N-methyl 4-deca-9'-ynyl-1',8'-dione-1,2,3-triazole.

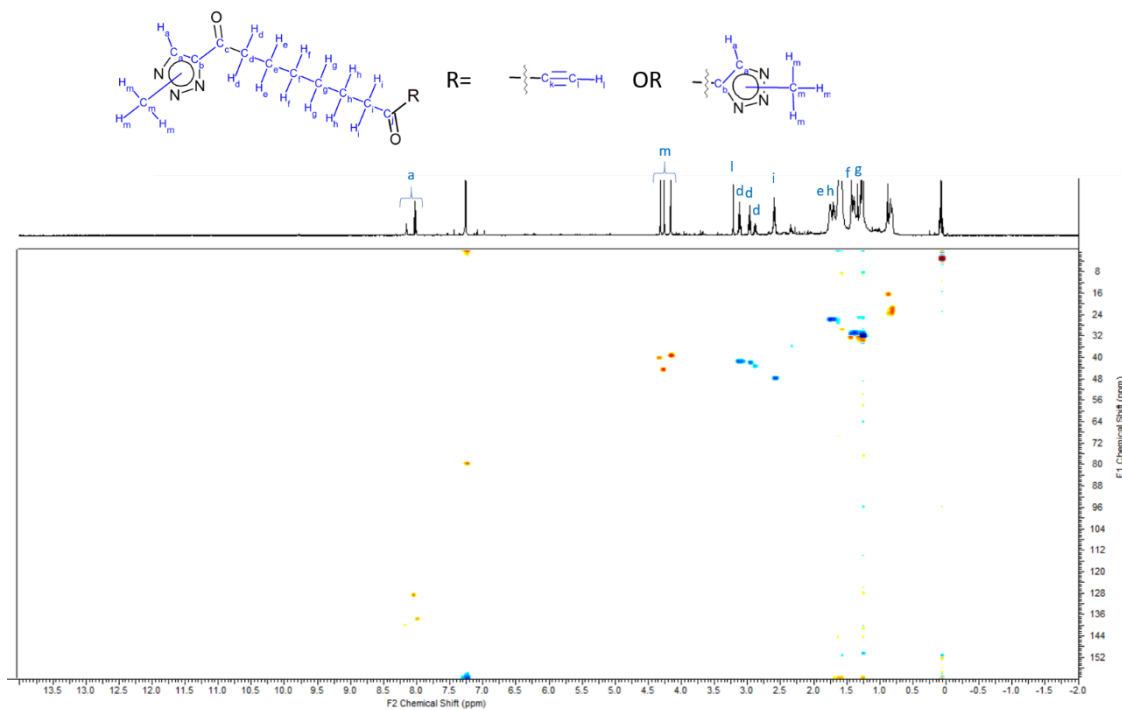


Figure S7.3.3.4.4. HSQC NMR spectrum (CDCl_3) of the reaction solution containing N-methyl 4-deca-9'-ynyl-1',8'-dione-1,2,3-triazole.

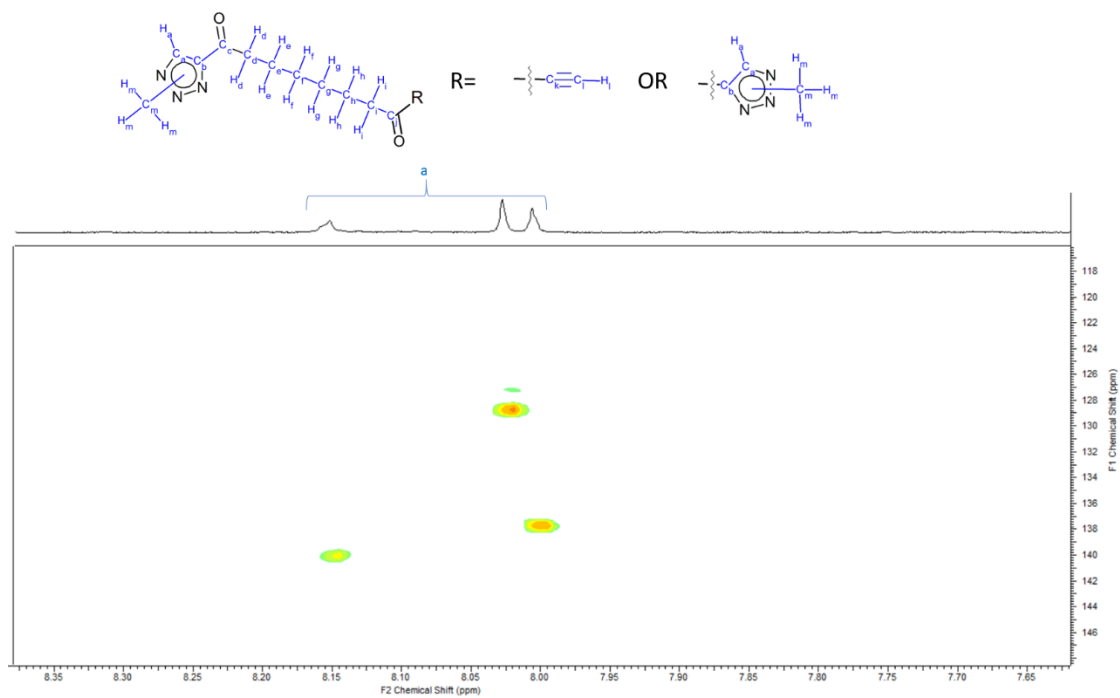


Figure S7.3.3.4.5. HSQC NMR spectrum (CDCl_3) of the reaction solution containing N-methyl 4-deca-9'-ynyl-1',8'-dione-1,2,3-triazole. Due to the small quantity of product isolated, the one-dimensional ^{13}C NMR obtained was not sufficient to identify signals pertaining to the target compound and hence no carbon spectrum is provided.

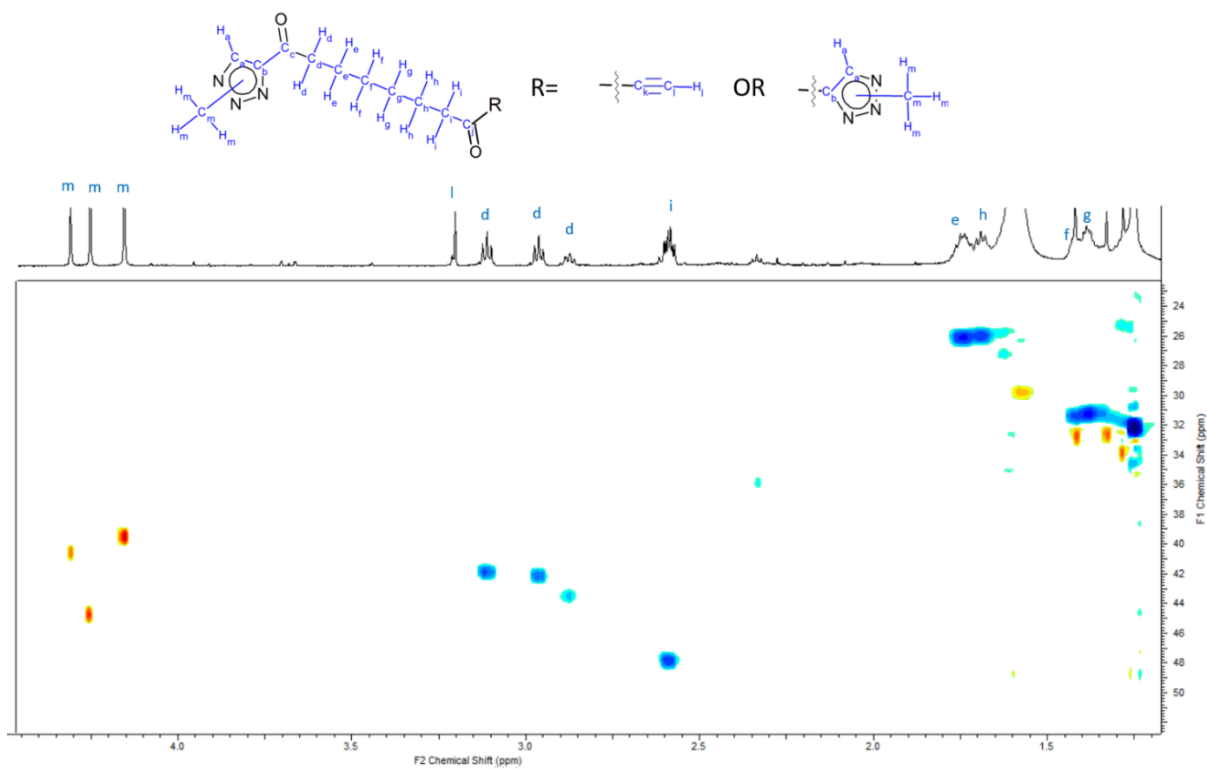


Figure S7.3.3.4.6. HSQC NMR Spectrum (CDCl_3) of the reaction solution containing N-methyl 4-deca-9'-ynyl-1',8'-dione-1,2,3-triazole.

7.3.4 High-resolution mass spectroscopy of the triazole products

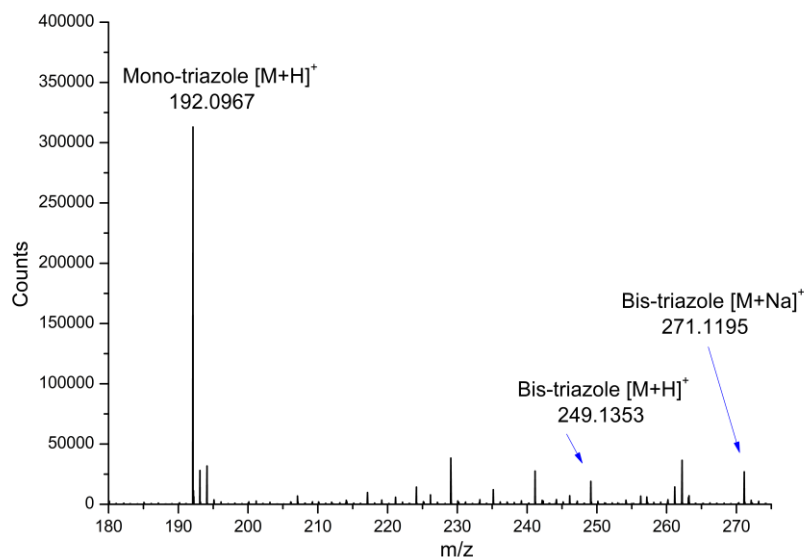


Figure S7.3.4.1. High-resolution mass spectrum obtained from the reaction mixture after alkylation of the triazolate complex **1**·[Mn(CO)₃(HT)] with MeBr. The triazole product, N-methyl 4-hex-5'-ynyl-1',4'-dione-1,2,3-triazole is observed as a [M+H]⁺ peak at m/z 192.0967. The peaks at m/z 249.1353 and m/z 271.1195 correspond to trace quantities of the bis triazole product ([M+H]⁺ and [M+Na]⁺, respectively).

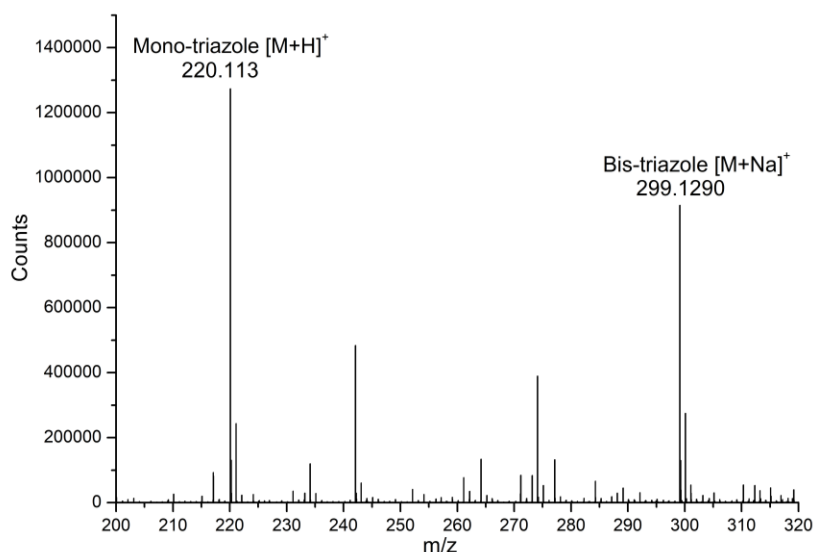


Figure S7.3.4.2 High-resolution mass spectrum obtained from the reaction mixture after alkylation of the triazolate complex **1**·[Mn(CO)₃(OT)] with MeBr. The triazole product, N-methyl 4-octa-8'-ynyl-1',6'-dione-1,2,3-triazole is observed as a [M+H]⁺ peak at m/z 220.0967. The peak at m/z 299.1290 corresponds to the bis-triazole product [M+Na]⁺, bis-1',6'-(N-methyl 1,2,3-triazol-4-yl)-1',6'-hexadione.

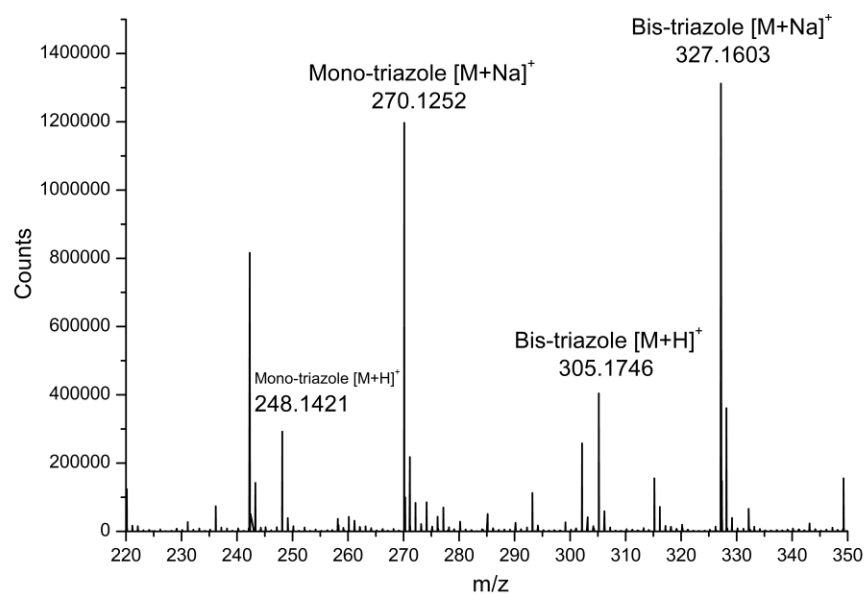


Figure S7.3.4.3 High-resolution mass spectrum obtained from the reaction mixture after alkylation of the triazolone complex $1 \cdot [\text{Mn}(\text{CO})_3(\text{DT})]$ with MeBr. The triazole product, N-methyl 4-deca-9'-ynyl-1',8'-dione-1,2,3-triazole is observed as a M^+H peak at m/z 248.1421 and $[\text{M}+\text{Na}]^+$ peak at m/z 270.1252. The peaks at m/z 305.1746 and m/z 327.1603 correspond to the bis-triazole product, bis-1',8'-(N-methyl 1,2,3-triazol-4-yl)-1',8'-octadione ($[\text{M}+\text{H}]^+$ and $[\text{M}+\text{Na}]^+$, respectively).

7.3.5. Single-crystal X-ray crystallography

7.3.5.1 X-ray crystal structure of $[\text{Mn}(\text{CO})_3(\text{bpm})(\text{DMT})]$ (where bpm = bis(3,5-dimethyl-1H-pyrazolyl)methane and DMT = dimethyl 4,5-dicarboxy-1,2,3-triazolate)

The compound crystallises in the space group $P-1$ with an asymmetric unit comprising one complete form of the complex and a toluene solvate moiety. The octahedral coordination sphere of the Mn(I) site comprises the chelating pyrazole nitrogen donors of the bpm ligand, three carbonyl ligands and the N(2) donor of the triazolate product. The CO ligands occupy a face of this octahedral coordination environment, giving rise to the expected facial isomer of the complex (Figure S7.5.1.1). The bond lengths and angles are comparable to those observed in the MOF (Table S7.5.2). Distinct from the identical triazolate moiety bound into the MOF **1**· $[\text{Mn}(\text{CO})_3\text{DMT}]$, the triazolate is clearly bound through the N2 nitrogen.

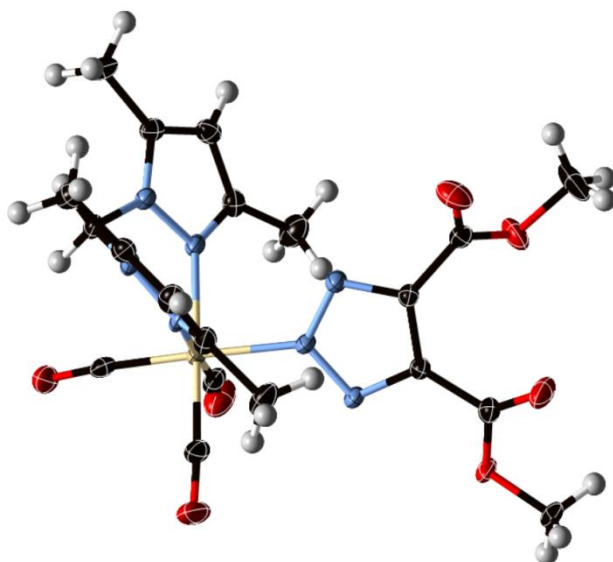


Figure S7.3.5.1.1. A perspective view of *fac*- $[\text{Mn}(\text{CO})_3(\text{bpm})(\text{DMT})]$ (where bpm = bis(3,5-dimethyl-1H-pyrazolyl)methane and DMT = dimethyl 4,5-dicarboxy-1,2,3-triazolate), showing the octahedral geometry and the N(2) triazolate coordination.

Table S7.3.5.2. A table comparing salient bond lengths and angles for *fac*-[Mn(CO)₃(bpm)(DMT)] and the MOF bound analogue **1**·[Mn(CO)₃DMT].

Parameter	<i>fac</i> -[Mn(CO) ₃ (bpm)(DMT)]	1 ·[Mn(CO) ₃ DMT]
<i>Bond lengths</i>		
Mn-N _{py} ^a	2.053(2) and 2.068(2)	2.062(5)
Mn-CO(eq) ^b	1.802(3) and 1.816(3)	1.791(9)
Mn-CO(ax) ^b	1.796(2)	1.70(2)
Mn-N _t ^c	2.039(2)	2.09(1)
<i>Bond angles</i>		
N _{py} -Mn-N _{py}	84.60(7)	87.2(2)

^a py = pyrazole

^b eq = equatorial with respect to the pyrazole nitrogen donors; ax = axial with respect to the pyrazole nitrogen donors.

^c t = triazole

7.3.5.2 Thermal ellipsoid plots for all structures at the 50% probability level

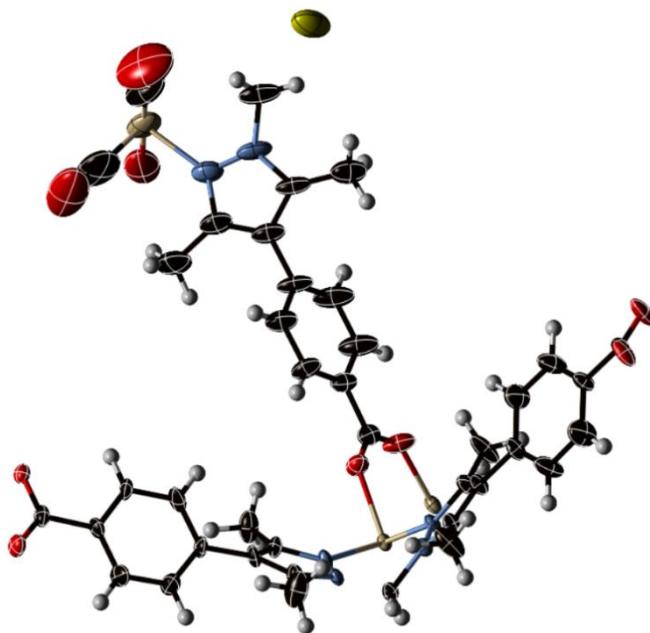


Figure S7.3.5.2.1. The asymmetric unit of $1 \cdot [\text{Mn}(\text{CO})_3(\text{H}_2\text{O})]\text{Br}$ with all non-hydrogen atoms represented by ellipsoids at the 50% probability level (C, black; H, white; N, aqua; O, red; Mn, beige; Br, yellow).

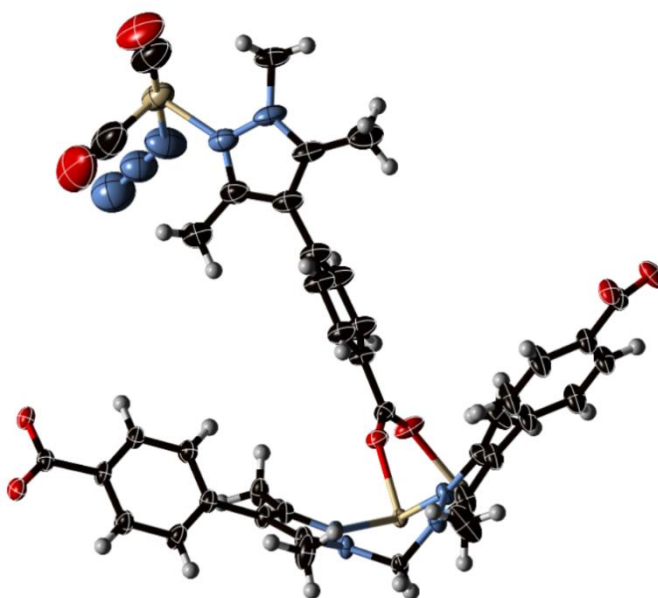


Figure S7.3.5.2.2. The asymmetric unit of $1 \cdot [\text{Mn}(\text{CO})_3\text{N}_3]$ with all non-hydrogen atoms represented by ellipsoids at the 50% probability level (C, black; H, white; N, aqua; O, red; Mn, beige).

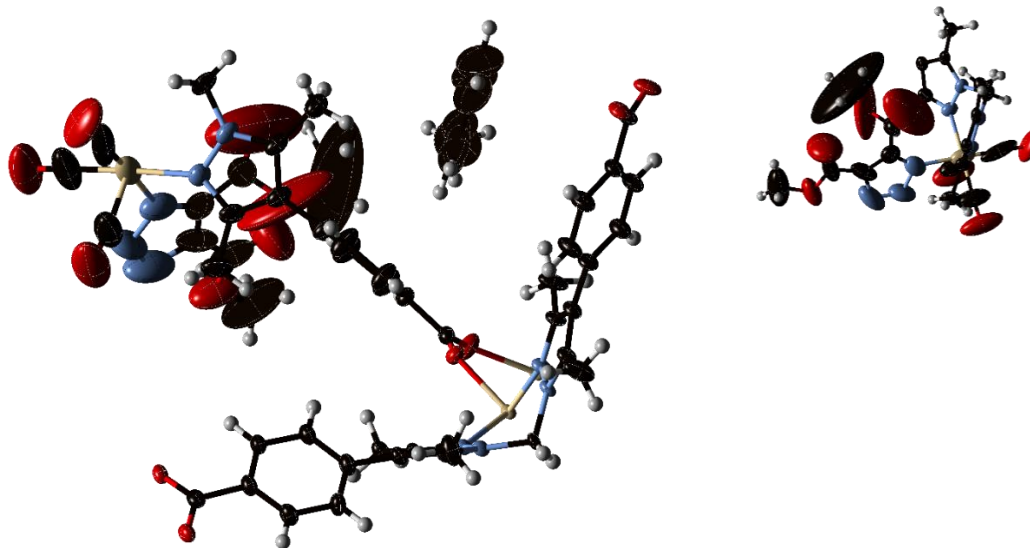


Figure S7.3.5.2.3. (left) The asymmetric unit of $\mathbf{1}\cdot[\text{Mn}(\text{CO})_3(\text{DMT})]$, including an ordered toluene molecule, with all non-hydrogen atoms represented by ellipsoids at the 50% probability level (C, black; H, white; N, aqua; O, red; Mn, beige). (right) A perspective view of the triazolate moiety in $\mathbf{1}\cdot[\text{Mn}(\text{CO})_3(\text{DMT})]$ with all non-hydrogen atoms represented by ellipsoids at the 50% probability level (C, black; H, white; N, aqua; O, red; Mn, beige).

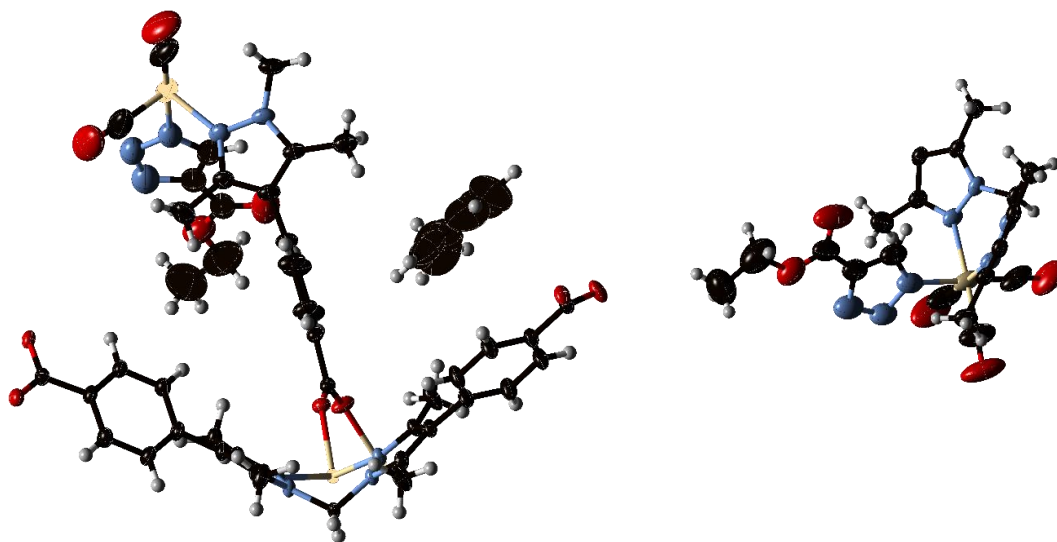


Figure S7.3.5.2.4. (left) The asymmetric unit of $1 \cdot [\text{Mn}(\text{CO})_3(\text{ET})]$, including an ordered toluene molecule, with all non-hydrogen atoms represented by ellipsoids at the 50% probability level. (right) A perspective view of the triazolate moiety in $1 \cdot [\text{Mn}(\text{CO})_3(\text{ET})]$ with all non-hydrogen atoms represented by ellipsoids at the 50% probability level (C, black; H, white; N, aqua; O, red; Mn, beige).

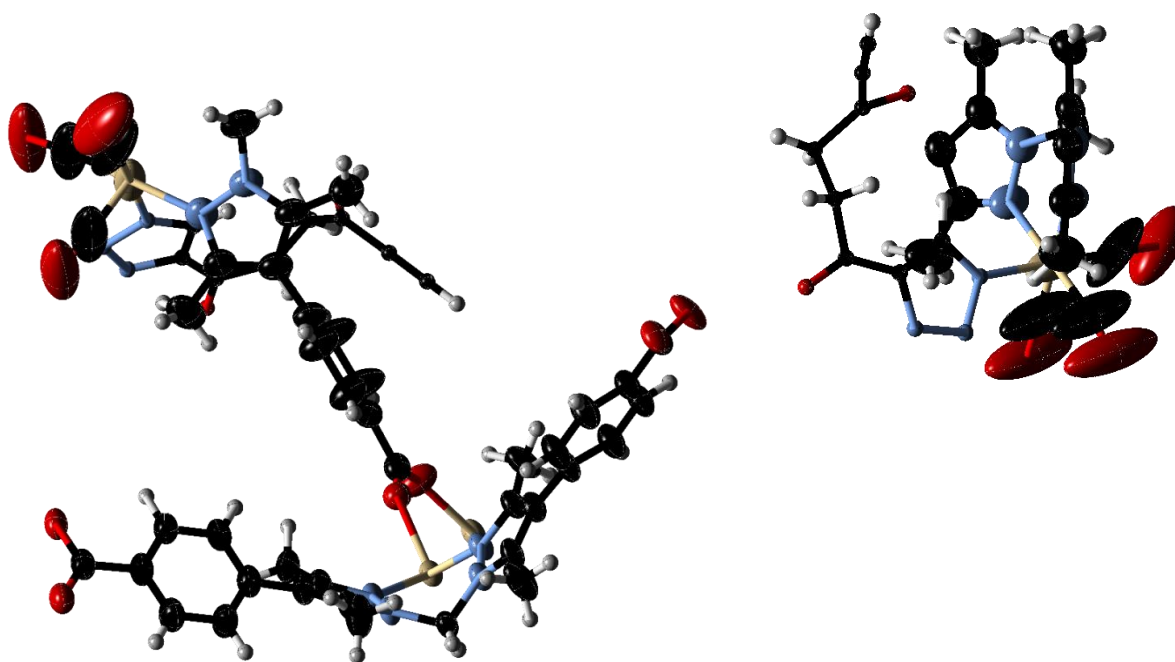


Figure S7.3.5.2.5. (left) The asymmetric unit of $1 \cdot [\text{Mn}(\text{CO})_3(\text{HT})]$ with all non-hydrogen atoms represented by ellipsoids at the 50% probability level (except for the 13 non-hydrogen atoms of the triazolate, which are shown in a ball and stick representation). (right) A perspective view of the triazolate moiety in $1 \cdot [\text{Mn}(\text{CO})_3(\text{ET})]$ with all non-hydrogen atoms represented by ellipsoids at the 50% probability level (C, black; H, white; N, aqua; O, red; Mn, beige).

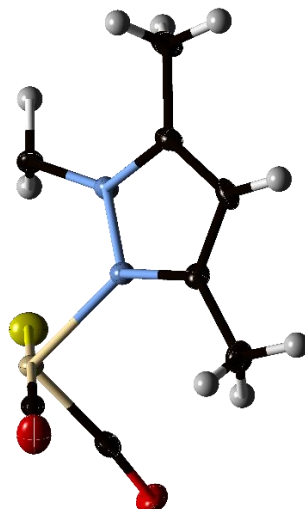


Figure S7.3.5.2.6. The asymmetric unit of $[\text{Mn}(\text{bpm})(\text{CO})_3\text{Br}]$ with all non-hydrogen atoms represented by ellipsoids at the 50% probability level (C, black; H, white; N, aqua; O, red; Mn, beige; Br, yellow).

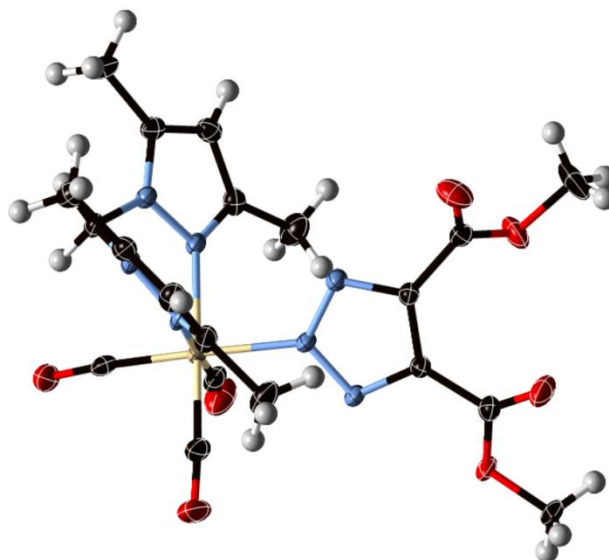


Figure S7.3.5.2.7. The asymmetric unit of $[\text{Mn}(\text{bpm})(\text{CO})_3(\text{DMT})]$ with an ordered solvent molecule (toluene) omitted for clarity and all non-hydrogen atoms represented by ellipsoids at the 50% probability level (C, black; H, white; N, aqua; O, red; Mn, beige).

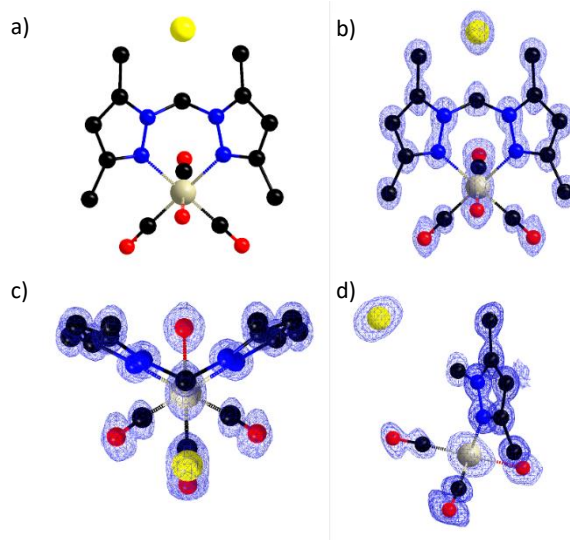
7.3.5.3 F_{obs} Electron density maps

Figure S7.3.5.3.1. (a) A perspective view of the chelated Mn(I) complex in $1 \cdot [\text{Mn}(\text{CO})_3(\text{H}_2\text{O})]\text{Br}$ and the overlaid electron density map as viewed from the (b) front, (c) top and (d) side of the complex.

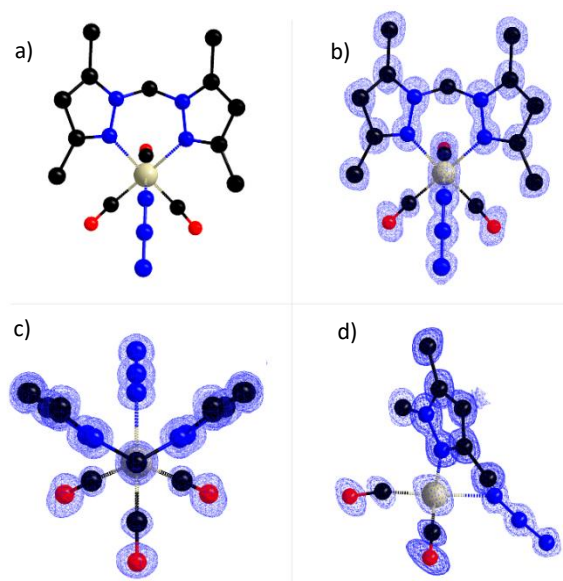


Figure S7.3.5.3.2. (a) A perspective view of the chelated Mn(I) complex in $1 \cdot [\text{Mn}(\text{CO})_3\text{N}_3]$ and the overlaid electron density map as viewed from the (b) front, (c) top and (d) side of the complex.

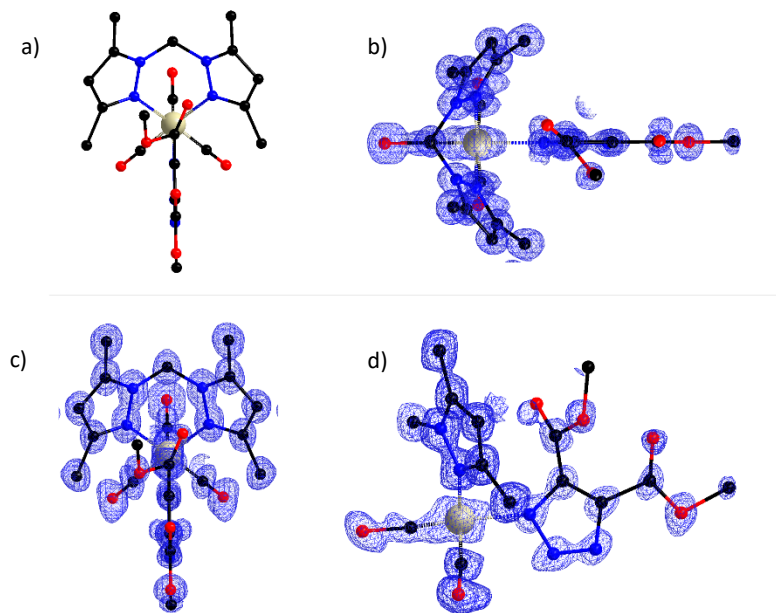


Figure S7.3.5.3.3. (a) A perspective view of the chelated Mn(I) complex in $1 \cdot [\text{Mn}(\text{CO})_3(\text{DMT})]$ and the overlaid electron density map as viewed from the (b) top, (c) front and (d) side of the complex.

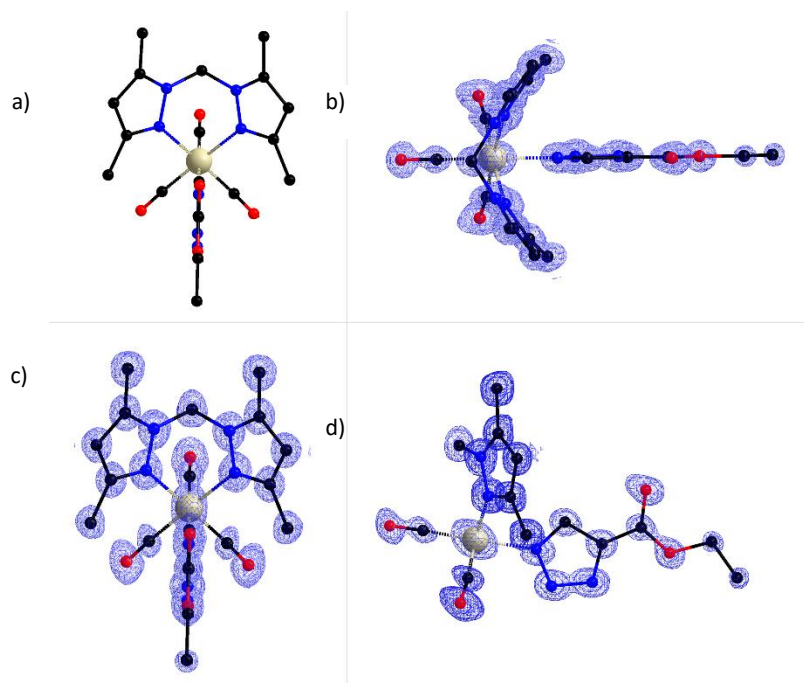


Figure S7.3.5.3.4. (a) A perspective view of the chelated Mn(I) complex in $1 \cdot [\text{Mn}(\text{CO})_3(\text{ET})]$ and the overlaid electron density map as viewed from the (b) top, (c) front and (d) side of the complex.

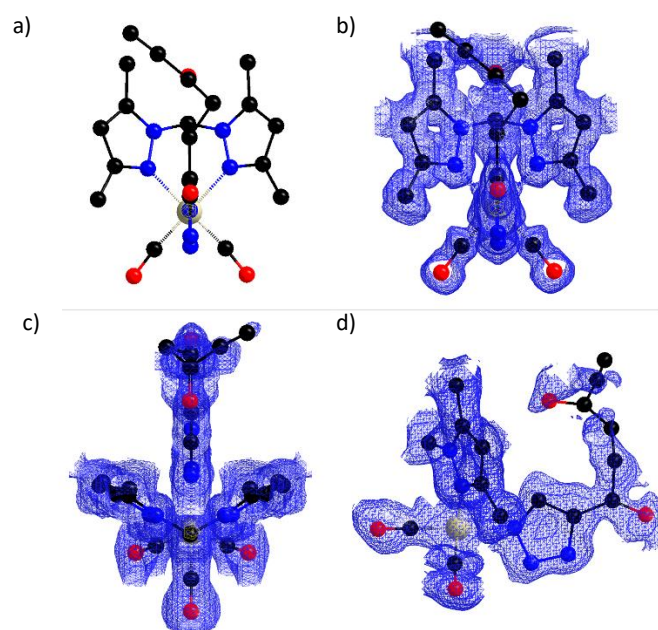


Figure S7.3.5.3.5. (a) A perspective view of the chelated Mn(I) complex in $1\text{-[Mn(CO)}_3\text{(HT)]}$ and the overlaid electron density map as viewed from the (b) top, (c) front and (d) side of the complex.

7.3.5.4 Additional refinement details

1·[Mn(CO)₃(H₂O)]Br. In order to subtract the contribution from the disordered solvent (ethanol), the SQUEEZE routine available in Platon⁷² was applied to the data, which gave a new HKL file. The number of located electrons is 554, which equates to approximately 12 ethanol molecules per unit cell and 3 per asymmetric unit. This has been added to the reported formula (as have the hydrogen atoms not located on the coordinated water).

1·[Mn(CO)₃N₃]. In order to subtract the contribution from the disordered solvent (toluene), the SQUEEZE routine available in Platon⁷² was applied to the data, which gave a new HKL file. The number of located electrons is 603, which equates to approximately 6 toluene molecules per unit cell and 1.5 per asymmetric unit. This has been added to the reported formula.

1·[Mn(CO)₃(DMT)]. In order to subtract the contribution from the disordered solvent (toluene; one toluene molecule was located and refined), the SQUEEZE routine available in Platon⁷² was applied to the data, which gave a new HKL file. The number of located electrons is 266, which equates to approximately 2 toluene molecules per unit cell and 0.5 per asymmetric unit. This has been added to the reported formula. There is some disorder of the triazole moiety in this structure and a series of DFIX, DANG and ISOR restraints were used in the refinement (24 in total).

1·[Mn(CO)₃(EP)]. In order to subtract the contribution from the disordered solvent (toluene; one toluene molecule was located and refined), the SQUEEZE routine available in Platon⁷² was applied to the data, which gave a new HKL file. The number of located electrons is 247, which equates to approximately 2 toluene molecules per unit cell and 0.5 per asymmetric unit. This has been added to the reported formula.

1·[Mn(CO)₃(OT)]. In order to subtract the contribution from the disordered solvent (toluene), the SQUEEZE routine available in Platon⁷² was applied to the data, which gave a new HKL file. The number of located electrons is 340, which equates to approximately 4 toluene molecules per unit cell and 1 per asymmetric unit. This has been added to the reported formula. The triazole moiety (13 atoms) shows some significant disorder, particularly for the CH₂CH₂C(O)CCH fragment and thus was refined with isotropic displacement parameters and restraints on the bond lengths, angles and thermal parameters (a series of DFIX, DANG, FLAT and ISOR restraints, 40 in total, were used). The modelled moiety fits the observed electron density map and is supported by other analyses.

7.3.5.5 Tables of X-ray crystallography data collection and refinement parameters

Table S7.3.5.5.1. Crystallographic data collection and refinement parameters for the metalated forms of **1**.

Sample	1 ·[Mn(CO) ₃ (H ₂ O)]Br	1 ·[Mn(CO) ₃ N ₃]
Crystallographic Parameter		
Formula	C ₄₅ H ₅₂ Br _{0.5} Mn ₂ N ₆ O ₁₁	C _{49.5} H ₄₅ Mn ₂ N _{7.5} O _{7.5}
FW	1002.76	974.81
T,K	100(2)	100(2)
Wavelength, Å	Synchrotron (λ = 0.7108)	Synchrotron (λ = 0.7108)
Crystal system, space group	Monoclinic, <i>P</i> 2 ₁ / <i>m</i>	Monoclinic, <i>P</i> 2 ₁ / <i>m</i>
Z	4	4
a, Å	12.3848(17)	12.418(3)
b, Å	33.886(5)	32.716(7)
c, Å	12.8929(12)	12.989(3)
α°	90	90
β, °	99.101(10)	94.42
γ°	90	90
V, Å ³	5342.6(11)	5261.3(18)
<i>d</i> _{calc} , g/cm ³	1.247	1.231
Absorption coefficient, mm ⁻¹	0.903	0.534
<i>F</i> (000)	2078.0	2018.0
Crystal size, mm ³	0.400 × 0.200 × 0.010	0.390 × 0.040 × 0.010
Theta range for data collection	4.874 to 54.998	3.29 to 54.998
Index range	-15 ≤ <i>h</i> ≤ 16, -43 ≤ <i>k</i> ≤ 44, -16 ≤ <i>l</i> ≤ 16	-16 ≤ <i>h</i> ≤ 16, -42 ≤ <i>k</i> ≤ 42, - 16 ≤ <i>l</i> ≤ 16
Reflections collected	49270	84539
Independent reflections	12282 [R _{int} = 0.1254, R _{sigma} = 0.1753]	11833 [R _{int} = 0.0498, R _{sigma} = 0.0266]
Data/restraints/parameters	12282/0/534	11833/0/523
GOF on F ²	0.920	1.027
Largest diff. peak and hole, e-Å ⁻³	0.90/-1.39	0.91/-2.10
R ₁ , [I > 2σ(I)]	0.0770	0.0719
wR ₂ ^a , all data	0.2169	0.2004
CCDC Number	1826675	1826678

$$^a R_1 = \frac{\sum ||F_o| - |F_c||}{\sum |F_o|}, wR_2 = \sqrt{\frac{\sum w(F_o - F_c)^2}{\sum w F_o^2}}$$

Table S7.3.5.5.2. Crystallographic data collection and refinement parameters for the metalated forms of **1**.

Sample	1-[Mn(CO) ₃ (DMT)]	1-[Mn(CO) ₃ (ET)]
Crystallographic Parameter		
Formula	C ₅₃ H _{49.5} Mn ₂ N _{7.5} O _{10.5}	C ₅₂ H ₄₈ Mn ₂ N _{7.5} O _{8.5}
FW	1069.38	1023.86
T, K	100(2)	100(2)
Wavelength, Å	Synchrotron (λ = 0.7108)	Synchrotron (λ = 0.7108)
Crystal system, space group	Monoclinic, <i>P21/m</i>	Monoclinic, <i>P21/m</i>
Z	4	4
a, Å	12.403(3)	12.422(3)
b, Å	33.488(7)	33.152(7)
c, Å	12.991(3)	13.004(3)
α°	90	90
β, °	96.43	95.44
γ°	90	90
V, Å ³	5361.9(19)	5331.1(19)
<i>d</i> _{calc} , g/cm ³	1.325	1.276
Absorption coefficient, mm ⁻¹	0.535	0.532
<i>F</i> (000)	2216.0	2122.0
Crystal size, mm ³	0.400 × 0.150 × 0.010	0.250 × 0.050 × 0.010
Theta range for data collection	3.304 to 52.006	2.458 to 54.998
Index range	-15 ≤ <i>h</i> ≤ 15, -41 ≤ <i>k</i> ≤ 41, -16 ≤ <i>l</i> ≤ 16	-16 ≤ <i>h</i> ≤ 16, -42 ≤ <i>k</i> ≤ 42, - 16 ≤ <i>l</i> ≤ 16
Reflections collected	74869	86003
Independent reflections	9923 [R _{int} = 0.0505, R _{sigma} = = 0.0249]	12237 [R _{int} = 0.0475, R _{sigma} = 0.0247]
Data/restraints/parameters	9923/24/658	12237/0/630
GOF on F ²	1.072	1.083
Largest diff. peak and hole, e ⁻ Å ⁻³	1.09/-1.56	1.54/-1.23
R ₁ , [I > 2σ(I)]	0.0786	0.0678
wR ₂ ^a , all data	0.2155	0.1899
CCDC Number		1826679

$$^a R_1 = \sum ||F_o| - |F_c|| / \sum |F_o|, wR_2 = {}^{721/2}$$

Table S7.3.5.5.3. Crystallographic data collection and refinement parameters for the metalated forms of **1**.

Sample	1-[Mn(CO) ₃ (HT)]	[Mn(CO) ₃ (bpm)Br]
Crystallographic Parameter		
Formula	C _{51.5} H _{45.5} N _{7.5} O _{8.5} Mn ₂	C ₁₄ H ₁₆ BrMnN ₄ O ₃
FW	1015.33	423.16
T, K	100.15	150(2)
Wavelength, Å	Synchrotron (λ = 0.7108)	Mo Kα (λ = 0.71073)
Crystal system, space group	Monoclinic, <i>P2₁/m</i>	Orthorhombic, <i>Pnma</i>
Z	4	4
a, Å	12.461(3)	10.1113(14)
b, Å	33.626(7)	14.6016(18)
c, Å	13.016(3)	11.3834(10)
α°	90	90
β, °	96.09(3)	90
γ°	90	90
V, Å ³	5423.1(19)	1680.7(3)
d _{calc} , g/cm ³	1.244	1.672
Absorption coefficient, mm ⁻¹	0.522	3.181
F(000)	2100.0	848.0
Crystal size, mm ³	0.31 × 0.08 × 0.01	0.200 × 0.100 × 0.100
Theta range for data collection	2.422 to 64.522	5.388 to 54.99
Index range	-17 ≤ h ≤ 17, -45 ≤ k ≤ 45, -19 ≤ l ≤ 19	-13 ≤ h ≤ 11, -17 ≤ k ≤ 18, -14 ≤ l ≤ 14
Reflections collected	96528	8468
Independent reflections	14254 [R _{int} = 0.0464, R _{sigma} = 0.0290]	1964 [R _{int} = 0.0510, R _{sigma} = 0.0477]
Data/restraints/parameters	14254/40/546	1964/0/114
GOF on F ²	1.068	1.056
Largest diff. peak and hole, e ⁻ Å ⁻³	1.85/-2.10	0.56/-0.56
R ₁ ^a , [I > 2σ(I)]	0.0830	0.0353
wR ₂ ^a , all data	0.2682	0.0706
CCDC Number	1826677	1826673

$$^a R_1 = \frac{\sum ||F_o| - |F_c||}{\sum |F_o|}, wR_2 = \frac{\sum w(F_o - F_c)^2}{\sum w F_o^2}^{1/2}$$

Table S7.3.5.5.4. Crystallographic data collection and refinement parameters for **1·[Mn(CO)₃(bpm)(DMT)]**.

Sample	[Mn(CO) ₃ (bpm)(DMT)]
Crystallographic Parameter	
Formula	C ₂₇ H ₃₀ Mn ₁ N ₇ O ₇
FW	619.52
T, K	150(2)
Wavelength, Å	Mo Kα (λ = 0.71073)
Crystal system, space group	Triclinic, <i>P</i> -1
Z	2
a, Å	9.2015(7)
b, Å	10.7157(8)
c, Å	15.6589(12)
α°, °	76.778(7)
β°, °	74.207(7)
γ°, °	84.676(6)
V, Å ³	1445.5(2)
<i>d</i> _{calc} , g/cm ³	1.423
Absorption coefficient, mm ⁻¹	0.514
<i>F</i> (000)	644.0
Crystal size, mm ³	0.490 × 0.100 × 0.050
Theta range for data collection	6.58 to 54
Index range	-11 ≤ <i>h</i> ≤ 11, -13 ≤ <i>k</i> ≤ 13, -20 ≤ <i>l</i> ≤ 20
Reflections collected	24604
Independent reflections	6289 [R _{int} = 0.0599, R _{sigma} = 0.0676]
Data/restraints/parameters	6289/0/386
GOF on F ²	1.022
Largest diff. peak and hole, e·Å ⁻³	0.36 and -0.42
<i>R</i> ₁ ^a , [I>2σ(I)]	0.0455
wR ₂ ^a , all data	0.0971
CCDC Number	1826674

$$^a R_1 = \frac{\sum ||F_o| - |F_c||}{\sum |F_o|}, wR_2 = \frac{\sum w(F_o - F_c)^2}{\sum w F_o^2}^{1/2}$$

7.3.6 Powder X-ray diffraction

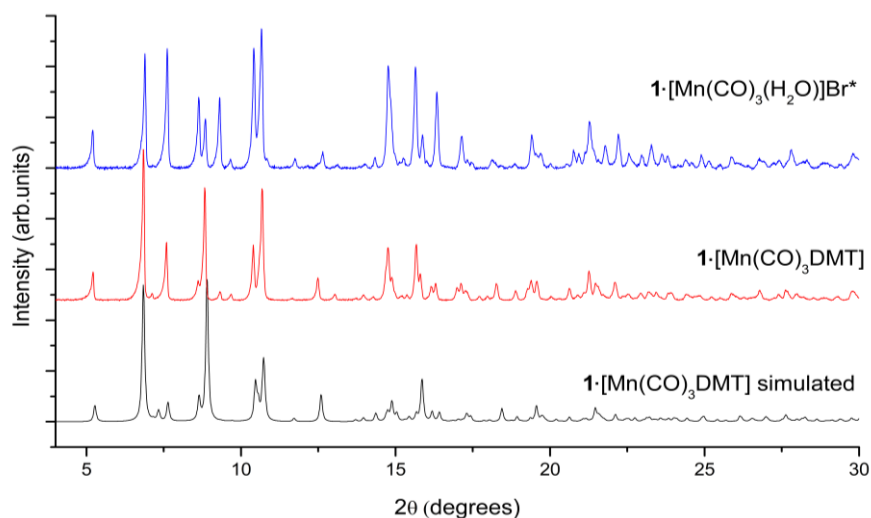


Figure S7.3.6.1. Simulated and experimental PXRD patterns for $1 \cdot [\text{Mn}(\text{CO})_3(\text{DMT})]$ and experimental PXRD pattern obtained following alkylation of $1 \cdot [\text{Mn}(\text{CO})_3(\text{DMT})]$ with MeBr.

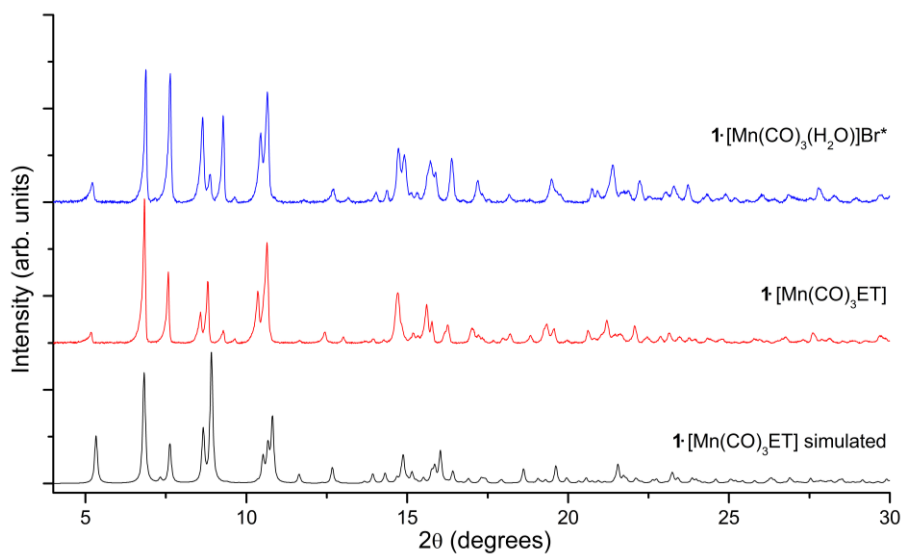


Figure S7.3.6.2. Simulated and experimental PXRD patterns for $1 \cdot [\text{Mn}(\text{CO})_3(\text{ET})]$ and experimental PXRD pattern obtained following alkylation of $1 \cdot [\text{Mn}(\text{CO})_3(\text{ET})]$ with MeBr.

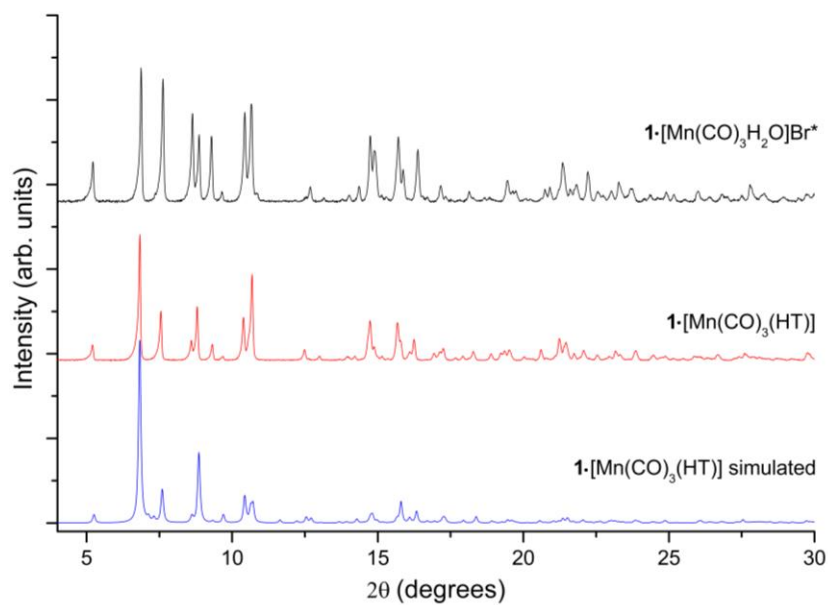


Figure S7.3.6.3. Simulated and experimental PXRD patterns for $1\cdot[\text{Mn}(\text{CO})_3(\text{HT})]$ and experimental PXRD pattern obtained following alkylation of $1\cdot[\text{Mn}(\text{CO})_3(\text{HT})]$ with MeBr.

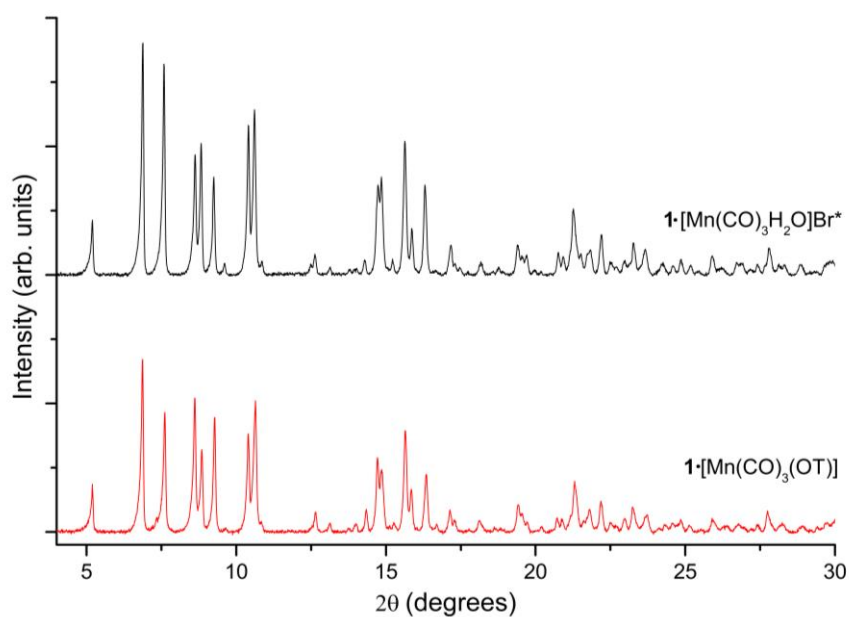


Figure S7.3.6.4. PXRD pattern for $1\cdot[\text{Mn}(\text{CO})_3(\text{OT})]$ and PXRD pattern obtained following alkylation of $1\cdot[\text{Mn}(\text{CO})_3(\text{OT})]$ with MeBr.

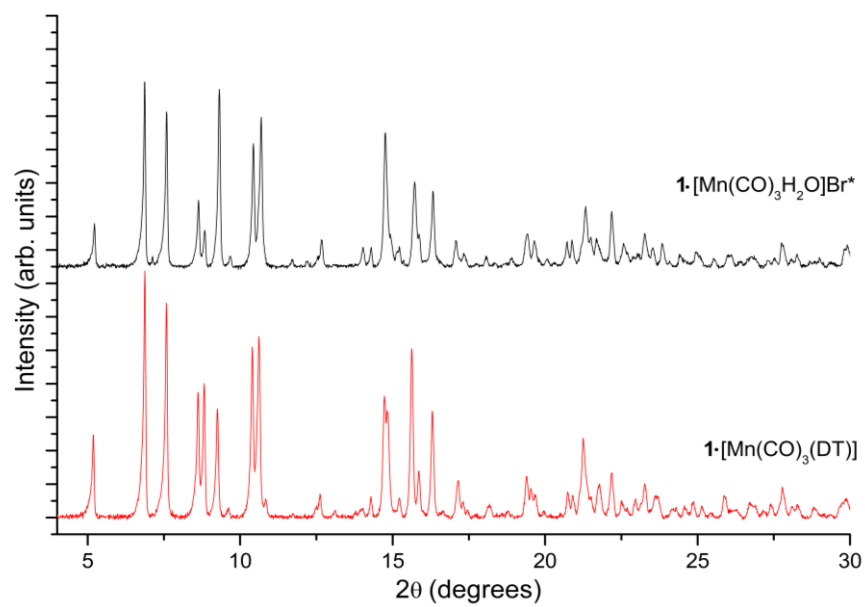


Figure S7.3.6.5. PXRD pattern for $1 \cdot [\text{Mn}(\text{CO})_3(\text{DT})]$ and the PXRD pattern obtained following alkylation of $1 \cdot [\text{Mn}(\text{CO})_3(\text{DT})]$ with MeBr.

7.3.7 IR spectroscopy

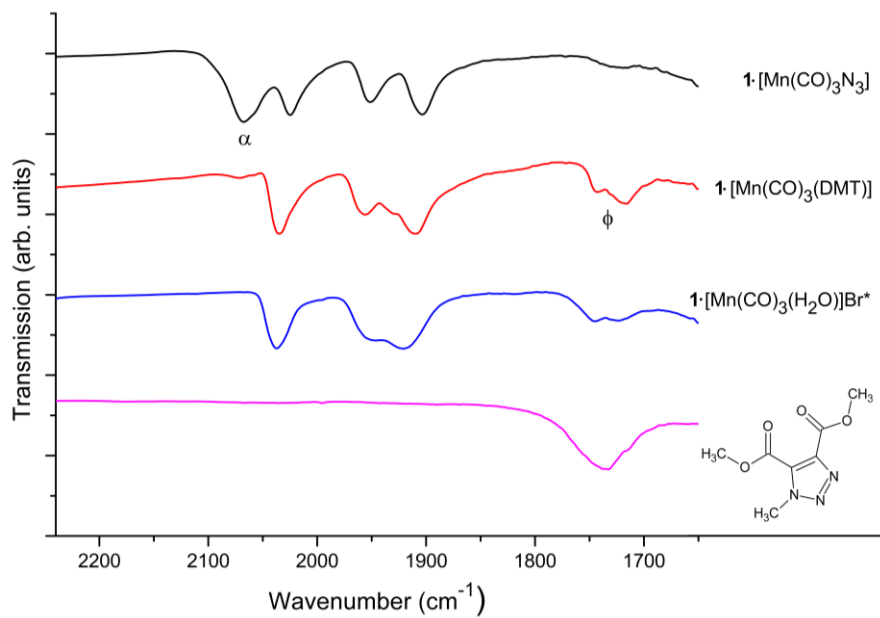


Figure S7.3.7.1. IR spectra for the click cycle involving dimethyl acetylene dicarboxylate (DMAD), displaying the loss of the azide stretch (α , 2070 cm^{-1}) and formation of methyl ester carbonyl stretches (ϕ , near 1700 cm^{-1}) upon reaction with DMAD, and reduction in the ester features upon reaction with MeBr to yield $1\text{-[Mn(CO)}_3\text{(H}_2\text{O)]Br}^*$.

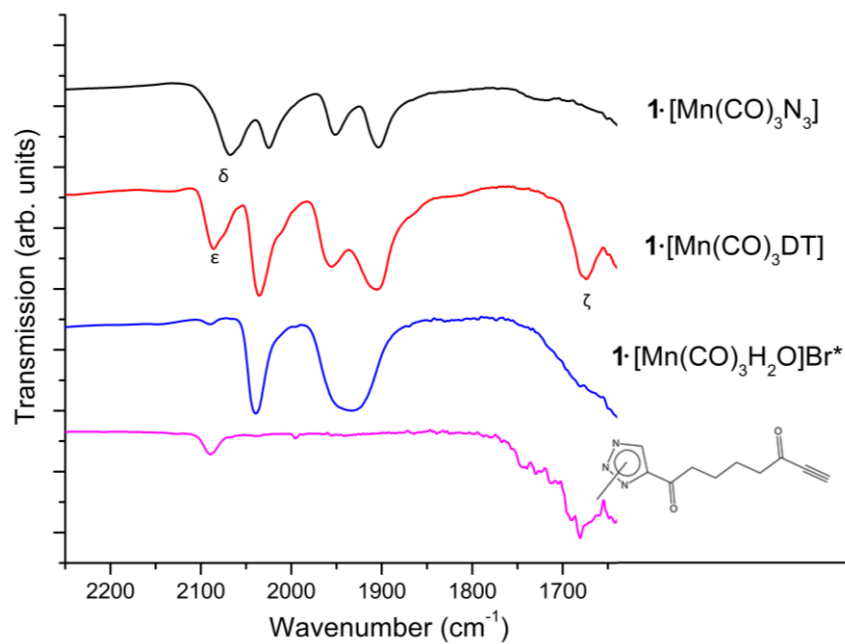


Figure S7.3.7.2. IR spectra for the click cycle involving DA3, displaying the loss of the azide stretch (δ , 2070 cm^{-1}) and formation of alkyne (ϵ) and ketone stretches (ζ) upon reaction with DA3. The ketone stretches are reduced upon reaction with MeBr to yield $1 \cdot [\text{Mn}(\text{CO})_3(\text{H}_2\text{O})]\text{Br}^*$ and the product released, 4-deca-9'-ynyl-1',8'-dione-1,2,3-triazole, displays spectroscopic properties consistent with that observed in $1 \cdot [\text{Mn}(\text{CO})_3(\text{DT})]$.

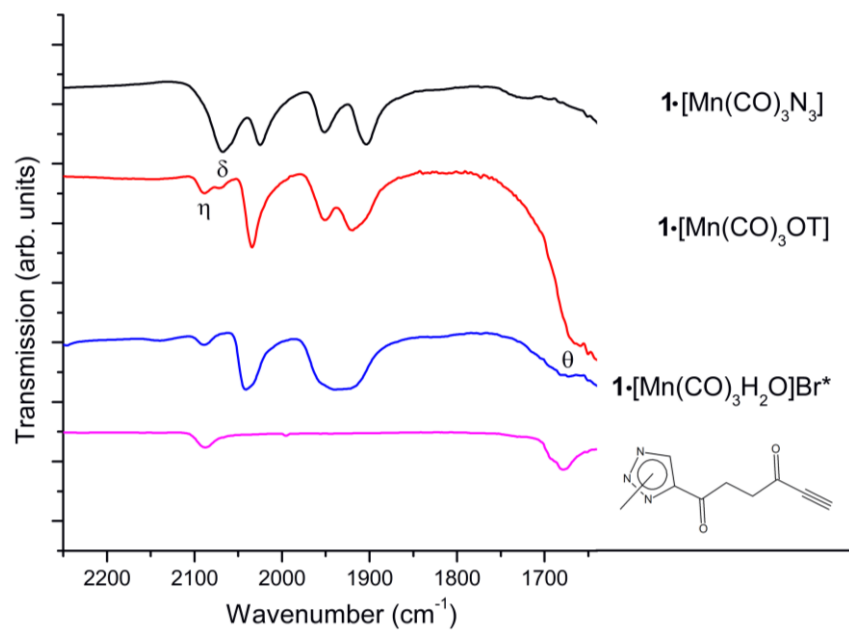


Figure S7.3.7.3. IR spectra for the click cycle involving DA2, displaying the loss of the azide stretch (δ , 2070 cm^{-1}) and formation of alkyne (η) and ketone stretches (θ) upon reaction with DA2. The ketone stretches are reduced upon reaction with MeBr to yield $\mathbf{1}\cdot[\text{Mn}(\text{CO})_3(\text{H}_2\text{O})]\text{Br}^*$ and the product released, 4-octa-7'-ynl-1',6'-dione-1,2,3-triazole, displays spectroscopic properties consistent with that observed in $\mathbf{1}\cdot[\text{Mn}(\text{CO})_3(\text{DT})]$.

7.3.8 Synthesis of dialkynes (DA1 and DA3) and molecular species

Synthesis of 1,8-bis(trimethylsilyl)-1,7-octadiyne-3,6-dione (2). Adapted from Wilbur *et al.*² Under an Ar atmosphere, a solution of succinyl chloride (0.6 ml, 5.4 mmol) and bis(trimethylsilyl)acetylene (2.04 g, 11.9 mmol) in freshly distilled dichloromethane (4 ml) was added dropwise to a stirred mixture of AlCl₃ (1.6 g, 12.0 mmol) in dichloromethane (10 ml) at 0°C. The mixture became black during the addition and was stirred for 30 minutes at 0°C, followed by 3 h at room temperature. The mixture was poured into a 50% mixture of 10% HCl/ice (200 ml). The organic phase was isolated and the aqueous phase extracted with dichloromethane (3 × 100 ml). The combined organic phases were washed with cold saturated NaHCO₃ solution (3 × 100 ml), water (100 ml) and dried over MgSO₄. The solvent was removed under reduced pressure to give crude 1,8-bis(trimethylsilyl)-1,7-octadiyne-3,6-dione as a black solid. The crude product was purified via column chromatography (silica gel, 1:1 dichloromethane : petroleum spirit) to afford **2** as an orange-brown oil (510 mg, 34%); ¹H NMR (600 MHz, CDCl₃) ppm: 2.91 (s, 4H, CH₂), 0.23 (s, 18H, TMS); ¹³C NMR (600 MHz, CDCl₃) ppm: 187.48 (C=O), 104.3 (C≡C), 101.55 (C≡C), 41.17 (CH₂), 1.83 (TMS); IR ν_{\max} (neat, cm⁻¹): 2952 (C-H), 2152 (C≡C), 1681 (C=O), 1407, 1251, 1104.

Synthesis of 1,7-octadiyne-3,6-dione (DA1). Adapted from Wilbur *et al.*² An aqueous solution of K₂CO₃ (6.2 × 10⁻³ M, 4ml) was added dropwise to a methanolic solution (8ml) of **2** (412 mg, 1.4mmol) at 0°C and the resulting solution was stirred at room temperature for 1 hr. Further K₂CO₃ solution was added until the pH reached 8.0. After stirring at pH 8.0 for 30 minutes, the solution was acidified to pH 3.0 via addition of 10% HCl and poured into water (200 ml). The resulting solution was filtered and extracted with diethyl ether (3 × 100 ml), the combined organic phases were washed with water (1 × 100 ml) and dried over MgSO₄. The solvent was removed under reduced pressure to yield 1,7-octadiyne-3,6-dione (**DA1**) as a yellow solid (162mg, 86%); ¹H NMR (600 MHz, CDCl₃) ppm: 3.28 (s, 2H, C≡C-H), 2.94 (s, 4H, CH₂); ¹³C NMR (600 MHz, CDCl₃) ppm: 184.25 (C=O), 80.80 (C≡C), 79.49 (C≡C), 38.47 (CH₂); IR ν_{\max} (neat, cm⁻¹): 3342 (C≡C-H), 2963 (C-H), 2918 (C-H), 2093 (C≡C), 1672 (C=O), 1401, 1303, 1261, 1092, 1022.

Synthesis of 1,12-bis(trimethylsilyl)-1,11-dodecadiyne-3,10-dione (3). Adapted from Wilbur *et al.*² Under an Ar atmosphere, a solution of octanedioyl dichloride (0.5 ml, 2.78 mmol) and bis(trimethylsilyl)acetylene (0.9686 g, 7.8 mmol) in freshly distilled dichloromethane (16 ml) was added dropwise to a stirred mixture of AlCl₃ (1.60 g, 11.99 mmol) in dichloromethane (40ml) at 0°C. The mixture became orange-brown during the addition and was stirred for 30 minutes at 0°C, followed by 3 h

at room temperature. The mixture was poured into a 50% mixture of 10% HCl/ice (25 ml). The organic phase was isolated and the aqueous phase extracted with dichloromethane (3 × 100 ml). The combined organic phases were washed with cold saturated NaHCO₃ solution (3 × 100 ml), water (100 ml) and dried over MgSO₄. The solvent was removed under reduced pressure to give crude 1,12-bis(trimethylsilyl)-1,11-octadiyne-3,10-dione as a yellow oil. The crude product was purified via column chromatography (silica gel, dichloromethane) to afford **3** as a pale-yellow oil (419.5 mg, 44.1%); ¹H NMR (600 MHz, CDCl₃) ppm: 2.52 (m, 4H, CH₂), 1.63 (m, 4H, CH), 1.31 (m, 4H, CH₂), 0.21 (s, 18H, TMS); ¹³C NMR (600 MHz, CDCl₃) ppm: 187.66 (C=O), 101.96 (C≡C), 97.67 (C≡C), 45.05 (CH₂), 28.5 (CH₂), 23.57 (CH₂); IR ν_{\max} (neat, cm⁻¹): 2958 (C-H), 2956 (C-H), 2149 (C≡C), 1677 (C=O), 1406, 1252, 1103.

Synthesis of 1,11-dodecadiyne-3,10-dione (DA3). Adapted from Wilbur *et al.*² An aqueous solution of K₂CO₃ (6.2×10⁻³ M, 6 mL) was added dropwise to a methanolic solution (16mL) of **3** (419.5 mg, 1.25 mmol) at 0°C and the resulting solution was stirred at room temperature for 1 h. Further K₂CO₃ solution was added until the pH reached 8.0. After stirring at pH 8.0 for 30 minutes, the solution was acidified to pH 3.0 via addition of 10% HCl and poured into water (200 ml). The resulting dark brown precipitate was collected via filtration, washed with water and dried to yield 1,11-dodecadiyne-3,10-dione (**DA3**) as a brown solid (74.2 mg, 31.1%); ¹H NMR (600 MHz, CDCl₃) ppm: 3.2 (s, 2H, C≡C-H), 2.58 (t, 4H, CH₂), 1.67 (m, 4H, CH₂), 1.33 (m, 4H, CH₂); ¹³C NMR (600 MHz, CDCl₃) ppm: 187.32 (C=O), 81.37 (C≡C), 78.42 (C≡C), 45.24 (CH₂), 28.49 (CH₂), 23.42 (CH₂); IR ν_{\max} (neat, cm⁻¹): 3253 (C≡C-H), 2935 (C-H), 2091 (C≡C), 1676 (C=O), 1405, 1252, 1102.

Synthesis of [Mn(bpm)(CO)₃Br]. Bis-(3,5-dimethyl-pyrazolyl)methane (250 mg, 10.7 mmol) and [Mn(CO)₅Br] (400 mg, 15.7 mmol) were combined in ethanol (38 ml) within a foil-wrapped Schlenk tube. The mixture was heated at 90°C for five hours and then left to stand at room temperature overnight. The resulting yellow-orange precipitate was filtered and washed with cold ethanol (100 ml) to yield [Mn(bpm)(CO)₃Br] as yellow/orange crystals (243 mg, 61%); ¹H NMR (500 MHz, CDCl₃) ppm: 6.04 (s, H, pyrazole CH), 5.71 (s, 1H, CH₂), 2.65 (s, 3H, CH₃), 2.38 (s, 3H, CH₃); IR ν_{\max} (nujol, cm⁻¹): 2025 (CO), 1949 (CO), 1909 (CO), 1735 (C=O ester), 1719 (C=O ester), 1461, 1376, 1320, 1284, 1271, 1225, 1180, 1167, 1089.

Synthesis of [Mn(bpm)(CO)₃N₃]. The synthesis was adapted from Simpson *et al.*³ [Mn(bpm)(CO)₃Br] (113 mg, 0.29 mmol) and AgOTf (114 mg, 0.44 mmol) were dissolved in acetone (10 ml) and the solution heated at reflux in the dark under N₂ for 5 h. The resulting solution was transferred via cannula into a

fresh Schlenk tube charged with argon and sodium azide (129 mg, 1.91 mmol) and then stirred at room temperature for 20 h. The solvent was evaporated under reduced pressure and the residue dissolved in dichloromethane, filtered through celite and dried under reduced pressure. The residue was dissolved in an acetone: dichloromethane mixture (1:1, 5 ml) and pentane (30 ml) was added while vigorously stirring. The resulting bright yellow precipitate was collected and washed with pentane (3 × 10 ml) to give [Mn(bpm)(CO)₃N₃] as bright yellow crystals (63 mg, 60%); ¹H NMR (500 MHz, CDCl₃) ppm: 6.02 (s, 2H, CH₂), 5.72 (b, CH, 2H), 2.61 (s, 6H, CH₃), 2.37 (s, 6H, CH₃); IR ν_{\max} (nujol, cm⁻¹): 2053 (s, N₃), 2008 (CO), 1936 (CO), 1932 (CO), 1462, 1419 (w), 1377, 1306 (w), 1284 (w).

Synthesis of [Mn(bpm)(CO)₃(DMT)]. [Mn(bpm)(CO)₃N₃] (50 mg) and DMAD (0.5 ml) were combined in toluene (5 ml) and heated at 50°C for 20 h without stirring. The resulting precipitate was collected and washed with cold toluene (2 × 5 ml) and diethyl ether (3 × 5 ml) to yield [Mn(bpm)(CO)₃(DMT)] as pale yellow crystals (32 mg, 49%). ¹H NMR (500 MHz, DMSO-D₆) 7.2 (m, triazole CH), 6.18 (s, 2H, CH₂), 3.72 (s, 6H, ester CH₃), 2.42 (s, 6H, CH₃), 2.3 (s, 3H, CH₃), 2.08 (s, 3H, CH₃); IR ν_{\max} (nujol, cm⁻¹): 2025 (CO), 1949 (CO), 1909 (CO), 1735 (C=O ester), 1719 (C=O ester), 1461, 1376, 1320, 1284, 1271, 1225, 1180, 1167, 1089. Single crystals obtained from the reaction mixture were suitable for single-crystal X-ray analysis.

7.3.9 References

- (1) Spek, A. L. *Acta Crystallogr. D Biol. Crystallogr.* **2009**, *65*, 148.
- (2) Wilbur, J. M.; Bonner, B. A. *J. Polym. Sci., Part A: Polym. Chem.* **1990**, *28*, 3747.
- (3) Simpson, P. V.; Skelton, B. W.; Raiteri, P.; Massi, M. *New J. Chem.* **2016**, *40*, 5797.

7.4 Computational Procedures for Chapter 4

7.4.1 Computational Procedures

Density functional theory (DFT) calculations were carried out to rationalize the experimental observations of the formation of the N(1)-bound complex in $\mathbf{1}\cdot[\text{Mn}(\text{CO})_3(\text{DMT})]$, which contrasts with the formation of the N(2)-bound complex in the corresponding molecular species, $\text{Mn}(\text{bpm})(\text{CO})_3(\text{DMT})$, where bpm = bis(3,5-dimethyl-pyrazolyl)methane. Calculations were carried out on a 306-atom neutral fragment of $\mathbf{1}\cdot[\text{Mn}(\text{CO})_3(\text{DMT})]$ and the 57-atom $\text{Mn}(\text{bpm})(\text{CO})_3(\text{DMT})$ (Figure SB1). The fragment was extracted from the structure of the crystallographically observed product (i.e. the N(1) isomer of $\mathbf{1}\cdot[\text{Mn}(\text{CO})_3(\text{DMT})]$) and consisted of the triazolate complex bonded to Mn(I) in the core of the framework and parts of the framework in close proximity to the complex. Both N(1)- and N(2)-coordinated triazolate ligands were considered in the calculations of the MOF fragment and corresponding molecular species. DFT calculations of molecular clusters as models for extended periodic MOF structures are a common approach to study MOFs when the property under investigation is localized.¹⁻⁹ A significant advantage of calculations at the cluster level is a considerable reduction in the computational costs without sacrificing accuracy in modelling properties of the framework in many cases.^{3,4}

All DFT calculations were performed with the Gaussian 09 software package¹¹ (Revision D.01) using the M06 functional, which has been shown to be accurate for organometallic thermochemistry and non-covalent interactions.¹² Constrained geometry optimizations of the MOF fragments were carried out in vacuo keeping all non-hydrogen atoms in the framework fixed at their positions in the experimental crystal structure except for the atoms in the immediate vicinity of the Mn(I) ion (see Figure SB1). The Stuttgart-Dresden effective core potential SDD¹³ was used for Mn ions and the 6-31G(d,p) basis set¹⁴ was used for all atoms. Single-point calculations were also performed on optimized geometries with the 6-31+G(d,p) basis set¹⁴ and SMD continuum solvation model¹⁵ with toluene as the solvent to match the experimental conditions. Due to the difficulty of achieving convergence with diffuse basis functions, the single-point calculations on the optimized geometries of the triazolate complexes in the framework and molecular species were obtained using a less tight convergence criterion of a root mean square (RMS) change in density matrix $<10^{-4}$ compared with the default criterion in Gaussian 09 of $<10^{-8}$, which corresponds approximately to a change of energy as 10^{-8} in atomic units.¹¹ Thus, this more relaxed convergence criterion had a small effect of the final single-point energies obtained.

Before optimizing the geometries of the MOF fragments, single-point energies calculated at the M06/6-31G(d,p)+SDD level of all possible spin states of the Mn(I) and two Mn(II) ions in the structure indicated that Mn(I) is in a low-spin configuration while the Mn(II) atoms are in high-spin states, as expected for an Mn(I) ion bound to strong-field carbonyl ligands and Mn(II) ions bound to a weak-field oxygen and a strong-field di-pyrazole ligand.¹⁶⁻¹⁸

To estimate the energy barrier to interconvert the N(1)- and N(2)-bound isomers in the MOF, a number of intermediate structures were interpolated between the N(1)- and N(2)-bound isomers by simultaneously rotating and translating the triazolate ligand while linearly interpolating the rest of the MOF structure, using uniform angular and translational increments. The geometries of these intermediate structures were then optimized using the same procedure and constraints as described above for MOF fragments, with the additional constraints that the positions of the N(2) nitrogen and one of the N(1) nitrogens in the triazolate ligand were fixed to maintain the relative orientation of the triazolate ring with respect to the rest of the MOF. Single-point energies were also obtained for these optimized geometries with the 6-31+G(d,p) basis set and SMD continuum solvation model with toluene solvent.

7.4.2 Computational Results

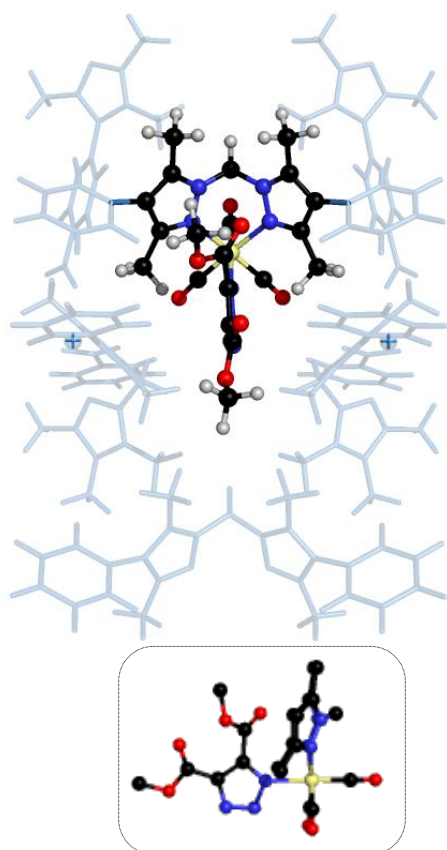
As can be seen in Figure SB2, the optimized structure of the N(1)-bound isomer in the MOF is very similar to that of the experimental X-ray crystal structure of **1**·[Mn(CO)₃(DMT)], with very small differences in the distances between the carbons of the methyl ester groups and those of the methyl groups bonded to phenyl and pyrazole groups in the two structures. Thus, the DFT method used in the calculations appears to accurately capture the experimental structure.

As shown in Table SB1, the N(2)-bound isomer is slightly higher in energy than the N(1)-bound isomer in the MOF framework when diffuse basis functions and the toluene solvent environment are considered, but the relative stabilities of the complexes is reversed in the corresponding molecular species, in agreement with experiment. Comparing the energies of the complexes in the MOF and corresponding molecular species, the framework stabilizes the N(1)-bound isomer with respect to the N(2)-bound isomer by 11.1 kJ/mol. The difference in stability of the N(1)- and N(2)-bound isomers in the framework relative to the molecular species appears to be due to differences in steric hindrance, with atoms in the methyl groups of the triazolate ligand in the N(2)-bound isomer exhibiting a larger number of contacts with atoms of the framework that are close to the sum of the van der Waals radii of the atoms (see

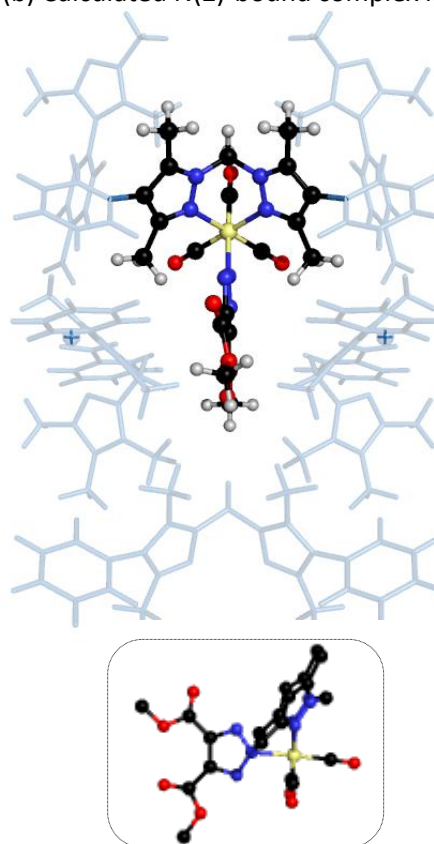
Figure SB3); in particular, two of the carbon–carbon contacts in the N(2)-bound isomer are less than 0.1 Å larger than the van der Waals diameter of carbon.¹⁹

The DFT calculations also indicate that the pathway to inter-convert the N(1)- and N(2)-bound isomers in the MOF is energetically inaccessible (Figure SB4) due to severe steric clashes between the triazolate ligand and MOF framework in the process of rotating the ligand (Figure SB5), with a barrier to interconversion of around 170 kJ/mol. Since the N(1)-bound isomer must form first in the click reaction,²⁰ the triazolate ligand becomes locked in this coordination because the pathway to forming the N(2)-bound isomer is sterically blocked. Overall, these results suggest that the MOF environment leads to selective and unusual coordination of the triazolate complex by restricting the rearrangement of products of the click reaction between coordination isomers and stabilizing the unusual coordination via steric hindrance.

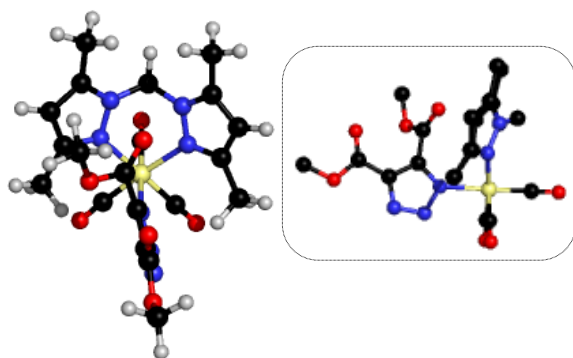
(a) Calculated N(1)-bound complex in MOF



(b) Calculated N(2)-bound complex in MOF



(c) Calculated N(1)-bound molecular species



(d) Calculated N(2)-bound molecular species

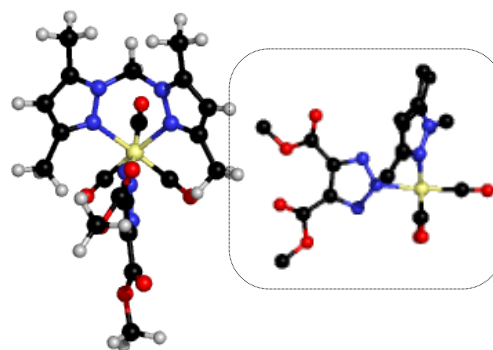
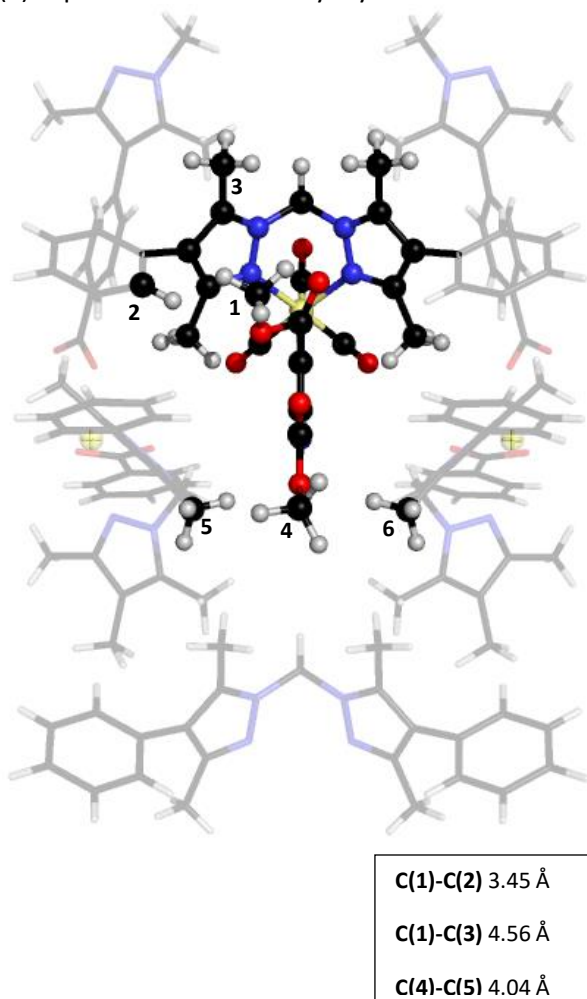


Figure SB1. DFT-optimized structures of simplified cluster models of the (a) N(1)- and (b) N(2)-bound isomers of the $1 \cdot [\text{Mn}(\text{CO})_3(\text{DMT})]$ MOF and the corresponding (c) N(1)- and (d) N(2)-bound molecular species. Besides all hydrogens, atoms whose positions were not constrained in the geometry optimizations to their positions in the experimental X-ray crystal structure are highlighted. Side views of the core metal complex in all structures are also shown in boxes. (Color code: black= carbon, light gray= hydrogen, blue= nitrogen, red= oxygen, pale yellow= manganese.)

(a) Experimental MOF X-ray crystal structure



(b) Calculated N(1)-bound complex in MOF

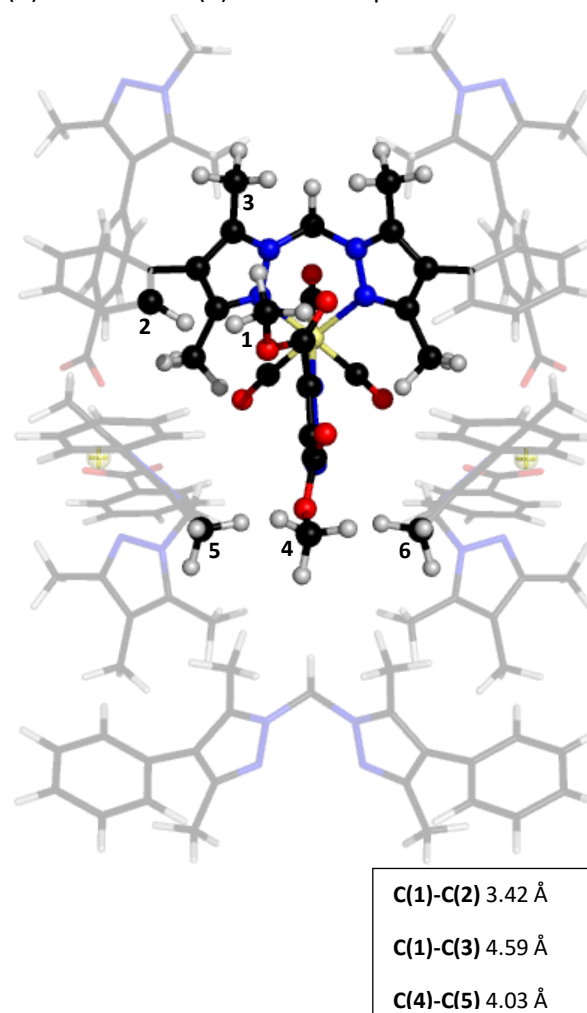
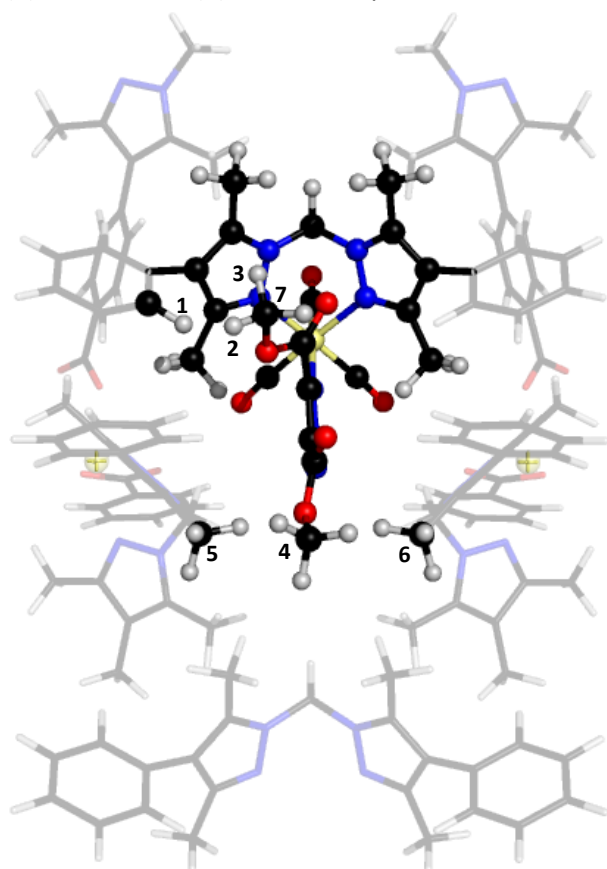


Figure SB2. Comparison of the (a) experimental X-ray crystal structure and (b) DFT-optimized structure of the N(1)-bound isomer of $1 \cdot [\text{Mn}(\text{CO})_3(\text{DMT})]$. (The colour coding of atoms is the same as in Figure SB1.)

Table SB1. Relative energies of the N(2)-bound complex with respect to the N(1)-bound complex in the MOF and corresponding molecular species.

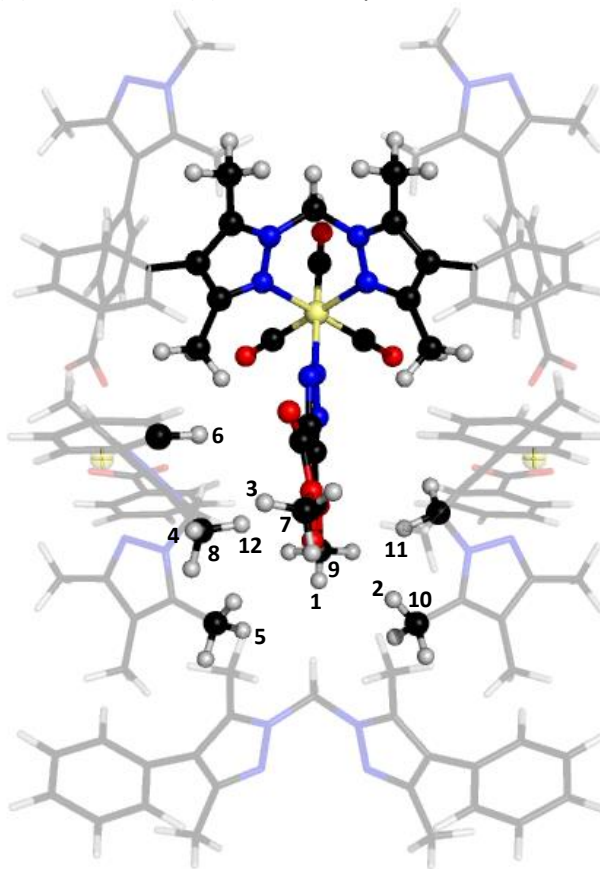
Basis set	Solvent	Energy (kJ/mol)	
		MOF	Molecular complex
6-31G(d,p)	none	3.79	4.17
6-31+G(d,p)	none	7.82	0.74
6-31+G(d,p)	toluene	2.57	-8.55

(a) Calculated N(1)-bound complex in MOF



H(1)-H(2) 2.40 Å
 H(1)-H(3) 2.48 Å
 C(4)-C(5) 4.03 Å

(b) Calculated N(2)-bound complex in MOF



H(1)-H(2) 2.44 Å
 H(3)-H(4) 2.54 Å
 H(1)-H(5) 2.56 Å
 H(3)-H(6) 2.58 Å
 C(7)-C(8) 3.61 Å
 C(9)-C(10) 3.62 Å

Figure SB3. Closest non-bonded H–H, C–C, and C–H atom contacts in the calculated (a) N(1)- and (b) N(2)-bound complexes in the framework. For comparison, the sum of the van der Waals radii for H+H, C+C, and C+H are approximately 2.20, 3.54, and 2.88 Å, respectively.¹⁸ (The colour coding of atoms is the same as in Figure SB1.)

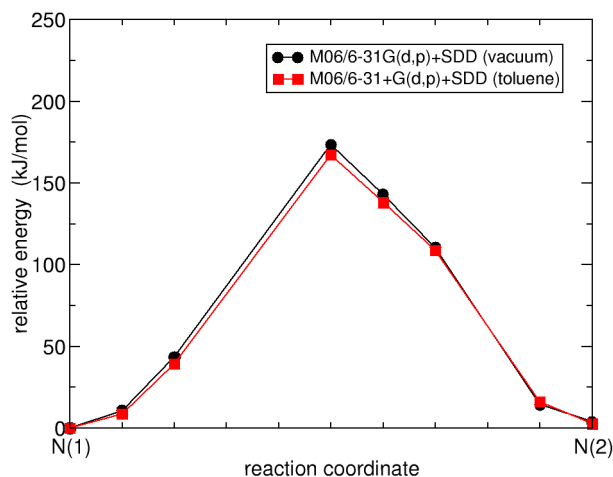


Figure SB4. Relative energies of structures along the pathway to convert the N(1)-bound complex into the N(2)-bound complex.

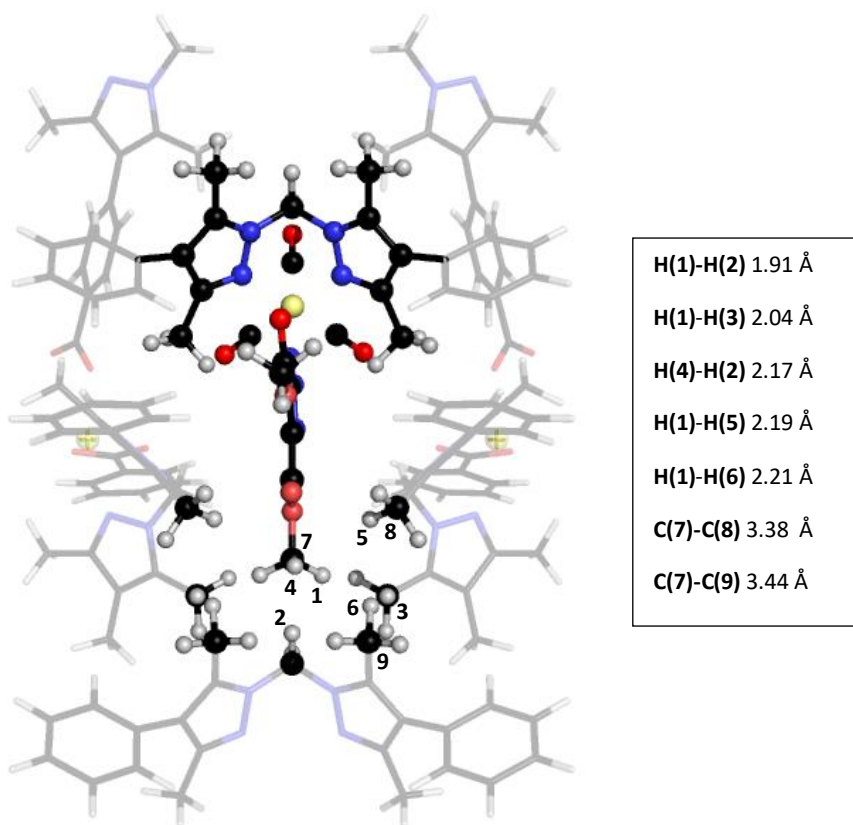


Figure SB5. Closest non-bonded H–H, C–C, and C–H atom contacts in the highest energy intermediate structure (see Figure SB4) along the pathway to convert the N(1)-bound complex into the N(2)-bound complex. Due to the approximate reflection symmetry of the structures in the plane bisecting the structure, only around half of the contacts have been shown for clarity. Almost all of the listed contacts are closer in distance than the sum of the van der Waals radii for H+H, C+C, and C+H (2.20, 3.54, and 2.88 Å, respectively),¹⁸ indicating substantial steric hindrance in the structure. (The colour coding of atoms is the same as in Figure SB1.)

7.4.3 References

- (1) Campbell, C.; Ferreiro-Rangel, C. A.; Fischer, M.; Gomes, J. R. B.; Jorge, M., *J. Phys. Chem. C* **2017**, *121* (1), 441–458.
- (2) Supronowicz, B.; Mavrandonakis, A.; Heine, T., *J. Phys. Chem. C* **2013**, *117* (28), 14570–14578.
- (3) Lee, K.; Isley, W. C.; Dzubak, A. L.; Verma, P.; Stoneburner, S. J.; Lin, L. C.; Howe, J. D.; Bloch, E. D.; Reed, D. A.; Hudson, M. R.; Brown, C. M.; Long, J. R.; Neaton, J. B.; Smit, B.; Cramer, C. J.; Truhlar, D. G.; Gagliardi, L., *J. Am. Chem. Soc.* **2014**, *136* (2), 698–704.
- (4) Bloch, W. M.; Burgun, A.; Coghlan, C. J.; Lee, R.; Coote, M. L.; Doonan, C. J.; Sumbly, C. J., *Nat. Chem.* **2014**, *6*, 906–12.
- (5) Xiao, D. J.; Bloch, D. E.; Mason, J. A.; Queen, W. L.; Hudson, M. R.; Planas, N.; Borycz, J.; Dzubak, A. L.; Verma, P.; Lee, K.; Bonino, F.; Crocella, V.; Yano, J.; Bordiga, S.; Truhlar, D. G.; Gagliardi, L.; Brown, C. M.; Long, J. R., *Nat. Chem.* **2014**, *6*, 590–95.
- (6) Bloch, E. D.; Hudson, M. R.; Mason, J. A.; Chavan, S.; Crocellà, V.; Howe, J. D.; Lee, K.; Dzubak, A. L.; Queen, W. L.; Zdrozny, J. M.; Geier, S. J.; Lin, L. C.; Gagliardi, L.; Smit, B.; Neaton, J. B.; Bordiga, S.; Brown, C. M.; Long, J. R., *J. Am. Chem. Soc.* **2014**, *136* (30), 10752–10761.
- (7) Wang, Y.; Yang, J.; Li, Z.; Zhang, Z.; Li, J.; Yang, Q.; Zhong, C., *RSC Adv.* **2015**, *5*, 33432–33437.
- (8) Verma, P.; Xu, X.; Truhlar, D. G., *J. Phys. Chem. C* **2013**, *117* (24), 12648–2660.
- (9) Maurice, R.; Verma, P.; Zdrozny, J. M.; Luo, S.; Borycz, J.; Long, J. R.; Truhlar, D. G.; Gagliardi, L., *Inorg. Chem.* **2013**, *52* (16), 9379–9389.
- (10) Odoh, O.; Cramer, C. J.; Truhlar, D. G.; Gagliardi, L., *Chem. Rev.* **2015**, *115* (12), 6051–6111.
- (11) a) Gaussian 09, Revision D.01, Frisch, M. J.; Trucks, G. W.; Schlegel, H. B.; Scuseria, G. E.; Robb, M. A.; Cheeseman, J. R.; Scalmani, G.; Barone, V.; Mennucci, B.; Petersson, G. A.; Nakatsuji, H.; Caricato, M.; Li, X.; Hratchian, H. P.; Izmaylov, A. F.; Bloino, J.; Zheng, G.; Sonnenberg, J. L.; Hada, M.; Ehara, M.; Toyota, K.; Fukuda, R.; Hasegawa, J.; Ishida, M.; Nakajima, T.; Honda, Y.; Kitao, O.; Nakai, H.; Vreven, T.; Montgomery, J. A., Jr.; Peralta, J. E.; Ogliaro, F.; Bearpark, M.; Heyd, J. J.; Brothers, E.; Kudin, K. N.; Staroverov, V. N.; Kobayashi, R.; Normand, J.; Raghavachari, K.; Rendell, A.; Burant, J. C.; Iyengar, S. S.; Tomasi, J.; Cossi, M.; Rega, N.; Millam, J. M.; Klene, M.; Knox, J. E.; Cross, J. B.; Bakken, V.; Adamo, C.; Jaramillo, J.; Gomperts, R.; Stratmann, R. E.; Yazyev, O.; Austin, A. J.; Cammi, R.; Pomelli, C.; Ochterski, J. W.; Martin, R. L.; Morokuma, K.; Zakrzewski, V. G.; Voth, G. A.; Salvador, P.; Dannenberg, J. J.; Dapprich, S.; Daniels, A. D.; Farkas, Ö.; Foresman, J. B.; Ortiz, J. V.; Cioslowski, J.; Fox, D. J., Gaussian Inc., Wallingford CT, **2013**; b) <http://gaussian.com/scf/>.
- (12) Zhao, Y.; Truhlar, D. G., *Theor. Chem. Acc.* **2008**, *120*, 215–241.

- (13) Andrae, D.; Häußermann, U.; Dolg, M.; Stoll, H.; Preuß, H., *Theor. Chem. Acta* **1990**, *77*, 123–141.
- (14) Hehre W. J.; Radom L.; Schleyer P. V. R.; Pople J. A., *Ab Initio Molecular Orbital Theory*. 1st ed., Wiley, New York, **1986**.
- (15) Marenich, A. V.; Cramer, C. J.; Truhlar, D. G., *J. Phys. Chem. B* **2009**, *113*, 6378–6396.
- (16) Cotton, F. A.; Wilkinson, G.; Gaus, P. L., *Basic Inorganic Chemistry*, 2nd ed., Wiley: New York, **1987**.
- (17) Yamamoto A., *Organotransition Metal Chemistry*, Wiley: New York, **1986**.
- (18) van Gorkum, R.; Buda, F.; Kooijman, H.; Spek, A. L.; Bouwman, E.; Reedijk, J., *Eur. J. Inorg. Chem.* **2005**, *2005*, 2255–2261.
- (19) Rowland, R. S.; Taylor, R., *J. Phys. Chem.* **1996**, *100*, 7384–7391.
- (20) Singh, K. S.; Kreisel, K. A.; Yap, G. P. A.; Kollipara, M. R., *J. Organomet. Chem.* **2006**, *691* (16), 3509-3518.

7.5. Supplementary Information for Chapter 5

7.5.1 Tables of Spectroscopic data for various Mn(I) complexes

Table 7.5.1.1: Mn(I) complexes with N,N-bipyridine and P,P-chelating ligands including photo-substituted complexes

Complex	$\nu(\text{CO})$ (cm^{-1})	IR system	Colour/ λ_{max} (nm)
<i>fac</i> - [Mn(bpy)(CO) ₃ Br]	1914, 1935, 2023 (¹)	THF	Yellow/430 nm ¹
<i>mer</i> - [Mn(bpy)(CO) ₃ Br]	1903, 1948, 2043 ^a (¹)	THF	Orange/510 nm ¹
[Mn(bpy)(CO) ₂ (CCPh)(MeCN)]	1843, \approx 1920 (²)	MeCN	-
[Mn(bpy)(CO) ₂ (Br)(MeCN)]	1857, 1940 (²)	MeCN	-
[Mn(bpy)(CO) ₂ (MeCN) ₂]Br	1883, 1961 (²)	MeCN	-
[Mn(bpy)(CO) ₂ (Br)(THFA)]	1838, \approx 1920 (²)	MeCN	-
[Mn(bpy)(CO) ₂ Br(2MeTHF)]	1842, 1921 (¹)	2-MeTHF, 135K	Red/630 nm
[Mn(bpy)(CO) ₂ (P(OMe) ₃) ₂]Br	1892, 1963 (¹)	THF, RT	-
[Mn(bpy)(CO) ₂ (Br)(THF)]	1849, 1923 (²)	THF	-
[Mn(bpy)(CO) ₂ (CCPh)(THF)]	1911, 1940 ^b (²)	THF	-
[Mn(bpy)(CO) ₂ (MeCN) ₂]PF ₆	1882, 1963 (²)	MeCN	Red
[Mn(ⁱ Pr ₂ Ph-DAB)(CO) ₂ (THF)Br]	1895, 1952 (³)	THF	-

^a The high frequency stretching mode (2043 cm^{-1}) is characteristically weak in the *mer*-isomer. ^b Listed as 1940 cm^{-1} by Yempally *et al.* in apparent error. THFA = Tetrahydrofurfurylamine, DAB = diazabutadiene, DEAD = Diethylacetylenedicarboxylate.

Table 7.5.1.2: Monosubstituted complexes generated from reaction of [Tpm'Mn(CO)₃]⁺ with Me₃NO^c

Compound	$\nu(\text{CO})$ (cm^{-1})	IR system	Colour
[Tpm'Mn(CO) ₃]PF ₆	1950, 2045 (⁴)	DCM	Yellow
[Tpm'Mn(CO) ₂ (PEt ₃)] ⁺	1864, 1942 (⁴)	DCM	Yellow
[Tpm'Mn(CO) ₂ (P(OEt ₃))] ⁺	1886, 1963 (⁴)	DCM	Yellow
[Tpm'Mn(CO) ₂ MeCN] ⁺	1877, 1960 (⁴)	DCM	Orange
[Tpm'Mn(CO) ₂ CNBut ^t] ⁺	1896, 1963 (⁴)	DCM	Yellow
[Tpm'Mn(CO) ₂ (PMe ₃)] ⁺	1866, 1945 (⁴)	DCM	Yellow
[Tpm'Mn(CO) ₂ (Pyridine)] ⁺	1861, 1945 (⁴)	DCM	Orange

^c UV photolysis results in decomposition rather than substitution, DCM = Dichloromethane

Table 7.5.1.3: Monosubstituted complexes generated from photolysis of $[XMn(CO)_3]$ (X= Cp, Cp')

Compound	$\nu(CO)$ (cm^{-1})	IR system	Colour
[CpMn(CO) ₃]	1939, 2024 ⁽⁵⁾	CS ₂	Yellow
	1944, 2027 ⁽⁶⁾	Cyclohexane	
	1940, 2028 ⁽⁷⁾	Nujol	
[CpMn(CO) ₂ (cyclooctene)]	1902, 1961 ⁽⁶⁾	Cyclohexane	-
	1893, 1956 ⁽⁵⁾	CS ₂	
[CpMn(CO) ₂ (cycloheptene)]	1895, 1958 ⁽⁵⁾	CS ₂	-
[CpMn(CO) ₂ (cyclopentene)]	1896, 1958 ⁽⁵⁾	CS ₂	-
	1896, 1951 ⁽⁸⁾	Benzene	
[CpMn(CO) ₂ (1-pentene)]	1902, 1973 ⁽⁹⁾	Iso-octane	-
[CpMn(CO) ₂ (η^2 -1,3,5-cycloheptatriene)]	1908, 1965 ⁽¹⁰⁾	n-heptane	-
[CpMn(CO) ₂ (η^2 -1,3,5-cyclooctatriene)]	1904, 1963 ⁽¹⁰⁾	n-heptane	-
[Cp'Mn(CO) ₂ (η^2 -1,3,5-cycloheptatriene)]	1908, 1964 ⁽¹⁰⁾	n-heptane	-
[CpMn(CO) ₂ THF]	1863, 1934 ⁽⁶⁾	Cyclohexane	Red
	1850, 1921 ⁽⁹⁾	THF	Red/400 nm
[CpMn(CO) ₂ pyridine]	1868, 1934 ⁽⁶⁾	Cyclohexane	Dark red ⁽¹³⁾
	1865, 1932 ⁽¹¹⁾	Cyclohexane	
[CpMn(CO) ₂ (3,5-dimethylpyrazole)]	1852, 1923 ⁽¹²⁾	THF	Orange
	1847, 1921 ⁽¹²⁾	THF	
[CpMn(CO) ₂ (imidazole)]	1843, 1918 ⁽¹²⁾	THF	Orange
[CpMn(CO) ₂ benzene]	1893, 1955 ⁽¹¹⁾	Cyclohexane	-
[CpMn(CO) ₂ mesitylene]	1889, 1958 ⁽¹¹⁾	Cyclohexane	-
[CpMn(CO) ₂ N ₂]	1928, 1979 ⁽⁶⁾	Cyclohexane	Red-brown ⁽¹⁴⁾
	1923, 1980 ⁽¹⁴⁾	n-hexane	
	1895, 1965 ⁽¹⁴⁾	KBr	
[CpMn(CO) ₂ PF ₃]	1942, 1998 ⁽¹⁵⁾	Cyclohexane	Light Yellow
[CpMn(CO) ₂ P(C ₆ H ₁₁) ₃]	1848, 1928 ⁽⁵⁾	CS ₂	Light yellow
	1869, 1931 ⁽¹⁵⁾	Cyclohexane	
[CpMn(CO) ₂ P(CH ₃) ₃]	1876, 1939 ⁽¹⁵⁾	Cyclohexane	Light yellow
[CpMn(CO) ₂ P(OCH ₃) ₃]	1891, 1954 ⁽¹⁵⁾	Cyclohexane	Light yellow
[CpMn(CO) ₂ P(OC ₆ H ₅) ₃]	1909, 1970 ⁽¹⁵⁾	Cyclohexane	Light yellow
	1900, 1963 ⁽⁵⁾	CS ₂	

	1861, 1930 (7)	Nujol	
[CpMn(CO) ₂ PPh ₃]	1874, 1938 (8)	Benzene	Yellow
	1874, 1934 (5)	CS ₂	
[CpMn(CO) ₂ AsPh ₃]	1854, 1916 (7)	Nujol	Pale yellow
	1872, 1935 (5)	CS ₂	
[CpMn(CO) ₂ As(OC ₆ H ₅) ₃]	1918, 1974 (5)	CS ₂	
[CpMn(CO) ₂ SbPh ₃]	1857, 1917 (7)	Nujol	Pale yellow
	1874, 1934 (5)	CS ₂	
[CpMn(CO) ₂ (π-phenylacetylene)]	1921, 1981 (16)	Cyclohexane	-
[Cp'Mn(CO) ₂ (π-phenylacetylene)]	1912, 1977 (17)	Pentane	Yellow
[Cp''Mn(CO) ₂ (π-phenylacetylene)]	1901, 1963 (17)	Pentane	Yellow
[CpMn(CO) ₂ (π-diphenylacetylene)]	1921, 1986 (8)	Benzene	-
	1902, 1957 (8)	Benzene	Yellow
[CpMn(CO) ₂ (ethylene)]	1919, 1981 (17)	Pentane	
[Cp'Mn(CO) ₂ (ethylene)]	1915, 1978 (17)	Pentane	Yellow
[Cp''Mn(CO) ₂ (ethylene)]	1902, 1962 (17)	Pentane	Yellow
[CpMn(CO) ₂ (MeC ₂ Me)]	1904, 1963 (17)	Pentane	Yellow
[Cp'Mn(CO) ₂ (MeC ₂ Me)]	1900, 1961 (17)	Pentane	Yellow
[Cp''Mn(CO) ₂ (MeC ₂ Me)]	1885, 1946 (17)	Pentane	Yellow
[CpMn(CO) ₂ (DEAD)]	1960, 2008 (8)	Benzene	-
[CpM(CO) ₂ (SO ₂)]	1969, 2028 (62)	Neat	Yellow-orange (18)
[Cp(CO) ₂ (CH ₃ CN)]	1890, 1950 (19)	Dichloromethane	Yellow
[CpMn(CO) ₂ (NBD)]	1903, 1963 (5)	CS ₂	-
[CpMn(CO) ₂ (Norbornylene)]	1903, 1963 (5)	CS ₂	-
[CpMn(CO) ₂ (η ¹ -dmpm)]	1861, 1927 (20)	THF	
[CpMn(CO) ₂ (η ¹ -dmpe)]	1861, 1927 (20)	THF	
[CpMn(CO) ₂ (η ¹ -dmpp)]	1861, 1926 (20)	THF	

Table 7.5.1.4: Monosubstituted complexes generated from photolysis of $[XMn(CO)_3]$ ($X=Tp, Tp'$)

Compound	$\nu(CO)$ (cm^{-1})	IR system	Colour
$[TpMn(CO)_3]$	1936, 2034 ⁽⁶⁾	Cyclohexane/THF	Yellow
$[TpMn(CO)_2(\text{cyclooctene})]$	1884, 1960 ⁽⁶⁾	Cyclohexane/THF	-
$[TpMn(CO)_2THF]$	1851, 1946 ⁽⁶⁾ 1825, 1948 ⁽¹⁵⁾	Cyclohexane/THF THF	- Red
$[TpMn(CO)_2\text{pyridine}]$	1849, 1936 ⁽⁶⁾	Cyclohexane/THF	-
$[TpMn(CO)_2N_2]$	1913, 1977 ⁽⁶⁾	Cyclohexane/THF	-
$[TpMn(CO)_2PF_3]$	1940, 2000 ⁽¹⁵⁾	cyclohexane	Light yellow
$[TpMn(CO)_2P(CH_3)_3]$	1865, 1941 ⁽¹⁵⁾	cyclohexane	Light yellow
$[TpMn(CO)_2P(OCH_3)_3]$	1887, 1961 ⁽¹⁵⁾	cyclohexane	Light yellow
$[TpMn(CO)_2P(OC_6H_5)_3]$	1901, 1974 ⁽¹⁵⁾	cyclohexane	Light yellow
$[TpMn(CO)_2P(C_6H_5)_3]$	1870, 1945 ⁽¹⁵⁾	cyclohexane	Light yellow
$[TpMn(CO)_2P(n-C_4H_9)_3]$	1861, 1937 ⁽¹⁵⁾	cyclohexane	Light yellow
$[TpMn(CO)_2P(i-C_3H_7)_3]$	1861, 1937 ⁽¹⁵⁾	cyclohexane	Light yellow
$[TpMn(CO)_2P(C_6H_{11})_3]$	1859, 1935 ⁽¹⁵⁾	cyclohexane	Light yellow
$[Tp'Mn(CO)_3]$	1927, 2032	Cyclohexane	Yellow
$[Tp'Mn(CO)_2PF_3]$	1925, 1988 ⁽¹⁵⁾	Cyclohexane	Light yellow
$[Tp'Mn(CO)_2P(CH_3)_3]$	1840, 1927 ⁽¹⁵⁾	Cyclohexane	Light yellow
$[Tp'Mn(CO)_2P(OCH_3)_3]$	1869, 1949 ⁽¹⁵⁾	Cyclohexane	Light yellow
$[Tp'Mn(CO)_2P(OC_6H_5)_3]$	1883, 1961 ⁽¹⁵⁾	cyclohexane	Light yellow
$[Tp'Mn(CO)_2P(n-C_4H_9)_3]$	1820, 1903 ⁽¹⁵⁾	THF	Light yellow

Table 7.5.1.5: Di-substitution of CO under photolysis of $[XMn(CO)_3]$ ($X = Tp, Tp', Cp, Cp'$)

Compound	$\nu(CO) \text{ cm}^{-1}$	IR system	Colour
$[TpMn(CO)(PF_3)_2]$	1958 ⁽¹⁵⁾	Cyclohexane	-
$[Tp'Mn(CO)(PF_3)_2]$	1948 ⁽¹⁵⁾	Cyclohexane	-
$[TpMn(CO)(P(OPh)_3)_2]$	1895 ⁽¹⁵⁾	CS ₂	-
$[TpMn(CO)(P(OCH_3)_3)_2]$	1871 ⁽¹⁵⁾	Cyclohexane	-
$[CpMn(CO)(PPh_3)_2]$	1836 ⁽⁷⁾	Nujol	Orange
$[CpMn(CO)(AsPh_3)_2]$	1836 ⁽⁷⁾	Nujol	Red-brown
$[CpMn(CO)(SbPh_3)_2]$	1825 ⁽⁷⁾	Nujol	Red-brown
$[CpMn(CO)DPB]$	1815 ⁽²¹⁾	Benzene	Orange
$[CpMn(CO)(PF_3)_2]$	1953 ⁽²²⁾	KBr	Yellow
$[Cp'Mn(CO)DPB]$	1815 ⁽²¹⁾	Benzene	Yellow
$[CpMn(CO)IMes]$ (agostic)	1817 ⁽²³⁾	n-heptane	-
$[CpMn(CO)dmpm]$ ²⁰	1844 ⁽²⁰⁾	n-heptane	Yellow ²⁴
	1808 ⁽²⁴⁾	CH ₂ Cl ₂	
$[CpMn(CO)dmpe]$	1827 ⁽²⁰⁾	THF	-
$[CpMn(CO)dmpp]$	1822 ⁽²⁰⁾	THF	-

DPB = 1,4-butylene(diphenylphosphine), IMes = 1,3-bis(2,4,6-trimethylphenyl)imidazol-2-ylidene, NBD = norbornadiene, dmpm = bis(dimethylphosphino)methane, dmpe = bis(dimethylphosphino)ethane, dmpp = bis(dimethylphosphino)propane.

7.5.2 Experimental

Unless otherwise stated, all chemicals were obtained from commercial sources and used as received. THF was distilled from Na/benzophenone and degassed with Ar prior to use. Toluene was distilled from sodium and stored over 4Å sieves, it was degassed with Ar prior to use. Acetonitrile was distilled from CaH₂ and degassed with Ar prior to use. The compounds **1** and **1**·[Mn(CO)₃(H₂O)] were prepared by methods reported previously²⁵ and stored in the dark. The samples were exposed to minimal light during handling to prevent premature CO evolution. The freshly distilled solvents toluene, dichloromethane, acetonitrile and THF were degassed with argon prior to use. Energy-dispersive X-ray spectroscopy (EDX) was performed with a Philips XL30 field emission scanning electron microscope. Infrared (IR) spectra were collected on a Perkin-Elmer Spectrum Two, with the sample distributed between two NaCl disks in Nujol. Thermal gravimetric analysis (TGA) was performed on a Perkin-Elmer STA-6000 instrument under a constant flow of N₂ gas at a temperature increase rate of 5 °C/min. Gas adsorption isotherm measurements were performed on an ASAP 2020 Surface Area and Pore Size Analyser. Activation of samples was carried out as described below. UHP grade (99.999%) N₂, H₂, and CO₂ were used for all measurements. The temperatures were maintained at 77 K using a liquid nitrogen bath or at room temperature using an insulated water-bath. A LEDLENSER M14 visible LED torch was used for visible photolysis experiments, while an NSC4 UV LED Spot curing machine with an L15 optical lens (365 nm) was employed for UV photolysis. Solid state UV-Vis spectra were recorded using a Cary 5000 UV-Vis-NIR Spectrophotometer equipped with a Harrick Praying Mantis diffuse reflection spectroscopy attachment, the sample was distributed in KBr for analysis.

1·[Mn(CO)₃Br] in toluene: Taking care to exclude as much light as possible, a batch of **1**·[Mn(CO)₃(H₂O)] (30 mg) was washed with ethanol (5x10 ml) followed by freshly distilled toluene (5x10 ml) under argon degas. The solvent was degassed with argon and the crystals were allowed to soak in the fresh solvent for 1 hour between each washing. This solvent exchange procedure yielded **1**·[Mn(CO)₃Br] as bright yellow crystals: IR (nujol, cm⁻¹): 2029 (s, CO), 1953 (s, CO), 1899 (s, CO), 1608 (C=O), 1552, 1510, 1407, 1303, 1272.

1·[Mn(CO)₃Br] in acetonitrile: Taking care to exclude as much light as possible, a batch of **1**·[Mn(CO)₃(H₂O)] (30 mg) was washed with ethanol (5x10 ml) followed by freshly distilled acetonitrile (5x10 ml) under argon degas. The solvent was degassed with argon and the crystals were allowed to soak in the fresh solvent for 1 hour between each washing. This solvent exchange procedure yielded

bright yellow crystals: IR (nujol, cm^{-1}): 2041 (s, CO), 1953 (s, CO), 1921 (s, CO), 1613 (C=O), 1556, 1304, 1273.

1·[Mn(CO)₃Br] in THF: Taking care to exclude as much light as possible, a batch of 1·[Mn(CO)₃(H₂O)] (30 mg) was washed with ethanol (5x10 ml) followed by freshly distilled toluene (5x10 ml) under argon degas. The solvent was degassed with argon and the crystals were allowed to soak in the fresh solvent for 1 hour between each washing. Following toluene exchange, the crystals were washed with freshly distilled THF (5x10 ml) and degassed with argon after each washing, allowing the crystals to soak for 1 hr between each exchange. This solvent exchange procedure yielded 1·[Mn(CO)₃Br] as bright yellow crystals: IR (nujol, cm^{-1}): 2029 (s, CO), 1951 (s, CO), 1906 (s, CO), 1613 (C=O), 1555, 1305, 1274.

In-situ IR spectroscopy/Visible photolysis: A sample of 1·[Mn(CO)₃Br] (approx. 5 mg) in dry THF was dried briefly under argon flow and distributed between two NaCl windows. An IR spectrum was recorded using a Perkin-Elmer Spectrum Two, after which the IR source and sensor windows were obscured with thick cardboard to prevent damage to the instrument and the sample irradiated with a Ledlenser M14 LED torch. The IR spectrum was recorded periodically throughout the photolysis experiment.

Visible photolysis in solution: A sample of 1·[Mn(CO)₃Br] (approx. 5 mg) in either dry toluene, dry acetonitrile or dry THF (5 ml) was placed in a 10 ml glass vial fitted with a rubber septum. Argon was bubbled gently through the solvent constantly throughout the experiment. A Ledlenser M14 LED torch was placed 10cm from the sample and the entire apparatus was surrounded by aluminum foil so that all stray light from the torch was reflected back onto the sample. The MOF crystals were irradiated with the torch for a total of two hours, the MOF crystals change from bright yellow to green within approx. 10 minutes of photolysis, from which they gradually become colorless after two hours.

Single crystal X-ray Crystallography

Single crystals were mounted in paratone-N oil on a nylon loop. Single-crystal X-ray data for 1·[Mn(CO)₃Br] and the photocrystallography experiment structures were collected at 100 K (unless specified otherwise) on the MX1 beamline of the Australian Synchrotron using the Blulce software interface,²⁶ $\lambda=0.7108 \text{ \AA}$.

Photocrystallography experiments for 1·[Mn(CO)₃Br] in THF: All structure determinations were conducted at the Australian Synchrotron MX1 beamline using the Blulce software interface,²⁶ $\lambda=0.7108 \text{ \AA}$.

Single crystals were mounted in paratone-N oil on a nylon loop. An initial structure was collected at 100 K, the crystal was then warmed to 270 K under N₂ cryostream. A Ledlenser M14 visible LED torch was then positioned approx. 10 cm from the sample and turned on, the crystal was rotated periodically to ensure even irradiation. After 30 minutes of irradiation the sample was cooled to 150 K under irradiation, after which the torch was removed, and a full sphere of data was collected. Following data collection, the crystal was warmed to 270 K and irradiated using the same procedure described above. This process of data-collection and irradiation was performed on the same single crystal for a total of 2 hr of irradiation time, giving 4 structures at 30, 50, 90 and 120 minute irradiation times.

A second experiment was performed in which a single crystal was irradiated for 15 minutes to probe the changes taking place early in the photolysis process. This second crystal was smaller than the first.

Photocrystallography experiments for 1·[Mn(CO)₃Br] in Toluene: Single crystal X-ray data was collected at 150(2) K on an Oxford X-Calibur single crystal diffractometer ($\lambda = 0.71073 \text{ \AA}$). Single crystals were mounted in paratone-N oil on a nylon loop. An initial structure was collected at 150 K, the crystal was then warmed to 270 K under N₂ cryostream. A Ledlenser M14 visible LED torch was then positioned approx. 10 cm from the sample and turned on, the crystal was rotated periodically to ensure even irradiation. After the specified irradiation time the sample was cooled to 150 K under irradiation, after which the torch was removed, and a full sphere of data was collected. N_{tot} reflections were merged to N unique (R_{int} quoted) after a multi-scan absorption correction (proprietary software) and used in the full matrix least-squares refinements on F^2 . Unless otherwise stated in the additional refinement details, anisotropic displacement parameter forms were refined for the non-hydrogen atoms; hydrogen atoms were treated with a riding model [weights: $(\sigma^2(F_o)^2 + (aP)^2 + (bP))^{-1}$; $P = (F_o^2 + 2Fc^2)/3$]. Neutral atom complex scattering factors were used; computation used the SHELXL2014 program.²⁷ Pertinent results are given in the text, while views of the asymmetric units, additional refinement details, and X-ray experimental and refinement data (Tables S7.5.7.1-3) are given in sections 7.5.6-7. Powder X-ray diffraction data were collected on a Bruker Advance D8 diffractometer equipped with a capillary stage using Cu K α radiation ($\lambda = 1.5418 \text{ \AA}$). For PXRD analysis, samples were gently crushed with a mortar and pestle and packed into a 0.5 mm glass capillary.

7.5.3 IR spectroscopy of metallated samples

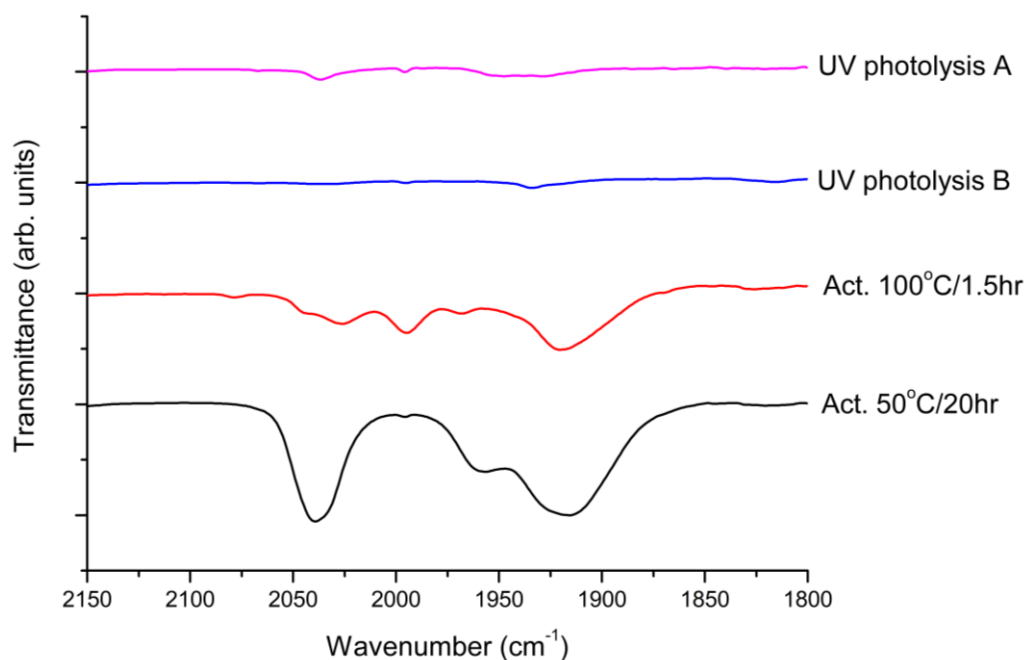


Figure S7.5.3.1. The IR spectrum of the material after activation under dynamic vacuum at 50°C and 100°C, low temperature activation retains the CO ligands of the Mn(I) complex while at 100°C the material undergoes CO loss, producing a more complex spectrum and bleaching the parent tricarbonyl bands. UV photolysis (365 nm) from hexane under vacuum (30 minutes, 100mW 365nm) results in complete CO loss (UV photolysis B) while similar results are observed after 365 nm irradiation under of a sample dried from toluene and irradiated under an Ar atmosphere (CO loss analysed by MS) (UV photolysis A).

7.5.4 Powder X-ray Diffraction Patterns for Metallated Samples of 1

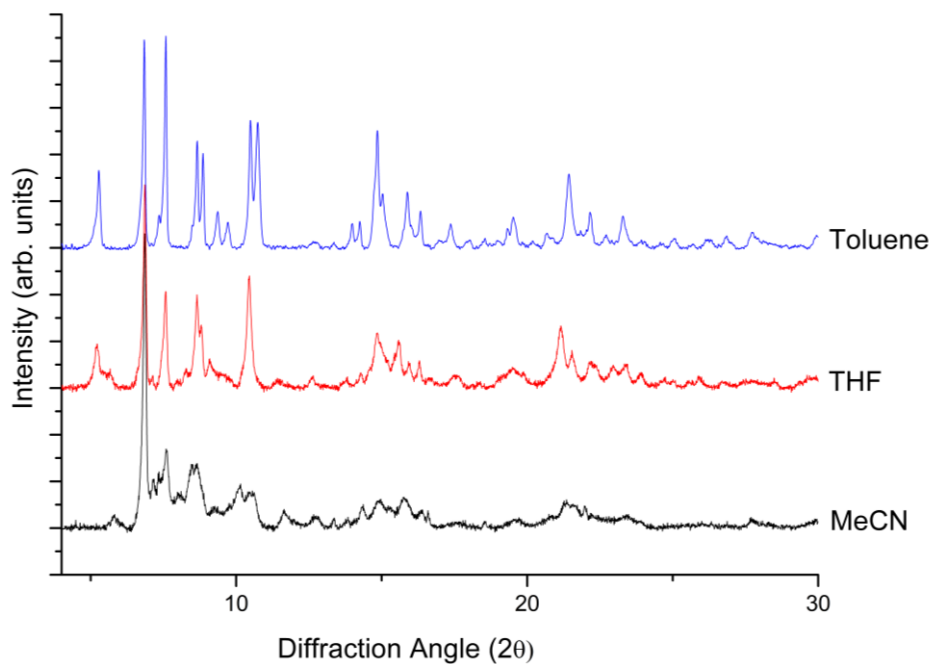


Figure S7.5.4.1. PXRD pattern obtained from samples of $1 \cdot [\text{Mn}(\text{CO})_3\text{Br}]$ following 3 hr of visible photolysis in dry THF, acetonitrile or toluene under constant argon flow.

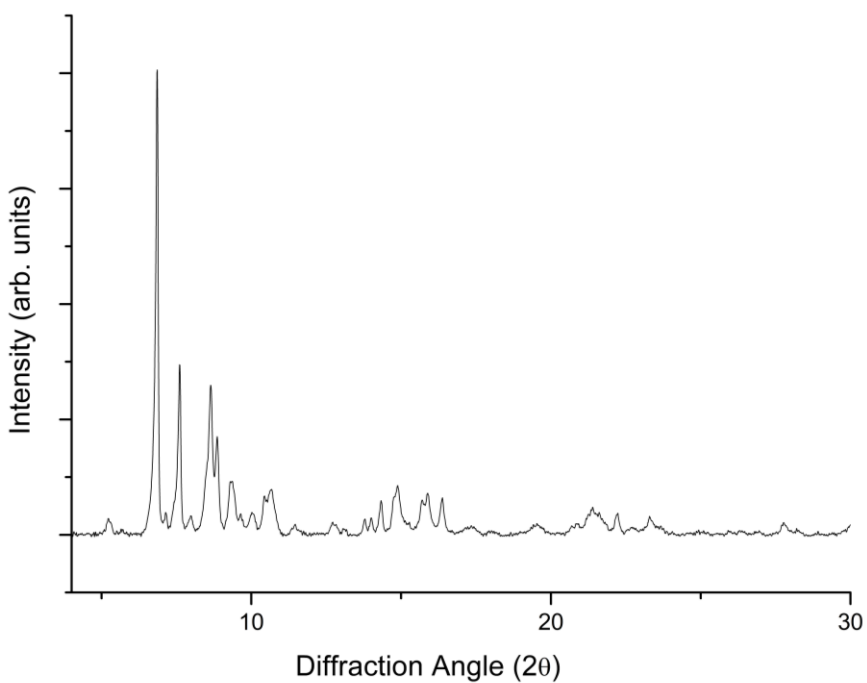


Figure S7.5.4.2. PXRD pattern obtained from a sample of $1 \cdot [\text{Mn}(\text{CO})_3\text{Br}]$ following activation from dry hexane at 50°C for 20 hr under dynamic vacuum.

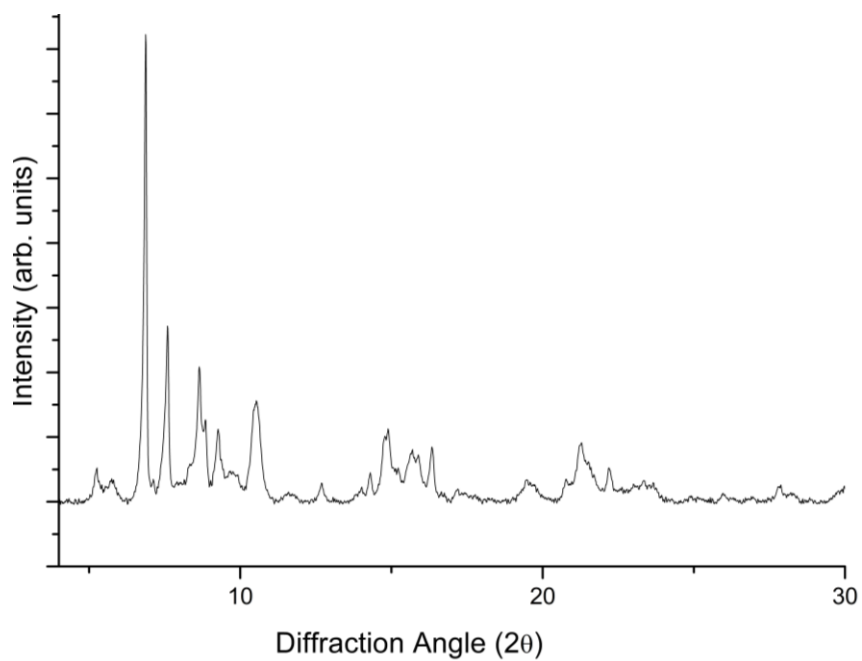


Figure S7.5.4.3. PXRD pattern obtained from a sample of $1 \cdot [\text{Mn}(\text{CO})_3\text{Br}]$ following activation from dry hexane at 50°C for 20 hr under dynamic vacuum and visible photolysis.

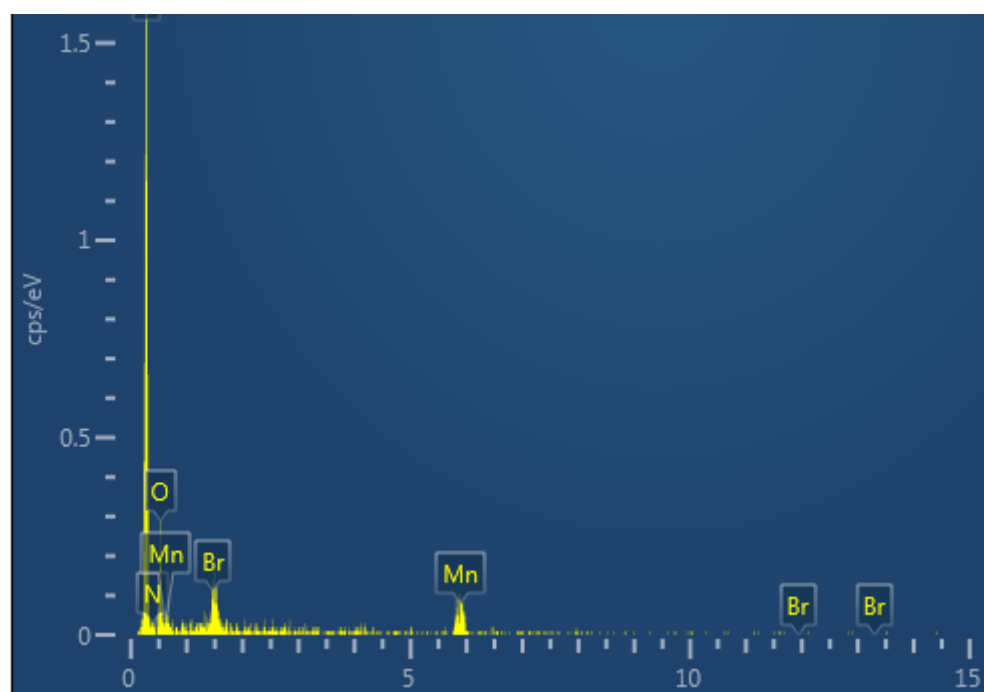
7.5.5. Scanning electron microscopy (SEM) images and energy dispersive X-ray analysis (EDX) of metalated samples of **1****Table S7.5.5.1:** Bromide anion occupancy determined via measurement of the Mn:Br ratio using EDX analysis.

Sample	Bromide occupancy (%) ^{a,b}	Std error (%)
1 ·[Mn(CO) ₃ (H ₂ O)]Br (As synthesised)	98	1.2
1 ·[Mn(CO) ₃ (H ₂ O)]Br (THF)	93	5.4
1 ·[Mn(CO) ₃ Br] (THF, soaked for 24hr after photolysis) ^c	92	5.0
1 ·[Mn(CO) ₃ Br] (MeCN) ^c	107	16
1 ·[Mn(CO) ₃ Br] (Toluene) ^c	101	14

^a Average atomic% obtained from three crystals.

^b Relative to full occupancy of the free chelation sites in **1**.

^c Following visible photolysis for 3 hr

**Figure S7.5.5.1.** Representative raw EDX spectra for **1**·[Mn(CO)₃(H₂O)]Br.

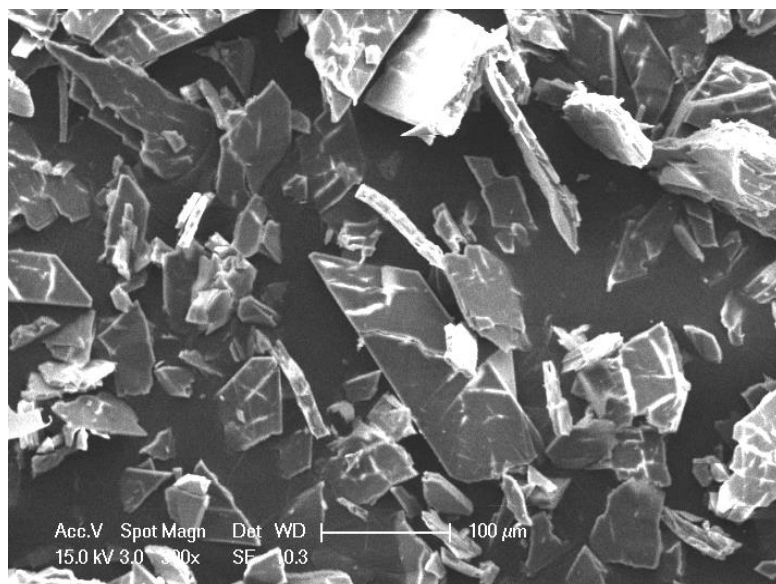


Figure S7.5.5.2. SEM image of a sample of $1 \cdot [\text{Mn}(\text{CO})_3\text{Br}]$ following visible photolysis.

7.5.6 Additional Crystallographic Refinement Details

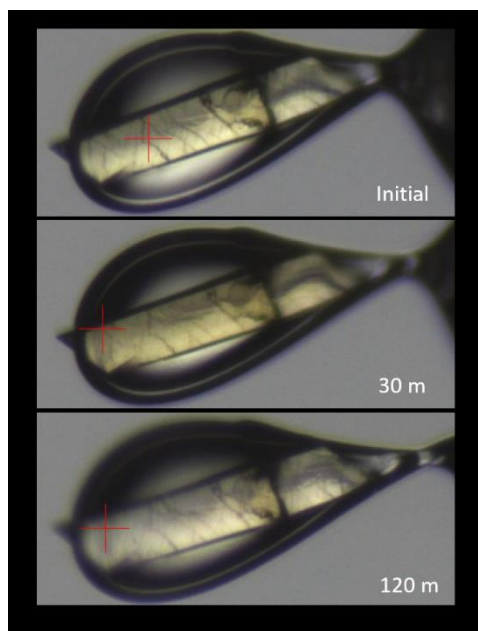


Figure 7.5.6.1: Video microscope images of the single crystal of $1 \cdot [\text{Mn}(\text{CO})_3\text{Br}]$ (THF solvate) used for the photocrystallography experiment described below. The grey background in the image makes colour differentiation difficult, however it is evident that the crystal is initially yellow but becomes colourless after 120 minutes of photolysis.

1·[Mn(CO)₃Br] in THF (initial)

The dataset was solved using SHELXS and refined using SHELXL interfaced through X-Seed. Rotational disorder of a phenyl moiety in the MOF was modelled by initially allowing the occupancy of the two positions (parts 1 and 2) to refine; the occupancy of the two positions was subsequently set at 60% and 40% respectively. Hydrogen atoms were incorporated at calculated positions. In order to subtract the contribution from the disordered solvent (THF; one THF molecule was located and refined), the SQUEEZE routine available in Platon²⁸ was applied to the data, which gave a new HKL file. The number of located electrons was 418, which equates to approximately 6 THF molecules per unit cell and 3 per asymmetric unit. This has been added to the reported formula.

1·[Mn(CO)₃Br] in Toluene

The dataset was solved using SHELXS and refined using SHELXL interfaced through X-Seed. Hydrogen atoms were incorporated at calculated positions. The occupancy of the disordered bromide anion residing in the pore-space was refined to be 16%. A Q-peak of magnitude 4.75 resides close to this bromide and likely corresponds to disordered bromide or solvent. DFIX restraints were used to restrain the Mn-CO bond length to chemically reasonable values. A single ordered toluene molecule was located and refined in the pore-space of the MOF, DFIX restraints were used to restrict the C-C bond lengths to chemically reasonable values. The EADP command was used to restrain the thermal displacement parameters of C86, C85 and C81 in the toluene phenyl ring to be equal to that of the adjacent ring member C82, this corrected the erroneously large thermal displacement parameters of C86, C85 and C81. In order to subtract the contribution from the disordered solvent (toluene; one toluene molecule was located and refined), the SQUEEZE routine available in Platon²⁸ was applied to the data, which gave a new HKL file. The number of located electrons was 346, which equates to approximately 4 toluene molecules per unit cell and 2 per asymmetric unit. This has been added to the reported formula.

1·[Mn(CO)₃Br] in THF (15 minutes of visible photolysis)

The dataset was solved using SHELXS and refined using SHELXL interfaced through X-Seed. Rotational disorder of a phenyl moiety in the ligand frame was modelled by allowing the occupancy of the two positions to refine, the occupancy of the two positions was subsequently set at 76 and 24% respectively. The EADP command was used to restrain the thermal displacement parameters of C26B in the less occupied phenyl ring to be equal to that of the adjacent ring member C25B, this corrected the erroneously large thermal displacement parameters of C26B. The DFIX command was used to enforce chemically reasonable bond lengths in the less occupied phenyl ring. A mixture of CO and THF disordered over the axial coordination site was modelled with isotropic displacement parameters. The site-occupancy of each molecule was allowed to refine and were subsequently fixed at 54 and 46% for the CO and THF respectively. DFIX restraints were used to restrain the Mn-CO bond lengths to chemically reasonable values. DFIX and DANG restraints were used to constrain the coordinated THF molecule to be chemically reasonable. A non-coordinated bromide anion was modeled in the pore-space adjacent to the Mn(I) center, and the occupancy of this site was refined to be 10%. This information, along with EDX data, was used to inform the occupancy of the axially coordinated bromide.

Hydrogen atoms were incorporated at calculated positions. In order to subtract the contribution from the disordered solvent (THF; one THF molecule was located and refined), the SQUEEZE routine available in Platon²⁸ was applied to the data, which gave a new HKL file. The number of located electrons was 250, which equates to approximately 3 THF molecules per unit cell and 1.5 per asymmetric unit. This has been added to the reported formula.

1·[Mn(CO)₃Br] in THF (30 minutes of visible photolysis)

The dataset was solved with SHELXS and refined using SHELXL interfaced through X-Seed. Rotational disorder of a phenyl moiety in the ligand frame was modelled by allowing the occupancy of the two positions to refine, the occupancy of the two positions was subsequently set at 80 and 20% respectively. The DFIX command was used to enforce chemically reasonable bond lengths in the less occupied phenyl ring. A mixture of CO and THF disordered over the axial coordination site was modelled with isotropic displacement parameters. The site-occupancy of each molecule was allowed to refine and were subsequently fixed at 70 and 30% for the CO and THF respectively. DFIX restraints were used to restrain the Mn-CO bond lengths to chemically reasonable values. DFIX and DANG restrains were used to constrain the coordinated THF molecule to be chemically reasonable. A non-coordinated bromide anion was modeled in the pore-space adjacent to the Mn(I) center, and the occupancy of this site was refined to be 10%. This information, along with EDX data, was used to inform the occupancy of the axially coordinated bromide. Hydrogen atoms were incorporated at calculated positions. In order to subtract the contribution from the disordered solvent (THF; one THF molecule was located and refined), the SQUEEZE routine available in Platon²⁸ was applied to the data, which gave a new HKL file. The number of located electrons is 318, which equates to approximately 4 THF molecules per unit cell and 2 per asymmetric unit. This has been added to the reported formula.

1·[Mn(CO)₃Br] in THF (50 minutes of visible photolysis)

The dataset was solved with SHELXS and refined using SHELXL interfaced through X-Seed. Disorder of the Mn(I) coordination sphere was accommodated by modelling two distinct Mn(I) centres, Mn3 and Mn3B. The occupancy of each metal centre was allowed to refine, and subsequently fixed at 60 and 40% for Mn3 and Mn3B respectively. The EADP command was used to constrain the anisotropic displacement parameter of Mn3 to be equal to that of Mn3B. DFIX restraints were used to enforce chemically reasonable bond lengths in the coordination sphere of the Mn(I) complex. A non-coordinated bromide anion was modeled in the pore-space adjacent to the Mn(I) centre, the occupancy of this site was refined to be 20%. This information, along with EDX data, was used to inform the occupancy of the axially disordered bromide, giving Br1 and Br2 occupancies of 30 and 50% respectively. The coordinated THF molecule was modeled with isotropic displacement parameters due to disorder. A CO ligand was modelled in the axial coordination site of Mn3 using DFIX restraints to enforce chemically reasonable bond lengths, and due to disorder in the complex the EADP restraint was used to limit the anisotropic displacement parameters of the CO ligand to equal those of the adjacent O atom. Hydrogen atoms were incorporated at calculated positions. A FLAT command was used to enforce planarity of the phenyl ring appended to the N,N-chelation site (the L'/bridging ligand is disordered but the disorder around the chelating site cannot be modelled). In order to subtract the contribution from the disordered solvent

(THF; one THF molecule was located and refined), the SQUEEZE routine available in Platon²⁸ was applied to the data, which gave a new HKL file. The number of located electrons is 273, which equates to approximately 4 THF molecules per unit cell and 2 per asymmetric unit. This has been added to the reported formula.

1·[Mn(CO)₃Br] in THF (90 minutes of visible photolysis)

The dataset was solved with SHELXS and refined using SHELXL interfaced through X-Seed. Disorder of the Mn(I) coordination sphere was accommodated by modelling two distinct Mn(I) centres, Mn3 and Mn3B. The occupancy of each metal centre was allowed to refine, and subsequently fixed at 40 and 60% respectively for Mn3 and Mn3B. The EADP command was used to constrain the anisotropic displacement parameter of Mn3 to be equal to that of Mn3B. DFIX restraints were used to enforce chemically reasonable bond lengths in the coordinated THF molecule which was modeled with isotropic displacement parameters due to disorder. DFIX restraints were used to enforce chemically reasonable bond lengths in the coordination sphere of the Mn(I) complex. A non-coordinated bromide anion was modeled in the pore-space adjacent to the Mn(I) center, the occupancy of this site was refined to be 20%. This information, in conjunction with EDX data, was used to inform the occupancy of the axially disordered bromide, giving Br1 and Br2 occupancies of 50 and 30% respectively. Hydrogen atoms were incorporated at calculated positions. A FLAT command was used to enforce planarity of the phenyl ring appended to the N,N-chelation site (the L'/bridging ligand is disordered but the disorder around the chelating site cannot be modelled). In order to subtract the contribution from the disordered solvent (THF; one THF molecule was located and refined), the SQUEEZE routine available in Platon²⁸ was applied to the data, which gave a new HKL file. The number of located electrons is 293, which equates to approximately 4 THF molecules per unit cell and 2 per asymmetric unit. This has been added to the reported formula.

1·[Mn(CO)₃Br] in THF (120 minutes of visible photolysis)

The dataset was solved with SHELXS and refined using SHELXL interfaced through X-Seed. Disorder of the Mn(I) coordination sphere was accommodated by modelling two distinct Mn(I) centres, Mn3 and Mn3B. The occupancy of each metal centre was allowed to refine, and subsequently fixed at 36 and 64% respectively for Mn3 and Mn3B. The EADP command was used to constrain the anisotropic displacement parameter of Mn3 to be equal to that of Mn3B. DFIX restraints were used to enforce chemically reasonable bond lengths in the coordinated THF molecule which was modeled with isotropic displacement parameters due to disorder. DFIX restraints were used to enforce chemically reasonable bond lengths in the coordination sphere of the Mn(I) complex. A non-coordinated bromide anion was modeled in the pore-space adjacent to the Mn(I) center, the occupancy of this site was refined to be 20%. This information, along with EDX data, was used to inform the occupancy of the axially disordered bromide in conjunction with the occupancy of the respective Mn(I) centres, giving Br1 and Br2 occupancies of 54 and 26% respectively. Hydrogen atoms were incorporated at calculated positions. A FLAT command was used to enforce planarity of the phenyl ring appended to the N,N-chelation site site (the L'/bridging ligand is disordered but the disorder around the chelating site cannot be modelled). In order to subtract the contribution from the disordered solvent (THF; one THF molecule was located and refined), the SQUEEZE routine available in Platon²⁸ was applied to the data, which gave a new HKL file.

The number of located electrons is 301, which equates to approximately 4 THF molecules per unit cell and 2 per asymmetric unit. This has been added to the reported formula.

7.5.7. Crystallographic Tables

Table S7.5.7.1. Crystallographic data collection and refinement parameters for the metalated forms of **1**.

Sample	1·[Mn(CO) ₃ Br] (THF)	THF (15m)	THF (30m)
Crystallographic Parameter			
Formula	C _{21.5} H _{19.9} N ₃ O _{4.25} Mn ₁ Br _{0.25}	C _{22.19} H _{22.34} Br _{0.25} Mn ₁ Br _{0.25}	C _{21.95} H _{21.7} N ₃ O _{4.25} Mn ₁ Br _{0.25}
FW	463.22	473.97	470.44
T,K	100	150	150
Wavelength, Å	Synchrotron (λ = 0.7108)	Synchrotron (λ = 0.7108)	Synchrotron (λ = 0.7108)
Crystal system, space group	Monoclinic, <i>P2₁/m</i>	Monoclinic, <i>P2₁/m</i>	Monoclinic, <i>P2₁/m</i>
Z	8	8	8
a, Å	12.337(3)	12.338(3)	12.344(3)
b, Å	32.664(7)	32.742(7)	32.785(7)
c, Å	12.964(3)	13.000(3)	12.996(3)
α°	90	90	90
β, °	93.65(3)	93.80(3)	93.93(3)
γ°	90	90	90
V, Å ³	5213.6(18)	5240.1(18)	5247.1(18)
<i>d</i> _{calc} , g/cm ³	1.180	1.200	1.191
Absorption coefficient, mm ⁻¹	0.917	0.913	0.912
<i>F</i> (000)	1901.0	1954	1937.0
Crystal size, mm ³	0.22x0.03x0.01	0.37x0.07x0.01	0.22x0.03x0.01
Theta range for data collection	2.494 to 55	2.484 to 55	2.484 to 55
Index range	-16 ≤ <i>h</i> ≤ 16, -42 ≤ <i>k</i> ≤ 42, -16 ≤ <i>l</i> ≤ 16	-15 ≤ <i>h</i> ≤ 15, -42 ≤ <i>k</i> ≤ 42, -16 ≤ <i>l</i> ≤ 16	-15 ≤ <i>h</i> ≤ 15, -42 ≤ <i>k</i> ≤ 42, -16 ≤ <i>l</i> ≤ 16
Reflections collected	78012	77983	78463
Independent reflections	12117 [R _{int} = 0.0538, R _{sigma} = 0.0335]	11187 [R _{int} = 0.0551, R _{sigma} = 0.0321]	12094 [R _{int} = 0.0533, R _{sigma} = 0.0340]
Data/restraints/parameters	12117/0/594	11187/19/604	12094/20/609
GOF on F ²	1.746	1.725	1.541
Largest diff. peak and hole, e·Å ⁻³	1.04/-4.54	4.70/-1.860	1.19/-2.42
R ₁ , [I > 2σ(I)]	0.1352	0.1352	0.1265
wR ₂ ^a , all data	0.4183	0.4197	0.3890

$$^a R_1 = \frac{\sum ||F_o| - |F_c||}{\sum |F_o|}, wR_2 = \frac{721}{2}$$

Table S7.5.7.2. Crystallographic data collection and refinement parameters for the metalated forms of **1**.

Sample	THF (50m)	THF (90m)	THF (120m)
Crystallographic Parameter			
Formula	C _{22.90} H _{24.50} Br _{0.25} Mn ₁ N ₃ O _{4.15}	C _{22.75} H _{24.5} N ₃ O ₄ MnBr _{0.25}	C _{22.75} H _{24.50} Br _{0.25} Mn ₁ N ₃ O ₄
FW	483.07	478.87	478.87
T, K	150	100	150
Wavelength, Å	Synchrotron (λ = 0.7108)	Synchrotron (λ = 0.7108)	Synchrotron (λ = 0.7108)
Crystal system, space group	Monoclinic, <i>P</i> ₂ ₁ / <i>m</i>	Monoclinic, <i>P</i> ₂ ₁ / <i>m</i>	Monoclinic, <i>P</i> ₂ ₁ / <i>m</i>
Z	8	8	8
a, Å	12.338(3)	12.319(3)	12.3330(3)
b, Å	32.702(7)	32.505(7)	32.5900(7)
c, Å	13.010(3)	13.008(3)	13.0190(3)
α°	90	90	90
β, °	93.82(3)	93.58(3)	93.60(3)
γ°	90	90	90
V, Å ³	5237.6(18)	5198.6(18)	5222.4(18)
<i>d</i> _{calc} , g/cm ³	1.225	1.215	1.215
Absorption coefficient, mm ⁻¹	0.915	0.914	0.914
<i>F</i> (000)	1999	1982.0	1982
Crystal size, mm ³	0.22x0.03x0.01	0.22x0.03x0.01	0.22x0.03x0.01
Theta range for data collection	2.49 to 55	2.49 to 55	2.49 to 55
Index range	-15 ≤ <i>h</i> ≤ 15, -42 ≤ <i>k</i> ≤ 42, -16 ≤ <i>l</i> ≤ 16	-16 ≤ <i>h</i> ≤ 16, -42 ≤ <i>k</i> ≤ 42, -16 ≤ <i>l</i> ≤ 16	-16 ≤ <i>h</i> ≤ 16, -42 ≤ <i>k</i> ≤ 42, -16 ≤ <i>l</i> ≤ 16
Reflections collected	78508	78067	78288
Independent reflections	12079 [R _{int} = 0.0480, R _{sigma} = 0.0303]	12160 [R _{int} = 0.0479, R _{sigma} = 0.0304]	12164 [R _{int} = 0.0498, R _{sigma} = 0.0318]
Data/restraints/parameters	12079/27/568	12160/24/561	12164/24/561
GOF on F ²	1.444	1.530	1.509
Largest diff. peak and hole, e·Å ⁻³	2.181/-2.185	2.10/-2.41	2.181/-2.185
R ₁ , [I > 2σ(I)]	0.1173	0.1242	0.1232
wR ₂ ^a , all data	0.3627	0.3817	0.3803

$${}^a R_1 = \sum ||F_o| - |F_c|| / \sum |F_o|, wR_2 = {}^{721/2}$$

Table S7.5.7.3. Crystallographic data collection and refinement parameters for the metalated forms of **1**.

Sample	1-[Mn(CO)₃Br] (toluene)
Crystallographic Parameter	
Formula	C _{22.75} H _{20.50} Br _{0.25} Mn ₁ N ₃ O _{3.50}
FW	466.84
T, K	100
Wavelength, Å	Synchrotron ($\lambda = 0.7108$)
Crystal system, space group	Monoclinic, <i>P</i> 2 ₁ / <i>m</i>
Z	8
a, Å	12.419(3)
b, Å	32.994(7)
c, Å	12.986(3)
α , °	90
β , °	94.89(3)
γ , °	90
V, Å ³	5301.6(19)
d_{calc} , g/cm ³	1.170
Absorption coefficient, mm ⁻¹	0.900
F(000)	1918
Crystal size, mm ³	0.3x0.05x0.01
Theta range for data collection	1.234 to 27.499
Index range	-16 ≤ h ≤ 16, -42 ≤ k ≤ 42, -16 ≤ l ≤ 16
Reflections collected	85753
Independent reflections	12332 [$R_{\text{int}} = 0.0427$, $R_{\text{sigma}} = 0.0257$]
Data/restraints/parameters	12332/6/564
GOF on F ²	1.040
Largest diff. peak and hole, e-Å ⁻³	10.55/-4.597
R_1 , [$I > 2\sigma(I)$]	0.0815
wR ₂ ^a , all data	0.2414

$$^a R_1 = \frac{\sum ||F_o| - |F_c||}{\sum |F_o|}, wR_2 = \sqrt{\frac{\sum w(F_o - F_c)^2}{\sum w F_o^2}}$$

7.5.8. Thermal Ellipsoid Plots of all structures at the 50% probability level

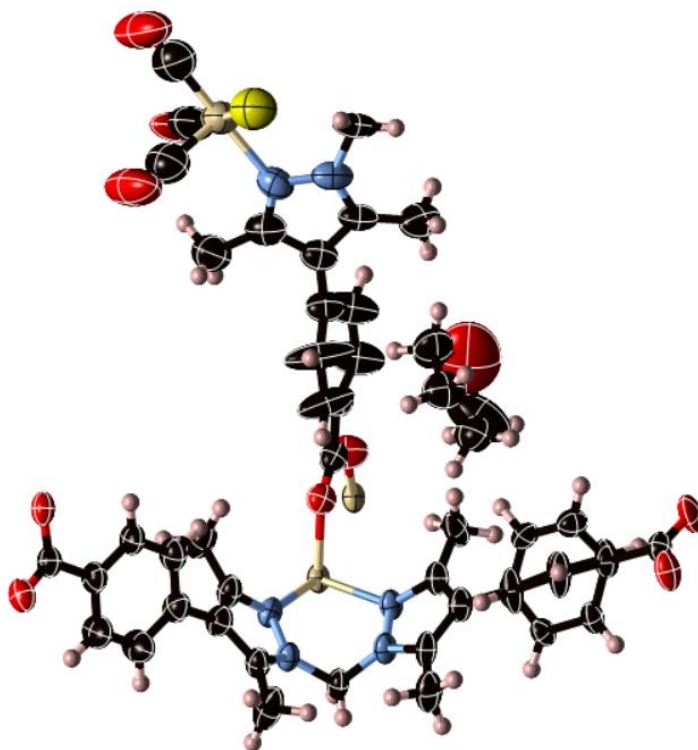


Figure S7.5.8.1: The asymmetric unit of **1**·[Mn(CO)₃Br] with all non-hydrogen atoms represented by ellipsoids at the 50% probability level (C, black; H, white; N, aqua; O, red; Mn, beige; Br, yellow).

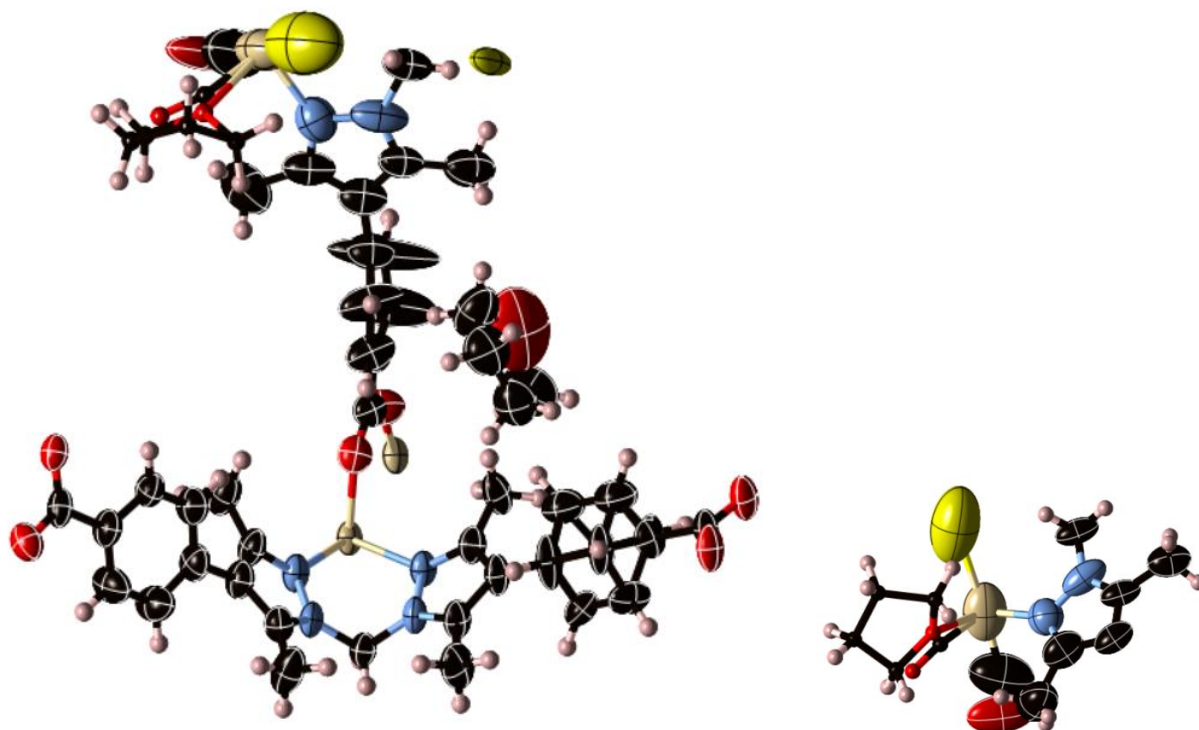


Figure S7.5.8.2: The asymmetric unit of $1 \cdot [\text{Mn}(\text{CO})_3\text{Br}]$ after 15 minutes of photolysis in THF. All non-hydrogen atoms are represented by ellipsoids at the 50% probability level (C, black; H, white; N, aqua; O, red; Mn, beige; Br, yellow).

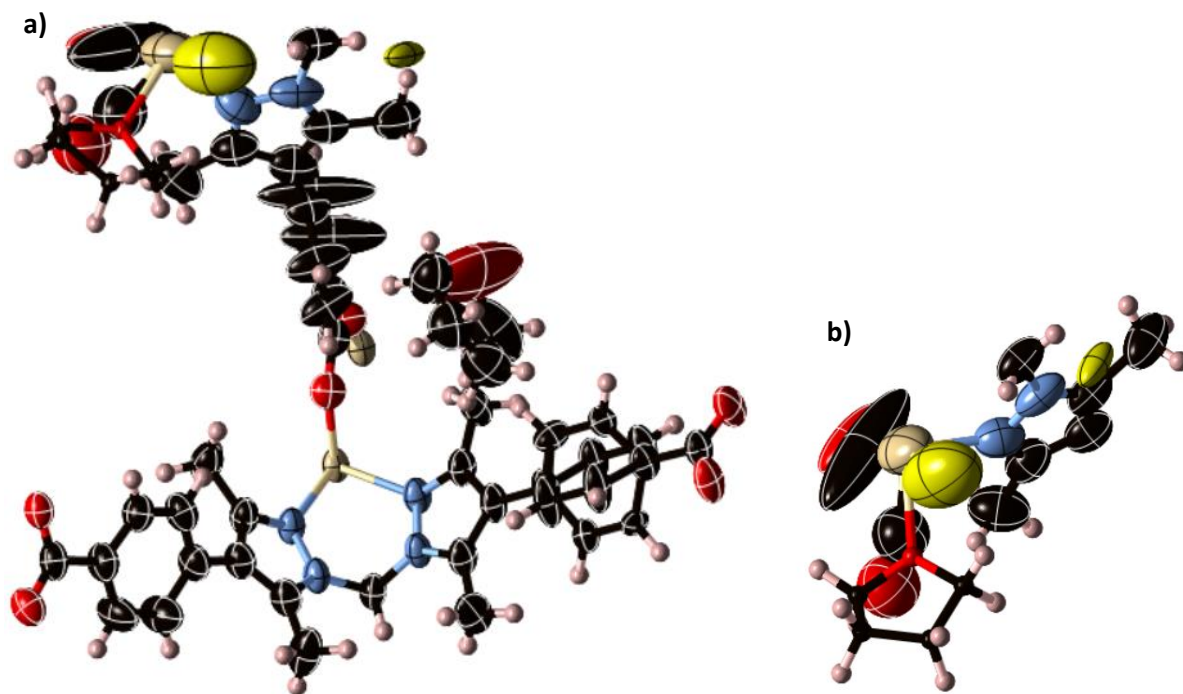


Figure 7.5.8.3: a) The asymmetric unit of unit of $1 \cdot [\text{Mn}(\text{CO})_3\text{Br}]$ after 30 minutes of photolysis in THF. All non-hydrogen atoms are represented by ellipsoids at the 50% probability level (C, black; H, white; N, aqua; O, red; Mn, beige; Br, yellow) b) perspective view of the Mn(I) coordination sphere represented by thermal ellipsoids at the 50% probability level.

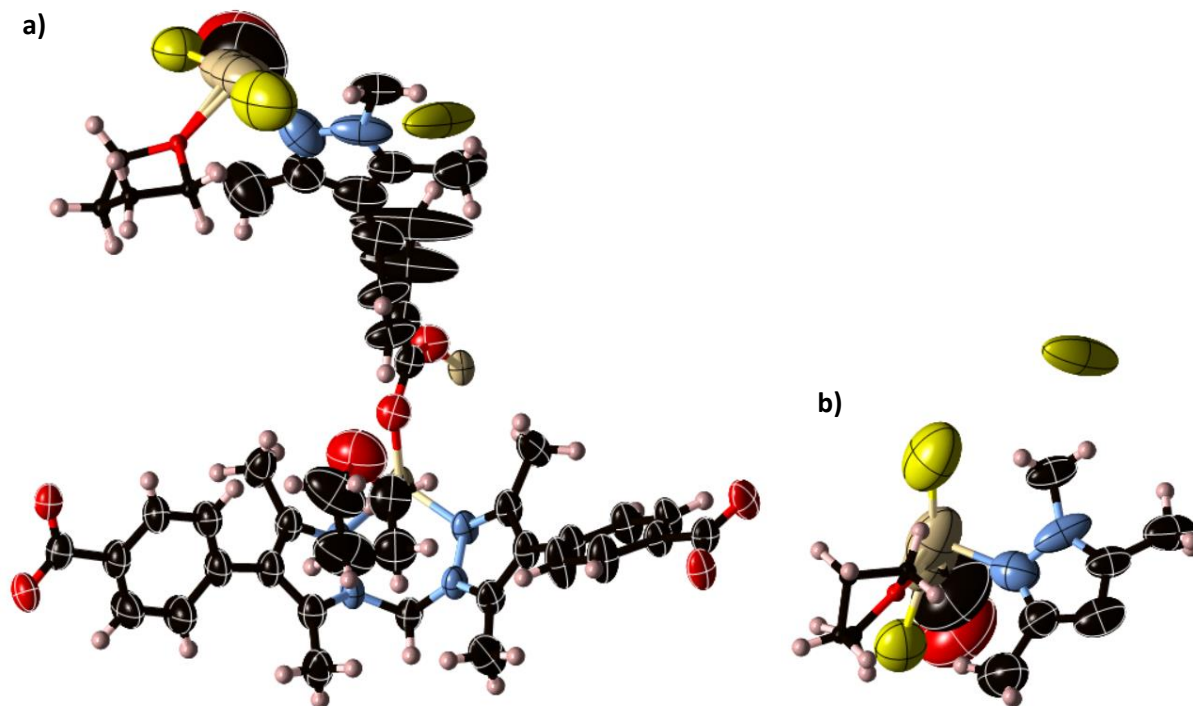


Figure 7.8.5.4: a) The asymmetric unit of unit of $1 \cdot [\text{Mn}(\text{CO})_3\text{Br}]$ after 50 minutes of photolysis in THF. All non-hydrogen atoms are represented by ellipsoids at the 50% probability level (C, black; H, white; N, aqua; O, red; Mn, beige; Br, yellow) b) perspective view of the Mn(I) coordination sphere represented by thermal ellipsoids at the 50% probability level.

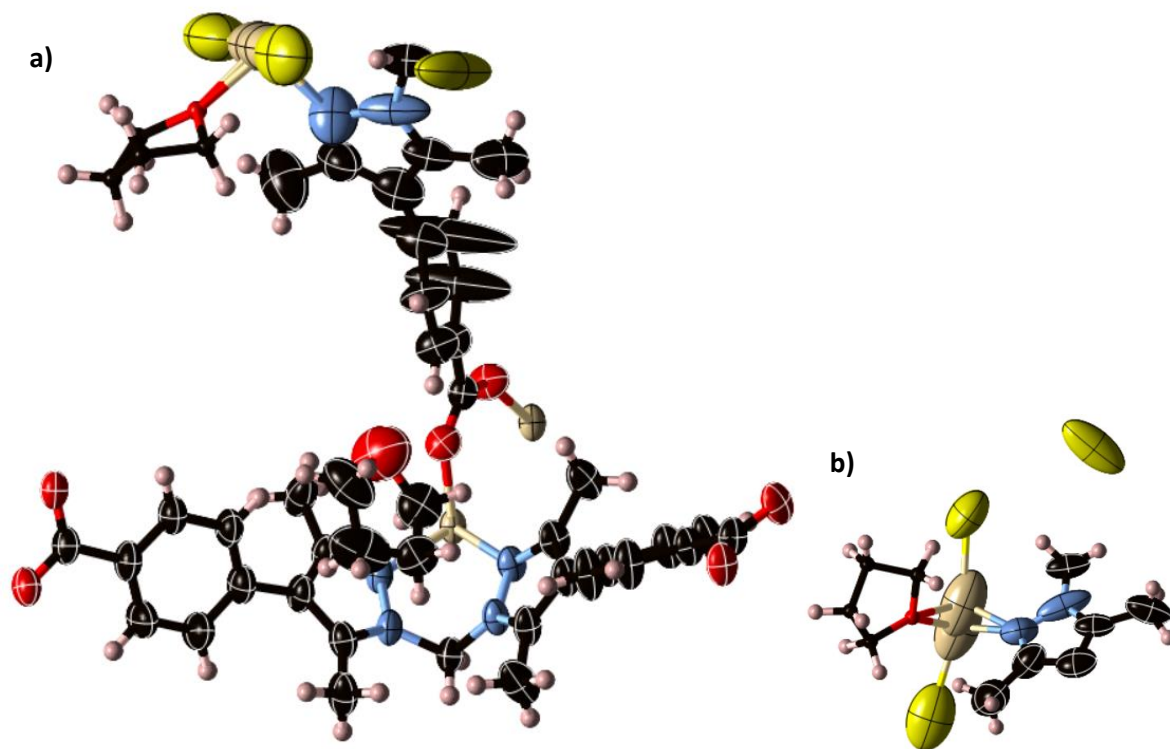


Figure 7.5.8.5: **a)** The asymmetric unit of unit of $1 \cdot [\text{Mn}(\text{CO})_3\text{Br}]$ after 90 minutes of photolysis in THF. All non-hydrogen atoms are represented by ellipsoids at the 50% probability level (C, black; H, white; N, aqua; O, red; Mn, beige; Br, yellow) **b)** perspective view of the Mn(I) coordination sphere represented by thermal ellipsoids at the 50% probability level.

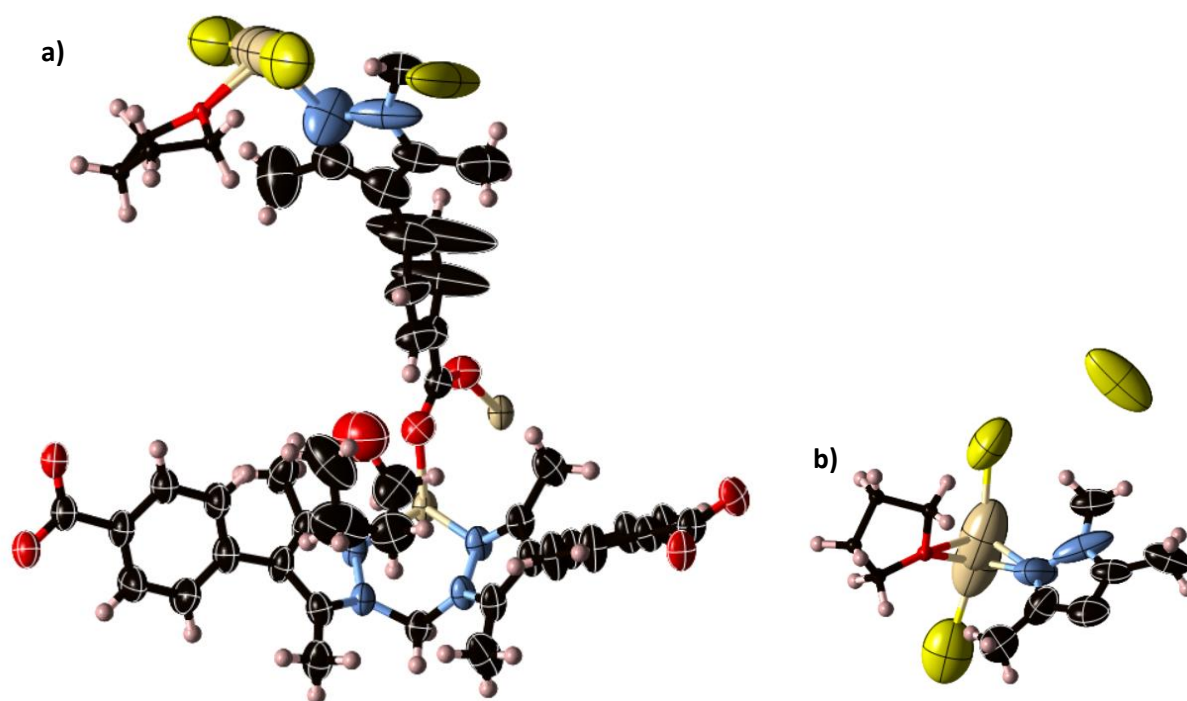


Figure 7.5.8.6: **a)** The asymmetric unit of unit of $1 \cdot [\text{Mn}(\text{CO})_3\text{Br}]$ after 120 minutes of photolysis in THF. All non-hydrogen atoms are represented by ellipsoids at the 50% probability level (C, black; H, white; N, aqua; O, red; Mn, beige; Br, yellow) **b)** perspective view of the Mn(I) coordination sphere represented by thermal ellipsoids at the 50% probability level.

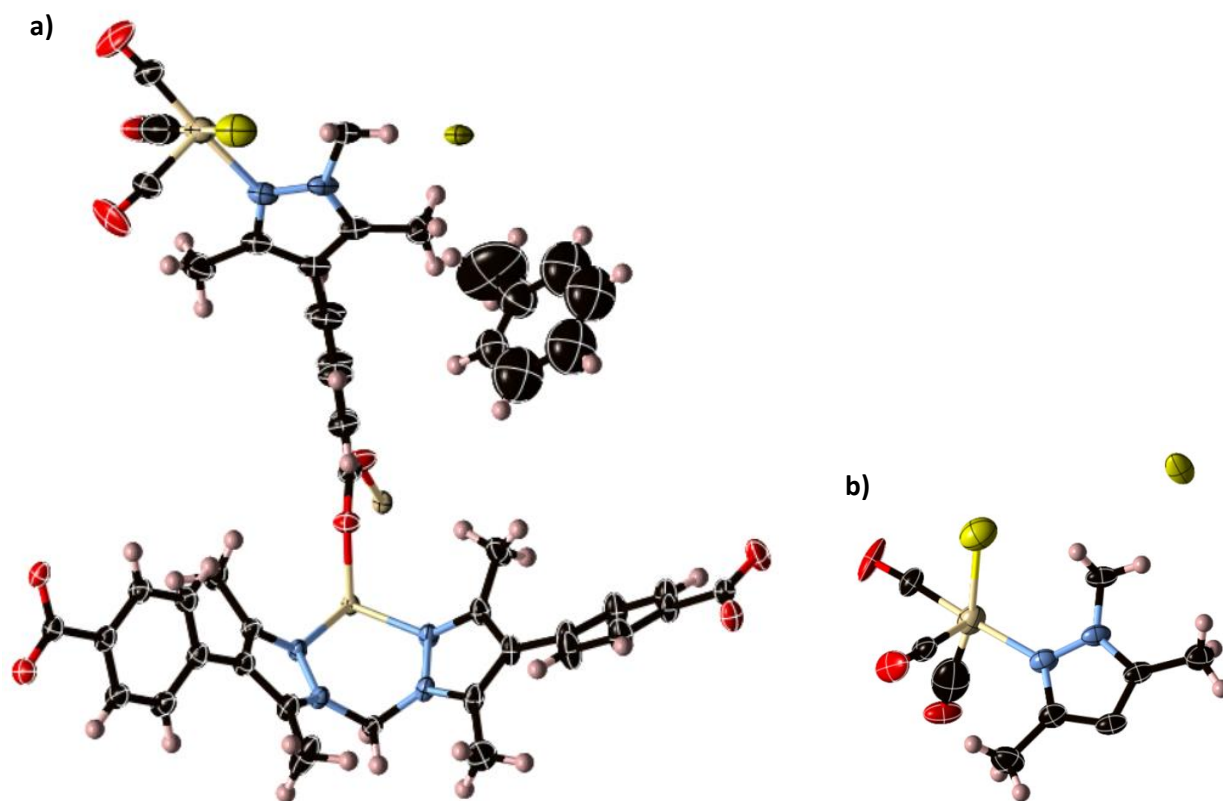


Figure 7.5.8.7: **a)** The asymmetric unit of $1 \cdot [\text{Mn}(\text{CO})_3\text{Br}]$ obtained from toluene with all non-hydrogen atoms represented by ellipsoids at the 50% probability level (C, black; H, white; N, aqua; O, red; Mn, beige; Br, yellow) **b)** perspective view of the Mn(I) coordination sphere represented by thermal ellipsoids at the 50% probability level.

7.5.9. Thermogravimetric Analysis

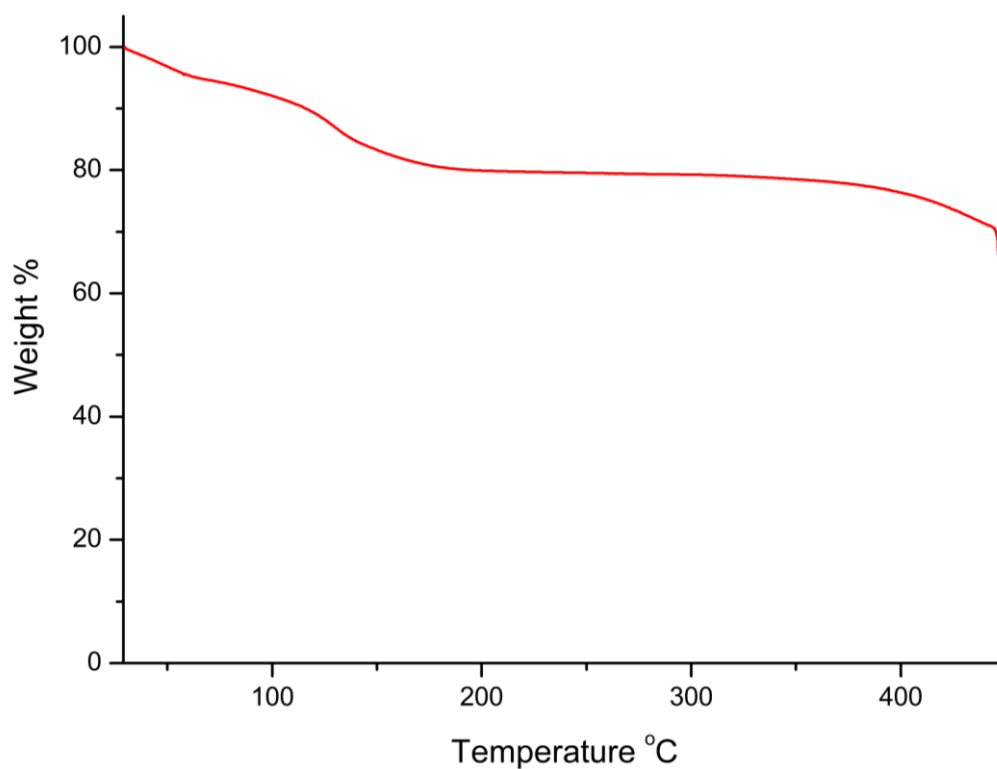


Figure S7.5.9.1. TGA of $1 \cdot [\text{Mn}(\text{CO})_3\text{Br}]$ sample following solvent exchange with dry hexane. The sample loses 20% of its starting weight by 200°C which corresponds to loss of solvent (hexane) as well as removal of CO from the Mn(I) complex. The expected mass loss associated with removal of three CO ligands is 4.9%. Considering that substantial CO loss is observed upon heating at 100°C (see text and Figure 7.5.3.1), the mass loss observed up to 200°C likely corresponds to the thermolysis of CO from the material. Thus, the observed mass loss of 20% is attributed to the removal of both hexane and CO from the material.

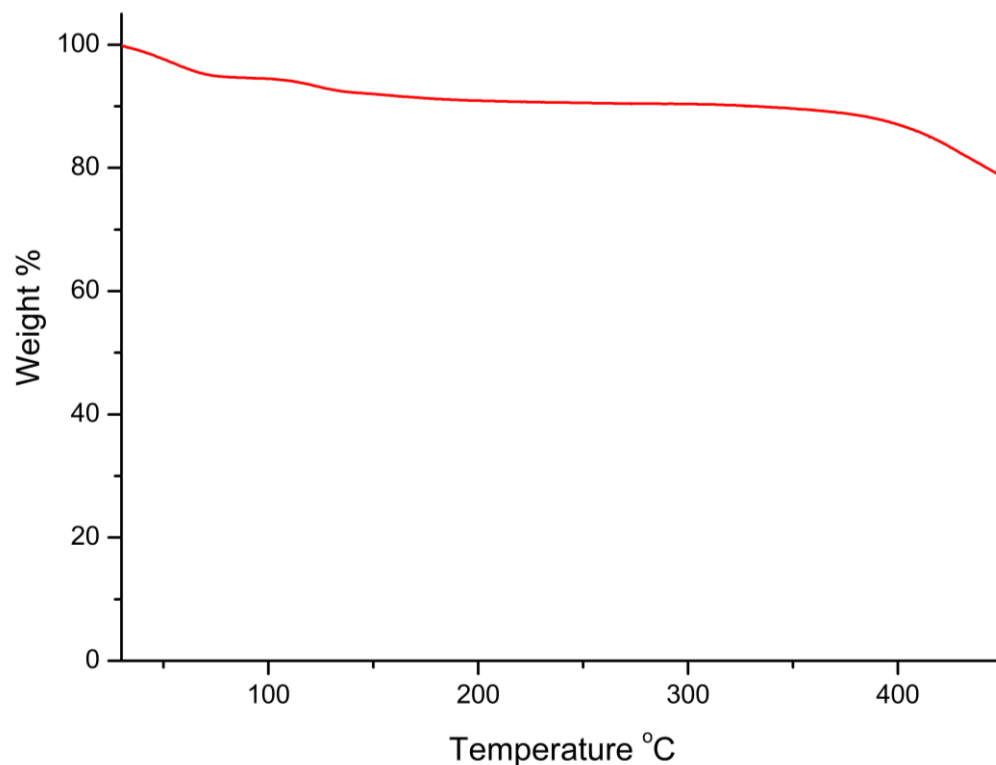


Figure S7.5.9.2. TGA of $1 \cdot [\text{Mn}(\text{CO})_3\text{Br}]$ sample following activation from dry hexane on an ASAP 2020 instrument at 50°C for 20hr under dynamic vacuum. The sample loses approx. 5.25% of its mass between 30 and 80°C which is attributed to the loss of adventitious moisture absorbed by the sample during preparation for TGA analysis. Between 80 - 200°C the TGA trace displays a step in which the sample loses a further 3.6% of its mass which corresponds well with the expected mass loss upon thermolysis of three CO ligands (4.9%) (it is likely possible that CO loss occurs below 80°C). This result confirms that the sample is activated using the activation conditions described, and that CO can be released by thermolysis above 80°C .

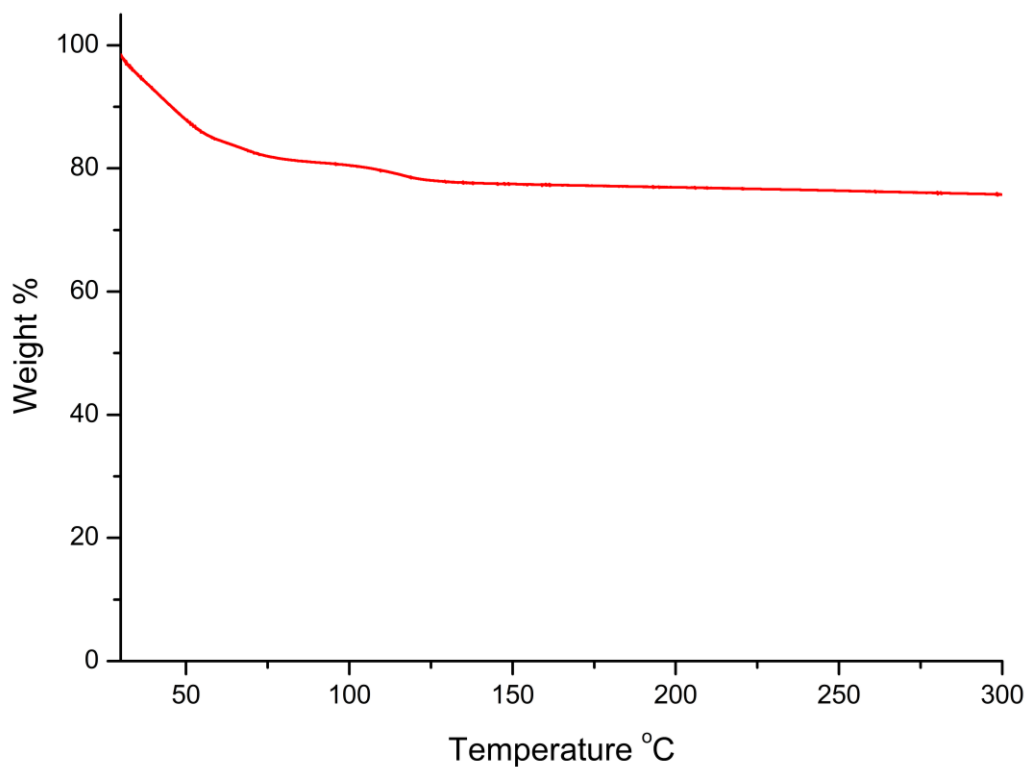


Figure S7.5.9.3. TGA of $1\cdot[\text{Mn}(\text{CO})_3\text{Br}]$ sample following solvent exchange with methanol. The sample loses approximately 23% of its starting weight by 200°C which corresponds to loss of solvent (methanol) as well as removal of CO from the Mn(I) complex. The expected mass loss associated with removal of three CO ligands is 4.9%. Considering that substantial CO loss is observed via IR upon heating at 100°C (see text), the mass loss 'step' observed up to between 80-150°C likely corresponds to the thermolysis of CO from the material and corresponds to a 4.05% loss in mass. Thus, the overall mass loss of 23% is attributed to the removal of both methanol and CO from the material.

7.5.10. Isotherms

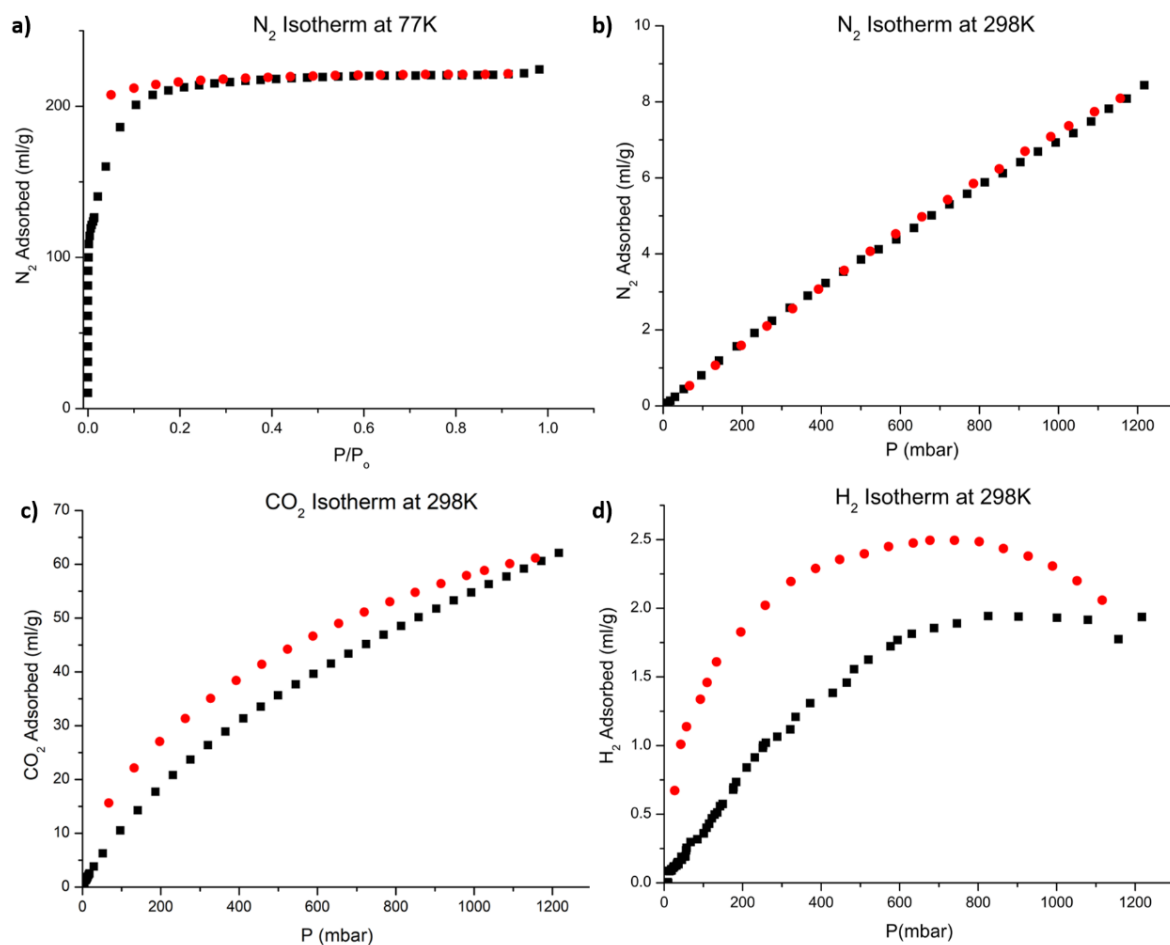


Figure S7.5.10.1 Isotherms collected in samples of $1 \cdot [\text{Mn}(\text{CO})_3\text{Br}]$ following activation from distilled hexane at $50^\circ\text{C}/20\text{hr}$ under vacuum **(a)** and following subsequent visible photolysis under vacuum **(b,c,d)** with no evidence of interaction between coordinatively unsaturated metal centres and N₂, CO₂ or H₂. Although an interaction between H₂ and coordinatively unsaturated Mn(I) centres during isotherm analysis would be expected to result in a significant hysteresis, the behaviour observed in the desorption phase of the H₂ isotherm **(d)** is likely an artefact from the extremely low uptake observed at room temperature. Black squares represent adsorption, red circles represent desorption.

7.5.11 References

- (1) Stor, G. J.; Morrison, S. L.; Stufkens, D. J.; Oskam, A. *Organometallics* **1994**, *13*, 2641.
- (2) Yempally, V.; Moncho, S.; Hasanayn, F.; Fan, W. Y.; Brothers, E. N.; Bengali, A. A. *Inorg. Chem.* **2017**, *56*, 11244.
- (3) Yempally, V.; Kyran, S. J.; Raju, R. K.; Fan, W. Y.; Brothers, E. N.; Darensbourg, D. J.; Bengali, A. A. *Inorg. Chem.* **2014**, *53*, 4081.
- (4) Hallett, A. J.; Angharad Baber, R.; Guy Orpen, A.; Ward, B. D. *Dalt. Trans.* **2011**, *40*, 9276.
- (5) Anderson, W. P.; Brill, T. B.; Schoenberg, A. R.; Stanger, C. W. *J. Organomet. Chem.* **1972**, *44*, 161.
- (6) Swennenhuis, B. H. G.; Poland, R.; DeYonker, N. J.; Webster, C. E.; Darensbourg, D. J.; Bengali, A. A. *Organometallics* **2011**, *30*, 3054.
- (7) Barbeau, C. *Canadian Journal of Chemistry* **1967**, *45*, 161.
- (8) Strohmeier, W.; Hellmann, H. *Chemische Berichte* **1965**, *98*, 1598.
- (9) Giordano, P. J.; Wrighton, M. S. *Inorg. Chem.* **1977**, *16*, 160.
- (10) Paulson, P. L.; Segal, J. A. *J.C.S Dalton* **1975**, 2387-2392.
- (11) Bengali, A. A.; Fan, W. Y.; Abdulrazak, K. T. *Organometallics* **2009**, *28*, 3123.
- (12) Kee, J. W.; Fan, W. Y. *J. Organomet. Chem.* **2013**, *729*, 14.
- (13) Crocock, B.; Long, C. *Acta Cryst. C* **1991**, *C48*, 1004.
- (14) Sellmann, D. *Angew. Chem., Int. Ed. Engl.* **1971**, *10*, 919.
- (15) Schoenberg, A. R.; Anderson, W. P. *Inorg. Chem.* **1972**, *11*, 85.
- (16) Nesmeyanov, A. N.; Aleksandrov, G. G.; Antonova, A. B.; Anisimov, K. N.; Kolobova, N. E.; Struchkov, Y., T. *J. Organomet. Chem.* **1976**, *110*, C36.
- (17) Alt, H. G.; Engelhardt, H. E. *J. Organomet. Chem.* **1988**, *342*, 235.
- (18) Strohmeier, W.; Guttenberger, J. F. *Chemische Berichte* **1964**, *97*, 1871.
- (19) Treichel, P. M.; Mueh, H. J. *Inorganica Chimica Acta* **1977**, *22*, 265.
- (20) Sorensen, A. A.; Yang, G. K. *J. Am. Chem. Soc.* **1991**, *113*, 7061.
- (21) Sandhu, S. S.; Mehta, A. K. *Inorg. Nucl. Chem. Letters* **1971**, *7*, 891.
- (22) Kruck, T.; Krause, V. *Naturforsch.*, **1972**, *27B*, 302.
- (23) Batool, M.; Martin, T. A.; Algarra, A. G.; George, M. W.; Macgregor, S. A.; Mahon, M. F.; Whittlesey, M. K. *Organometallics* **2012**, *31*, 4971.
- (24) King, R. B.; Raghuveer, K. S. *Inorg. Chem.* **1984**, *23*, 2482.

- (25) Huxley, M. T.; Burgun, A.; Ghodrati, H.; Coghlan, C. J.; Lemieux, A.; Champness, N. R.; Huang, D. M.; Doonan, C. J.; Sumbly, C. J. *J. Am. Chem. Soc.* **2018**, *140*, 6416.
- (26) McPhillips, T.; McPhillips, S.; Chiu, H.; Cohen, A. E.; Deacon, A. M.; Ellis, P. J.; Garman, E.; Gonzalez, A.; Sauter, N. K.; Phizackerley, R. P., *et al.* *J. Synchrotron Rad.* **2002**, *9*, 401.
- (27) Sheldrick, G. M. *Acta Crystallogr. C Struct. Chem.* **2015**, *71*, 3.
- (28) Spek, A. L. *Acta Crystallogr C Struct Chem* **2015**, *71*.

7.6. Supplementary Computational Details for Chapter 5

Density functional theory (DFT) calculations were carried out with the Gaussian 16 (Revision B.01) software package,¹ following the same methodology employed in our previous work,^{2,3} which has been shown previously to give excellent accuracy for organometallic complexes and MOFs. Calculations were carried out on a simplified model of the Mn MOF, comprising only atoms in close proximity to the Mn center. Geometries of gas-phase minimum energy structures were optimized using the M11-L meta hybrid functional,^{4,5} SDD effective core potential and basis set^{6,7} for Rh and Br atoms, and 6-31G(d,p) basis set⁸⁻¹⁰ for all other atoms, using the experimental X-ray crystal structure as the starting geometry. Vibrational frequencies were calculated for the optimized geometries at the M11-L/6-31G(d,p)+SDD level, with the mass of the hydrogen atoms at the positions where the complex would be connected to the rest of the framework set to a really high value (9999 amu to simulate attachment of the complex to a rigid extended structure).

7.6.2 References

- (1) M. J. Frisch, G. W. Trucks, H. B. Schlegel, G. E. Scuseria, M. A. Robb, J. R. Cheeseman, G. Scalmani, V. Barone, G. A. Petersson, H. Nakatsuji, X. Li, M. Caricato, A. V. Marenich, J. Bloino, B. G. Janesko, R. Gomperts, B. Mennucci, H. P. Hratchian, J. V. Ortiz, A. F. Izmaylov, J. L. Sonnenberg, D. Williams-Young, F. Ding, F. Lipparini, F. Egidi, J. Goings, B. Peng, A. Petrone, T. Henderson, D. Ranasinghe, V. G. Zakrzewski, J. Gao, N. Rega, G. Zheng, W. Liang, M. Hada, M. Ehara, K. Toyota, R. Fukuda, J. Hasegawa, M. Ishida, T. Nakajima, Y. Honda, O. Kitao, H. Nakai, T. Vreven, K. Throssell, J. A. Montgomery, Jr., J. E. Peralta, F. Ogliaro, M. J. Bearpark, J. J. Heyd, E. N. Brothers, K. N. Kudin, V. N. Staroverov, T. A. Keith, R. Kobayashi, J. Normand, K. Raghavachari, A. P. Rendell, J. C. Burant, S. S. Iyengar, J. Tomasi, M.

- Cossi, J. M. Millam, M. Klene, C. Adamo, R. Cammi, J. W. Ochterski, R. L. Martin, K. Morokuma, O. Farkas, J. B. Foresman, and D. J. Fox, Gaussian, Inc., Wallingford CT, 2016.
- (2) W. M. Bloch, A. Burgun, C. J. Coghlan, R. Lee, M. L. Coote, C. J. Doonan, C. J. Sumbly, *Nat. Chem.* 2014, 6, 906-912
- (3) Burgun, A.; Coghlan, C. J.; Huang, D. M.; Chen, W.; Horike, S.; Kitagawa, S.; Alvino, J. F.; Metha, G. F.; Sumbly, C. J.; Doonan, C. J. *Angew. Chem., Int. Ed.* 2017, 56, 8412
- (4) R. Peverati, D.G. Truhlar, *J. Phys. Chem. Lett.* 2012, 3, 117-124.
- (5) 11. K. Lee et al., *J. Am. Chem. Soc.* 2013, 136, 698-704.
- (6) D. Andrae, U. Haeussermann, M. Dolg, H. Stoll, H. Preuss, *Theor. Chim. Acta* 1990, 77, 123-141.
- (7) M. Dolg, U. Wedig, H. Stoll, H. Preuss, *J. Chem. Phys.* 1987, 86, 866-872.
- (8) R. Ditchfield, W. J. Hehre, J. A. Pople, *J. Chem. Phys.* 1971, 54, 724-728.
- (9) W. J. Hehre, R. Ditchfield, J. A. Pople, *J. Chem. Phys.* 1972, 56, 2257-2261.
- (10) P. C. Hariharan, J. A. Pople, *Theor. Chem. Acc.* 1973, 28, 213-222.